High-Level Control Algorithms for Maximising Energy Efficiency of Solar Nano-Grids Designed for Energy Access

Cephas Samende

Linacre College

University of Oxford

A thesis submitted for the degree of

Doctor of Philosophy

Trinity 2020

Abstract

Peer-to-peer interconnection of households having on-site batteries, four-port DC-DC converters and solar panels to form four-port DC-DC converter-enabled solar nano-grids is an emerging bottom-up approach for providing affordable energy access to rural areas. However, power losses which include battery charge and discharge losses, distribution losses and converter losses are one of the technical barriers hindering the practical deployment and operation of solar nano-grids in rural areas. Power losses reduce the energy efficiency of solar nano-grids. This research aimed to answer the following research question: *What control algorithms can be developed to address the problem of maximising energy efficiency of four-port DC-DC converter enabled solar nano-grids that are designed for energy access?*

Solar nano-grids with star and hybrid distribution network configurations were considered in this research. Three novel high-level control algorithms were developed to answer the research question. The first one was a centralised control algorithm, the second one was a quasi-consensus based distributed control algorithm and the third one was a distributed state-of-charge based droop control algorithm. Numerical and simulation results carried out in Python showed the effectiveness of the developed control algorithms for addressing the research question through the considered solar nano-grid configurations.

The first and second control algorithms addressed the research question for the star solar nano-grid configuration through optimisation. Firstly, a high fidelity steady-state model of the solar nano-grid was developed and a new two-stage convex power loss optimisation problem was formulated. The formulated optimisation problem did not require either linearisation or convex relaxation of power flow equations, making it scalable and computationally efficient. Then, the first and second control algorithms were developed to solve the formulated optimisation problem in a centralised and quasi-distributed manner respectively.

The third algorithm addressed the research question for both the star and hybrid solar nano-grid configurations through balancing the state-of-charge of the batteries in a distributed manner. In this algorithm, household distribution voltages were adjusted in proportional to the state-of-charge of their local batteries, creating an automatic power flow between the households each time there was a slight change in the battery state-of-charge. Due to the automatic power flow between the households, the magnitude of current flow at every time instant in the solar nano-grid was low, thus, keeping the power losses to a minimum.

The present work aimed to contribute towards the universal energy access agenda by focussing specifically on the third target of the United Nation's Sustainable Development Goal 7 - doubling the global rate of improvement in energy efficiency by 2030. There is a lot of work that still needs to be done to achieve this goal. Nonetheless, the present research has made a significant step towards improving energy efficiency by developing control algorithms that minimise the solar nano-grid power losses.

Keywords: Energy access, solar nano-grids, four-port DC-DC converter, power losses, energy efficiency, state-of-charge balancing, centralised and distributed control algorithms.

Dedication

To my late brother, *Kennedy* and sister, *Ireen*. I miss you.

Acknowledgements

Sincere gratitude goes to my supervisor, Professor Malcolm McCulloch for his supervision, support and guidance during my DPhil study. Its beyond word to describe how much I have learnt from him. I would also like to thank Dr. Sivapriya M. Bhagavathy for the useful discussions, advice, encouragements and feedback on my scholarly writing.

Thanks to my family: Mwambwa (aka MAS), Natania, Chrispin, Luwi and Evans for being patient and showing some love to me during the dark moments of my journey. Special thanks goes to my mum and dad for the unwavering support and belief in me. I am also most grateful to the Rhodes Trust for the financial support rendered to me during my studies. To the entire EPG crew, Dr. Norbert Nthala and many other friends who have been with me during this journey, I say thank you. Above all, many thanks goes to the Almighty God Jehovah for giving me life.

Contents

List of Figures

List of Tables

Nomenclature

Abbreviations

A	Amperes
AC	Alternating Current
BMS	Battery Management System
CC	Constant Current
CBDG	Central Battery with Distributed Generation
CGCB	Central Generation with Central Battery
CGDB	Central Generation with Distributed Battery
CO_2	Carbon dioxide
CV	Constant Voltage
DC	Direct Current
DGDB	Distributed Generation with Distributed Battery
EA	Elektro Automatik
EL	Electronic Load
ESR	Equivalent Series Resistance
FPC	Four Port DC-DC Converter
FPGA	Field Programmable Gate Array
FBC	Full Bridge Converter
FLIA	Fast Lambda Iteration Algorithm
FVIA	Fast Voltage Iteration Algorithm
GDP	Gross Domestic Product
GD	Gate Driver
GIS	Geographic Information System
HBC	Half Bride Converter
HDI	Human Development Index
HFT	High Frequency Transformer
HVDC	High Voltage Direct Current
ICT	Information and Communication Technology
ILCA	Incremental Loss Consensus Algorithm
IEA	International Energy Agency
I-V	Current-Voltage
KCL	Kirchhoff's Current Law
KHz	Kilo-Hertz
KKT	Karush-Kuhn-Tucker
kW	Kilowatt
kWh	Kilowatt-hour
Kg	Kilo-gram
km	Kilo-meter
KVL	Kirchhoff's Voltage Law

LED	Light Emitting Diode
m	Meter
MOSFET	Metal Oxide Semiconductor Field-Effect Transistor
MPP	Maximum Power Point
MPPT	Maximum Power Point Tracking
MT	Metric tonne
MTF	Multi-Tier Framework
MW	Mega-Watt
NSE	Natural Steinmetz Extension
OBDP	Optimal Battery Dispatch Problem
OCFP	Optimal Current Flow Problem
OCP	Over Current Protection
OPF	Optimal Power Flow
OVP	Over Voltage Protection
PAYG	Pay-As-You-Go
P2P	Peer-to-Peer
PI	Proportional-Integral
PS	Power Supply
PV	Photo-Voltaic
P-V	Power-Voltage
QCDCA	Quasi-Consensus Based Distributed Control Algorithm
RMS	Root Mean Square
SSA	Sub-Saharan Africa
SDG	Sustainable Development Goal
SHS	Solar Home System
SoC	Sate-Of-Charge
STC	Standard Test Conditions
TV	Television
TABC	Triple Active Bridge Converter
UN	United Nations
UNDP	United Nations Development Programme
US	United States
V	Volts
VCA	Voltage Consensus Algorithm
W	Watt
Wh	Watt-hour
Wp	Watt-peak

Chapter 1

Introduction

This thesis answers the following research question:

What control algorithms can be developed to address the problem of maximising energy efficiency of four-port DC-DC converter enabled solar nano-grids that are designed for energy access?

To give context to the present research, Section 1.1 defines energy access and its importance to human development. It then spells out the enormous need for advancing energy access efforts in remote areas, particularly those in sub-Saharan Africa (SSA) through off-grid energy systems such as solar nano-grids. Section 1.2 provides a description of a Four-Port DC-DC Converter (FPC) enabled solar nano-grid that is considered in the present research. The section concludes by situating the present research into context, covering the power loss problem of solar nano-grids and the challenges to be considered before addressing the power loss problem. Having set the research problem, the scope of the research is described in Section 1.3. A breakdown of the primary research question into five secondary research questions which are subsequently answered in each chapter, forming the thesis structure is outlined in Section 1.4. Section 1.5 outlines the key contributions made to knowledge through the present research. Finally, Section 1.6 presents a list of published and submitted papers for publication which are a result of this research.

1.1 Context

1.1.1 Benefits of Gaining Access to Energy

The International Energy Agency (IEA), defines energy access as the “percentage of the country’s population that has a reliable, affordable and sufficient amount of electricity which is enough to supply a basic bundle of energy services - at a minimum, several light bulbs, phone charging, a radio and potentially a fan or television (TV) - and with the level of service capable of growing over time” [9].

Energy access is essential for increasing household incomes [10–15], creating new opportunities [13, 16], saving the environment [17–19] and enhancing the delivery of education and health services [20, 21]. For example, halving costs of kerosene, torches or candles by having access to solar lights would save US$50 billion for people living on less than US$2.50 per day [19]. These benefits are reflected in a positive correlation between the Human Development Index (HDI)[1] and the extent of energy access in a country as shown in Figure 1.1. Figure 1.1 shows that wealthier countries with high human development (HDI $>$ 0.8) such as

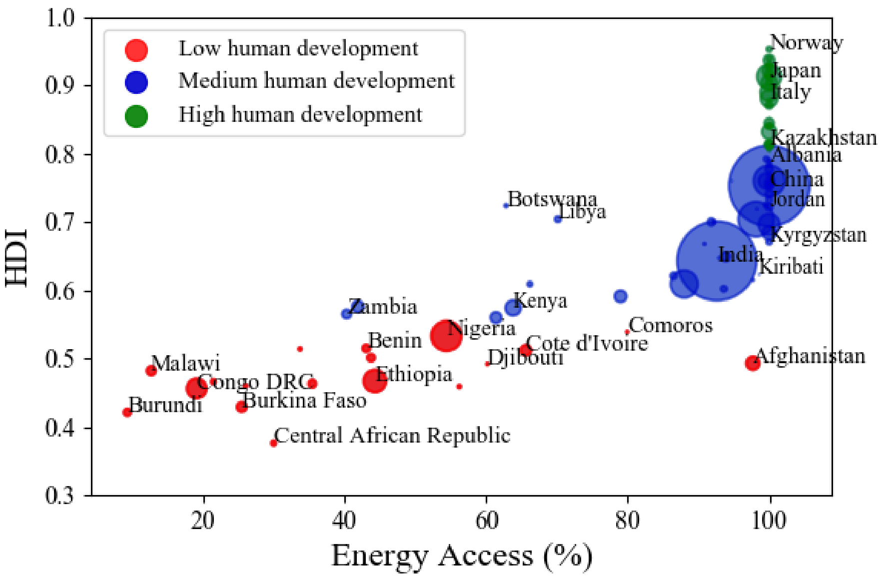

Figure 1.1: The HDI and energy access are closely linked, with a steep growth in HDI once a country reaches 100% energy access. The dot size is proportional to population. The author plotted the graph using population and energy access data from World Bank [1], and HDI data from the United Nations Development Programme (UNDP) [2].

---

[1] HDI is a summary measure of average achievement in key dimensions of human development: a long and healthy life, being knowledgeable and have a decent standard of living [2].

Norway tend to have high rates of energy access than poor countries (mostly those in SSA) with low human development (HDI < 0.55). Botswana and Libya are outliers because they have high Gross Domestic Product (GDP) per capita [22]. Energy access is therefore a key enabler of wealth creation and human development.

1.1.2 The Energy Access Problem

Unfortunately, even in 2019, about 840 million people (1 out of 7) in the world still lived without access to energy [9]. Figure 1.2 shows that the vast majority of these people live in SSA, particularly in the rural areas. In addition to the 840 million people lacking energy access, hundreds of millions either experience insufficient or unreliable energy due to challenges with the transmission and distribution infrastructure of their national grids [23]. Unreliable energy supply and costs associated with operation and maintenance, costs Africa for example, 2-4 percent of annual GDP [19].

To close this energy deficit gap, the United Nations (UN) through the adoption of the Sustainable Development Goal (SDG) 7 has set 2030 as a target year by which access to affordable, reliable, sustainable and modern energy for all must be achieved [3].

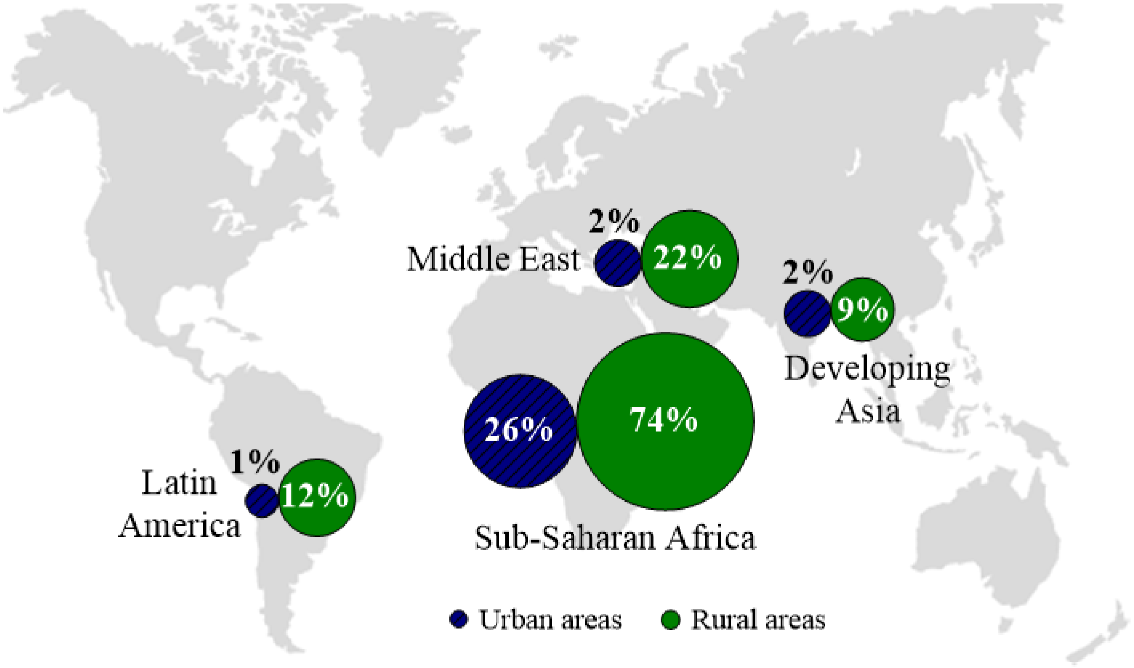

Figure 1.2: Proportion of the population in the Middle East, Latin America, Developing Asia and Sub-Saharan Africa without access to energy in 2018. The author made the image based on energy access data from the World Bank [1]

However, the 2020 SDG 7 tracking report [24] shows that with the current political will, population growth and financial commitments, other regions of the world except SSA are likely to achieve the energy access target by 2030; it will take SSA up to 2080 to achieve the same energy access target [19, 22]. If business continues as usual (before taking Covid-19 effects into account), one out of three people (approximately 530 million people) in the region will still live without access to energy in 2030 [3]. The World Bank reports that SSA requires on average about 60 million new people gaining access to energy every year and annual average investments of about US$55 billion in order to achieve the 2030 target - due to the population growth which is projected to grow by half a billion in 2040 [9, 19]. These figures demonstrate the enormous need for robust electrification efforts in SSA, especially those which target the populations in the rural areas where majority of the population without access to energy live and which are hard to reach by extending the national grid through the grid extension technology.

To date, off-grid energy systems, which are electrical power networks that can either operate autonomously using their own generation and distribution components or connected to the national grid, have proved to be the most cost effective solution for providing last mile energy access to both developing and developed countries [10]. The IEA predicts that if universal access to energy is to be achieved by 2030, 70% of new connections are expected to come from off-grid energy systems [25]. The main drivers pushing for the uptake of off-grid energy systems are:

- Concerns of climate change make it difficult to encourage electrification of un-electrified areas through existing national grids which mainly use fossil fuels such as coal and diesel.
- Off-grid energy systems mostly operate using renewable energy sources including solar, wind, biomass and small hydro, which are clean and readily available in most regions with high populations without access to energy. For example, Africa has an average sun radiation of 5.5 kWh per square metre per day [26].
- Off-grid energy systems are quick to deploy in sparsely populated and hard to reach

locations where extending the national grid is prohibitively expensive and may take many years to reach.

- Key components of off-grid energy systems including batteries, power electronic converters and solar panels are cheap on the global market due to mass production and development in technology [10].
- Off-grid energy systems attract high involvement of the private sector with successful business models such as the Pay-As-You-Go (PAYG) payment scheme [17].

1.1.3 Types of Off-Grid Energy Systems

The energy access needs of a household are well defined and measured beyond the conventional (have or have no energy access) binary metrics using a Multi-Tier Framework (MTF)[2] [5]. Table 1.1 shows the MTF, where Tier 0 (even though it is not shown in the table) represents a household that has no energy access and the successive higher tiers represents the increase in household energy access level, with Tier 5 being the highest. The MTF helps to capture the different types of energy systems that can be used to deliver energy access while satisfying the energy demands of the desired energy services and appliances. For example, solar lights (with power capacities between 3 W and 49 W) are well suited for providing energy access to households with Tier 1 appliances while national grids (with unlimited power capacity) are more appropriate for providing energy access to households with Tier 5 energy services and appliances.

There are two main types of off-grid energy systems that can be used to provide energy access, namely stand-alone and mini-grid/micro-grid energy systems. Stand-alone systems are small autonomous energy systems that can be directly installed on a single household or appliance to supply immediate energy [3]. They may operate autonomously or connected to a national grid. Stand-alone systems include pico solar products, Solar Home Systems (SHS) and mobile rechargeable batteries, which differ based on the amount of installed generation

---

[2] The MTF tracks the energy access needs of a household beyond the conventional (have or have no energy access) binary metrics which does not show whether the household that has energy access actually uses the energy for human development or does not use the energy at all or uses the energy to power some appliances while using charcoal for cooking.

Table 1.1: Multi-tier Framework for measuring energy access [5]

Energy access level	Tier 1	Tier 2	Tier 3	Tier 4	Tier 5
Energy services and appliances	Very low-power appliances (e.g., Task lighting, phone charging and radio)	Low-power appliances (e.g., Multi-point general lighting, fan, TV and computer)	Tier 2 & any medium-power appliances (e.g., Food processor, rice cooker and refrigerator)	Tier 3 & any high-power appliances (e.g. Washing machine, sewing machine, water pump, hair-dryer)	Tier 4 & any very high-power appliances (e.g., air conditioning units, water heater, electric cooker)
Power capacity in watts (W)	3 - 49	50 - 199	200 - 799	800 - 1,900	$\geq$2,000
Daily consumption capacity in watt-hour (Wh) per household	12 - 199	200 - 999	1,000 - 3,300	3,400 - 8,100	$\geq$8,200
Annual consumption capacity in kilo-watt-hour (kWh) per household	4.5 - 72	73 - 364	365 - 1,249	1,250 - 2,999	$\geq$3,000

capacity. Pico solar products such as solar lanterns have up-to 11 Wp installed generation capacity capable of providing energy access to Tier 1 appliances [17] . SHSs consist of a solar panel and battery with greater than 11 Wp installed generation capacity [17]. They can provide energy access of up-to Tier 3 depending on the installed generation capacity. Mobile rechargeable batteries do not have any installed generation capacity but rely on charging stations for charging; they are generally used to meet the energy demands of up-to Tier 2 appliances depending on the battery size [27]. The key advantage of stand-alone systems is that they can be deployed in hard to reach locations and provide affordable immediate energy access to a user without complex installations. However, they can hardly supply power to beyond Tier 2 appliances due to limited installed capacity. They also lack diversity in energy generation, resulting in un-utilised capacities due to oversized generation and energy storage systems [28].

Mini-grid or micro-grid energy systems are local grids usually with three phase power transmission and distribution infrastructure providing energy access to a specific settlement [3]. Similar to stand-alone systems, they also operate either autonomously or connected to a national grid. There is no proper distinction between mini-grid and micro-grid energy systems. However, micro-grids have a lower installed generating capacity than mini-grids. The key advantage of mini-grid or micro-grid energy systems is better degree of quality and energy supply reliability than stand-alone systems, which is capable of providing energy access to all the tiers in Table 1.1 due to high installed generation capacity of up-to 10 Mega Watts (MW) [9, 29]. The main disadvantage of mini-grid or micro-grid energy systems is the high electricity costs and upfront investment costs in sparsely populated and hard to reach areas due to the need to construct a generation plant and distribution infrastructure [30].

The choice between stand-alone and mini-grid or micro-grid energy systems also depends on other factors such as distance to the national grid, complexity of terrain and income of customers as illustrated in Figure 1.3. As shown in Figure 1.3, stand-alone systems are the most cost-effective option for providing energy access to communities that belong to a ‘stand-alone system space’, which is characterised by scattered households, complex terrains, longer distances to the national grid, low population densities and incomes. Grid extension, mini-grids and micro-grids are cost effective for communities that are clustered together with high population densities and economic growth potential. Since most remote and hard to reach areas belong to the stand-alone system space, stand-alone systems are

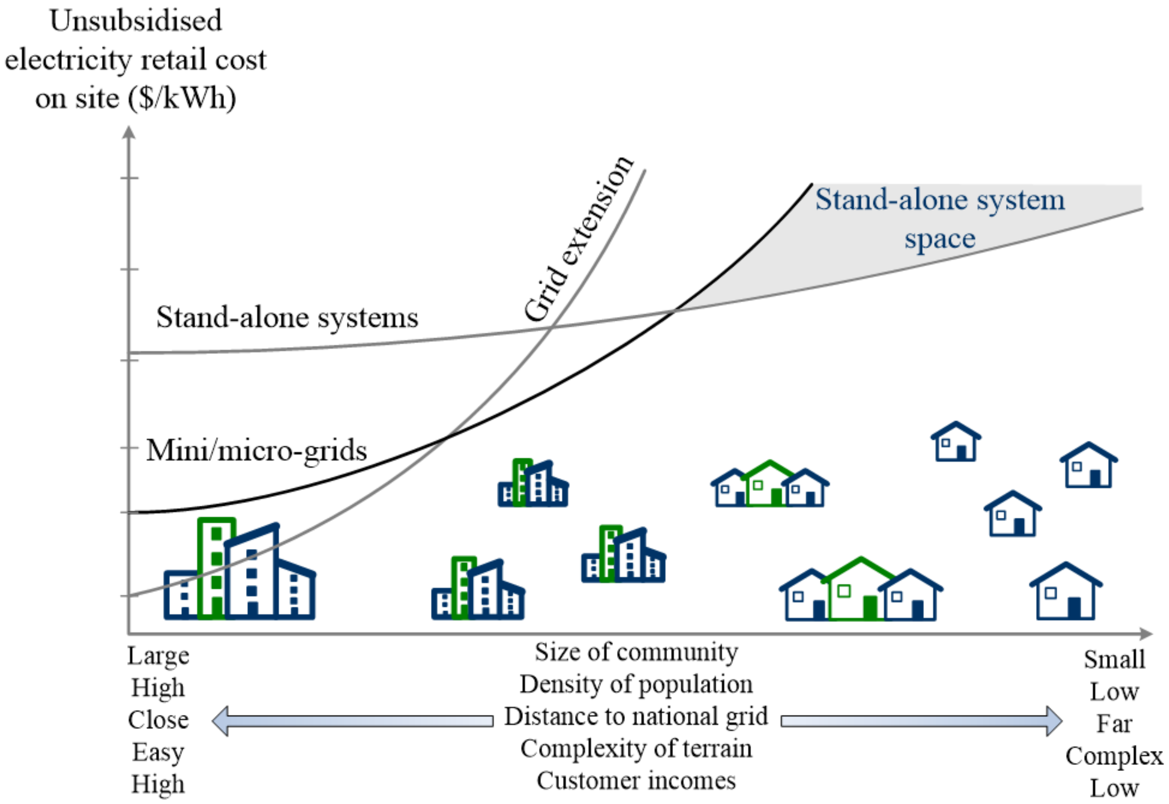

Figure 1.3: Factors influencing the choice of stand-alone and mini-grid or micro-grids for energy access (Author’s own depiction based on [3]).

therefore the best option for providing affordable energy access to such areas.

The illustration in Figure 1.3 is consistent with the results published in [30, 31] which shows that stand-alone systems are the cheapest option for providing energy access to low-density communities that have Tier 1 and Tier 2 energy access levels. Grid extension, mini-grids and micro-grids are cheaper options for providing energy access to high-density communities (above 50 households/km^2) having Tiers 3, 4 and 5 energy access levels.

Despite the suitability of stand-alone systems for providing energy access to the rural communities, their limitations cannot be overlooked. The major drawback of stand-alone systems is their failure to provide affordable energy access to beyond Tier 2 energy access levels (which are crucial for rapid poverty reduction and economic growth) due to significant increase in system size and cost as the household energy needs increase up the energy ladder towards Tier 5 [32].

To address the aforementioned drawback, an innovative solution under research is a swarm electrification approach [33], which is based on the fact that households in rural communities are clustered together in groups (villages) having between three and hundred households. If two or more households in a village have stand-alone systems, the approach seeks to remedy the aforementioned drawback by gradually interconnecting the stand-alone systems forming a diverse peer-to-peer (P2P) grid (hereafter referred to as solar nano-grid), which can expand towards a national grid by interconnecting with other solar nano-grids or mini-grids, and eventually interconnect with the national grid. This kind of a bottom-up approach supports the bidirectional exchange of energy between households and offers the following advantages [34]:

- **Increased diversity in power generation and consumption:** Households do not generate the same amount of energy (due to different installed generation capacities) and do not use energy at the same time (due to different types of appliances). This creates different energy generating and consumption patterns (profiles) among the households, which increases power generation diversity as the number of connected households increase.

- **Opportunity for energy trading:** Due to the bidirectional energy exchange, households can trade energy with their neighbours especially at night when there is no solar to earn an income. For households which are financially stable, this can be a motivation to invest in more generation and storage capacity.

- **Supports productive use of energy:** Due to the cumulative effect of multiple battery units in the solar nano-grid and the diversity in power generation and consumption, high power rated appliances in Tier 3 and above can be supported without necessarily increasing the existing power generation and storage capacity. A surplus or deficit of power in one household can be balanced by a second household through power exchange.
- **Supports the connection of new households without stand-alone systems:** Some households may not have access to a complete stand-alone system for cost reasons but may be willing to gain access to energy either for free or at a fee. These can be connected to the solar nano-grid to benefit from the pool of energy sources created by households with stand-alone systems.

The solar nano-grid concept is one of the six key research areas identified by the World bank that require further research if the SDG 7 is to be achieved by 2030 [10].

1.2 Four-Port DC-DC Converter-Enabled Solar Nano-Grid

There are several configurations of solar nano-grids in literature. These will be discussed in Chapter 2. In this research, a solar nano-grid that uses DC technology and FPCs to manage the power flow is considered for the reasons outlined in Chapter 2.

1.2.1 Structure of the considered Solar Nano-Grid

Figure 1.4 shows the structure of the considered solar nano-grid, which is being piloted in Kenya by the University of Oxford [35].

It consists of multiple households (labelled H1 to H*n*) that are connected to a central hub. The households and hub all have batteries as energy storage units in order to charge power

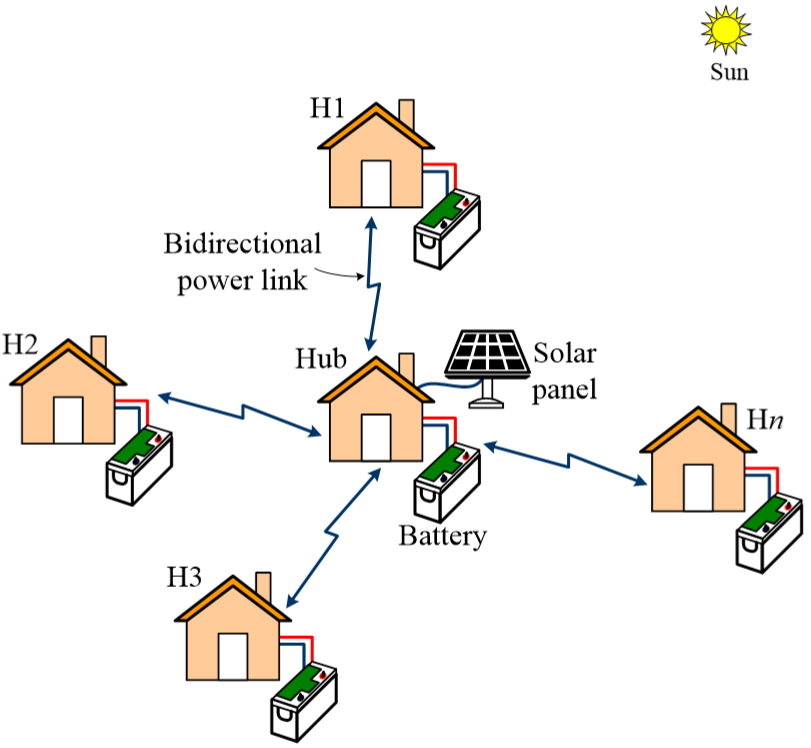

Figure 1.4: Solar nano-grid configuration where households (H1 to H*n*) are connected to a central hub.

whenever there is excess generation from the solar panels and to discharge power otherwise. The battery in the hub should be small in size to allow the generated solar power to also charge the neighbouring batteries. The type of batteries used in this research are Lithium-ion batteries due to their light weight, low self-discharge and capability of storing huge amounts of energy in comparison to their weight and volume [36]. This makes them suitable for deployment in hard to reach locations where performance and weight of the batteries is of importance. To cut the upfront investment costs, solar panels are optional at the households but mandatory at the hub. That is, a household can choose to either install solar panels or not depending on the household's financial situation. For consistency, the optional connectivity of solar panels at the households is not shown in Figure 1.4.

The hub can be a village headman's house or a communal facility such as a market, clinic, shop, palace or Telecom tower having up-to Tier 5 energy access level. The hub is connected to the surrounding households in a spoke and hub arrangement. This reduces the cost associated with the few number of distribution lines, making the solar nano-grid affordable. In addition, the spoke and hub configuration prevents energy theft especially in crowded places such as markets through illegal connections. The distance between each household and the hub can be up-to 600 m. Power flow in the distribution lines is bidirectional thereby allowing power exchange between a household and the hub and also between households. This enables a very smart grid where each household can both optimize its energy use and provide community energy services. A maximum distribution voltage of 120 V is adopted for use in order to make the distribution lines safe to touch by users [37]. The hub can be grid-ready to enable the connection of the solar nano-grid to the national grid when it arrives to the village or community. When similar solar nano-grids exist in the vicinity, these can be interconnected to form a large and diverse solar micro-grid.

There are however, two key components of the considered solar nano-grid which are not shown in Figure 1.4, namely, the FPC and solar nano-grid controller. These are briefly described as follows.

Four-Port DC-DC Converters

At the heart of the considered solar nano-grid are low cost FPCs which implement control decisions to provide active power flow control within and between the households and the hub. Figure 1.5 shows the integration of appliances (hereafter referred to as DC loads or loads), solar panels, batteries and the distribution network in each household and hub using the FPC.

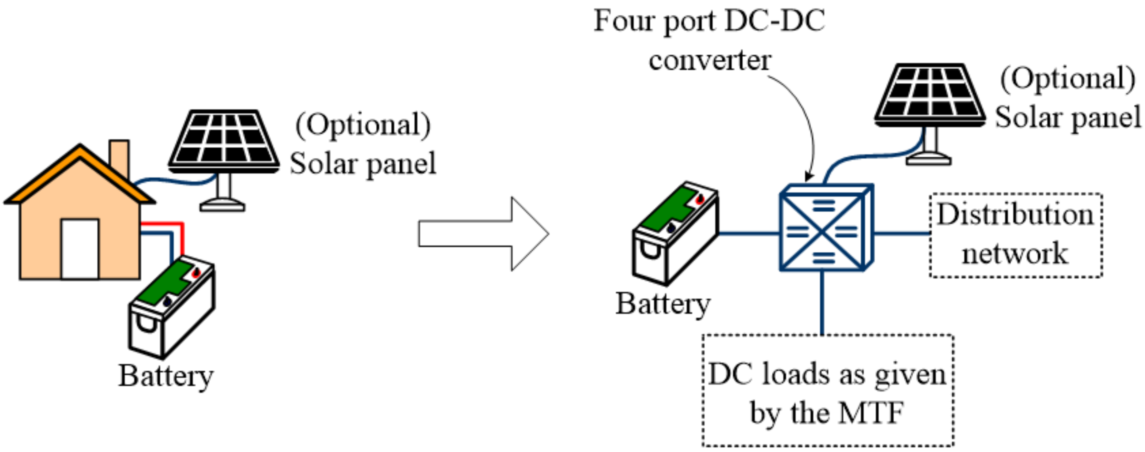

Figure 1.5: Integration of the solar panel (which is optional in households), battery, DC loads and the distribution network using a four-port DC-DC converter.

Figure 1.6 shows a detailed circuit diagram of the FPC, which has been developed by the Oxford University team working on the solar nano-grid pilot in Kenya. It consists of a Triple Active Bridge Converter (TABC) and four Half Bridge Converters (HBC), namely; HBC-A, HBC-B, HBC-C and HBC-D. The switches; $Q_1, \ldots, Q_{12}$ and $Q_a, \ldots, Q_h$ are all Metal Oxide Semiconductor Field-Effect Transistor (MOSFET) switches. The MOSFET switches operate in synchronous rectification mode where they allow a reverse current to flow from the source to the drain provided that a sufficient gate to source voltage is applied to the MOSFET [38]. The terminals of the HBCs A, B, C and D constitute the four ports 1, 2,3 and 4 of the FPC respectively. The TABC consists of three Full Bridge Converters (FBC), namely FBC-A, FBC-B and FBC-C which are coupled through a High Frequency Transformer (HFT) with turns ratios $n_1 : n_2$ and $n_1 : n_3$. The TABC and HBCs allow bidirectional current flow through the ports. Since the solar panels can only generate power and the considered DC loads can only consume power, the FPC has a total number of sixteen different practical operating modes. The TABC and the four HBCs are operated as a single power processing stage. This has advantages of reduced cabling costs, size and volume due to the reduced number of physical separate converters and their associated circuits. The in-depth operation of the FPC is described in Chapter 3.

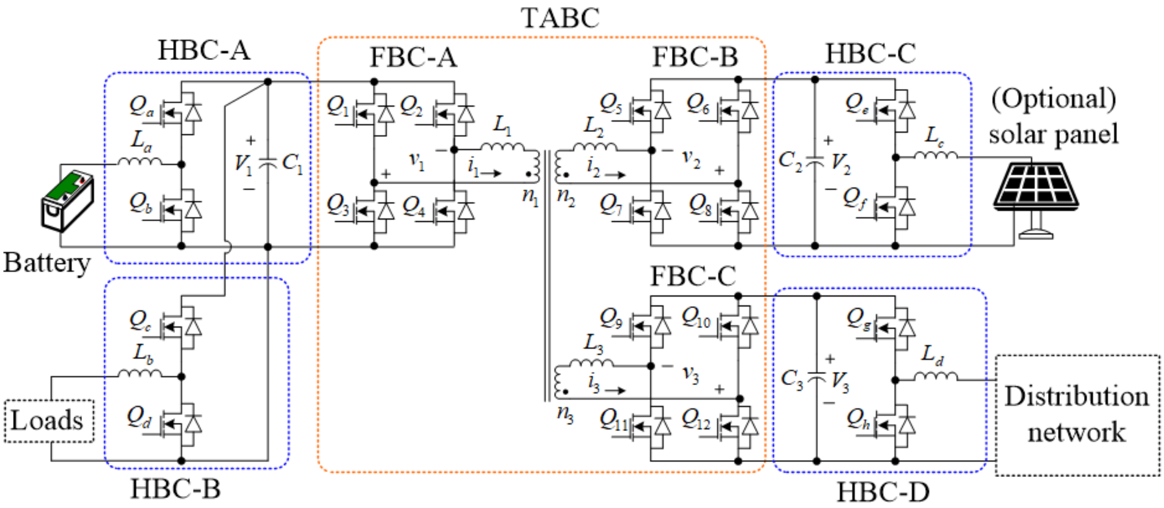

Figure 1.6: Showing detailed circuit diagram of a four port DC-DC converter integrating the battery, DC loads, distribution network and the solar panel.

Central to the structure of the considered FPC is the presence of the HFT which allows power transfer between the ports to happen through the principle of magnetic induction.

Due to the magnetic coupling between the ports, port 3 connecting the solar panel can be left open in households that do not have solar panels without affecting the overall operation of the FPC. Further, the magnetic coupling allows the power flow through the four ports to be controlled independently. For example, port 4 connecting the distribution network is controlled to regulate the distribution voltage between 100 V and 120 V, thus controlling the power flow in the distribution network. Port 3 is operated to regulate the solar panel output voltage between 24V and 35 V. Port 2 connecting the DC loads is operated to maintain a constant load voltage of 12 V, which is a common voltage rating for most DC loads in rural areas including LED bulbs. Port 1 connecting the battery is not regulated, allowing the battery to charge and discharge power whenever there is a power surplus or a power deficit in the household respectively. Furthermore, HFT helps to match the different voltage levels of the solar panel, distribution network, DC loads and battery through the turns ratios, thus simplifying their interconnection.

In practice however, the use of a FPC at the hub easily suffers from power limitations when the solar nano-grid grows in size. This requires either an oversized FPC before hand which can be expensive and can cause high power losses or frequent replacement of the FPC with a higher power rated FPC each time there is growth in energy demand, resulting in interrupted operations. To circumvent this drawback in practice, the solar nano-grid components at the hub can be interfaced via separate dual-port converters [39], which can be upgraded separately without interrupting the operations of the whole solar nano-grid.

Solar Nano-Grid Controller

Key to the successful operation of the solar nano-grid is the solar nano-grid controller (even though it is not shown in Figure 1.4), which is a hardware device that runs a set of predefined control algorithms in form of computer programs to give control decisions to the FPCs. Thus, the solar nano-grid controller is the ‘brain’ of the solar nano-grid based on which the practicability and deployment of the solar nano-grid depends.

Like all power systems, proper operation of the solar nano-grid must obey different control objectives including:

- Supervision of power flow in the solar nano-grid to ensure that power generation matches load demand at every given time interval.
- Control of voltage and current for power flow within and between households and hub.
- Optimisation of power loss.
- Smooth transition of a household and hub between autonomous and interconnected operation.

These objectives are of different time scales and control complexities. Practically, the objectives can be achieved through the widely accepted multilevel control scheme [40], which generally consists of two control levels; high level control and low level control as shown in Figure 1.7. The high level control coordinates the efficient power flow between the households at time scales greater than a second [41]. It also facilitates the optimal operation of the solar nano-grid by minimising specific cost functions e.g. the power loss function. The low level control is directly interfaced with the FPCs. It uses control decisions from the high

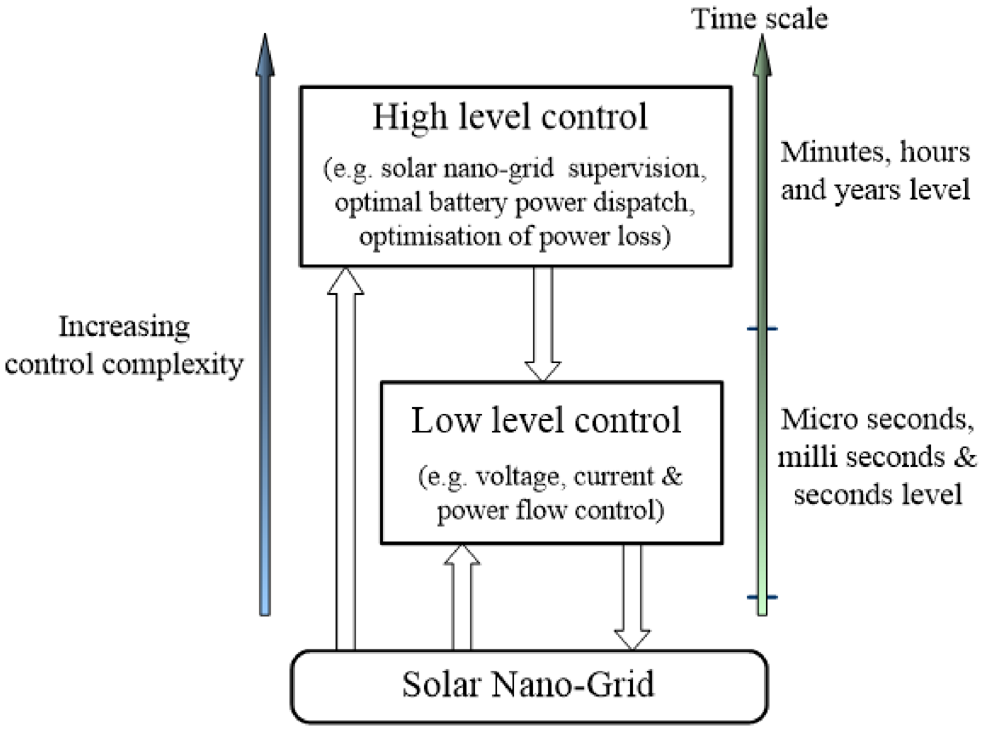

Figure 1.7: Multi-level control scheme of the solar nano-grid.

level control and sensor information to change the operating state of the solar nano-grid by adjusting the terminal currents and voltages of the FPCs.

The various control methods that can be implemented at every control level are detailed in Chapter 2.

1.2.2 Power Loss Problem in Solar Nano-Grids

Power has to be distributed from the solar panels of the solar nano-grid through the FPC and distribution lines to the appliances and batteries for consumption and storage respectively. Similarly, power has to be distributed from batteries through the FPC and distribution lines to the appliances when power generated from the solar panels is less than the appliances' power demand. However, at every stage of this distribution process, heat is produced in the associated components as current passes through them, which leads to power losses. Unfortunately, no matter how well the solar nano-grid is designed, power losses will always be present because even the best metallic conductors (e.g. copper and silver) have some resistance, which produces heat when current is passed through them.

The main types of power losses in the solar nano-grid are distribution line losses, battery charge and discharge losses and FPC losses. Distribution line losses occur as power flows through the distribution lines during the power distribution process due to the resistance of the distribution lines [37, 42, 43]. Battery charge and discharge losses occur in the battery during the charging and discharging process due to the inherent internal resistance [44–46]. FPC losses occur during the conversion of current and voltage from one form to another in the FPC [47–49].

The power loss problem is one of the key technical challenges that is experienced by solar nano-grids deployed in off-grid communities, that is, in the context of cost and energy saving. The goal of solar nano-grids is to provide affordable and reliable energy access for productive uses. However, due to the scalable nature of the solar nano-grid, low distribution voltage levels and significant distances that exist between households in most communities, the power loss problem still limits the progress of solar nano-grids in rural communities as follows:

- **Low distribution voltage levels:** According to [37], distribution voltages lower than 120 V are reported to be the most appropriate distributions voltage levels for solar nano-grids in off-grid communities. This is because, they are considered safe to touch by the users without the need of advanced grounding and protective conductors, which are often expensive. However, studies have shown that distributing power at voltages lower than 120 V significantly increases the distribution power losses. The power losses are higher as the distribution voltage levels get lower than 120 V as reported in [37, 42, 43]. On the other hand, distribution voltage levels greater than 120 V greatly reduce the power losses as reported in [50–56]. However, higher voltages are dangerous and require advanced hardware and protection systems because of significant user and equipment safety implications. This can be expensive particularly for solar nano-grid that are supposed to be affordable in order to accelerate the energy access agenda. Thus, there exists a trade-off between power losses and user safety.

- **Significant distribution distances:** The distance between households has been cited in [57, 58] as the barrier for deployment of solar nano-grids in off-grid communities. The distance between households in rural villages can be in the range of 0.1-2 km as reported in [59, 60]. The distance between villages range from 600 m to 5 km [59]. For a given distribution line material, it is well known that its resistance increases linearly with distance. Since distribution power losses are proportional to the resistance of a distribution line, the losses also increase linearly with the distribution line distance. Owing to the low distribution voltage levels in the solar nano-grid, the losses are significant for most of the distribution line materials and distances [43]. Studies however indicate that using distribution line conductors with larger wire gauge areas can significantly reduce the losses. In [42], it is shown that a 2.5 mm^2 wire can reduce the power loss by 40% compared to a 1.5 mm^2 when used to supply a load of 500 W. Similar results have been reported in [37, 43]. However, the cost of a distribution line conductor increases linearly with the increase in the wire gauge area [42]. The larger the wire gauge area the higher the cost per metre of the distribution line and the lower the power loss. Thus, there also exists a trade-off between the cost of the distribution line and the power loss.

- **Scalability nature of the solar nano-grid:** Generally, the total power loss of the solar nano-grid also depends on the number of interconnected households. The power loss can be small if one or two households are interconnected in the solar nano-grid. However, as the number of interconnected households increases, the total power loss can be significant owing to the increase in the number of distribution lines, batteries and FPCs, which all contribute to the total power loss.

Minimising the power losses can tremendously improve the energy efficiency of the solar nano-grid. This further can reduce the cost of providing energy access to rural areas because the saved energy can be used to supply extra households nearby without necessarily increasing the existing generation and storage capacity. Solar nano-grids can have energy efficiencies as low as 50% especially for distribution voltages less than 120 V [37], which certainly deserves consideration.

Nowadays, energy efficiency improvement regardless of the power system in consideration has become countries' top priority because of its critical role in boosting economic growth, addressing the energy access problem and avoiding greenhouse gas emissions [61]. Studies indicate that a 1.2% improvement in the global energy efficiency is equivalent to a gain in global GDP of about US$1.6 trillion [61]. In fact energy efficiency improvement is the third target in the UN's SDG 7 agenda - doubling the global rate of improvement in energy efficiency by 2030 [3].

For a solar nano-grid that is yet to be built, energy efficiency can be improved at the design stage by optimising the solar nano-grid components, i.e. FPCs, loads, batteries and distribution lines with efficiency as the design parameter [62]. Recent studies indicate that the upfront cost of off-grid energy systems including solar nano-grids can be reduced by as much as 50% if efficient components are used [63]. For a solar nano-grid in operation, energy efficiency improvement for the entire system can be achieved by coordinating the operation of the solar nano-grid components in order to minimise the power losses through an appropriate control strategy. The aim of this research was to develop appropriate control algorithms that can minimise power losses of an operational solar nano-grid.

1.2.3 Challenges of Minimising Power Losses in the Considered Solar Nano-Grid

Addressing the power loss problem in the considered solar nano-grid is however a challenging control task for several reasons.

Constraints of Battery Storage Units

Different from the DC load and solar panel, a battery behaves like an energy source when it discharges power (supplying power to the network) and as a DC load when it charges power (absorbing power from the network). It has a maximum power that it can be charged and discharged with at any given time instant as one of its constraints. Exceeding these charge and discharge power limits leads to overheating and subsequent failure of the battery. Another battery constraint is its State-of-Charge (SoC) that indicates the charge level just like fuel gauges do in motor vehicles e.g. run by diesel. That is to say, the battery has a limit too on the amount of energy it can store in a given period of time. The SoC is maximum when the battery is fully charged and it is minimum when the battery is empty. The battery SoC at every time instant must be maintained within the maximum and minimum SoC range to avoid over-charging and over-discharging the battery respectively.

In the solar nano-grid considered in Figure 1.4, batteries are not directly controlled so that they can charge and discharge power whenever and wherever there is need. Yet even when they continue doing so, their constraints at every time instant must be carefully monitored, making sure that the constraints are not violated in order to prolong the lifetime of the batteries. This increases the computational time of the control problem.

Intermittency of Power Generation

It is well known in literature that power generated from the solar panels is intermittent in nature, varying at every time instant with changes in solar irradiance and atmospheric temperature. This introduces a time-varying power mismatch between the generated power and the load demand. However, for a stable operation of the solar nano-grid, power generation must always be equal to the prevailing load demand at every time instant. This means that the designed control algorithm must be fast enough and capable of always matching power generation to the load demand. Moreover, the lack of a national grid connection to the solar nano-grid means that there is no substation with unconstrained power injection that would compensate for any power mismatch in the solar nano-grid.

Non-Linear Power Flow Equations

Power flow equations in DC power systems including solar nano-grids are inherently non-linear and non-convex [64, 65]. This increases the complexity of the power loss problem.

Scalable Solar Nano-Grid

A solar nano-grid is always under constant growth through additions of extra households as it provides energy access to off-grid communities. This increases the number of batteries in the solar nano-grid, which in turn increases the control dimensionality. In addition, the growth of the solar nano-grid also means that its configuration can change with time due to physical and technical constraints such as position of the households and distance between the households. Designing a control algorithm that supports this growth regardless of the configuration taken by the solar nano-grid at any given time is a challenge.

1.3 Scope of this Research

The considered solar nano-grid configuration shown in Figure 1.4 has all the households connected to the central hub. This is technically possible if there are few households in the served community. However, as the size of the solar nano-grid grows to serve communities with a large number of households, radial connection of all the households to the hub might not be possible due to the location of the households. Households that are located far away from the hub may be suitably served with energy if they are connected to their neighbours than directly connecting them to the hub in order to reduce the distribution line loss and the cost of the long distribution line.

In this research, two different solar nano-grid configurations, namely star and hybrid configurations with increasing levels of complexity are therefore considered:

- **Star configuration:** In this configuration, all the households are connected to the central hub as shown in Figure 1.4. Thus, it is more suitable for a community where radial connection of the households to the hub is both physically and technically possible.
- **Hybrid configuration:** Figure 1.8 shows this kind of a solar nano-grid configuration. It consists of some households that are connected to their neighbours due to distance and other technical challenges such as voltage drops. The configuration is more suitable for a large community with households clustered together.

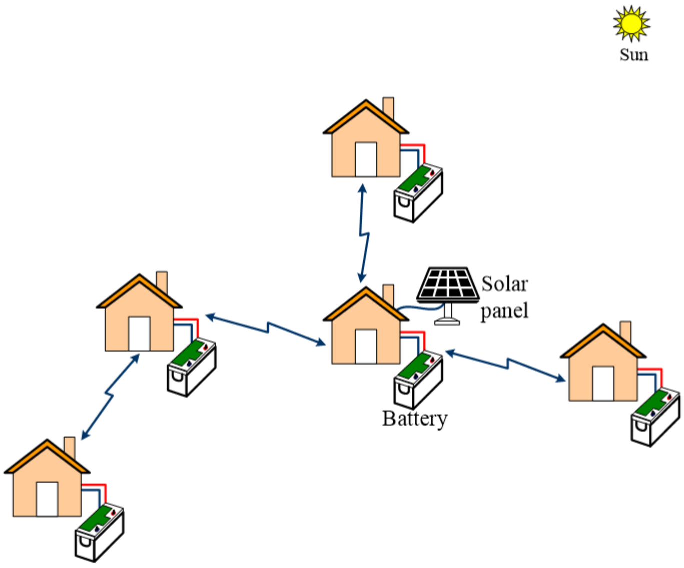

Figure 1.8: Hybrid solar nano-grid configuration where some households are connected to their neighbours.

The focus of this research is to develop novel high level control algorithms that can be used to minimise power losses in each of the considered solar nano-grid configurations while considering the challenges outlined in Subsection 1.2.3 and other relevant solar nano-grid constraints including voltage limits. The developed algorithms for the configurations form Chapters 3, 4, 5 and 6 of this thesis.

The developed algorithms are intended to run in the high level control of the multi-level control scheme shown in Figure 1.7, providing optimal reference control signals to the low level control. That means, the design of the low level control which includes the low time scale dynamics (less than a minute) of the solar nano-grid is beyond the scope of the current research.

The success of the developed algorithms is based on their ability to 1) facilitate power exchange while obeying operational constraints in the considered solar nano-grid configurations, 2) minimise power losses during power exchange by comparing the results where possible to those obtained from other existing control methods, and 3) weakly depend on communication networks for reliability and cost reasons. Since the developed algorithms are to be implemented in the high level control, simulation results of the considered solar nano-grids are sufficient to verify the performance of the developed algorithms. Where a communication network is used, its design and how information is handled over the associated communication links including cyber security issues is out of scope of this research. In addition, the protection system of the considered solar nano-grid configurations is not addressed.

This research neither intends to design and size the components of the considered solar nano-grid configurations nor does it intend to develop household load profiles. The developed control algorithms are intended to be capable of minimising the power losses of the considered solar nano-grid configurations regardless of design and size of the components involved. Thus, existing components and pre-known daily load and solar irradiance profiles are used for verifying the effectiveness of the developed algorithms. The influence of the stochastic nature of power generation and the need for forecasting power generation and load demand on the accuracy of the results is not addressed.

1.4 Thesis Outline

The over-arching research question investigated in this research therefore is:

What control algorithms can be developed to address the problem of maximising energy efficiency of four-port DC-DC converter-enabled solar nano-grids that are designed for energy access?

The FPC-enabled solar nano-grid configurations considered in this research are shown in Figure 1.4 and Figure 1.8. Each chapter of this thesis contributes towards answering the over-arching research question through the considered solar nano-grid configurations and the following five secondary research questions:

- *How can the solar nano-grid e.g. with a star configuration as shown in Figure 1.4 be modelled at steady-state and have a convex power loss optimisation problem formulated?*
- *How can the power losses of the star solar nano-grid configuration be quantified and minimised?*
- *How can the power losses of the star solar nano-grid configuration having many households be minimised?*
- *How can the power losses of a solar nano-grid that has a hybrid configuration as shown in Figure 1.8 be minimised?*
- *Is there an all-in-one control algorithm that can reduce the power losses of a solar nano-grid that has an arbitrary configuration and number of households?*

Figure 1.9 shows a graphical summary of the thesis outline and how different thesis chapters combine towards answering the over-arching research question. The work done by other researchers in literature that make a case for the current research is presented in Chapter 2.

In this research, efficiency of FPC-enabled solar nano-grids is maximised by minimising the solar nano-grid power losses which are discussed in Subsection 1.2.2. From an optimisation point of view, the solar nano-grid power loss problem can be considered as an optimisation problem. Thus, before addressing it, the power loss problem must first be formulated as a mathematical optimisation problem. However, to formulate it, a mathematical representation (model) of the solar nano-grid is needed. Chapter 3 therefore, presents the steady state model of the solar nano-grid and the formulation of the power loss optimisation problem. Since all the considered solar nano-grid configurations have similar components, only the solar nano-grid shown in Figure 1.4 is modelled. In Chapters 4 and 5, developed control algorithms that solve the power loss optimisation problem for the solar nano-grid

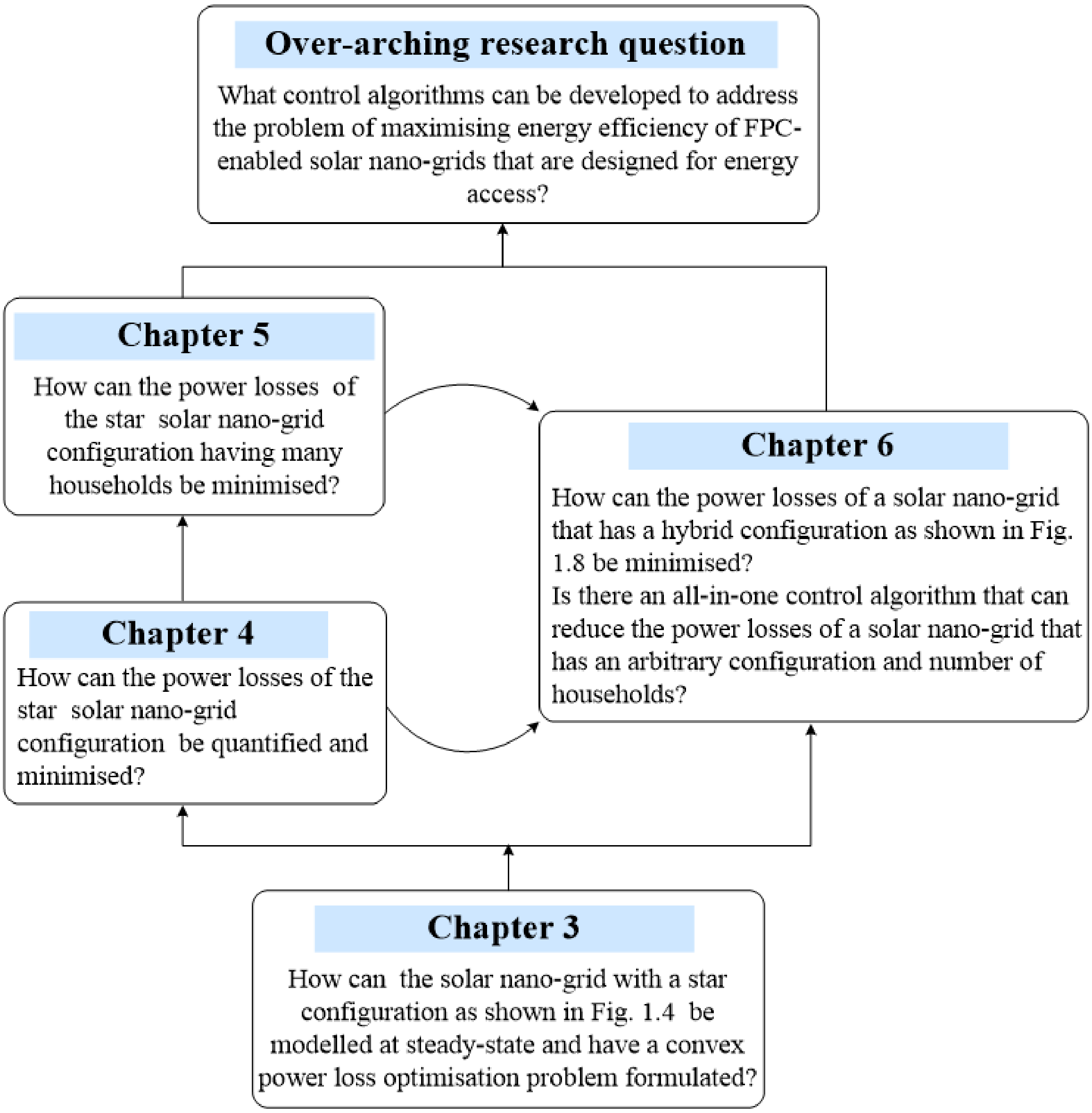

Figure 1.9: Thesis outline showing the secondary research questions and the chapters in which they are answered.

with a star configuration are discussed. Chapter 4 considers a star solar nano-grid configuration that has few number of connected households and shows how a centralised control algorithm can effectively minimise the power loss. In Chapter 5 the solar nano-grid with a star configuration is extended to include more households. A quasi-consensus based distributed control algorithm is presented so as to move away from the central decision making algorithm in order to increase resiliency of the individual households. In Chapter 6, the hybrid solar nano-grid configuration is considered and a fully distributed SoC based droop control algorithm is presented. The proposed algorithm addresses the solar nano-grid power loss problem in a distributed manner without having to solve a power loss optimisation problem.

The Chapters 3, 4, 5 and 6 all present technical content and performance analysis is performed in each chapter to verify the effectiveness of the developed control algorithms based on the performance metrics described in Section 1.3.

Finally, the thesis is concluded in Chapter 7 by assessing the extent to which the work has answered the overarching research question and highlighting some of the key issues to be considered for further understanding and work, which are critical for the maturity of solar nano-grid technology.

1.5 Thesis Contributions

The main contributions of this research are summarised as follows:

1. A realistic and high fidelity model of a FPC-enabled solar nano-grid is developed, which can be used for simulation and power flow studies (Chapter 3).

2. A detailed FPC power loss model is developed which can be used to optimise the design of the FPC (Chapter 3).

3. A simplified FPC loss model which is expressed as a quadratic function of power consumed by the DC loads is developed from experimental FPC loss results. The developed loss model is computationally efficient and suitable for real time applications (Chapter 3).

4. A convex power loss optimisation problem of the solar nano-grid which does not require either convex relaxation or linearisation of power flow equations is formulated (Chapter 3).

5. A centralised control algorithm which addresses the power loss problem of the solar nano-grid with a star configuration is developed and the power losses of the solar nano-grid are quantified (Chapter 4).

6. A quasi consensus-based distributed control algorithm is developed to address the power loss problem of the star solar nano-grid configuration having many households (Chapter 5).
7. A distributed state of charge-based droop control algorithm is developed to address the power loss problem of a solar nano-grid with arbitrary distribution network configuration such as the hybrid solar nano-grid configuration (Chapter 6).

1.6 List of Research Publications

The list of research publications relevant to this thesis along with the chapters which are based on them are as follows.

1.6.1 Journal Publications

1. C. Samende, S. Mothilal Bhagavathy, F. Gao, and M. McCulloch, ‘Decentralized Voltage Control for Efficient Power Exchange in Interconnected DC Clusters, IEEE Trans. Sustain. Energy, vol. 3029, no. c, pp. 113, 2020 (partly Chapter 6).
2. C. Samende, S. M. Bhagavathy, and M. McCulloch, ‘Power Loss Minimization of Off-Grid Solar DC Nano-GridsPart I: Centralized Control Algorithm’, in IEEE Transactions on Smart Grid, doi: 10.1109/TSG.2021.3108236 (Chapter 4).
3. C. Samende, S. M. Bhagavathy, and M. McCulloch, ‘Power Loss Minimisation of Off-Grid Solar DC Nano-GridsPart II: A Quasi-Consensus Based Distributed Control Algorithm’, in IEEE Transactions on Smart Grid, doi: 10.1109/TSG.2021.3111779 (Chapter 5).
4. C. Samende, S. M. Bhagavathy, and M. McCulloch, ‘Distributed State of Charge-based Droop Control Algorithm for Reducing Power Losses in Multi-Port Converter-Enabled Solar DC Nano-Grids’, in IEEE Transactions on Smart Grid, doi: 10.1109/TSG.2021.3089362 (Chapter 6).

1.6.2 Conference Publications

1. C. Samende, N. Mugwisi, D. J. Rogers, E. Chatzinikolaou, F. Gao, and M. Mcculloch, ‘Power Loss Analysis of a Multiport DC DC Converter for DC Grid Applications’, IECON 2018 - 44nd Annu. Conf. IEEE Ind. Electron. Soc. Control Instrum., vol. 1, pp. 14121417, 2018 (Chapter 3).

2. C. Samende, S. M. Bhagavathy and M. McCulloch, ‘State of Charge Based Droop Control for Coordinated Power Exchange in Low Voltage DC Nanogrids,’ 2019 IEEE 13th International Conference on Power Electronics and Drive Systems (PEDS), Toulouse, France, 2019, pp. 1-6 (partly Chapter 6).

Chapter 2

Literature Survey

This chapter presents a review of past studies that relate to the current research. Section 2.1 presents the state-of-the-art solar nano-grid configurations and shows how solar nano-grids that are enabled by multi-port converters (e.g. Four-Port DC-DC Converter (FPC)) are cheaper than those enabled by dual port converters. Section 2.2 contains a review of different control strategies that can be used to control solar nano-grids. The purpose of reviewing the different control strategies is to provide a strong theory for the developed control algorithms which are presented in the subsequent chapters. Section 2.3 provides a review and gap analysis related to the primary question answered by this research. Finally, a summary of research gaps which form the basis of this research are outlined at the end of this chapter.

2.1 Literature Review on Solar Nano-Grid Configurations

This section presents the different configurations of solar nano-grids. A solar nano-grid configuration is a description of the way the key components of the solar nano-grid (e.g. batteries, distribution lines, and solar panels) are physically arranged and connected to each other. The configuration influences many factors such as cost, controllability, resiliency, robustness, scalability, power loss and resource utilisation of the solar nano-grid [40, 66]. There are several solar nano-grid configurations which have been reported in literature. These are different on four fronts: (i) distribution network topology, (ii) location of power generation and energy storage units, (iii) converter technology and (iv) whether AC or DC technology is used. Figure 2.1 shows an overview of solar nano-grid configurations.

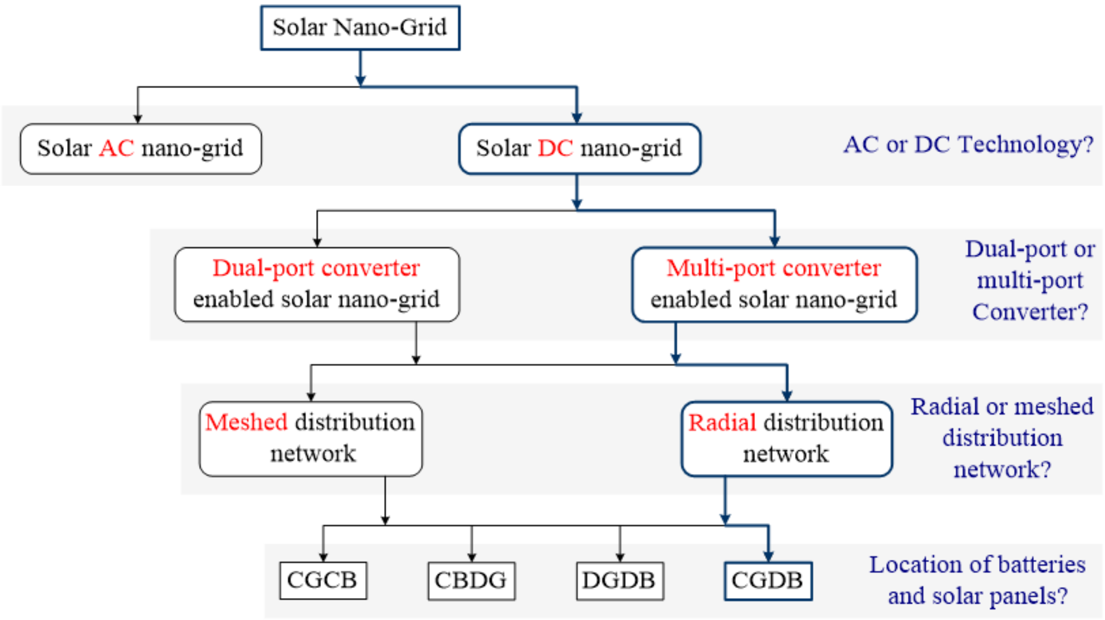

Figure 2.1: Overview of solar nano-grid configurations.

Generally, there are two main types of solar nano-grids, namely, solar AC nano-grid [42, 50, 56] and solar DC nano-grid [67–69]. The solar AC nano-grid uses the conventional AC technology while the solar DC nano-grid uses DC technology for distribution. The solar DC nano-grid has also been categorised in this research into two main groups according to the converter technology as dual-port [26, 70] and multi-port converter [35, 47, 71, 72] enabled solar nano-grids. Further, based on the configuration of the distribution network, these are classified to have either a meshed [34, 73] or radial [35, 37, 69, 74] distribution network. However, it should be noted that a combination of both mesh and radial configurations is possible with the advent of Geographic Information System (GIS)-based methods which take into account the physical spread of the households in remote areas in order to minimise the layout costs [75]. Depending on the location of battery and solar panels in the solar nano-grid, the dual-port and multi-port converter enabled solar nano-grids are identified as Central Generation with Central Battery (CGCB) [74, 76–80], Central Generation with Distributed Battery (CGDB) [35, 60, 69, 79], Central Battery with Distributed Generation (CBDG) [79, 81] and Distributed Generation with Distributed Battery (DGDB) [26, 73, 76, 79].

2.1.1 Solar DC Nano-Grids Versus Solar AC Nano-Grids

Conventionally, AC technology has been the standard choice for generating, transmitting and distributing power from points of generation to points of consumption. This is because of the ease with which AC voltages can be converted from one form to another using a transformer in order to reduce transmission and distribution losses. Most of our existing national grids operate on an AC system. However, due to the paradigm shift towards renewable energy sources such as solar Photo-Voltaic (PV) which generate DC power and the advancement of power electronics converter technology, DC technology has received much attention in the research community, especially for DC power systems which are used to provide energy access to rural communities. In fact, DC power systems are expected to be the right candidates for future energy systems despite the AC power systems being predominant at the moment [82].

The main difference between solar AC nano-grids and solar DC nano-grids is that the former first converts the DC power generated from the solar panels into AC for distribution using inverters and later re-convert the AC back into DC for usage. On the other hand, the solar DC nano-grids directly distributes and uses the generated DC power without converting it into AC. Solar AC nano-grids are mostly applied to households that have a connection to the national grid in order to synchronise the two power systems and to avoid having two separate distribution networks in the same household. Examples of such kind of solar AC nano-grids have been proposed in [42, 50, 56]. Due to mature inverter technology and their availability on the market, solar AC nano-grids have also found application in off-grid communities for providing energy access [83]. However, there are many operational challenges which include synchronisation of different energy sources, difficult in voltage control and system stability in solar AC solar nano-grids than they are in solar DC nano-grids [82]. For this reason, solar DC nano-grids have become the favourable approach of providing energy access to off-grid communities.

Other reasons pushing for the adoption of solar DC nano-grids instead of solar AC nano-grids for off-grid energy access include:

- Usage of DC technology which eliminates AC-DC conversion losses which make up on average 14% of the AC load [56, 84].

- Majority of AC electrical appliances in rural areas such as electronic lighting (fluorescent and LED bulbs), mobile phone charger, radios, TVs and DC motors (driving fans, pumps) are DC-compatible [42, 84].
- Ease of future expansion without synchronisation issues due to lack of frequency in solar DC nano-grids.
- It is safe to touch as it is mainly low voltage.

Solar DC nano-grids however do not have proper voltage standards, leading to different DC voltage levels being adopted [43]. The existing voltage levels vary between 12 V and 400 V, which are inspired by old DC applications including automotive truck industry with 12 V, data centres with 380 V, and telecommunication applications with 48 V. In solar DC nano-grids, voltages levels between 12 V and 48 V are mainly used for storage and those between 48 V and 400 V are used for distribution. Example of solar DC nano-grids with distribution voltages of 24 V, 48 V, 100 V, 120 V, 220 V and 380 V have been proposed in [67, 70], [26, 43], [68], [37], [69, 74] and [52, 60] respectively. Due to the trade off between distribution losses, cost of the protection system and safety of users, a solar DC nano-grid distribution voltage of 120 V is recommended [37]. Meanwhile, EMerge Alliance, an open industry association is in the process of developing standards and promoting market development for DC power systems that will eventually lead to adoption of new standards including voltage levels for future solar DC nano-grids [85].

2.1.2 Solar DC Nano-Grids: Classification According to Converter Technology

Power electronic converters act as interfaces to the key components of the solar nano-grid, i.e. DC loads, batteries, solar panels and distribution network as shown in Figure 2.2. Based on the converter technology used to integrate the components, solar DC nano-grids (or just solar nano-grids for ease of reference) have been classified in this research as dual-port and multi-port converter enabled solar nano-grids.

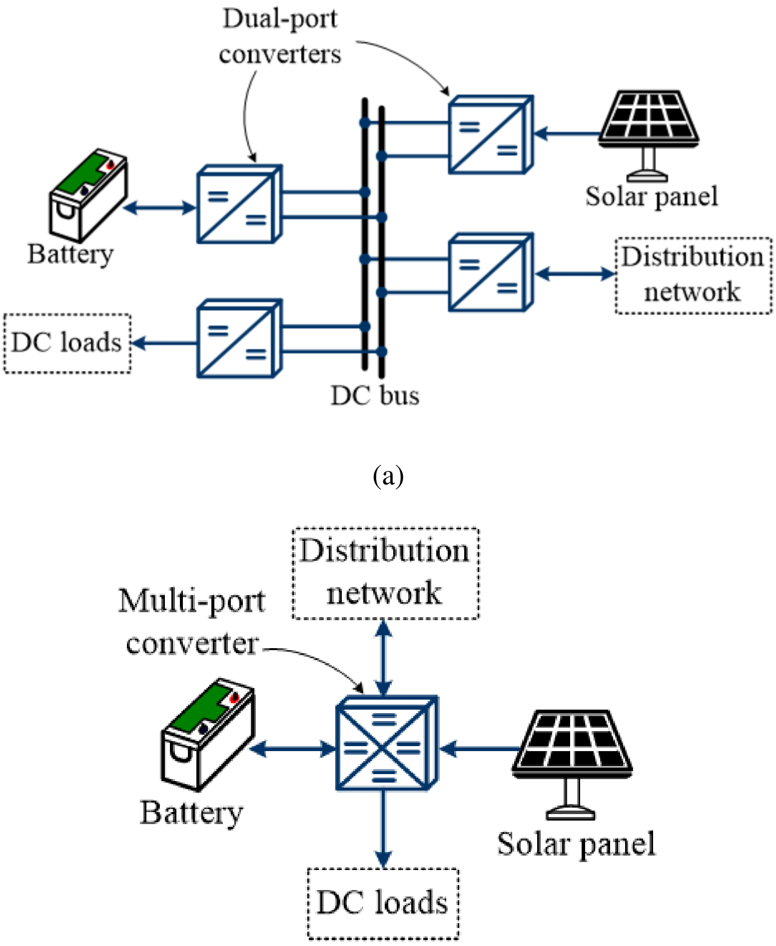

(a)

(b)

Figure 2.2: Integration of the DC loads, batteries, distribution line and solar panels using (a) dual-port DC-DC converters and (b) multi-port DC-DC converters in a single household of the solar nano-grid.

Dual-Port Converter Enabled Solar Nano-grid

In dual-port converter enabled solar nano-grids, multiple dual-port DC-DC converters (which have a single input and a single output) are employed in every household to interface the components as shown in Figure 2.2a. The DC bus connects the converters together and acts as a medium of power exchange between the components. Examples of dual-port DC-DC converters include buck-boost converter [86], dual active bridge converter [87] and current-fed push-pull converter [88]. Dual-port converter enabled solar nano-grids form the majority of solar nano-grids in literature as proposed for example in [26, 60, 67, 68, 70] due to mature dual-port converter technology.

Multi-Port Converter Enabled Solar Nano-grid

A multi-port converter enabled solar nano-grid uses a single multi-port DC-DC converter in every household to integrate the components of the solar nano-grid as shown in Figure 2.2b, where a FPC is used. Several multi-port converters have been proposed in literature [89–91]. One example of such multi-port DC-DC converters is the FPC considered in this research, which is shown in Figure 1.6. The unique feature about multi-port DC-DC converters is the presence of the High Frequency Transformer (HFT) which provides magnetic coupling and galvanic isolation between the components enabling them to be integrated even when they have different terminal voltage magnitudes. There is limited literature on multi-port converter enabled solar nano-grids [35, 47, 71, 72] compared to dual-port converter enabled solar nano-grids due to premature multi-port DC-DC converter technology.

Comparison between Dual-Port and Multi-Port Converter Enabled Solar Nano-grids

Table 2.1 gives a comparison between the dual-port and multi-port converter enabled solar nano-grids. From Table 2.1, it can be observed that multi-port converter-enabled solar nano-grids have several advantages including few physical converters and cables required to interconnect the components than dual-port converter-enabled solar nano-grids. Thus, multi-port converter-enabled solar nano-grids have low upfront investment cost, making them a good

Table 2.1: Comparison between dual-port and multi-port converter solar nano-grids

Solar nano-grid type	Dual-port converter enabled [26, 68]	Multi-port converter enabled [47, 72, 90]
DC bus needed?	yes	no
Medium of power exchange between components	DC bus	transformer magnetic flux
Galvanic isolation between components?	no	yes
Number of physical converters in a household	more than one	one
Power flow management	complicated, slow	simple fast
Implementation effort	high	low
Installation space requirement in a household	high	low
Amount of cables in a household	high	low
Upfront investment cost	High	Low

candidate for providing affordable energy access in off-grid communities.

2.1.3 Solar DC Nano-Grids: Classification According to Distribution Network Topology

Solar nano-grids can be classified according to the layout/topology of the distribution lines which connect the households to each other. In this research, different distribution line layouts were categorised into two main groups, namely radial [35, 37, 69, 74] and mesh layouts [34, 73] as shown in Figure 2.3, where H1, H2 and H3 are households. However, it should be noted that with the advent of GIS-based methods which take the physical spread of the households and layout costs into account, other distribution layouts are possible. These generally are either an extension or a combination of the radial and mesh layouts [75].

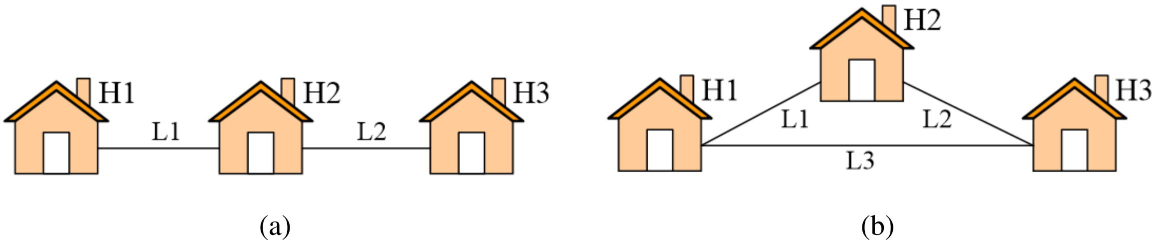

Figure 2.3: Interconnection of households, H1, H2 and H3 using (a) radial and (b) mesh distribution network layouts, where L1, L2, L3 are distribution lines.

The cost of the distribution network layout increases with the number of distribution lines. The higher the number of distribution lines, the more expensive the layout. Comparing the radial and mesh layouts in Figure 2.3, it can be deduced that the mesh layout is more expensive than the radial layout. On the other hand, high number of distribution lines achieves redundancy and reduces line congestion leading to low distribution line losses during operation. It is demonstrated in [92] that the mesh layout achieves low distribution line losses compared to the radial layout. Thus, despite the radial layout being less expensive (due to fewer number of distribution lines compared to the mesh), it has more distribution line losses as summarised in Table 2.2. Since low-cost solar nano-grids are required in rural areas for affordability, the radial layout is suitable for such solar nano-grids and methods that can reduce the distribution line losses are required.

Table 2.2: Comparison of radial and mesh distribution network layouts

Distribution network layout	Radial [35, 37, 69, 74]	Mesh [34, 73]
Description	One household (which is referred to as the central hub) is connected to all other households.	Each household is connected to a minimum of two other households.
Number of distribution lines for n households	n-1	$\leq n(n-1)/2$
Upfront investment cost	Low due to few number of distribution lines	High due to multiple distribution lines
Redundancy of distribution lines	None due to one distribution line per household	High due to multiple distribution lines per household
Robustness	Low due to one distribution line per household	High due to multiple distribution lines per household through which power can be re-routed if one distribution line fails
Line congestion	High due to lack of redundancy	Low due to redundancy
Distribution line losses	High	Low
Examples of practical solar nano-grid projects with radial or mesh distribution network layouts	RELCON project in Kenya [35], SONG project in Bangladesh [69] and the Solar nano-grid of Doulatpur, kushtia district in Bangladesh, installed by Solar Intercontinental (SOLARIC) Limited [74]	Smart peer-to-peer microgrid in Bangladesh by ME SOLshare Ltd [73]

2.1.4 Solar DC Nano-Grids: Classification According to Position of Power Generation and Battery Storage

Solar nano-grids can also be classified based on the location of the solar panels and batteries at the households as shown in Figure 2.4. The comparison between the different configurations is given in Table 2.3.

As shown in Table 2.3, the CGDB configuration is the most affordable option due to small battery capacities in the households required at onset [35] and given that batteries are more expensive than solar panels [10].

2.2 Literature Review on Types of Control Strategies

To manage power and energy in a solar nano-grid, effective control strategies are required. It should be noted that the focus of this section is on solar DC nano-grids control only. Control of solar AC nano-grids is different due to the presence of frequency. Power electronics converters are key controllable devices that can be used to achieve the proper operation of the solar nano-grid. This is because they provide a direct interface to the components of the solar nano-grid. Thus, controlling them in a proper manner coordinates the operation of

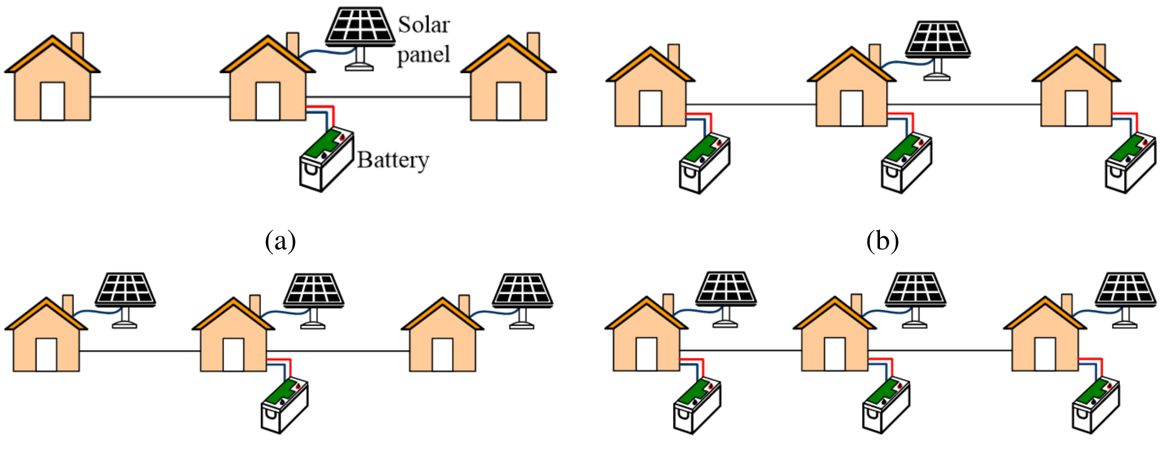

(a) (b)

(c) (d)

Figure 2.4: Classification of solar DC nano-grids based on the location of the solar panel and batteries at the households as (a) CGCB, (b) CGDB, (c) CBDG and (d) DGDB.

Table 2.3: Comparison between CGCB, CGDB, CBDG and DGDB solar nano-grid configurations

Solar nano-grid configuration	CGCB [74, 76–80]	CGDB [35, 60, 69, 79]	CBDG [79, 81]	DGDB [26, 73, 76, 79]
Description	Solar panels and batteries are located in one central place	Solar panels are located in one place while batteries are distributed in every household	Batteries are located in one place while solar panels are distributed in every household	Both solar panels and batteries are distributed in every household
Power flow direction	Unidirectional-from the central location to the households	Bidirectional	Bidirectional	Bidirectional
Upfront investment cost	High due to large battery capacity at onset	Low due to small battery capacities at onset	High due to large battery capacity at onset	Medium due multiple solar panels and small battery capacities at onset
Installation space requirements	Large piece of land is required to install the large battery and solar panel	A large piece of land may be required for installation of solar panels if the community is large	No separate land is required-solar panels can be installed on rooftops of individual households	No separate land is required to install the solar panels
Distribution efficiency	Low due to unidirectional power flow	Medium due to centralised generation	Low due to centralised storage	High due to distributed storage and generation
Maintenance and monitoring requirements	Low because both generation and storage are in a single place	Medium due to centralised generation and distributed storage	High due to distributed generation whose operation needs to be carefully monitored	High due to distributed generation and storage
Examples of practical solar nano-grid projects with CGCB, CGDB, CBDG or DGDB solar nano-grid configurations	Solar DC micro grids in Sitapur and Barabanki districts in Uttar Pradesh by Mera Gao Power [93] and the Solar nano-grid of Doulatpur, kushtia district in Bangladesh, installed by Solar Intercontinental (SOLARIC) Limited [74]	RELCON project in Kenya [35], SONG project in Bangladesh [69] and the Villaya DC micro grids supplied by Schneider Electric [94]	Open energy system in Okinawa, Japan [81]	Smart peer-to-peer microgrid in Bangladesh by ME SOLshare Ltd [73]

the components. Coordinated operation of the components ensures power flow, voltage and current control, which are crucial for a reliable and functional solar nano-grid. The main control objectives of a solar nano-grid are outlined in Subsection 1.2.1.

There are several control strategies in literature that can be used to control the operation of the solar nano-grid. These have been grouped into two sections as proposed in [40] as basic control strategies and multi-level control strategies. Basic control strategies include centralised, decentralised and distributed control strategies. These are discussed in Subsection 2.2.1. Multi-level control strategies take a hierarchical approach where control of the solar nano-grid is implemented through different control levels which are different in hierarchy. Multi-level control strategies can consist of either two or three control levels depending on the solar nano-grid configuration. At each control level, one of the basic control strategies is used. Multi-level control strategies are discussed in Subsection 2.2.2.

2.2.1 Basic Control Strategies

The operation of the solar nano-grid can be achieved through three main control strategies, namely, centralised, decentralised and distributed control strategies. These differ from each other based on the communication topology, which is an infrastructure in place for communication between the households in the solar nano-grid as shown in Figure 2.5.

Centralised Control Strategy

With centralised control strategy, local controllers in the households are controlled from a single central place by a centralised controller as shown in Figure 2.5a [95, 96]. The centralised controller has access to every local controller in the solar nano-grid through digital communication links. The centralised controller collects information such as power generation and power consumption from the local controllers, processes it in order to make optimal control decisions and sends the control decisions back to the local controllers for control implementation by the converter. The information is collected and sent back to the local controllers through the communication links. Thus, the centralised control strategy heavily relies on communication links for implementation.

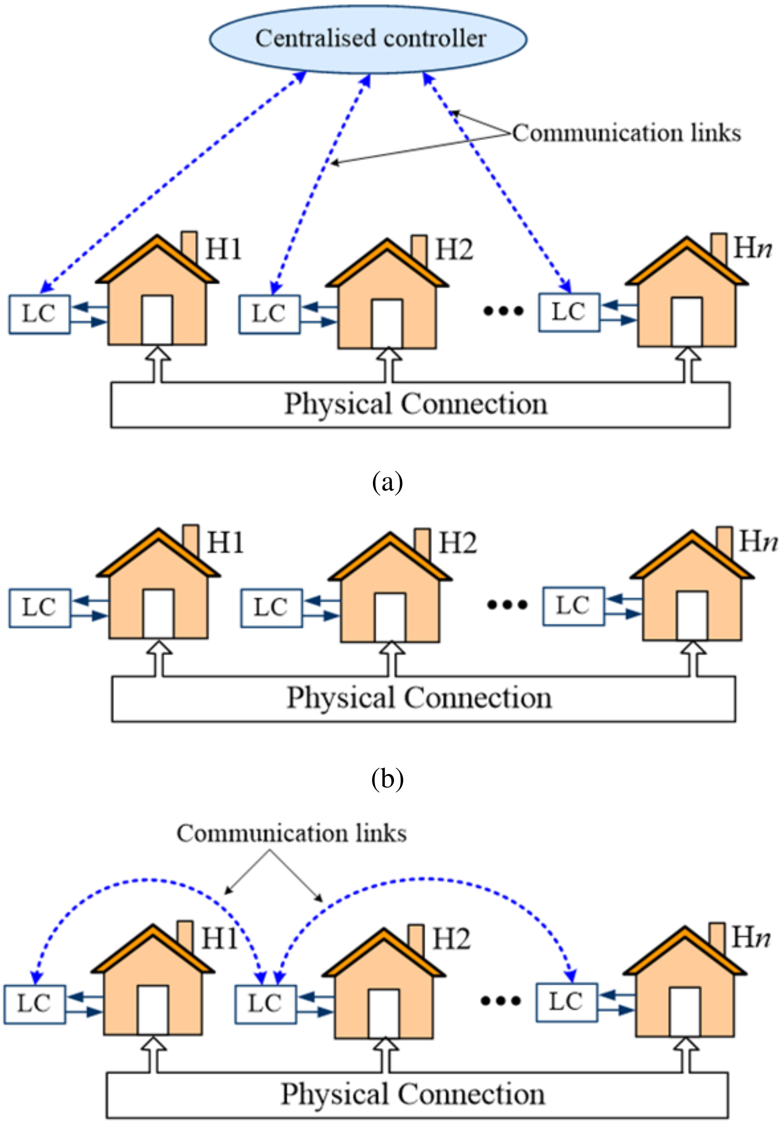

(a)

(b)

(c)

Figure 2.5: Basic control strategies of a solar nano-grid, i.e. (a) centralised control, (b) decentralised control and (c) distributed control. LC: Local Controller.

The main advantages of the centralised control strategy include; fast generation of accurate control decisions, strong observability and controllability of the whole solar nano-grid [40]. Due to the central decision making, the strategy suffers from reduced scalability, single point of failure, heavy computation burden and high storage and processor requirement by the controller [97]. This scheme therefore is suitable for small solar nano-grids where information to be collected is limited [95].

Centralised control strategies are the most used control strategies in literature for controlling solar nano-grids because they are easy to implement. For example, they were used in [34, 47, 98, 99] to achieve power sharing between multiple households.

Decentralised Control Strategy

Unlike the centralised control strategy, decentralised control strategy does not require any physical communication network between local controllers as shown in Figure 2.5b. Control decisions are arrived at and implemented locally within the individual local controllers by using local information without communicating with neighbouring local controllers [41]. Thus, it is highly scalable, robust, reliable and inexpensive compared to the centralised control strategy [100]. However, due to lack of communication between the local controllers, there is no guarantee that the control decisions made are the best [96].

An example of a decentralised control strategy is the famous droop control approach [97, 101], which can be divided into two main groups; voltage and battery SoC based droop control approaches. The voltage based droop control approach determines the suitable distribution voltage of each household in the solar nano-grid by subtracting from a pre-determined voltage reference value a small amount of voltage which is proportional to either the distribution current and power or DC bus voltage [41, 102, 103]. This approach is widely applied to dual-port converter enabled solar nano-grids where the solar panel and battery converters are in parallel as they supply either a local load demand within a single household or a communal load demand of the solar nano-grid [26, 41, 68, 104]. In this case, the current drawn by the DC load or the variations of the DC bus voltage acts as a signal to adjust the distribution voltage through the voltage based droop. The voltage based droop approach, however, cannot be used in multi-port converter enabled solar nano-grids due to the absence of a DC bus and the fact that the medium of power exchange between the components in every household is the transformer magnetic flux.

On the other hand, the SoC based droop control approach adjusts the distribution voltage based on the local battery SoC [105]. This control approach is widely used in autonomous DC micro-grids where batteries are connected in parallel with the objective of balancing the battery SoCs in order to avoid overuse of one battery, accelerated battery degradation, reduction of battery capacity and uneven overcharge and overdischarge [105–111]. The application of the SoC based droop control approach to dual-port converter enabled solar nano-grids is limited and its application to multi-port converter enabled solar nano-grids is non-existent to the best knowledge of the author. For dual-port converter enabled solar nano-grids, the SoC based droop control approach is proposed in [26, 68, 112] with the control objective of achieving power exchange between the individual households and micro-grids.

Distributed Control Strategy

A distributed control strategy combines advantages of both the centralised and decentralised control strategies. Unlike the decentralised control strategy, the distributed control strategy allows information exchange between the local controllers as shown in Figure 2.5c, thus guaranteeing optimality of the control decisions. The local controllers exchange information with their neighbours through a sparse communication network and have less computational complexity [113]. Unlike the centralised control strategy, the distributed control strategy allows the control decisions to be made locally by the local controllers using local information and the exchanged information from their neighbours, thus reducing on the drawbacks of the centralised control strategy [114]. The distributed control strategy is therefore a good option for a large solar nano-grid. The main drawback with the distributed control strategy is that it takes time for the local controllers to reach consensus on the best control decision [100].

Examples of distributed control strategies include consensus based algorithms [115, 116], gossip algorithms [117] and alternating direction method of multipliers [118]. The usage of distributed control strategies in DC systems and dual-port converter enabled solar nano-grids has been considered in [118–121]. Usage of distributed control strategies in multi-port converter enabled solar nano-grids is however not documented in literature.

Comparison between Centralised, Decentralised and Distributed Control Strategies

Table 2.4 summarizes the comparisons between the three basic control strategies.

It can be noted from Table 2.4 that the choice of the right control strategy depends on the desired feature of the particular control strategy that suits the intended application. Under

Table 2.4: Comparison between centralised, decentralised and distributed control strategies

Control strategy	Centralised [95, 96]	Decentralised [41, 97, 101]	Distributed [118–121]
Advantages	• Straightforward implementation • Accurate control decisions • Strong solar nano-grid observability and controllability	• Robust, reliable and scalable • No physical communication network • Inexpensive to implement	• Suitable for large solar nano-grids • Low computational burden • No single point of failure • Scalable
Disadvantages	• Heavy computation burden • Single point of failure • Suitable for small solar nano-grids • Requires highbandwidth communication links	• best control decisions are not assured • Accuracy is limited by solar nano-grid configuration	• Slow to yield control decisions • Requires a communication network • Convergence rates may be affected by communication network topology

the paradigm of solar nano-grids, which are constantly growing in size, distributed control strategies are suitable since they are scalable and have low computational burdens.

2.2.2 Multi-Level Control Strategy

As indicated in Subsection 1.2.1, proper operation of the solar nano-grid must obey different control objectives including supervision of power flow and control of voltage and current, which cover different time scales and physical levels. A multi-level control strategy which is shown in Figure 1.7 is a widely accepted standard solution for DC systems that can be used to achieve the control objectives.

The control levels, i.e. high level control (also known as tertiary level) and low level control (also known as primary level) can be implemented as a centralised, decentralised or distributed control based on the intended control objective and its time scale. The main role of the high level control is to supervise the power flow between components in the solar nano-grid in order to achieve a specific control objective such as minimisation of power losses and operational costs [114, 122]. Centralised and distributed controllers are used to supervise the power flow because of the global information such as power generation and consumption of the all the households in the solar nano-grid which is required to achieve the task [122]. Collection of the global information requires time, thus the high level control is regarded to have long time scale dynamics, e.g. in minutes, hours and years [41].

The main role of the low level control is to control the voltage and current of the solar nano-grid. Its other role is to maintain stability of the solar nano-grid by damping oscillations which may be created by constant power loads [123, 124]. Since oscillations in a system happen very fast (usually in micro or milli-seconds), the low level control is considered to be a low time scale control level [122]. Decentralised control strategy such as droop control is the preferred method in the low level control because it does not require information from elsewhere other than the local information [41]. Thus, the delay associated with information exchange is eliminated and the control action can be very fast.

It should be noted that the multi-level control strategy shown in Figure 1.7 is suitable for multi-port converter enabled solar nano-grids because of the absence of the common DC bus, which otherwise must be regulated to maintain a constant DC bus voltage. For dual-port converter enabled solar nano-grids which have a DC bus, a third control level (which is referred to as the secondary level) is always included in the multi-level control strategy between the high and low level control levels as considered in [68, 112]. The main function of the secondary level in the multi-level control strategy is to restore the voltage of the DC buses to the nominal value. The secondary level is mainly implemented using centralised and distributed control strategies because of the communication required to collect the DC bus voltage information [96, 120].

2.3 Literature Review on Power Loss Minimisation Control Approaches

The key problem for solar nano-grids deployed in off-grid communities is the power loss problem as described in Subsection 1.2.2. Owing to the limited generation capacity and lack of national grid connection, it is important to address the power loss problem in order to save energy and make the solar nano-grids affordable for energy access.

Given that the concept of solar nano-grids is relatively new, having officially come to light in 2012 [125], most of the research focus has been on the feasibility of the concept [33, 57], design and sizing of solar nano-grids [27, 32], modelling of solar nano-grids under droop control [126], technical benefits [34, 58, 127], and financial benefits [128, 129].

Few studies have attempted to consider the power loss problem. In [130], a data analysis tool which optimises the distribution network topology of the solar nano-grid was developed with the aim of achieving an efficient power flow between the households. A similar study was reported in [131, 132] where a methodology for selecting efficient distribution network topology of solar based DC micro-grids with respect to village orientation is presented. A distribution loss analysis is presented in [133] with the aim of optimally planning and designing a DC micro-grid architecture with minimum distribution losses.

While the aforementioned research focused on optimal planning and designing of the solar nano-grids, it is to the best knowledge of the author that there are no studies that focus on developing control algorithms that address the power loss problem for operational solar nano-grids. The few existing control methods in literature focus on addressing the power loss problem of conventional DC micro-grids [39, 134] and High Voltage Direct Current (HVDC) systems [135] as follows.

In [136], a decentralised voltage control method which works in a perturb and observe manner is proposed to minimise distribution losses in an islanded DC micro-grid. Battery and converter losses were however not considered. An Optimal Power Flow (OPF) based control scheme is proposed in [135] to minimise power losses in multi-terminal HVDC systems for offshore wind power plants. Transmission losses were considered in the control scheme while battery and converter losses were ignored. A dynamic optimal power flow strategy with the objective of minimising the battery losses and distribution line losses of a DC micro-grid is proposed in [46]. The strategy first converted the non-convex power loss problem to a convex problem through linearisation of power flow equations and then solved the convex power loss problem using software packages. However, converter losses were ignored and the linearisation of the power flow equations can lead to less accurate results and high computational times. Converter losses were considered in [65, 137], where battery losses were however not considered.

Greedy algorithms including coalition game theory are proposed in [138–141] to minimise power losses in clusters of DC micro-grids by prioritising energy exchange between nearby DC micro-grids. Despite simplicity with the proposed algorithms, greedy algorithms are known to be sub-optimal; their optimality depends on the number of participating micro-grids, i.e. the higher the number of micro-grids, the higher the number of possible coalitions and therefore the lower the power loss [141]. In addition, greedy algorithms can lead to overuse of batteries in households which are close together, requiring frequent battery replacements, which can be expensive.

Consensus-based algorithms are proposed in [142] where only the battery losses of a DC micro-grid were minimised. The distribution losses were minimised in [143–145] using the consensus-based algorithms and in [118] using the alternating direction method of multipliers. However, battery and converter losses were not considered.

Heuristic methods such as genetic algorithms are proposed in [146] to minimise the distribution line losses while ignoring the battery and converter losses. They are also proposed in [147] to minimise both the distribution losses and the converter losses while ignoring battery losses. The use of genetic algorithm for minimising the power loss however, means that the solution is sub-optimal.

2.4 Summary

This review has shown that:

- Multi-port converter (e.g. FPC) enabled solar nano-grids that has a radial distribution network and a central generation with distributed batteries are a potential low cost solution for providing energy access in rural areas.
- To the best knowledge of the author, there are no studies in the literature that focus on developing control algorithms that can minimise power losses, i.e. battery, distribution and converter losses of multi-port converter-enabled solar nano-grids, particularly the FPC-enabled solar nano-grids.

- Existing control algorithms address the power loss problem of conventional DC microgrids and HVDC systems. Moreover, these do not consider all the three types of solar nano-grid power losses, i.e. battery, distribution and converter losses at the same time. The algorithms that attempt to consider any two of the three power losses tend to have sub-optimal solutions, high model complexity and high computational times due to linearisation or convex relaxation of power flow equations [46, 141, 147]. This makes the existing control algorithms unsuitable for addressing the power loss problem of multi-port converter-enabled solar nano-grids, which require all the three solar nano-grid power losses to be minimised and the control algorithms to be scalable and computationally efficient for real-time implementation.

Chapters 3, 4, 5 and 6 of this thesis will present control algorithms developed in this research which attempt to close the aforementioned research gaps.

Chapter 3

Steady-State Modelling and Power Loss Optimisation Problem Formulation of a Solar Nano-Grid

This chapter presents steady state modelling and power loss optimisation problem formulation of a Four-Port DC-DC Converter (FPC)-enabled solar nano-grid (hereafter referred to as solar nano-grid). The star solar nano-grid configuration shown in Figure 1.4 is considered since it is the simplest configuration from which other solar nano-grid configurations can be derived.

To increase the energy efficiency of a solar nano-grid, it is important that the control objective in the high level control (shown in Figure 1.7) addresses the power loss problem of the solar nano-grid. The power loss problem can be addressed through optimisation by first formulating it as a mathematical optimisation problem and then solving the formulated optimisation problem using control algorithms on a computer. The formulated optimisation problem should be convex [148] in order to preserve the scalability of the solar nano-grid and to guarantee the global optimality of the solution to the optimisation problem.

Before formulating the optimisation problem (and even solving it), it is key to represent the solar nano-grid by mathematical relationships (such as equalities and inequalities) that describe its operational characteristics and that can be numerically computed by a computer.

The mathematical representation of the solar nano-grid is hereafter referred to as the solar nano-grid model and the development of the model as solar nano-grid modelling. Since the optimisation problem is to be solved in the high level control, a steady state model of the solar nano-grid which ignores the low level control dynamics is required.

In addition to formulating the power loss optimisation problem, the solar nano-grid model is used to:

- Develop high level control algorithms which solves the power loss optimisation problem as presented in Chapters 4 and 5.
- Simulate the solar nano-grid in Python programming language in order to validate the algorithms developed and to visualise the results on a computer subject to the algorithms developed .

The solar nano-grid model is required to maintain good compromise between computational complexity on one hand and accuracy, and reliability on the other hand, since the more accurate the model is, the more complex and expensive it is in terms of computations and processor requirements.

Section 3.1 to Section 3.6 presents individual models of the key components of the solar nano-grid i.e. FPCs, solar panels, DC loads, batteries and distribution lines. Modelling of the FPC forms a bigger part of this chapter because two models, namely the detailed and simplified power loss model of the FPC were required. The detailed FPC power loss model was required for an in-depth understanding of the FPC operation and its constituent power losses, and for further optimisation of the FPC design which is beyond the scope of this research. The simplified power loss model of the FPC was used in this research to model the solar nano-grid and formulate the power loss optimisation problem. The solar nano-grid model is presented in Section 3.7. The formulation of the power loss optimisation problem of the solar nano-grid is presented in Section 3.8.

3.1 Detailed Four-Port DC-DC Converter Modelling

The key physical phenomena of the FPC are the power losses which occur as current and voltage are converted from one form to another. In this section, the detailed FPC power loss model which can be used to optimise the FPC design is presented. The loss model is developed from a FPC switching circuit which is shown in Figure 1.6. It should be noted that the FPC considered in this research is new and has not been reported anywhere in literature. For this reason, a comprehensive development of the loss model at steady state was necessary.

The development of the loss model consisted of four main steps:

1. **Operation analysis** for gaining an understanding on how the FPC works.
2. **Current and voltage waveform modelling** for evaluating the magnitude of currents and voltages in the FPC at every time instant.
3. **Determination of control signals, e.g. phase shift ratios and duty cycles** for obtaining a typical representation of the FPC operating point and power loss calculations.
4. **Power loss calculation** for estimating the FPC power losses at every time instant.

Since the physical structure of the FPC consists of the Triple Active Bridge Converter (TABC) and the Half bridge Converters (HBCs) as shown in Figure 1.6, which are different in construction and operation, Step 1 to Step 3 were performed separately for the TABC and HBCs. Step 4 was common to both the TABC and HBCs due to the overlap in the type of power losses estimated. Figure 3.1 gives a summary of the steps followed for developing the detailed FPC power loss model.

3.1.1 Operation of the Triple Active Bridge Converter

Figure 3.2 shows the circuit diagram of the TABC, which is taken from Figure 1.6. The $L_1,\ldots,L_3$ are transformer leakage inductors which are the main energy transfer elements of the TABC. The $i_1,\ldots,i_3$ and $v_1,\ldots,v_3$ respectively represent the AC currents and AC voltages of the transformer. The $I_1,\ldots,I_3$ and $V_1,\ldots,V_3$ respectively represent the input DC

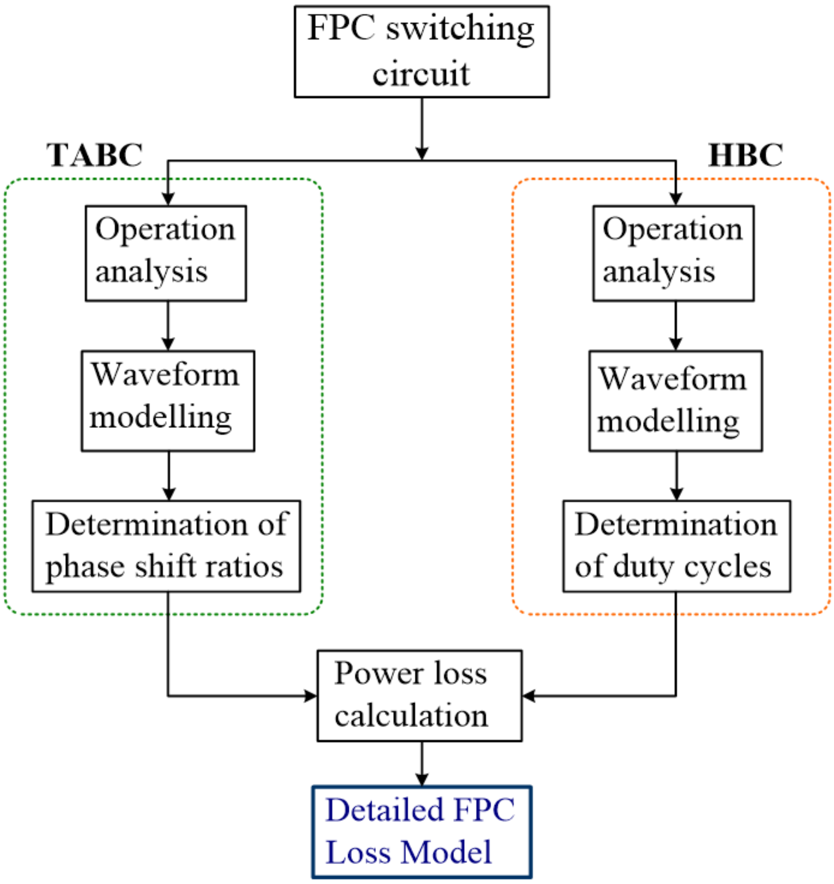

Figure 3.1: Development process of the detailed FPC loss model from a FPC switching circuit which is shown in Figure 1.6.

currents and DC voltages to the Full Bridge Converters (FBCs). The main function of the FBCs is to either convert DC currents and DC voltages from the HBCs to AC currents and AC voltages in the High Frequency Transformer (HFT) respectively or the other way round.

Every FBC of the TABC consists of two parallel branches of Metal Oxide Semi-conductor Field Effect Transistors (MOSFET) switches, which are switched at a fixed duty cycle of 50% and at a constant switching frequency of 100 kHz. For example, the FBC-A in Figure 3.2 has Q_1 and Q_3 on the left branch and Q_2 and Q_4 on the right branch. The MOSFETs on the same branch are complementary switched, i.e. when the top MOSFET is switched on, the bottom MOSFET is switched off. The switching operation for both branches of a FBC in one switching cycle follows that when the diagonal MOSEFTs are switched on, the off-diagonal MOSEFTs are switched off. This switching pattern generates square AC voltage

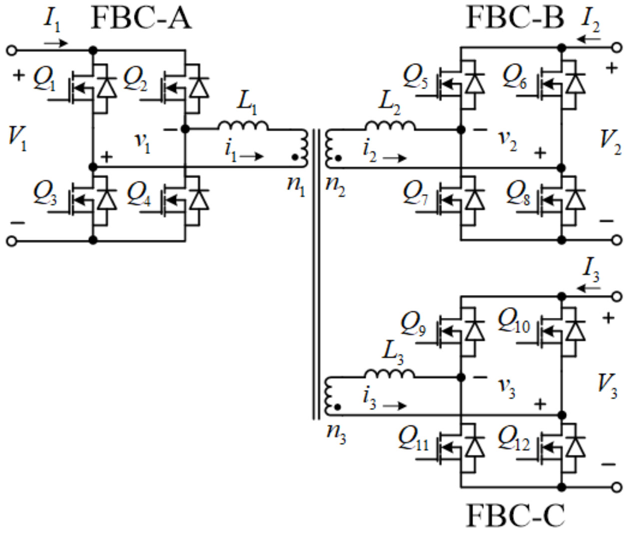

Figure 3.2: Schematic diagram of a TABC.

waveforms, $v_1, \ldots, v_3$ which are in phase at the terminals of the transformer. Taking FBC-A, switching on Q_1 and Q_4 while switching off Q_2 and Q_3 in the first half of the switching cycle establishes AC current flow direction and AC voltage polarity as shown in Figure 3.3a. Meanwhile, switching off Q_1 and Q_4 and switching on Q_2 and Q_3 in the second half of the switching cycle reverses the current flow direction and voltage polarity as shown in Figure 3.3b. Figure 3.4 shows the idealised gate signals (which switches on and switches off the MOSFETs) and the resulting square-wave AC voltage for a switching period, T_s.

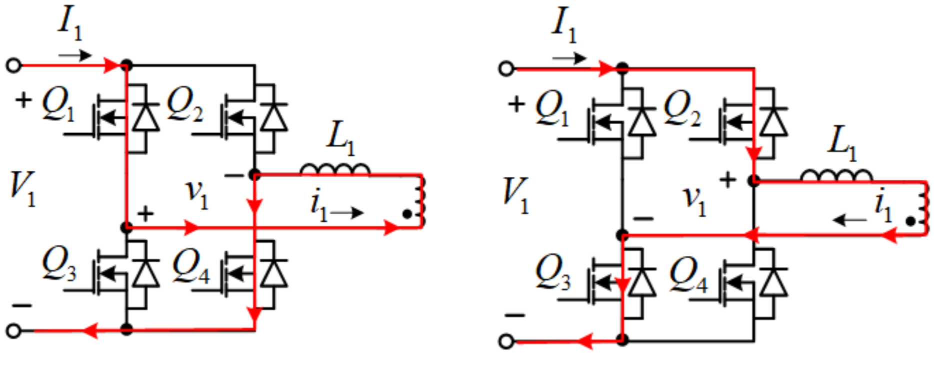

(a) (b)

Figure 3.3: Conversion of DC current and DC voltage to AC current and AC voltage in the primary winding of the transformer by (a) switching on Q_1 and Q_4 in the first half of the switching cycle while Q_2 and Q_3 remain switched off and (b) switching on Q_2 and Q_3 in the second half of the switching cycle while Q_1 and Q_4 are switched off.

The operation of the FBC-A depicted in Figure 3.3 and the generation of the square-wave

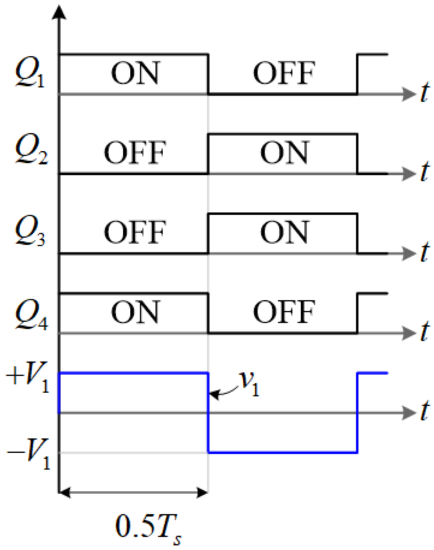

Figure 3.4: Idealised switching signals for FBC-A and the AC voltage waveform established by the switching pattern of the MOSFET switches.

AC voltage waveform shown in Figure 3.4 also applies to FBC-B and FBC-C. Neglecting voltage drops in the MOSFETs, the $v_1,\dots,v_3$ waveforms are equal in magnitude to their associated input DC voltages, $V_1,\dots,V_3$ respectively.

The magnitude and power flow direction between the FBCs is controlled by shifting the phase angles of the v_2 and v_3 voltage waveforms with respect to the v_1 voltage waveform as shown in Figure 3.5. The phase shift angles for v_1, v_2 and v_3 waveforms are represented by ϕ_1, ϕ_2 and ϕ_3 respectively. Since the v_1 voltage waveform is the reference, its phase shift angle, ϕ_1 is equal to zero. Where one voltage waveform leads a second voltage waveform, the phase shift angle of the leading voltage waveform is considered to be positive and negative otherwise. Practically, the ϕ_1, ϕ_2 and ϕ_3 are provided by a controller as control signals to FBC-A, FBC-B and FBC-C respectively. Due to the difference in phase shift angles, power and current flow between the FBCs is controlled accordingly.

3.1.2 Current and Voltage Waveform Modelling of the Triple Active Bridge Converter

To determine the power flow between the FBCs and to model the current and voltage waveforms generated through the switching of the FBCs at steady state, the transformer circuit

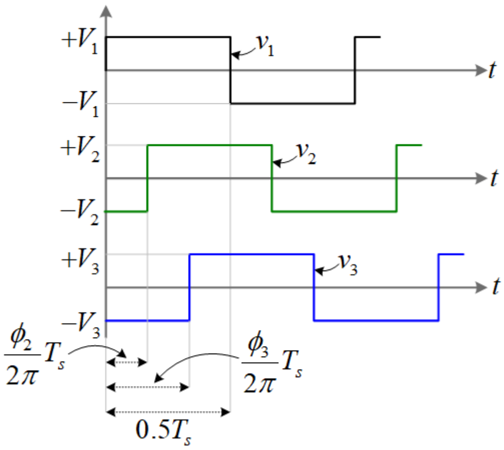

Figure 3.5: Idealised square-wave AC voltage waveforms of v_1, v_2 and v_3 which are phase shifted from each other, where $\phi_1 = 0$, ϕ_2 and ϕ_3 are phase shift angles (in radians) of v_1, v_2 and v_3 respectively.

is first represented using its star and delta equivalent circuits [4]. In this case, the transformer circuit was viewed as a network of inductors, $L_1, \ldots, L_3$ supplied by phase shifted square-wave voltage sources, $v_1, \ldots, v_3$. Figure 3.6a shows the star equivalent circuit of the transformer obtained by referring the v_2, v_3 and the L_2, L_3 on the secondary and tertiary winding of the transformer to its primary winding using (3.1).

$$v_j^{'} = \frac{n_1}{n_j} v_j \tag{3.1a}$$

$$i_j^{'} = \frac{n_j}{n_1} i_j \tag{3.1b}$$

$$L_j^{'} = \left(\frac{n_1}{n_j}\right)^2 L_j \tag{3.1c}$$

where n_1 is the number of turns of the primary winding and n_j, $j = 2, 3$ is the number of turns of either the secondary or tertiary winding.

To implicitly identify the power flows between the voltage sources and the FBCs thereof, the star equivalent circuit in Figure 3.6a was converted to a delta equivalent circuit as shown in Figure 3.6b using the relationships expressed in (3.2). Both equivalent circuits ignore the transformer magnetisation inductance because it was considered to be large compared to the

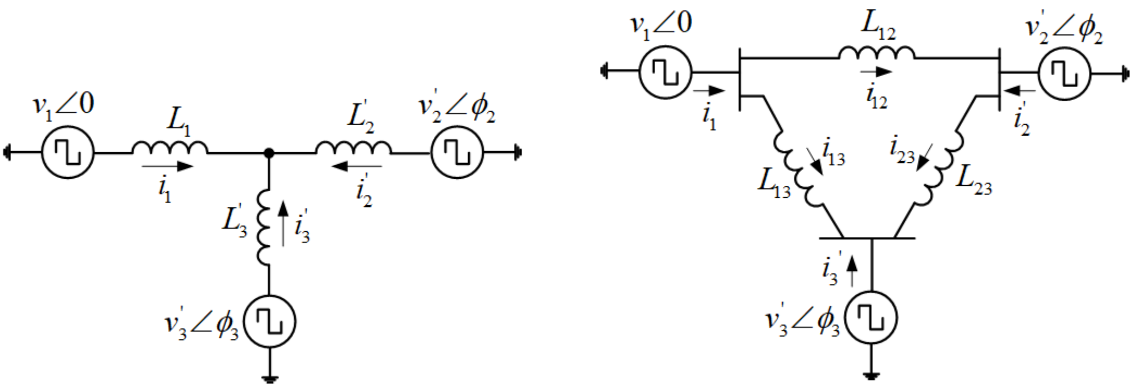

(a) (b)

Figure 3.6: Equivalent circuit of the transformer (a) star equivalent circuit and (b) delta equivalent circuit [4].

leakage inductances [4].

$$L_{12} = \frac{L_1L_2^{'} + L_1L_3^{'} + L_2^{'}L_3^{'}}{L_3^{'}} \tag{3.2a}$$

$$L_{13} = \frac{L_1L_2^{'} + L_1L_3^{'} + L_2^{'}L_3^{'}}{L_2^{'}} \tag{3.2b}$$

$$L_{23} = \frac{L_1L_2^{'} + L_1L_3^{'} + L_2^{'}L_3^{'}}{L_1} \tag{3.2c}$$

Current Flow and Power Transfer between any Two Full Bridge Converters

AC current flow in the linkage inductors in Figure 3.6b is established due to the square-wave AC voltage sources which are shifted in phase. To make clear the analysis of the AC current flow and the power transfer thereof between the voltage sources in Figure 3.6b, a case involving two arbitrary voltage sources, $v_j^{'}$ and $v_k^{'}$ as shown in Figure 3.7 was considered.

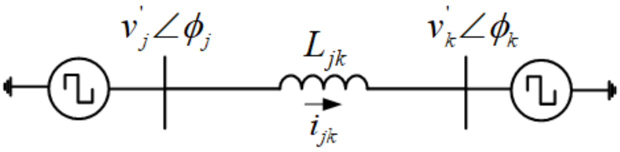

Figure 3.7: Equivalent circuit of two FBCs.

Instantaneous Inductor Current

The inductor voltage v_{Ljk} across L_{jk} in Figure 3.7, which determines the waveform of the inductor current, i_{jk} was expressed from $v_j^{'}$ and $v_k^{'}$ as follows

$$v_{Ljk} = L_{jk}\frac{di_{jk}(t)}{dt} = v_j^{'} - v_k^{'} \tag{3.3}$$

The idealised waveforms for $v_j^{'}$, $v_k^{'}$, v_{Ljk} and i_{jk} are shown in Figure 3.8, where the magnitude of $v_k^{'}$ was assumed to be larger than that of $v_j^{'}$. The instantaneous inductor current, i_{jk} in the time interval, $t_s \leq t \leq t_f$ was obtained from (3.3) as

$$\begin{aligned} i_{jk}(t) &= \int_{t_s}^{t_f}\left(\frac{v_j^{'} - v_k^{'}}{L_{jk}}\right) + i_{jk}(t_s) \\ &= \left(\frac{v_j^{'} - v_k^{'}}{L_{jk}}\right)(t_f - t_s) + i_{jk}(t_s) \end{aligned} \tag{3.4}$$

where $i_{jk}(t_s)$ is initial current at $t = t_s$, t_s and t_f are start time and finish time respectively for each switching interval.

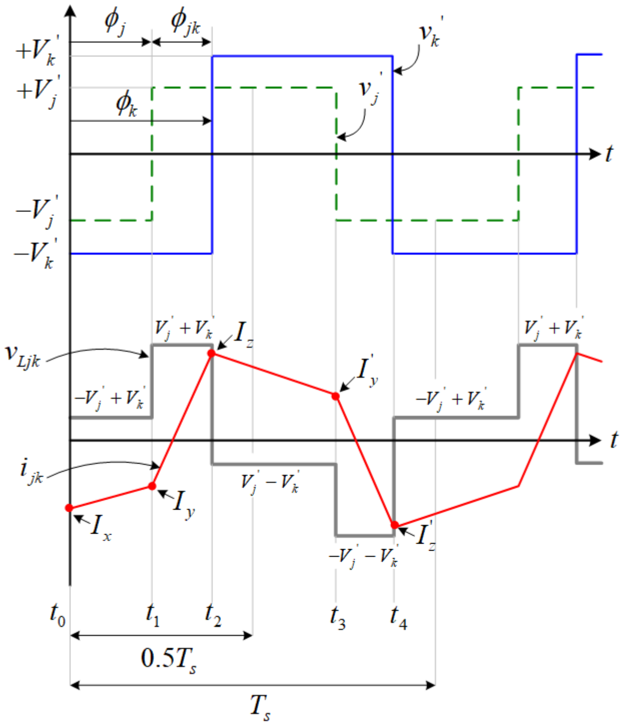

Figure 3.8: Idealised waveforms of $v_j^{'}$, $v_k^{'}$, v_{Ljk} and i_{jk} in Figure 3.7.

For a switching period T_s as shown in Figure 3.8, $i_{jk}(t)$ in (3.4) was simplified as follows

$$i_{jk}(t) = \begin{cases} I_x + \left(\frac{-V_j^{'}+V_k^{'}}{L_{jk}}\right)(t-t_0)\,, \text{ if } t_0 \leq t \leq t_1 \\ I_y + \left(\frac{V_j^{'}+V_k^{'}}{L_{jk}}\right)(t-t_1)\,, \text{ if } t_1 < t \leq t_2 \\ I_z + \left(\frac{V_j^{'}-V_k^{'}}{L_{jk}}\right)(t-t_2)\,, \text{ if } t_2 < t \leq t_3 \\ I_y^{'} + \left(\frac{-V_j^{'}-V_k^{'}}{L_{jk}}\right)(t-t_3)\,, \text{ if } t_3 < t \leq t_4 \\ I_z^{'} + \left(\frac{-V_j^{'}+V_k^{'}}{L_{jk}}\right)(t-t_4)\,, \text{ if } t_3 < t \leq T_s \end{cases} \tag{3.5}$$

The switching times, t_0, t_1, t_2, t_3 and t_4 were obtained from Figure 3.8 as follows

$$\begin{cases} t_0 = 0\,, \quad t_1 = d_j \frac{T_s}{2}\,, \quad t_2 = d_k \frac{T_s}{2}\,, \\ t_3 = t_1 + \frac{T_s}{2}\,, \quad t_4 = t_2 + \frac{T_s}{2} \end{cases} \tag{3.6}$$

where $d_j = \frac{\phi_j}{\pi}$ and $d_k = \frac{\phi_k}{\pi}$, which are hereafter referred to as phase shift ratios.

The $i_{jk}(t)$ in Figure 3.8 is an odd symmetric waveform. Therefore, the following relationships hold true in a switching period, T_s

$$i_{jk}(t_1) = I_y = -i_{jk}(t_3) = -I_y^{'} \tag{3.7a}$$

$$i_{jk}(t_2) = I_z = -i_{jk}(t_4) = -I_z^{'} \tag{3.7b}$$

The critical current points I_x, I_y, I_z, $I_y^{'}$ and $I_z^{'}$ were obtained by solving (3.7) using (3.5) and (3.6) as follows

$$I_x = I_y - \left(\frac{-V_j^{'}+V_k^{'}}{L_{jk}}\right)(t_1-t_0) = -\frac{T_s}{4L_{jk}}\left(2V_k^{'}d_k - V_k^{'} + V_j^{'} - 2V_j^{'}d_j\right) \tag{3.8a}$$

$$I_y = -I_y^{'} = -\frac{T_s}{4L_{jk}}\left(2V_k^{'}d_{jk} - V_k^{'} + V_j^{'}\right) \tag{3.8b}$$

$$I_z = -I_z^{'} = \frac{T_s}{4L_{jk}}\left(2V_j^{'}d_{jk} + V_k^{'} - V_j^{'}\right) \tag{3.8c}$$

where $d_{jk} = d_k - d_j$ is the difference between the phase shift ratios of the voltage waveforms.

Root Mean Square and Average Inductor Current

Due to the symmetry of the i_{jk} waveform, the referred average current $i^{'}_{avg}$ supplied by $v^{'}_{j}$ was obtained by integrating i_{jk} given by (3.5) for a half switching period, $0.5T_s$ as follows

$$\begin{aligned} i^{'}_{avg} &= \frac{2}{T_s}\left(\int_{t_0}^{t_1} i_{jk}(t)dt + \int_{t_1}^{t_2} i_{jk}(t)dt + \int_{t_2}^{0.5T_s} i_{jk}(t)dt\right) && \text{(3.9a)} \\ &= \frac{T_s v^{'}_{k}}{2L_{jk}} d_{jk}\left(1-\left|d_{jk}\right|\right) && \text{(3.9b)} \end{aligned}$$

The referred average power $P^{'}_{jk}$ supplied by $v^{'}_{j}$ was found by multiplying $i^{'}_{avg}$ by $v^{'}_{j}$ to get $P^{'}_{jk} = v^{'}_{j} i^{'}_{avg}$. The expressions of the average current in (3.9) and the resulting average power, $P^{'}_{jk}$ are also reported in [149] and [150], which confirms that the expressions given by (3.1) to (3.9) are correct.

According to (3.9), for a given linkage inductor, L_{jk}, the direction and the amount of average current and power flow between two square-wave voltage sources depends on the difference between the phase shift ratios of the voltage waveforms, i.e. $d_{jk} = d_k - d_j$. Thus, if $v^{'}_{j}$ leads $v^{'}_{k}$ i.e. $d_k > d_j$ as shown in Figure 3.8, power is supplied by $v^{'}_{j}$ to $v^{'}_{k}$ and power is absorbed otherwise. The supplied average current and power are maximum when $d_{jk} = 0.5$. The Root Mean Square (RMS) inductor current was obtained by integrating i_{jk} given by (3.5) as follows

$$i^{'}_{RMS} = \left[\frac{2}{T_s}\left(\int_{t_0}^{t_1} i^{2}_{jk}(t)dt + \int_{t_1}^{t_2} i^{2}_{jk}(t)dt + \int_{t_2}^{0.5T_s} i^{2}_{jk}(t)dt\right)\right]^{\frac{1}{2}} \tag{3.10}$$

Current Flow and Power Transfer between the Three Full Bridge Converters

In the previous subsection, current and power flow between two arbitrary FBCs was analysed. In this subsection, current and power flow between the three FBCs of the TABC is presented.

Without loss of generalisation, (3.9) shows that current flow in Figure 3.6b and the TABC thereof is achieved by adjusting d_{jk} of the AC voltage waveforms. Since the TABC has two controllable phase shift ratios, d_{12}, d_{13} with $d_1 = 0$, there exists a total of six different combinations of current flow directions, which define the operating modes of the TABC as shown in Figure 3.9.

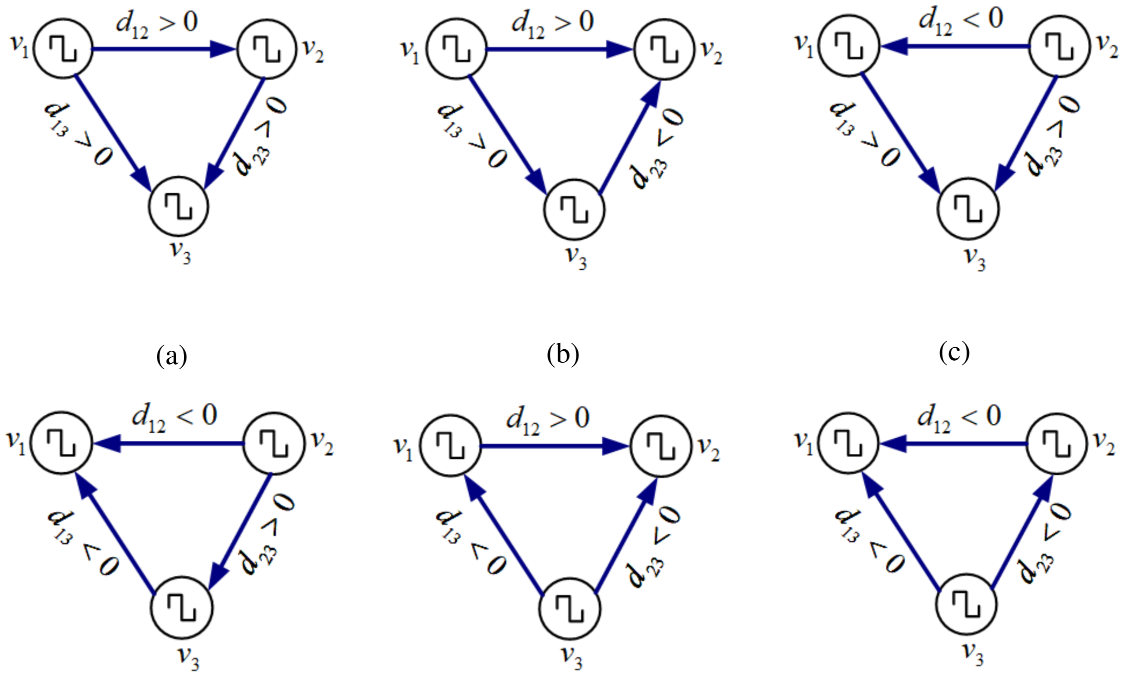

(a) (b) (c)

(d) (e) (f)

Figure 3.9: The six operating modes of the TABC based on the phase shift ratios. The arrows show the direction of current flow.

Instantaneous Current through a MOSFET and Transformer Winding

Figure 3.10 shows the key switching waveforms of the TABC developed for the six different operating modes shown in Figure 3.9. The voltage waveforms were developed based on the possible combinations of the phase shift ratios according to Figure 3.8 and Figure 3.9. The inductor current, $i_{jk}(t)$ for $j,k = 1,2,3$ and $j \neq k$ between any two voltage sources was carefully described for each of the operating modes in Figure 3.10 using the analysis presented in (3.3) to (3.8). The referred instantaneous current, $i_j^{'}(t)$, $j = 1,2,3$ through the j-th transformer winding and the associated MOSFETs for each operating mode was obtained as follows

$$i_j^{'}(t) = \sum_{\substack{k=1 \\ k \neq j}}^{3} i_{jk}(t) \tag{3.11}$$

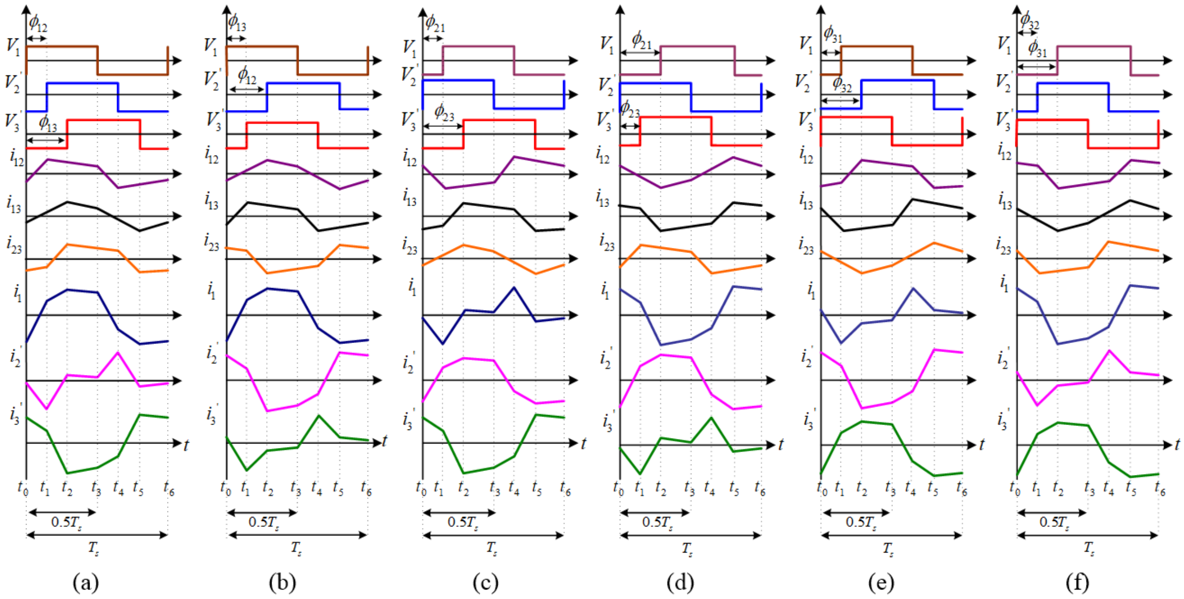

Figure 3.10: Idealized (six) voltage and current waveforms of a TABC corresponding to the operating modes in Figure 3.9.

Then the instantaneous current $i_j(t)$ in each j-th winding of the transformer in Figure 3.2 was obtained by substituting (3.11) in (3.1b) as follows

$$i_j(t) = \frac{n_1}{n_j} \sum_{\substack{k=1 \\ k \neq j}}^{3} i_{jk} \tag{3.12}$$

Root Mean Square and Average Current through a MOSFET and Transformer Winding

Similar to (3.9), the average current of the $i_j(t)$ waveform for each operating mode in Figure 3.10, which is equal to the input current I_j was obtained by integrating (3.12) over a half switching period, $0.5T_s$ (since i_{jk} is an odd symmetric waveform) as follows

$$I_j = \frac{2}{T_s}\left(\int_{t_0}^{t_1} i_j(t)dt + \int_{t_1}^{t_2} i_j(t)dt + \int_{t_2}^{0.5T_s} i_j(t)dt\right) \tag{3.13a}$$

$$= \sum_{\substack{k=1 \\ k \neq j}}^{3} \frac{n_1^2 T_s V_k}{2n_j n_k L_{jk}} d_{jk}\left(1 - |d_{jk}|\right) \tag{3.13b}$$

where t_0, t_1 and t_2 for each operating mode are as defined in Figure 3.10.

The average power, P_j, $j = 1,2,3$ which is ideally equal to the input powers of the FBCs was obtained by multiplying (3.13) by V_j as follows

$$P_j = \sum_{\substack{k=1 \\ k \neq j}}^{3} \frac{n_1^2 T_s V_j V_k}{2 n_j n_k L_{jk}} d_{jk} \left(1 - \left|d_{jk}\right|\right) \tag{3.14}$$

The average power in (3.14) is a standard power transfer equation of a TABC [4, 149]. Since the average powers for each operating mode in Figure 3.10 were equal to the expression in (3.14), the characteristic waveforms in Figure 3.10 were considered to be accurate.

Figure 3.11 shows the variation of the power P_j of the TABC with the phase shift ratios of the FBCs.

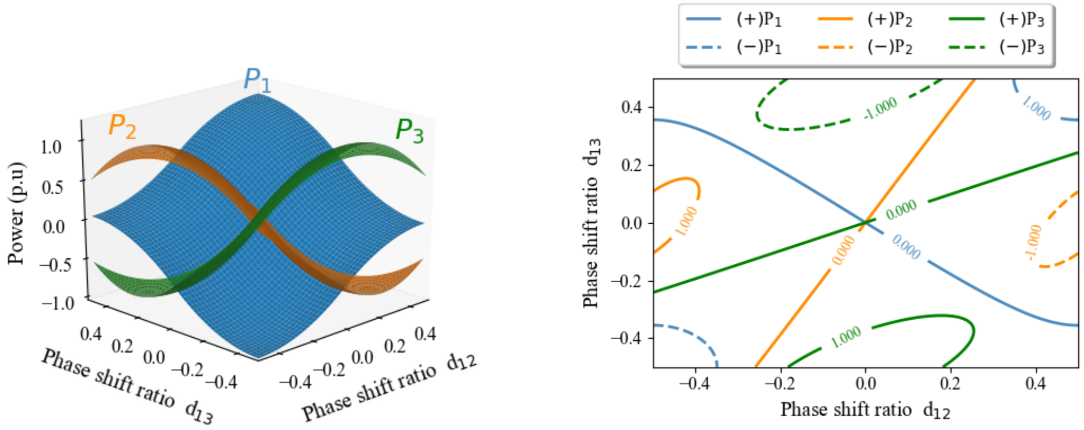

(a) (b)

Figure 3.11: Variation of input/output powers, P_1, P_2 and P_3 of the TABC with the phase shift ratios, d_{12} and d_{13}: (a) surface plot and (b) contour plot.

As shown in Figure 3.11a and Figure 3.11b, P_1 has absolute maximum power when both d_{12} and d_{13} are equal to ± 0.5, P_2 has absolute maximum power when $d_{12} = \pm 0.5$ and $d_{13} = 0$ and lastly, P_3 has absolute maximum power when $d_{12} = 0$ and $d_{13} = \pm 0.5$. In other words, the TABC carries maximum power when d_{12} and/or d_{13} is equal to ± 0.5.

The RMS current through the j-th transformer winding and the associated MOSFETs was obtained as

$$I_{j(RMS)} = \left[\frac{2}{T_s}\left(\int_{t_0}^{t_1} i_j^2(t)dt + \int_{t_1}^{t_2} i_j^2(t)dt + \int_{t_2}^{0.5T_s} i_j^2(t)dt\right)\right]^{\frac{1}{2}} \tag{3.15}$$

3.1.3 Determination of the Phase Shift Ratios

Practically, the phase shift ratios are provided to the TABC by low time scale based Proportional-Integral (PI) controllers which maintain constant DC voltages, V_1, V_2 and V_3 at the terminals of the TABC. To analyse the power losses of the TABC, numerical determination of the phase shift ratios for each operating mode in Figure 3.10 was required.

Since $P_j,\ j = 1,2,3$ is known at every time instant from the power inputs and outputs of the HBCs, the phase shift ratios, d_{12} and d_{13} were obtained by iteratively solving (3.14) based on Newton's Raphson method as follows:

$$\mathbf{X}^{(q+1)} = \mathbf{X}^{(q)} + \mathbf{J}^{-1}\left(\mathbf{Y} - \mathbf{P}^{(q)}\right) \tag{3.16}$$

where q is the iteration number, $\mathbf{X}^{(q)} = \left[d_{12}^{(q)}, d_{13}^{(q)}\right]^T$ is a vector of phase shift ratios approximated at q-th iteration, $\mathbf{Y} = [P_2, P_3]^T$ is a vector of known input and output powers of FBC-B and FBC-C (FBC-A being the reference bridge), $\mathbf{P}^{(q)} = \left[P_2^{(q)}, P_3^{(q)}\right]^T$ is a vector of calculated input and output powers of FBC-B and FBC-C using (3.14) and $\mathbf{X}^{(q)}$ at q-th iteration, and $\mathbf{J}$ is a 2×2 Jacobian matrix which is a partial derivative of P_j in (3.14) with respect to each d_{1j}, $j = 2,3$ evaluated at $\mathbf{X}^{(q)}$ as follows

$$\mathbf{J}\Big|_{\mathbf{X}^{(q)}} = \begin{bmatrix} \frac{\partial P_2}{\partial d_{12}} & \frac{\partial P_2}{\partial d_{13}} \\ \frac{\partial P_3}{\partial d_{12}} & \frac{\partial P_3}{\partial d_{13}} \end{bmatrix} \tag{3.17}$$

Starting with a zero initial approximation of the phase shift ratios, i.e. $\mathbf{X}^{(0)} = [0,0]^T$ and known input and output powers, $\mathbf{Y} = [P_2, P_3]^T$, the iteration of the algorithm (3.16) was stopped when the desired solution accuracy, ζ_p was achieved, i.e. when $\left|\mathbf{X}^{(q+1)} - \mathbf{X}^{(q)}\right| \leq \zeta_p$. With the phase shift ratios known at every time instant, the operating mode of the TABC and the switching times of the waveforms shown in Figure 3.10 were derived at every operating point.

3.1.4 Operation of the Half Bridge Converter

In this subsection, the well known operation of a bidirectional HBC is briefed. Figure 3.12 shows the schematic diagram of a generic HBC of the FPC shown in Figure 1.6. It consists of a filter inductor, L_γ, filter capacitor, C_j and two MOSFET switches; Q_x and Q_y. The main function of the HBC is twofold; to step up and to step down voltage and current. For example, HBC-A in Figure 1.6 is used to step down the 19 V across C_1 to the required battery voltage of 12 V during battery charging, and conversely, to step up the 12 V to 19 V when the battery discharges.

The HBC allows current flow in both directions depending on the operation of the switches. When the terminal current, i_t flows in the direction shown in Figure 3.12, the HBC operates in boost mode, where it steps up the terminal voltage, V_t on the low voltage side to V_j on the high voltage side. The HBC operates in a buck mode where it steps down V_j to V_t when the direction of i_t in Figure 3.12 is reversed. In both operating modes, the Q_x and Q_y are switched in a complementary manner, i.e., when Q_x is switched on, Q_y is switched off and vice versa. A dead time in the order of nanoseconds is provided between the gating signals of the Q_x and Q_y, a period in which the intrinsic body diode, D_y conducts to prevent Q_x and Q_y from being on at the same time. Unlike the TABC where power flow is achieved by varying the phase shift angles of the FBCs, power flow in the HBC is achieved by varying the duty cycle of the switching signals.

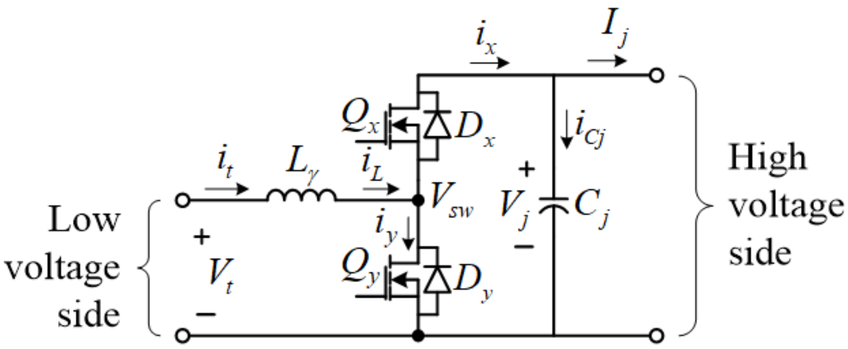

Figure 3.12: Schematic diagram of the half bridge converter.

Operation of HBC in Buck Mode

In the buck operating mode, Q_x is switched on first while Q_y is switched on after Q_x is switched off. Thus, Q_x is referred to as the control MOSFET while the Q_y the synchronous MOSFET. The complementary switching of Q_x and Q_y, and the resulting current flow direction is depicted in Figure 3.13.

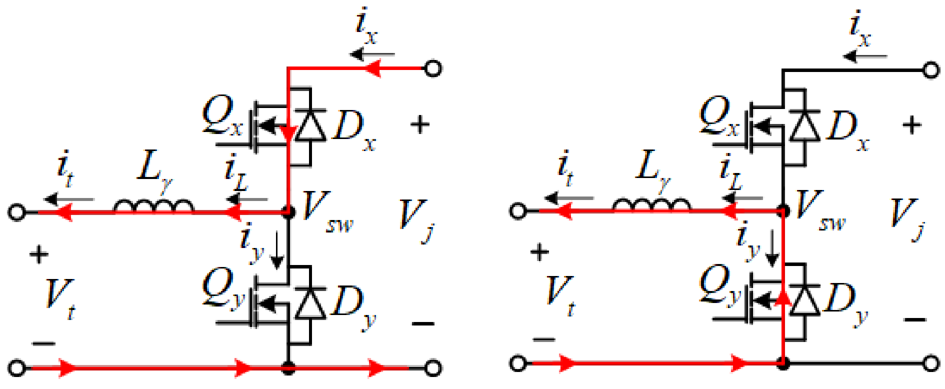

(a)

(b)

Figure 3.13: Operation of HBC in buck mode when (a) Q_x is switched on while Q_y is switched off in the first half of the switching cycle and when (b) Q_y is switched on while Q_x is switched off in the second half of the switching cycle.

3.1.5 Current and Voltage Waveform Modelling of HBC in Buck Mode

Figure 3.14 shows idealised steady state waveforms of the voltage across the inductor L_γ, inductor current, i_L and currents, i_x and i_y respectively through Q_x and Q_y in one complete switching period, T_s assuming a continuous flow of inductor current. Due to very short dead time (in nanoseconds) which is shorter than half a switching cycle (=5μs), the current and voltage waveforms of D_x and D_y has been neglected. The instantaneous and RMS current expressions for the inductor and MOSFETs describing the waveforms in Figure 3.14 were derived as follows.

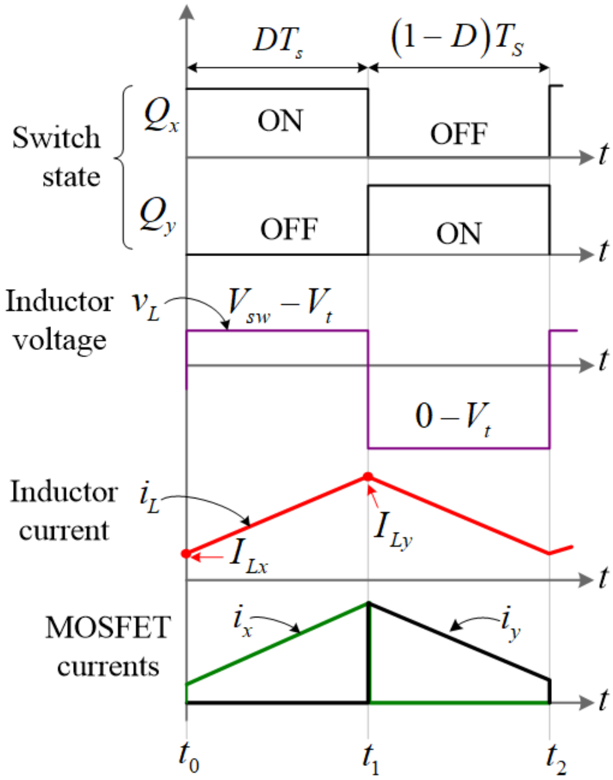

Figure 3.14: Voltage and current waveforms of an idealised operation of the half bridge converter in buck mode.

Inductor Voltage Expression

The inductor voltage, $v_L(t)$ was given by

$$v_L(t) = L_\gamma \frac{di_L(t)}{dt} = \begin{cases} V_{sw} - V_t\,, & \text{if } t_0 \leq t \leq t_1 \\ -V_t\,, & \text{if } t_1 \leq t \leq t_2 \end{cases} \tag{3.18}$$

where $V_{sw} = V_j$, $t_0 = 0$, $t_1 = DT_s$, $t_2 = T_s$ and D is the steady state duty ratio.

Instantaneous and RMS Inductor Current

The instantaneous inductor current, i_L was expressed from (3.18) as

$$i_L(t) = \begin{cases} \frac{(V_{sw}-V_t)}{L_\gamma}(t-t_0) + I_{Lx}\,, & \text{if } t_0 \leq t \leq t_1 \\ \frac{-V_t}{L_\gamma}(t-t_1) + I_{Ly}\,, & \text{if } t_1 \leq t \leq t_2 \end{cases} \tag{3.19}$$

where I_{Lx} is the initial inductor current at $t_0 = 0$ and I_{Ly} is the inductor current at $t_1 = DT_s$. From Figure 3.14 and (3.19), the I_{Lx} and I_{Ly} are related as follows

$$I_{Ly} - I_{Lx} = \frac{(V_{sw} - V_t)}{L_\gamma} DT_s \quad V_{sw} = V_j \tag{3.20}$$

Since $i_L(t_0) = i_L(t_2)$, the average inductor current, I_{Lavg}, which is equal to terminal current i_t was obtained as

$$I_{Lavg} = \frac{I_{Lx} + I_{Ly}}{2} = i_t \tag{3.21}$$

From (3.20) and (3.21), I_{Lx} and I_{Ly} were obtained as follows

$$\begin{cases} I_{Lx} = i_t - \frac{(V_{sw}-V_t)}{2L_\gamma} DT_s \\ I_{Ly} = 2i_t - I_{Lx} \end{cases} \tag{3.22}$$

Substituting (3.22) in (3.19), the simplified expression of the instantaneous $i_L(t)$ was obtained as

$$i_L(t) = \begin{cases} i_t + \frac{\Delta I_x}{2}\left(\frac{2t-DT_s}{DT_s}\right), & \text{if } t_0 \leq t \leq t_1 \\ i_t - \frac{\Delta I_x}{2}\left(\frac{2t-DT_s-T_s}{(1-D)T_s}\right), & \text{if } t_1 \leq t \leq t_2 \end{cases} \tag{3.23}$$

where

$$\Delta I_x = \frac{(V_{sw} - V_t)}{L_\gamma} DT_s \tag{3.24}$$

The RMS inductor current, $i_{L(RMS)}$ was obtained from (3.23) as follows

$$\begin{aligned} i_{L(RMS)} &= \frac{1}{T_s} \int_{t_0}^{t_2} i_L^2(t) dt \\ &= \sqrt{i_t^2 + \frac{\Delta I_x^2}{12}} \end{aligned} \tag{3.25}$$

Instantaneous and RMS Current of Control MOSFET, Q_x

Based on Figure 3.13 and (3.23), the instantaneous current through Q_x was obtained as follows

$$i_x(t) = \begin{cases} i_t + \frac{\Delta I_x}{2}\left(\frac{2t-DT_s}{DT_s}\right), & \text{if } t_0 \leq t \leq t_1 \\ 0, & \text{if } t_1 \leq t \leq t_2 \end{cases} \tag{3.26}$$

The RMS current, $i_{x(RMS)}$ through Q_x was obtained from (3.26) as

$$\begin{aligned} i_{x(RMS)} &= \frac{1}{T_s}\int_{t_0}^{t_2} i_x^2(t)dt \\ &= \sqrt{Di_t^2 + \frac{\Delta I_x^2}{12}D} \end{aligned} \tag{3.27}$$

Instantaneous and RMS Current of Synchronous MOSFET, Q_y

Similarly, the instantaneous current through Q_y was obtained as follows

$$i_y(t) = \begin{cases} 0, & \text{if } t_0 \leq t \leq t_1 \\ i_t + \frac{\Delta I_x}{2}\left[\frac{T_s-(2t-DT_s)}{(1-D)T_s}\right], & \text{if } t_1 \leq t \leq t_2 \end{cases} \tag{3.28}$$

The RMS current, $i_{y(RMS)}$ through Q_y was obtained from (3.28) as

$$\begin{aligned} i_{y(RMS)} &= \frac{1}{T_s}\int_{t_0}^{t_2} i_y^2(t)dt \\ &= \sqrt{(1-D)\,i_t^2 + \frac{\Delta I_x^2}{12}(1-D)} \end{aligned} \tag{3.29}$$

3.1.6 Determination of Duty ratio of HBC in Buck Mode

Using the principle of inductor volt-second balance that at steady state, the average inductor voltage over one switching cycle is zero [151], the duty ratio, D was determined from (3.30) as given in (3.31), which is a standard equation for duty ratio of an HBC operating in buck mode.

$$\frac{1}{T_s}\int_{t_0}^{T_s} v_L(t)dt = 0 \tag{3.30}$$

$$D = \frac{V_t}{V_j} \tag{3.31}$$

According to (3.31), with knowledge of V_t and V_j, the steady state duty cycle D was computed.

Operation of HBC in Boost Mode

Unlike the operation of the HBC in buck mode, in boost mode, Q_y is switched on first while Q_x is switched on in the second half of the switching cycle. Therefore, in the boost mode, Q_x is referred to as the synchronous MOSFET while Q_y is referred to as the control MOSFET. Figure 3.15 shows the operation of the HBC in boost mode.

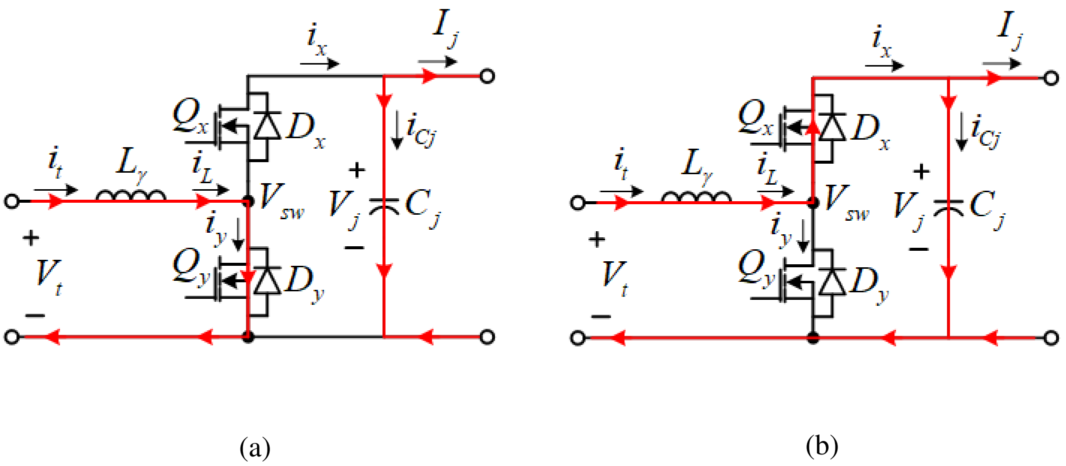

Figure 3.15: Operation of HBC in boost mode when (a) Q_y is switched on while Q_x is switched off in the first half of the switching cycle and when (b) Q_x is switched on while Q_y is switched off in the second half of the switching cycle.

3.1.7 Current and Voltage Waveform Modelling of HBC in Boost Mode

Figure 3.16 shows idealised steady state current and voltage waveforms of the HBC operating in a boost mode. Similar to the buck operation mode, the operation time of the body diodes is in nanoseconds, thus their current and waveforms were omitted from Figure 3.16. The same process of determining the instantaneous and RMS current expressions of the waveforms which are presented for the buck operation mode in Subsection 3.1.4 was also applied to the boost operation mode in this subsection as follows.

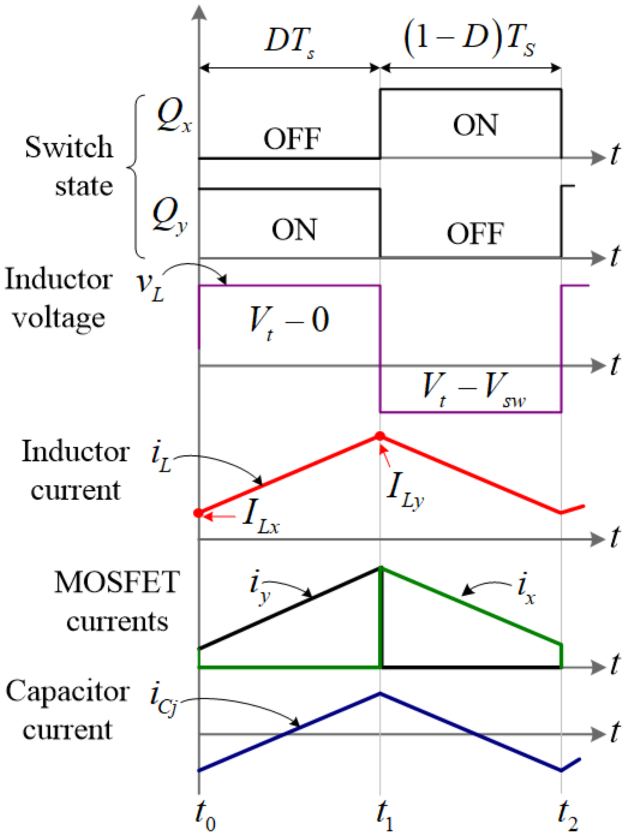

Figure 3.16: Voltage and current waveforms of an idealised operation of the half bridge converter in boost mode.

Inductor Voltage Expression

The inductor voltage, $v_L(t)$ was obtained as

$$v_L(t) = \begin{cases} V_t\,, & \text{if } t_0 \le t \le t_1 \\ V_t - V_{sw}\,, & \text{if } t_1 \le t \le t_2 \end{cases} \tag{3.32}$$

Instantaneous and RMS Inductor Current

The instantaneous inductor current, i_L was expressed from (3.32) as

$$i_L(t) = \begin{cases} \frac{V_t}{L_\gamma}(t - t_0) + I_{Lx}\,, & \text{if } t_0 \le t \le t_1 \\ \frac{V_t - V_j}{L_\gamma}(t - t_1) + I_{Ly}\,, & \text{if } t_1 \le t \le t_2 \end{cases} \tag{3.33}$$

The I_{Lx} and I_{Ly} were obtained as follows

$$\begin{cases} I_{Lx} = i_t - \frac{\Delta I_y}{2} \\ I_{Ly} = 2i_t - I_{Lx} \end{cases} \tag{3.34}$$

where

$$\Delta I_y = \frac{V_t}{L_\gamma} DT_s \tag{3.35}$$

The RMS inductor current, $i_{L(RMS)}$ was obtained from (3.33) and (3.34) as follows

$$i_{L(RMS)} = \sqrt{i_t^2 + \frac{\Delta I_y^2}{12}} \tag{3.36}$$

Instantaneous and RMS Current of Synchronous MOSFET, Q_x

The instantaneous current, $i_x(t)$ through Q_x was obtained as follows

$$i_x(t) = \begin{cases} 0, \text{ if } t_0 \leq t \leq t_1 \\ i_t + \frac{\Delta I_y}{2}\left(\frac{T_s-(2t-DT_s)}{(1-D)T_s}\right), \text{ if } t_1 \leq t \leq t_2 \end{cases} \tag{3.37}$$

The RMS current, $i_{x(RMS)}$ through Q_x was obtained from (3.37) as

$$\begin{aligned} i_{x(RMS)} &= \frac{1}{T_s}\int_{t_0}^{t_2} i_x^2(t)dt \\ &= \sqrt{(1-D)\, i_t^2 + \frac{\Delta I_y^2}{12}(1-D)} \end{aligned} \tag{3.38}$$

Instantaneous and RMS Current of Control MOSFET, Q_y

The instantaneous current, $i_y(t)$ through Q_y was obtained as follows

$$i_y(t) = \begin{cases} i_t + \frac{V_t}{2L_\gamma}(2t - DT_s), \text{ if } t_0 \leq t \leq t_1 \\ 0, \text{ if } t_1 \leq t \leq t_2 \end{cases} \tag{3.39}$$

The RMS current, $i_{y(RMS)}$ through Q_y was obtained from (3.39) as

$$\begin{aligned} i_{y(RMS)} &= \frac{1}{T_s}\int_{t_0}^{t_2} \left(i_y(t)\right)^2 dt \\ &= \sqrt{Di_t^2 + \frac{\Delta I_y^2}{12}D} \end{aligned} \tag{3.40}$$

Instantaneous and RMS Current of the Capacitor

The instantaneous current, i_{Cj} through the capacitor was expressed as follows

$$i_{Cj}(t) = C_j \frac{dv_j(t)}{dt} = \begin{cases} -\frac{\Delta I_y}{2} + \frac{\Delta I_y}{DT_s}t\,, & \text{if } t_0 \le t \le t_1 \\ \frac{\Delta I_y}{2} - \frac{\Delta I_y}{(1-D)T_s}\left(t - DT_s\right)\,, & \text{if } t_1 \le t \le t_2 \end{cases} \tag{3.41}$$

The RMS current, $i_{C(RMS)}$ through the capacitor was obtained from (3.41) as

$$\begin{aligned} i_{C(RMS)} &= \frac{1}{T_s}\int_{t_0}^{t_2} i_{Cj}^2(t)dt \\ &= \sqrt{\frac{\Delta I_y^2}{12}} \end{aligned} \tag{3.42}$$

3.1.8 Determination of Duty ratio of HBC in Boost Mode

The duty ratio, D was determined from (3.32) using (3.30) as follows

$$D = 1 - \frac{V_t}{V_j} \tag{3.43}$$

Thus, with the knowledge of the input and output voltage of the HBC, the duty cycle at every operating condition can be determined.

3.1.9 Power Loss Calculation

This subsection describes the estimation of power losses for different components of the FPC for each switching cycle. The losses were categorised into three main groups: MOSFET losses, passive component losses and transformer losses. Because of the operation of MOSFETs in synchronous rectification mode [38], the power loss contribution by the body diodes was ignored. For simplicity, the influence of temperature on the power loss of the components was also ignored. The losses were calculated using (1) design parameters of the FPC, (2) manufacturers' datasheet information of the FPC components and (3) FPC operating point which is given by the current and voltage waveforms described in the previous subsections.

MOSFET Losses

Power losses in MOSFETs were categorised into three parts: on-state losses, transient losses and gate drive losses. There are 20 MOSFETs in the FPC, thus the total MOSFET losses were obtained by summing the constituent losses for all the 20 MOSFETs.

On-state Losses

The on-state loss for each MOSFET in the FPC was estimated by the following expression

$$P_j^{sw(C)} = I_{RMS}^2 R_{DS} \tag{3.44}$$

where R_{DS} is the on-state resistance between drain and source of the MOSFET, which is given in the manufacturer's datasheet information of the MOSFET, and I_{RMS} is the RMS value of the current flowing through the MOSFET.

Transient Losses

Transient losses result from the process of turning on and turning off the MOSFET switches. Each MOSFET turns on while its body diode is initially conducting, resulting in low turn on losses because of low voltage drop across the MOSFET which is given by the voltage drop of the conducting forward-biased body diode which in most cases is less than 1 V. Thus, turn on losses were ignored and only turn off losses, $P_j^{sw(off)}$ (which occur due to a non-negligible voltage drop across the MOSFET) were computed using the following expression [152]

$$P_j^{sw(off)} = \frac{1}{2} |i(t)| V_{sw} t_{off} f_s \tag{3.45}$$

where $i(t)$ is the instantaneous value of the current through the MOSFET, V_{sw} is the instant voltage drop across the MOSFET, $f_s = 100$ kHz is the switching frequency of the FPC and t_{off} is the turn off time of the MOSFET (given in the manufacturer's datasheet).

Gate Drive Losses

The turn on and turn off process of the MOSFET involves charging and discharging the input gate capacitance of the MOSFET, which results in a gate drive loss $P_{sw(GD)}$ as follows [152]

$$P_j^{sw(GD)} = Q_G V_{gs} f_s \tag{3.46}$$

where Q_G is total gate charge provided by manufacturers and V_{gs} is the voltage applied between the gate and the source to turn on the MOSFET, which is also provided by the manufacturer.

Passive Component Losses

Passive components including filter capacitors, $C_j,\ j = 1,2,3$ and filter inductors, $L_\gamma,\ \gamma = a,b,c,d$ also introduce losses into the FPC due to their equivalent series resistance (ESR). The loss in each passive component j was approximated by

$$P_j^p = I_{p(RMS)}^2 R_{ESR} \tag{3.47}$$

where R_{ESR} is the equivalent series resistance of either the capacitor or the filter inductor which is given by the manufacturer's datasheets and $I_{p(RMS)}$ is the RMS current flowing through each passive component.

Transformer Losses

Power losses in the transformer are due to the resistance of the windings, hysteresis and eddy currents in the magnetic core. The transformer losses were therefore classified into two groups as copper losses and magnetic core losses.

Copper Losses

The copper losses were estimated as follows

$$P_{Trx(cu)} = \sum_{j=1}^{3} i_{j(RMS)}^{2} R_j \tag{3.48}$$

where $i_{j(RMS)}$ and R_j are RMS current and DC resistance of winding j respectively. Each winding j was printed on a circuit board as shown in Figure 3.17. The R_j was calculated for each printed circuit board winding using the following expression [153]

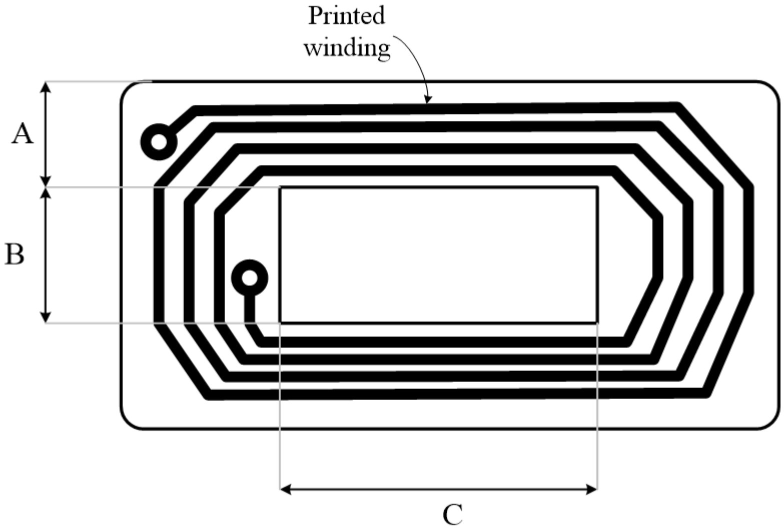

Figure 3.17: Dimensions relating to a printed circuit board winding.

$$R_j = 2L_t n_j R_{trace} \tag{3.49}$$

where $R_{trace} = 165\mu\Omega$/mm is the DC resistance of the copper trace having a line thickness of 1.02 mm, n_j is the number of turns of the copper traces and L_t is the mean length turn in milimeters expressed as [153]

$$L_t = 2B + 2C + 2.82A \tag{3.50}$$

where A = 8.1 mm, B = 10 mm and C = 27.9 mm for the FPC shown in Figure 1.6.

Magnetic core losses

The magnetic core losses consist of the hysteresis and eddy current losses in the magnetic core [154]. The total magnetic core loss under square wave voltages with duty cycle, D was approximated by the Natural Steinmetz Extension (NSE) equation [155]

$$P_{Trx(core)} = k_N f_s^{\alpha_f} \hat{B}^{\beta_b} \left[\left(\frac{2}{D} \right)^{\alpha_f} + \left(\frac{2}{1-D} \right)^{\alpha_f} (1-D) \right] V_{core} \tag{3.51}$$

where $\hat{B}$ is the maximum flux density in the core, α_f is the frequency coefficient of the core, β_b is the magnetic density coefficient of the core, V_{core} is the volume of the core and k_N is defined as

$$k_N = \frac{C_m \left(C_{to} - C_{t1} T + C_{t2} T^2 \right)}{\left(2^{\beta_b + 1} \right) \pi^{\alpha_f - 1} \left(0.2761 + \frac{1.7061}{\alpha_f + 1.354} \right)} \tag{3.52}$$

where T is temperature of the core in Celsius, C_m, C_{to}, C_{t1} and C_{t2} are empirical parameters specific to a ferrite material of the core [6]. The values of these parameters together with $\hat{B}$, α_f, β_b and V_{core} in (3.51) for a 3F3 ferrite material of the FPC are given in Table 3.1.

Table 3.1: Parameters to calculate the magnetic core loss for a 3F3 ferrite material [6]

Parameter symbol	Value	Units
$\hat{B}$	0.1	T
α_f	1.63	-
β_b	2.45	-
D	0.5	-
C_m	0.25×10^{-3}	-
C_{to}	1.26	-
C_{t1}	1.05×10^{-2}	-
C_{t2}	0.79×10^{-4}	-
T	100	°C
f_s	100	kHz
V_{core}	1.15×10^{-5}	m^3

Total FPC Loss

The total loss of the FPC at every operating condition was determined as follows

$$\begin{aligned} p^{c}_{loss} =& K_{FPC} + P_{Trx(cu)} + P_{Trx(core)} + \sum_{j=1}^{3} P_j^{p(C)} + \sum_{j=1}^{4} P_j^{p(I)} \\ & \sum_{j=1}^{20} \left(P_j^{sw(C)} + P_j^{sw(off)} + P_j^{sw(GD)} \right) + \end{aligned} \tag{3.53}$$

where K_{FPC} is standby loss of the FPC, $P_j^{p(C)}$ is passive loss of each filter capacitor and $P_j^{p(I)}$ is passive loss of each filter inductor as expressed in (3.47).

3.1.10 Detailed FPC Power Loss Model

The current and voltage waveform modelling and power loss calculations presented in Subsection 3.1.2 to Subsection 3.1.9 together constitute the detailed FPC power loss model. The ultimate purpose of developing the loss model was to optimise the FPC design (even though this was beyond the scope of the current research) with efficiency as the design parameter. For this reason, a Python program was developed to autonomously handle the waveform modelling and power loss calculations as given by the flowchart in Figure 3.18.

The program consists of five main steps:

1. **Inputs:** The operating point, design parameters and manufacturers' datasheet information of the FPC components were the inputs to the program, replacing the FPC switching circuit in Figure 3.1. The operating point include currents and voltages at the ports of the FPC during operation. The design parameters include the leakage inductors of the transformer, filter capacitors, filter inductors and number of parallel MOSFETs. From the datasheets, information such as the on-resistance and gate-to-source voltage of the MOSFETs were obtained. Computations of referred quantities of the transformer were also carried out at this stage.

2. **Loss calculation of the HBCs:** Since the TABC depends on the power inputs and outputs from the HBCs, the power losses of the HBCs were firstly computed using the inputs in Step 1. Depending on the direction of current flow, the operation of each HBC

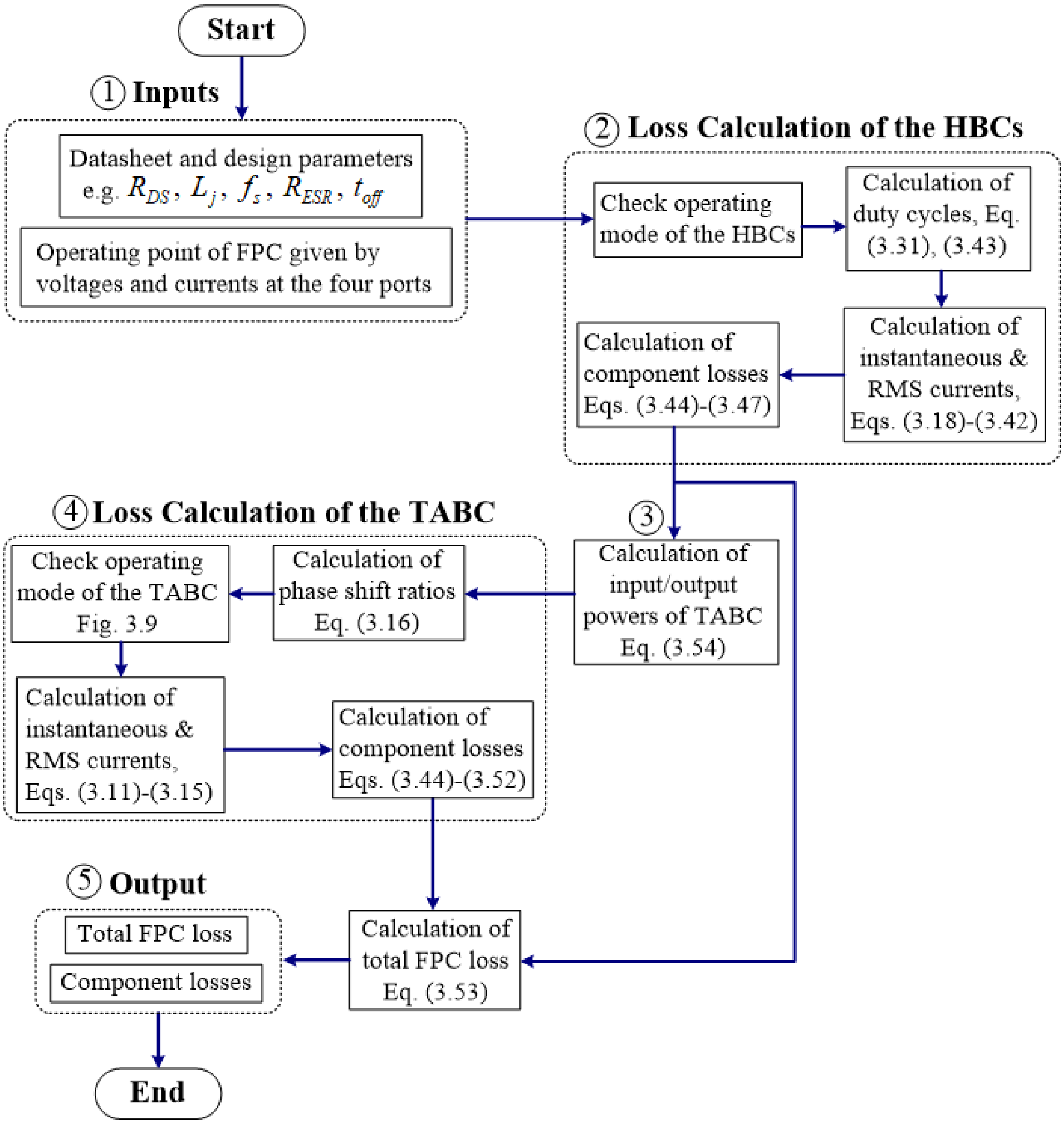

Figure 3.18: Program of the proposed detailed FPC power loss model.

was classified as either buck or boost operating mode as presented in Section 3.1.4. Based on the operating mode, the associated steady state duty ratios were calculated by using (3.31) for the buck mode and (3.43) for the boost mode. The instantaneous and RMS currents in the MOSFETs, filter capacitors and filter inductors were thereafter computed using (3.18) to (3.42) based on the operating mode. Using the computed currents, the component losses of the HBCs were calculated using (3.44) to (3.47).

3. **Calculation of input and output powers of the TABC:** This step computed the power inputs to the FBCs of the TABC. Denoting the terminal power and the total power loss

of a particular HBC as P_t and $P_{loss(HBC)}$ respectively, the power input to the associated FBC was calculated as

$$P_j = P_t - P_{loss(HBC)} \tag{3.54}$$

Since FBC-A was operated with a pre-known reference phase shift ratio, only power inputs to FBC-B and FBC-C were required to be computed.

4. **Loss calculation of the TABC:** Using P_j in (3.54), the phase shift ratios of the TABC were calculated iteratively from (3.16). The resulting phase shift ratios were thereafter used to obtain the operating mode of the TABC based on Figure 3.9. From the identified operating mode, the corresponding instantaneous and RMS currents through the MOSFETs and the transformer windings were computed using (3.11) to (3.15). The component losses of the TABC were thereafter computed using the power loss expressions given in (3.44) to (3.52).

5. **Outputs:** The outputs of the program were the component losses and system power loss of the FPC.

3.1.11 Experimental Validation

This subsection validates the performance of the detailed FPC loss model developed in the previous subsection using an experimental test set up. To achieve this, the list of equipment shown in Table 3.2 were used. The experiment was set up as shown in Figure 3.19. It should be noted that the TABC, HBC-A, HBC-B, HBC-C and HBC-D all exist as a single power

Table 3.2: List of key experimental equipment.

No.	Equipment	Abbreviation	Description	Quantity
1	Four-port DC-DC converter	FPC	power converter	1
2	EA Elektro-Automatik EA-EL 3400 400V/25A/400W	EL3400	DC electronic load	1
3	EA Elektro-Automatik EA-EL 3160 160V/60A/400W	EL3160	DC electronic load	1
4	EA Elektro-Automatik PS 2342-06B 42V/6A/100W	PS2342	Triple output variable DC power supply	2
5	EA Elektro-Automatik PS 2384-05B 84V/5A/160W	PS2384	Triple output variable DC power supply	1
6	Field Programmable Gate Array	FPGA	controller	1
7	Desk or laptop computer	-	1	-

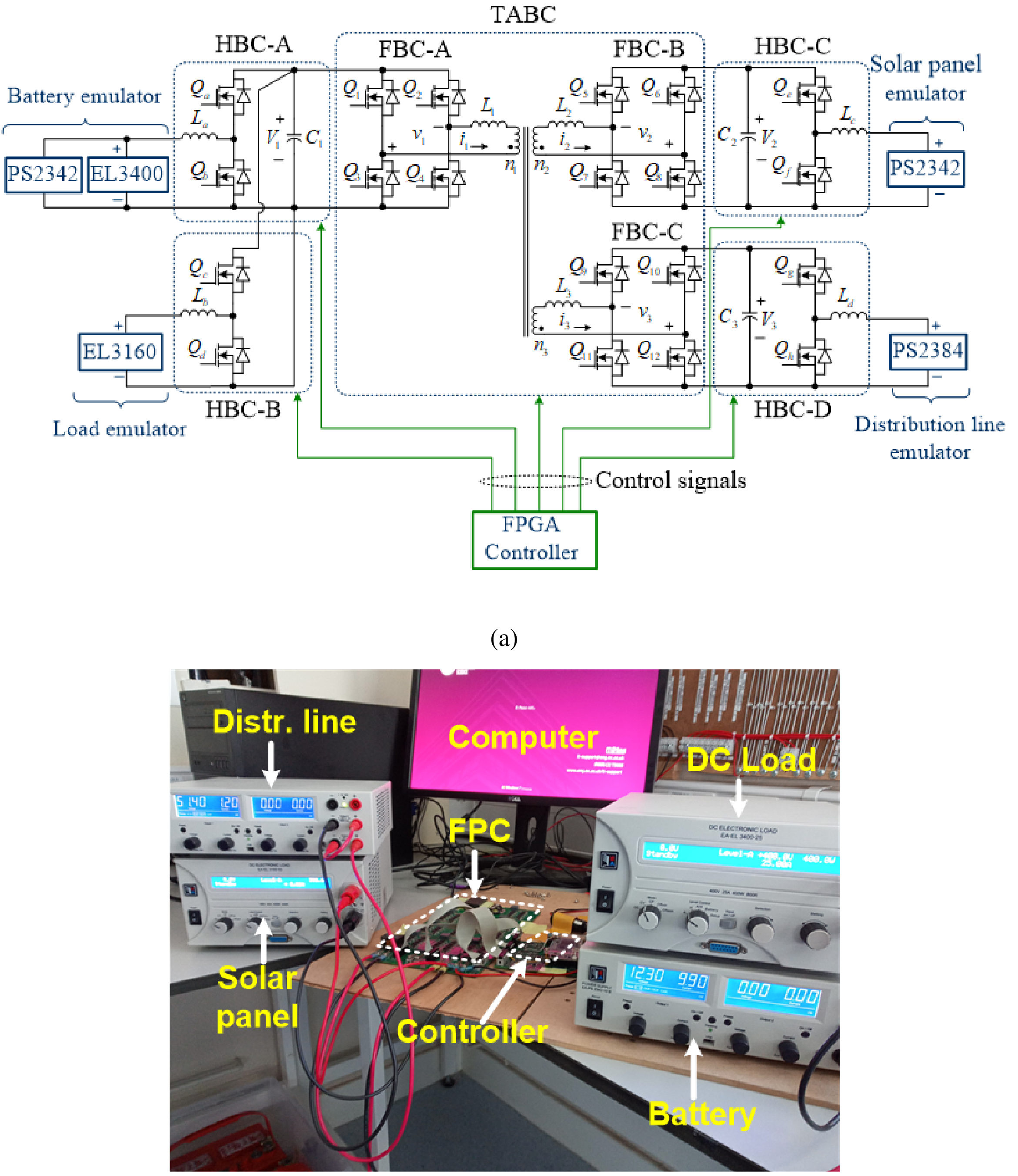

(a)

(b)

Figure 3.19: Experimental set up for validating the power loss model: (a) electrical drawing and (b) physical layout of the equipment.

processing stage, which is the FPC. The electrical parameters of the FPC are shown in Table 3.3. The type and ratings of the MOSFETs used for FBC-A, FBC-B, FBC-C, HBC-A, HBC-B, HBC-C and HBC-D are given in Table 3.4. The power rating of each terminal of HBC-A, HBC-B, HBC-C and HBC-D was 500 W.

Table 3.3: Circuit parameters of the FPC.

Parameter description	Symbol	Value	Units
Voltage	$V_1/V_2/V_3$	$19/38/152$	V
Leakage inductance	$L_1/L_2/L_3$	$0.720/3/44$	μH
Filter inductance	$L_a/L_b/L_c/L_d$	$3.3/3.3/22/47$	μH
Filter capacitance	$C_1/C_2/C_3$	$300/48/4.8$	μF
Transformer core material	-	3F3	-
Maximum flux density	B	0.1	T
Transformer turn ratio	$n_1 : n_2 : n_3$	1:2:8	-

Table 3.4: Type and ratings of MOSFETs.

MOSFET type	Voltage rating (V)	Current rating (A)	On-state resistance	Application
MOSFET FDD8896/FDU8896	30	94	5.7 mΩ	FBC-A, HBC-A & HBC-B
MOSFET FDD10AN06A0_F085	60	50	10.5 mΩ	FBC-B & HBC-C
MOSFET FQD18N20V2	200	15	140 mΩ	FBC-C & HBC-D

Experimental Procedure

To emulate the battery for both charge and discharge processes, the EL3400 and one unit of PS2342 were connected in parallel as shown in Figure 3.19a. Both the EL3400 and the PS2342 were set in Constant Voltage (CV) mode. The voltage of EL3400 was set to 12.3 V, slightly higher than 12 V which was set for PS2342 in order to avoid the situation where PS2342 supplies power to EL3400.

To emulate the DC loads, the EL3160 was set in Constant Current (CC) mode and the FPGA was programmed to maintain its voltage at 12 V. The solar panel was emulated by one of the PS2342 power supplies. The PS2342 was set in CV mode and the FPGA was programmed to maintain its voltage at 25 V. The PS2384 switch mode power supply was used to emulate the distribution line. Two of its output terminals were set in CV and were connected in series by enabling its tracking function while setting each terminal to 50 V in order to obtain a total distribution voltage of 100 V. The 100 V was further maintained constant by the FPGA controller.

To avoid overheating the FPC and minimise errors in measurements, the experiment was automated. So, the electronic DC loads and switch mode power supplies were programmed in order to accomplish the following tasks:

- Switch on-and off.

- Set Over Voltage Protection (OVP) and Over Current Protection (OCP) (as given by manufacturers).
- Set desired voltage and current values as received from the computer.
- Measure and send FPC voltage and current measurements to the computer.

To analysis the FPC loss, the following four main operating conditions (modes) of the FPC were investigated:

1. **Mode 1:** Battery discharging to supply the DC load while power from both the solar panel and distribution line is zero.
2. **Mode 2:** Battery discharging and distribution line supplying the DC load while power from the solar panel is zero.
3. **Mode 3:** Solar panel supplying the DC load while the battery charges the surplus power and discharges the deficit power. Power from distribution line is zero.
4. **Mode 4:** Solar panel and distribution line both supplying the DC load while the battery charges the surplus power and discharges the deficit power.

The aforementioned modes are the extreme operating modes of the FPC. The other operating modes of the FPC are a combination of the above modes and their resulting FPC loss were considered to be between those of the aforementioned operating modes.

Table 3.5 shows the considered current and power values of the solar panel (PS2342), distribution line (PS2384) and DC loads (EL3160) that were adjusted remotely during the experimental investigation of the FPC loss through the four main operating modes. The current and power values of the battery (which is emulated by PS2342 and EL3400) were not adjusted because the battery in this research was considered to be a back-up generator, charging and discharging power whenever the sum of distribution line and solar panel power was either greater than or less than the DC load power respectively.

For each of the considered operating modes, the battery power supply, PS2342 was switched on first to a voltage of 12 V (while the other power supply units remained in standby

Table 3.5: Current and power values of the electronic load and power supplies during experiment for the four operating modes.

	PS2342		PS2384		EL3160	
Operating mode	Current (A)	Power (W)	Current (A)	Power (W)	Current (A)	Power (W)
Mode 1	0	0	0	0	1-6.83	12-82
Mode 2	0	0	0.5	50	1-6.83	12-82
Mode 3	2	50	0	0	1-6.83	12-82
Mode 4	2	50	0.5	50	1-6.83	12-82

mode) in order to power the control circuits. Thereafter, the other units i.e. PS2342, PS2384 and EL3160 were assigned the values given in Table 3.5. The current of EL3160 was remotely varied between 1.00-6.82 A (sufficient to capture the battery and discharge process) while maintaining its voltage constant at 12 V by the FPGA controller. That gave a DC load power range of 12-82 W. After each operating mode, the computer automatically displayed the power values of the solar panel, battery and distribution line. Based on the obtained power values, the FPC loss was computed as follows

$$p^{c}_{loss} = P_b + P_{pv} + P_{dc} - P_L \tag{3.55}$$

where P_b is battery power (positive when discharging and negative when charging), P_{dc} is distribution line power (positive when supplying to the FPC and negative otherwise), P_{pv} is power from the solar panel and P_L is DC load power.

Results

A FPC standby loss of $K_{FPC} = 12.58$ W was obtained when the experiment was switched on using the battery while the solar panel, distribution line and DC load remained off. Varying the DC load as indicated in Table 3.5 for both the experiment and the loss model presented in Subsection 3.1.9 yielded the FPC loss results shown in Figure 3.20.

Figure 3.20 shows that the results of the loss model developed were consistent with the experimental results. This suggests that the FPC loss model developed is accurate for approximating the power losses of the FPC, which is crucial for optimising the design of the FPC. The errors between the loss model and experimental results in Figures 3.20a, 3.20b, 3.20c and 3.20d were within ±1 W, ±1 W, ±2 W and ±6 W respectively. The consistency

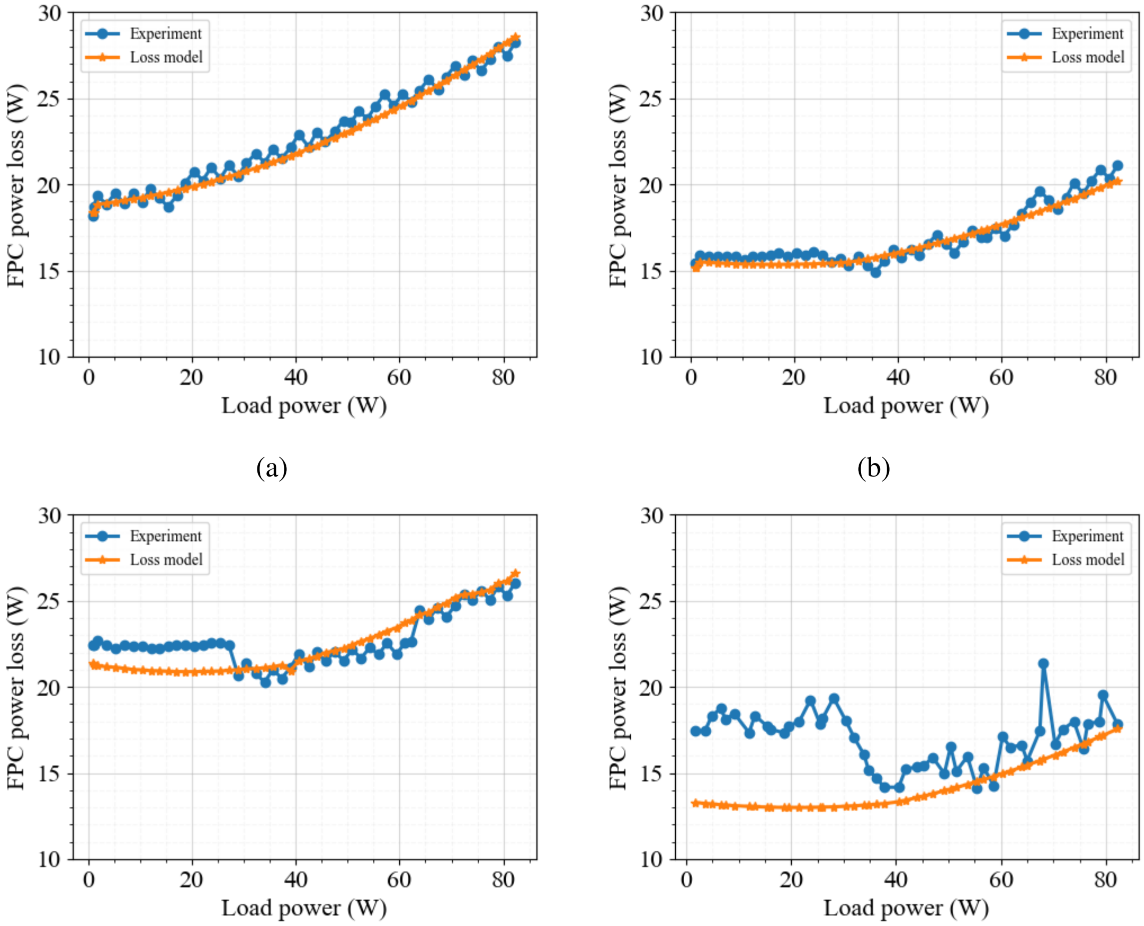

(a) (b)

(c) (d)

Figure 3.20: Comparison of FPC loss results between the loss model developed and the experiment for operating (a) Mode 1, (b) Mode 2, (c) Mode 3 and (d) Mode 4. The experimental results have an accuracy of ±2%.

in the results can be attributed to the fact that the experiment was automated with the results of each operating mode being obtained within a minute, thus keeping the influence of temperature on the FPC loss to a minimum. The FPC loss for Modes 3 and 4 in Figure 3.20c and Figure 3.20d respectively first decreases before increasing with the DC load power because of battery's transition from the charge to discharge state.

3.2 Simplified Four-Port DC-DC Converter Modelling

Despite the accuracy of the detailed FPC loss model developed which is described in the previous section for approximating the FPC loss, its dependency on the operating point of the FPC makes it highly non-linear and complex to be included in a real time optimisation problem. A simplified version of the loss model that is less complex was therefore required.

3.2.1 Simplified FPC Loss Model

Plotting the experimental results for all the four operating modes in Figure 3.20 on one graph, Figure 3.21 was obtained.

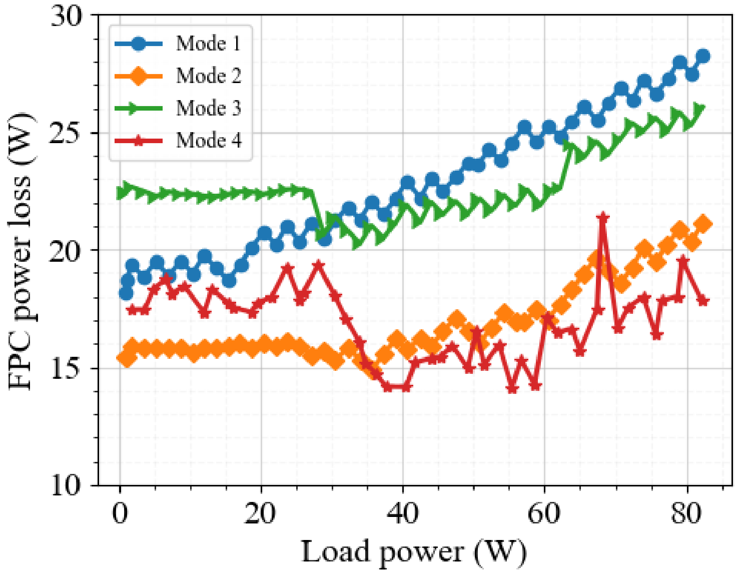

Figure 3.21: Variation of the experimental FPC loss with DC load power for four operating modes. The FPC loss for Modes 3 and 4 first decreases before increasing with the DC load power because of the battery's transition from charge to discharge states respectively.

From Figure 3.21, it is shown that the variation of the FPC loss with the DC load power is quadratic with the FPC loss reaching maximum values when the DC load power is maximum for each of the considered operating modes. Furthermore, the difference between the highest and the lowest FPC loss values of the different FPC loss curves at the same DC load power is less than 10 W. Thus, an experimental representative FPC loss curve can be obtained by averaging the FPC loss curves shown in Figure 3.21 using the mean ordinate method [156] as follows

$$\bar{X}_j = \frac{1}{4}\sum_{j=0}^{4} x_j \quad \bar{Y}_j = \frac{1}{4}\sum_{j=0}^{4} y_j \tag{3.56}$$

where x_j and y_j are the DC load power and FPC loss on an individual curve respectively, $\bar{X}_j$ and $\bar{Y}_j$ are the DC load power and FPC loss on the representative FPC loss curve respectively.

Figure 3.22 shows the experimental and representative FPC loss curve (hereafter referred to as simplified FPC loss model) obtained by (3.56) and Python curve fitting techniques respectively. The average percentage error between the simplified FPC loss model and the experimental curve is 1.07%. The standard deviation of the experimental curve was obtained as 1.59 W. The simplified FPC loss model was expressed as

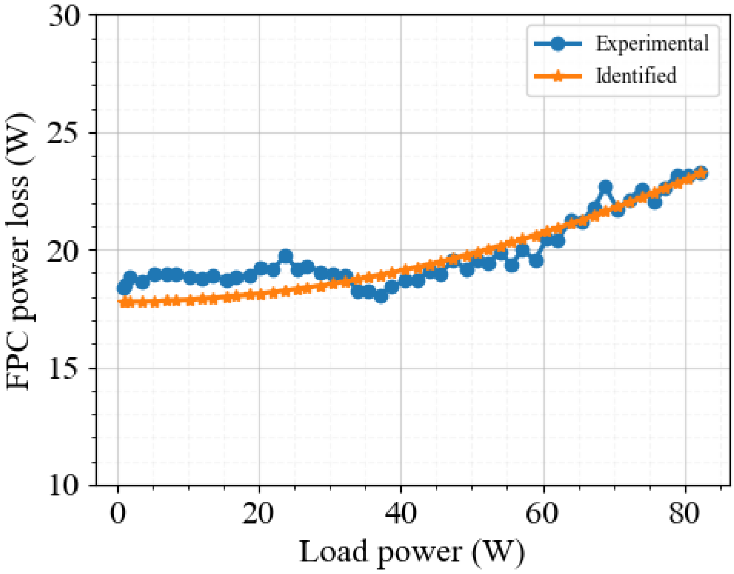

Figure 3.22: Experimental and identified representative FPC loss curves.

$$p^c_{loss} = x_0 + x_1 P_L + x_2 P_L^2 \tag{3.57}$$

where $x_0 = 17.765$, $x_1 = 1.754 \times 10^{-3}$ and $x_2 = 7.906 \times 10^{-4}$.

With reference to the FPC losses described in Subsection 3.1.9, the constant loss term, x_0 represents the standby losses and gate drive losses given in (3.46), which are independent of the current and power flow in the FPC. The linear loss term, $x_1 P_L$ represents the losses that increase linearly with the current flow in the FPC such as the transient losses expressed by (3.45). The non-linear loss term, $x_2 P_L^2$ represents power losses that increase as a square of FPC current such as passive component and on-state losses, which are given by (3.47) and (3.44) respectively.

The simplified FPC loss model given in (3.57) is simple and was used in this research to approximate the power loss of the FPC at every operating condition.

3.2.2 Equivalent Circuit Model of the FPC

Apart from the FPC loss, the other key feature of the FPC is the HFT which requires special consideration if modelling of the FPC is to be complete. Due to the presence of the HFT, power flow in the FPC is magnetically coupled. This means that the distribution line, solar panels, battery and DC loads which are coupled through the HFT as shown in Figure 1.6 do not physically share a common voltage, making the power flow analysis complex.

To handle the HFT, the FPC loss which is given by (3.57) was viewed as an additional DC load, r_c connected to an ideal FPC. Then the steady state dynamics of the HFT and the FPC thereof were represented by an ideal four winding DC transformer equivalent circuit as shown in Figure 3.23.

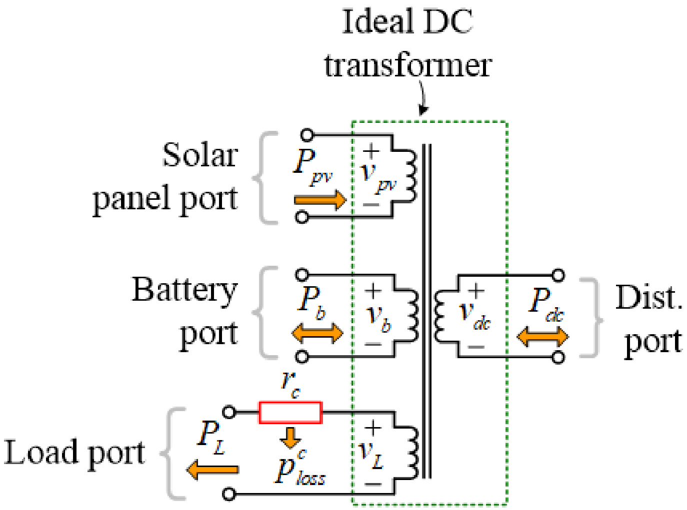

Figure 3.23: Equivalent circuit model of the FPC.

3.3 Load Modelling

Load modelling refers to the mathematical representation of the relationship between the load voltage and the power consumed. Loads which consume reactive power were not of interest in the present research since the solar nano-grid considered uses DC technology. The total power consumed by the load(s) at a particular time, t was referred to as load demand. There are two main types of load models [157], namely, static and dynamic load models. Static models are used to represent the load demand as a function of load voltage. Dynamic models express the load demand as a function of load voltage and time using differential equations. Dynamic models (e.g. the equivalent circuit of an induction motor) are mainly used for dynamic power system studies including transient stability and frequency stability [157]. The present research was interested in steady state analysis, thus dynamic models were not considered. Furthermore, changes in load demand due to user behaviour were also not considered. The commonly used static models are as follows [158].

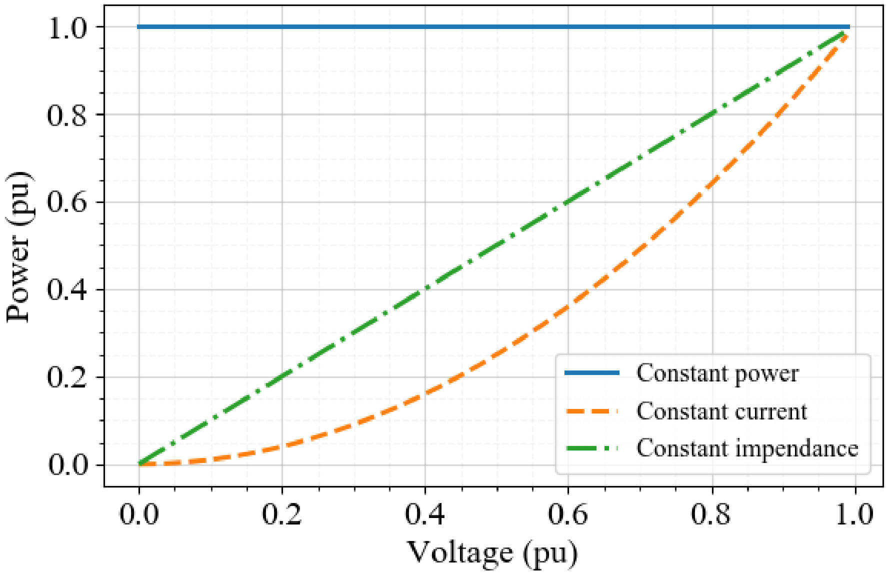

Figure 3.24: Load characteristics for constant power, constant current and constant impedance loads.

3.3.1 Constant Power Load Model

Constant power load model represent load demands, P_L that are constant regardless of the changes in the magnitude of load voltage, V_L as follows

$$P_L = P_0 \left(\frac{V_L}{V_0}\right)^0 = P_0 \tag{3.58}$$

where P_0, V_0 are rated power and rated voltage values respectively.

Examples of constant power loads include; motoring loads such as sewing machines and water pumps [159], lighting loads such as LED lights and electronic loads such as TVs, radios and computers [160]. The power-voltage characteristics of constant power loads is shown in Figure 3.24.

3.3.2 Constant Current Load Model

A load model where the load demand is directly proportional to the load voltage magnitude as follows

$$P_L = P_0 \left(\frac{V_L}{V_0} \right)^1 \tag{3.59}$$

Loads that can be modelled using (3.59) are few in practice. Examples include welding units, smelting and electroplating processes [159]. Their load characteristics is depicted in Figure 3.24.

3.3.3 Constant Impedance Load Model

A load model where the load demand is directly proportional to the square of the load voltage magnitude as

$$P_L = P_0 \left(\frac{V_L}{V_0} \right)^2 \tag{3.60}$$

Incandescent lamps, water heaters and stove tops are some of examples of constant impedance loads that can be modelled using (3.60). Their load characteristics is shown in Figure 3.24.

3.3.4 Polynomial Load Model

Polynomial load model represents loads that have characteristics which are a mixture of any two or all of the three load characteristics shown in Figure 3.24. Examples of such loads include dishwashers which are both constant impedance loads (due to the heating element) and constant power loads (due to the motor) [159]. The load demand of polynomial loads varies as an affine function of the load voltage magnitude as follows

$$P_L = P_0 \left[a_0 + a_1 \left(\frac{V_L}{V_0} \right) + a_2 \left(\frac{V_L}{V_0} \right)^2 \right] \tag{3.61}$$

where $a_0, \ldots, a_2$ are constant parameters of the load model. The sum of the parameters equals to one, i.e. $a_0 + a_1 + a_2 = 1$ and indicates how the rated power, P_0 is divided among the three load models presented in the previous subsections.

3.3.5 Exponential Load Model

Exponential load model represents load demand as an exponential function of the load voltage magnitude as follows

$$P_L = P_0 \left(\frac{V_L}{V_0} \right)^{n_p} \tag{3.62}$$

where n_p is a constant parameter of the load models. With n_p equal to 0, 1, or 2, the model represents the constant power, constant current and constant impedance load models respectively.

3.3.6 Preferred Load Model

Most of the common DC loads in rural areas such as LED lights, TVs, water pumps fall under constant power loads [160]. For this reason, the preferred load model was the constant power load model. Maintaining the load voltage, v_L constant, the current drawn by the DC loads at t was expressed as

$$i_L(t) = \frac{P_L(t)}{v_L} \tag{3.63}$$

3.4 Solar Panel Modelling

The key feature of the solar panel is the amount of output power, P_{pv} it produces from the available solar irradiance, G and atmospheric temperature, T_c at every time instant as shown in Figure 3.25. In this research, solar panel modelling refers to the mathematical representation of the produced power as a function of the solar irradiance and atmospheric temperature.

Several models of solar panels already exists in literature.These were categorised into two groups as circuit-based models [161–163], and non-circuit based models [146, 164].

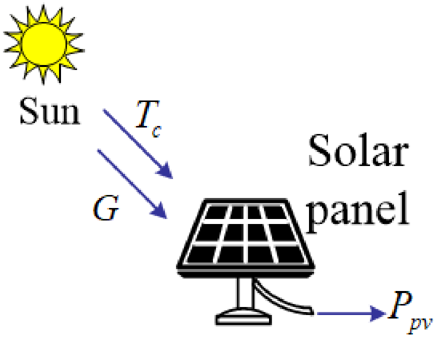

Figure 3.25: Schematic diagram of power production by a solar panel.

3.4.1 Circuit-based Solar Panel Model

Circuit-based models are where Photo Voltaic (PV) cells of the solar panel are represented by their electrical equivalent circuits. The output current and voltage of the equivalent circuit are obtained by Kirchhoff's voltage and current laws. The produced power is expressed as a product of the output current and voltage. Since these models use detailed electrical equivalent circuits, they have high-fidelity and high accuracy than the non-circuit based models. In addition, circuit-based models require designing a Maximum Power Point Tracker (MPPT) which ensures that the produced power is always maximum, hence they closely represent the physical behaviour of the solar panels. However, due to the use of electrical equivalent circuits and the MPPT design, it means that they are more complex than the non-circuit based models.

3.4.2 Non-circuit-based Solar Panel Model

Non-circuit-based models are where the produced power from the solar panel is directly expressed as a function of solar irradiance and atmospheric temperature without using equivalent circuits and designing the MPPT. Hence, they are less complex than circuit-based models. However, due to lack of electrical equivalent circuits and the MPPT design, they have low-fidelity.

3.4.3 Preferred Solar Panel Model

The circuit-based solar panel model was the preferred model due to its high-fidelity and high-accuracy. Furthermore, the electrical equivalent circuit model of the solar panel made it possible to integrate it with the FPC equivalent circuit model developed in Figure 3.23.

There are many different circuit-based solar panel models in literature. One of the most widely used model is the single diode model which is shown in Figure 3.26, due to its simplicity and accuracy [161, 165–167]. The model can be expressed mathematically as [167]

$$i_{pv} = I_{ph} - I_s \left[\exp\left(\frac{v_{pv} + r_{pv} i_{pv}}{V_T} \right) - 1 \right] - \frac{v_{pv} + r_{pv} i_{pv}}{r_{sh}} \tag{3.64}$$

where $i_{pv,i}$ and v_{pv} are DC output current and voltage of the panel, respectively, I_s is saturation current, r_{pv} and r_{sh} are series and shunt resistance of the panel, respectively, V_T is thermal voltage of the diode, D and I_{ph} is photocurrent of the panel.

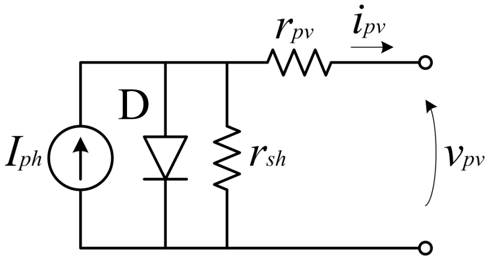

Figure 3.26: Single diode model of a solar panel.

The shunt resistance, r_{sh} is commonly considered to be very large, i.e. $r_{sh} \to \infty$ as it does not produce noticeable effects near the Maximum Power Point (MPP) (where the solar panel normally operates) [168]. Thus, assuming $r_{sh} \to \infty$, (3.64) was expressed (with v_{pv} as the subject) as follows

$$v_{pv} = V_T \ln\left(1 + \frac{I_{ph} - i_{pv}}{I_s} \right) - r_{pv} i_{pv} \tag{3.65}$$

For steady state simulation purposes, it is normally desirable to express (3.65) in a form that has parameters (e.g. open circuit voltage) which can be easily obtained from solar panel data sheets provided by manufacturers. Following the simplifications outlined in [161], (3.65) was simplified as follows

$$v_{pv} = v_{oc}^{pv} + V_{T(STC)} \left(\frac{T_c}{T_{STC}} \right) \ln \left[1 - \left(i_{pv}/I_{ph} \right) \right] - i_{pv} r_{pv} \tag{3.66}$$

where

$$v_{oc}^{pv} = V_{oc(STC)}^{pv} \left[1 + \beta_{pv} \left(T_c - T_{STC} \right) \right] + V_{T(STC)} \ln \left(G/G_{STC} \right), \quad G > 0 \tag{3.67a}$$

$$r_{pv} = \frac{V_{mp}}{I_{mp}} - \frac{2V_{mp} - V_{oc(STC)}^{pv}}{I_{mp} + \left(I_{sc(STC)} - I_{mp} \right) \ln \left(1 - I_{mp}/I_{sc(STC)} \right)} \tag{3.67b}$$

$$V_{T(STC)} = \frac{\left(2V_{mp} - V_{oc(STC)}^{pv} \right) \left(I_{sc(STC)} - I_{mp} \right)}{I_{mp} + \left(I_{sc(STC)} - I_{mp} \right) \ln \left(1 - I_{mp}/I_{sc(STC)} \right)} \tag{3.67c}$$

$$I_{ph} = I_{ph(STC)} \left(\frac{G}{G_{STC}} \right) \left[1 + \alpha_{pv} \left(T_c - T_{STC} \right) \right] \tag{3.67d}$$

STC is Standard Test Conditions[1], $V_{T(STC)}$ is thermal voltage at STC, $I_{ph(STC)}$ is photocurrent at STC, which is approximately equal to short circuit current at STC, $I_{sc(STC)}$ [161]. The other parameters in (3.66) and (3.67) describe the specifications of a solar panel as given by the manufacturer; these are defined in Table 3.6 e.g. for a 250 W, 24 V Suntech monocrystalline solar panel [7].

Equation (3.66) can be pictorially represented as shown in Figure 3.27 [161]. The diode in the figure models the second term on the right hand side of (3.66) and should not be confused with its physical operating behaviour. The produced power from the solar panel was obtained by multiplying (3.66) by the output current as follows

$$P_{pv} = v_{pv} i_{pv} \tag{3.68}$$

---

[1] Conditions under which solar panels are tested, which are solar irradiance, G_{STC} = 1000 W/m^2, T_{STC} = 25°C and Air Mass (AM) coefficient, AM = 1.5.

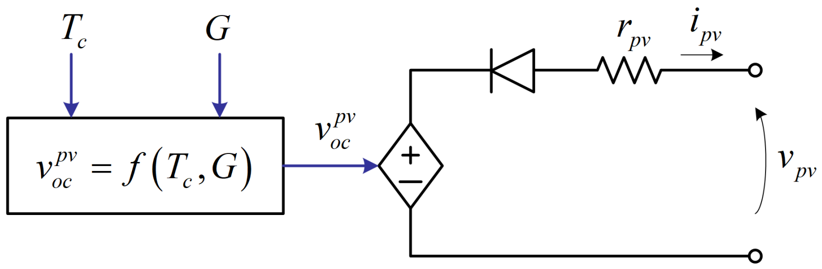

Figure 3.27: Circuit representation of equation (3.66).

Table 3.6: Manufacturer's datasheet information for a 250 W, 24 V Suntech monocrystalline solar panel [7].

Parameter description	Symbol	Value	Units
Power at Maximum Power Point (MPP) at STC	P_{mp}	250	W
Open circuit voltage at STC	$V_{oc(STC)}^{pv}$	30.7	V
Voltage at MPP and at STC	V_{mp}	30.7	V
Short circuit current at STC	$I_{sc(STC)}$	8.63	A
Current at MPP and at STC	I_{mp}	8.15	A
Temperature coefficient of v_{oc}^{pv}	β_{pv}	-0.34	%/°C
Temperature coefficient of I_{sc}^{STC}	α_{pv}	0.050	%/°C
Temperature at STC	T_{STC}	25	°C
Solar irradiance at STC	G_{STC}	1000	W/m^2

Solar Panel Model Verification

Figure 3.28 compares at STC the Current-Voltage (I-V) and Power-Voltage (P-V) characteristics of a 250 W, 24 V Suntech monocrystalline solar panel as provided by the manufacturer and those obtained using the model given by (3.67)-(3.68). As shown in the figure, the model accurately tracks the characteristic curves provided by the manufacturer. There is one point on each curve given by (v_{mp}, i_{mp}) on the I-V curve and (v_{mp}, P_{mp}) on the P-V curve where P_{pv} is maximum. This point is referred to as the Maximum Power Point (MPP). Because P_{mp} is equal to 250 W which is the rating of the solar panel at STC, the model was considered to be accurate.

Maximum Power Point Tracking Algorithm

The P_{mp} in Figure 3.28 usually varies with changes in T_c and G due to changes in weather conditions including cloud cover, dust and shade from trees and buildings. To maximise the power generated from the solar panel, P_{pv} should always be equal to P_{mp}. This is normally achieved by operating the solar panel in MPPT mode which involves finding values of i_{pv}

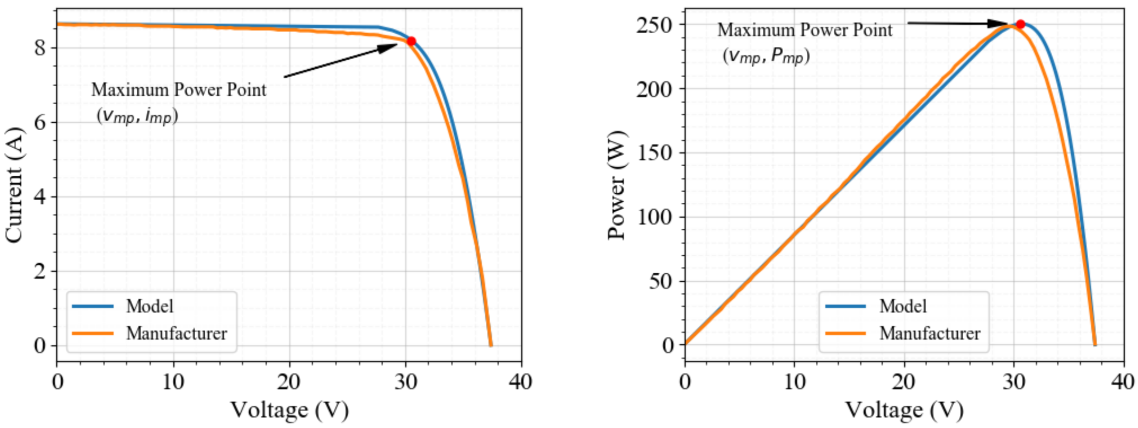

(a) (b)

Figure 3.28: Comparison of (a) I-V and (b) P-V characteristics of a 250 W, 24 V Suntech monocrystalline solar panel as provided by the manufacturer and those obtained using the model given by (3.67)-(3.68).

and v_{pv} such that $i_{pv} = i_{mp}$ and $v_{pv} = v_{mp}$ so that $P_{pv} = P_{mp}$.

The fact that the slopes of both the I-V curve and the P-V curve in Figure 3.28 are zero when $P_{pv} = P_{mp}$, a root-finding technique which uses Newton Raphson method was developed to iteratively track the MPP as follows:

Equating to zero the derivative of P_{pv} with respect to i_{pv} as proposed in [161], the expression given by (3.69) was obtained.

$$\begin{aligned} \left.\frac{\partial\left(v_{pv}i_{pv}\right)}{\partial i_{pv}}\right|_{i_{pv}=i_{mp}} &= f\left(i_{mp}\right) \\ &= v_{oc}^{pv} + V_T \ln\left(1-\frac{i_{mp}}{I_{ph}}\right) - V_T\left(\frac{i_{mp}}{I_{ph}-i_{mp}}\right) - 2r_{pv}i_{mp} = 0 \end{aligned} \tag{3.69}$$

Equation (3.69) was solved for i_{mp} using the following Newton Raphson-based MPPT algorithm

$$i_{mp}^{(k+1)} = i_{mp}^{(k)} - \frac{f\left(i_{mp}^{(k)}\right)}{\partial f\left(i_{mp}^{(k)}\right)/\partial i_{mp}^{(k)}} \tag{3.70}$$

where k is the iteration number and $i_{mp}^{(k+1)}$ is the approximation of i_{mp} at $(k+1)$-th iteration using the previous approximation, $i_{mp}^{(k)}$ obtained at k-th iteration.

To avoid a logarithmic error (given by $\ln(0)$), the MPPT algorithm was initialised as $i_{mp} = I_{ph} - \xi_{ph}$ where ξ_{ph} is a very small number (e.g. $\xi_{ph} = 0.0001$). After i_{mp} was determined, v_{mp} was obtained by substituting i_{mp} in (3.66). The P_{mp} was obtained by substituting i_{mp} and v_{mp} in (3.68).

Figure 3.29 shows a flowchart that was developed to implement the MPPT algorithm. This flowchart for example was used to generate the MPPs shown in Figure 3.28.

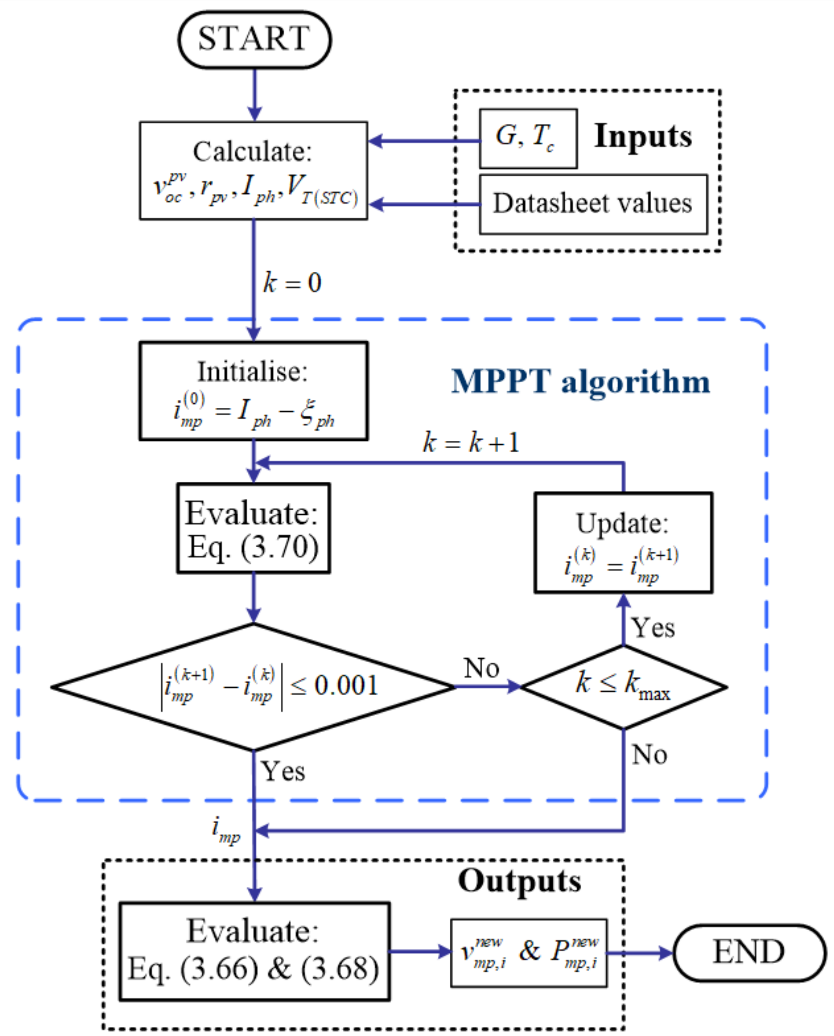

Figure 3.29: Algorithm for solar panel model and the MPPT.

3.5 Battery Modelling

The key physical properties of a battery are its charge and discharge power and State of Charge (SoC). In this research, battery modelling refers to the mathematical representation of the battery charge and discharge power as a function of the SoC.

3.5.1 Existing Battery Models

Several battery models can be found literature. Thermal-electrochemical models are proposed in [169, 170], which are derived from electrochemical principles and thermodynamics concepts. These are highly accurate, however due to the heavy partial differential equations involved, they are too complex for the present application. Low-order empirical models are proposed in [8, 171, 172], which are parametrised using time and frequency domain experimental data. These models have lower computational demands than thermal-electrochemical models and they are more suited to applications in Battery Management Systems (BMS). Simplified low-order empirical models (hereafter referred to as steady state equivalent circuit models) which neglects the frequency, time and temperature dependent parameters of low-order empirical models are proposed in [173–175]. These models have average complexity and they have good performance at steady-state.

3.5.2 Preferred Model

The preferred model from the battery models reviewed in the previous subsection was the steady state equivalent circuit model of the battery due to its average complexity and the good performance at steady state. The other models were too complex (due to the partial differential equations) to be used for steady state analysis, which is the focus of the present research.

Using the steady state equivalent circuit model, the steady state dynamics of the battery were represented by a voltage source, V_{oc}^b connected in series with a resistor, r_b as shown in Fig. 3.30. When the output current i_b is negative, the battery is charging, otherwise it is discharging. The v_{oc}^b and r_b were expressed as functions of the SoC as follows [8]

$$r_b = \left(\frac{V_n^b}{C_b}\right)\left(\frac{0.86}{3.7}\right)\Big[a_0 + a_1 SoC - a_2 SoC^2 + a_3 SoC^3 + a_4 e^{-a_5 SoC} + a_6 e^{-a_7 SoC} + a_8 e^{-a_9 SoC}\Big] \tag{3.71}$$

$$v_{oc}^b = \left(\frac{V_n^b}{3.7}\right)\Big[b_0 + b_1 SoC - b_2 SoC^2 + b_3 SoC^3 + b_4 e^{-b_5 SoC}\Big] \tag{3.72}$$

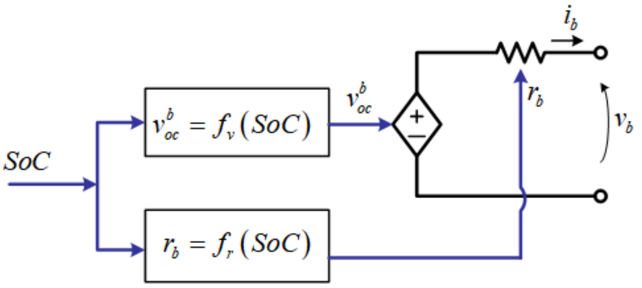

Figure 3.30: Equivalent circuit model of a battery.

where V_n^b is rated voltage of the battery, C_b in ampere-hour (Ah) is rated capacity of the battery which defines the maximum amount of energy that a battery can deliver or store, $a_0,\ldots,a_5$ and $b_0,\ldots,b_9$ are coefficients of r_b and v_{oc}^b expressions respectively, which are given in Table 3.7 and SoC is SoC of the battery which is estimated in discrete time domain by the following expression [176]

$$SoC = SoC_0 - \frac{\eta_b \Delta t}{C_b} i_b \tag{3.73}$$

where SoC_0 is the initial SoC of the battery, Δt is duration of a battery charge and discharge and η_b is battery charge and discharge efficiency. Depending on the direction of i_b, η_b was expressed as follows

Table 3.7: Battery model parameters for a Lithium-ion cell [8].

Resistance, r_b (Ω)		Voltage, v_{oc}^b (V)	
Coefficient	Value	Coefficient	Value
a_0	0.1762	b_0	3.6297
a_1	0.0584	b_1	0.5590
a_2	0.1747	b_2	0.5100
a_3	0.1288	b_3	0.5080
a_4	0.1463	b_4	-0.852
a_5	30.270	b_5	63.867
a_6	0.1063	-	-
a_7	62.490	-	-
a_8	0.0712	-	-
a_9	61.400	-	-

$$\eta_b = \begin{cases} v_{oc}^b / v_b, & \text{if } i_b < 0 \\ v_b / v_{oc}^b, & \text{otherwise} \end{cases} \tag{3.74}$$

where v_b is the output voltage of the battery which was obtained from Figure 3.30 as

$$v_b = \frac{v_{oc}^b + \sqrt{(v_{oc}^b)^2 - 4r_b P_b}}{2} \tag{3.75}$$

The battery charge and discharge power, P_b was expressed as

$$P_b = i_b v_b \tag{3.76}$$

The variation of v_{oc}^b and r_b with SoC was plotted as shown in Figure 3.31, where increasing the SoC towards 100% or decreasing the SoC towards 0% increased the r_b. Higher values of r_b often results in excessive power loss in the battery which consequently heats up the battery during operation. Figure 3.31 also demonstrates the importance of keeping the SoC of the battery within certain limits, e.g. between $SoC = 20\%$ and $SoC = 80\%$ not only to avoid over charging and over discharging the battery but to also limit the value of r_b.

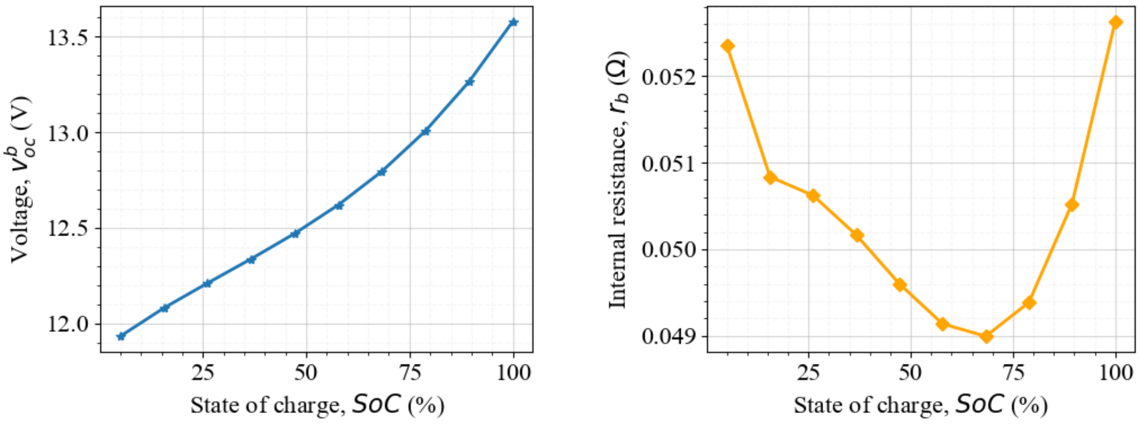

(a) (b)

Figure 3.31: Variation of open circuit voltage and internal resistance of a 12 V, 10 Ah Lithium-ion battery with state of charge.

3.6 Distribution Line Modelling

The key physical features of a distribution line are its resistance to current flow and its sending and receiving distribution voltages. Distribution line modelling in the present research refers to the mathematical relationship between current, resistance and the distribution line voltages.

In this research, the distribution lines in the solar nano-grid are connected to the same DC bus bar (or simply DC bus) in the hub as shown in Figure 3.32.

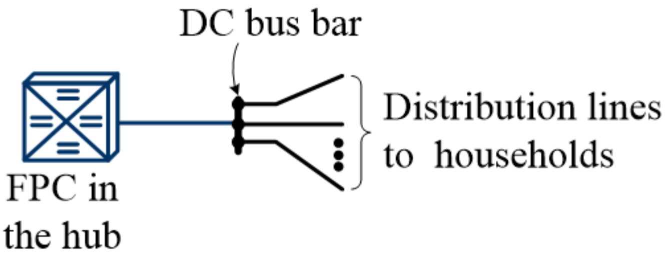

Figure 3.32: Connection of distribution lines to a common DC bus bar in the hub.

Figure 3.33 shows the universally accepted representation of a distribution line for DC networks including solar nano-grids, where it is shown connecting an *i*-th household to the DC bus in the hub. The distribution line is represented by a pure resistance, $R_{dc,i}$,

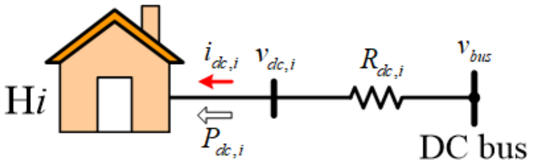

Figure 3.33: Equivalent circuit model of a distribution line connecting an *i*-th household to the DC bus in the hub.

$i = 0, 1, \ldots, n$ due to the absence of low time scale dynamics of the solar nano-grid at steady state. This assumption is widely accepted for steady state analysis of DC networks as reported in [37, 177]. The effect of temperature on $R_{dc,i}$ is also ignored in this research due to fairly constant annual average temperatures of about 25 °C in sub-Saharan Africa [178] which is the focus region of the research.

The resistance, $R_{dc,0}$ of the cable connecting the FPC in the hub to the DC bus as shown in Figure 3.32 was assumed to be non-negligible. In practice, $R_{dc,0}$ represents a lumped resistance of the DC bus bar, the protection equipment and the connection cables.

The current, $i_{dc,i}$ received by Hi, $i = 0, 1, \ldots, n$ in Figure 3.33 was expressed as follows

$$i_{dc,i} = \left(\frac{v_{bus} - v_{dc,i}}{R_{dc,i}} \right) \tag{3.77}$$

where the index $i = 0$ represents the hub, $v_{dc,i}$ is distribution voltage of Hi and v_{bus} is the voltage at the DC bus.

According to Kirchhoff's Current Law (KCL), the algebraic sum of $i_{dc,i}$, $i = 0, 1, \ldots, n$ taken at the DC bus must be zero, i.e. $\sum\limits_{i=0}^{n} i_{dc,i} = 0$. Using this law, the v_{bus} was expressed as follows

$$v_{bus} = \frac{\sum\limits_{i=0}^{n} \frac{v_{dc,i}}{R_{dc,i}}}{\sum\limits_{i=0}^{n} \frac{1}{R_{dc,i}}} \tag{3.78}$$

The received power, $P_{dc,i}$ by Hi from the distribution line was expressed as

$$P_{dc,i} = v_{dc,i} \left(\frac{v_{bus} - v_{dc,i}}{R_{dc,i}} \right) \tag{3.79}$$

Both $i_{dc,i}$ and $P_{dc,i}$ flows in both directions on the distribution line; they were taken to be positive when they flow towards Hi as shown in Figure 3.33 and negative otherwise.

3.7 Overall Model of the Solar Nano-Grid

This section presents the overall model of the solar nano-grid. The individual equivalent circuit models which have been presented in Section 3.2 to Section 3.6 were systematically combined to form an equivalent circuit model of a household and thereafter a solar nano-grid. Mathematical equations representing the behaviour of the solar nano-grid were then derived.

3.7.1 Equivalent Circuit Model of a Household or Hub

Figure 3.34 shows a generic equivalent circuit model of a single household or hub, which was formed by combining the circuits given in Figures 3.23, 3.27, 3.30 and 3.33. However, the presence of the transformer circuit made the derivation of mathematical relationships between the circuits on the left hand side and the right hand side of the transformer difficult. The circuit in Figure 3.34 was simplified to that shown in Figure 3.35a in order to get rid of the ideal DC transformer by referring the circuits on the left hand side of the ideal DC transformer to the right hand side following the voltage transformation ratios given in (3.80).

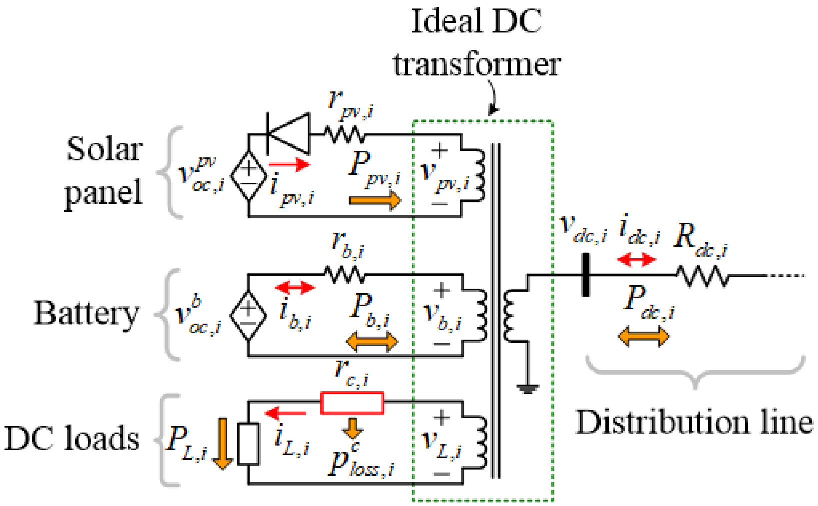

Figure 3.34: Equivalent circuit model of H*i* in the solar nano-grid.

$$n_{pv,i} = v_{dc,i}/v_{pv,i} \tag{3.80a}$$

$$n_{b,i} = v_{dc,i}/v_{b,i} \tag{3.80b}$$

$$n_{L,i} = v_{dc,i}/v_{L,i} \tag{3.80c}$$

Since $P_{pv,i}$ and $P_{L,i}$ are externally determined from atmospheric weather conditions and the power consumed by the DC loads in the solar nano-grid respectively, and that $p_{loss,i}^{c}$ is a function of $P_{L,i}$, these were treated as constants at every time interval. The difference between $P_{pv,i}$, $P_{L,i}$ and $p_{loss,i}^{c}$ at every time interval was expressed in terms of a mismatch current, $I_{m,i}$ as follows

$$I_{m,i} = \frac{P_{pv,i} - \left(P_{L,i} + p_{loss,i}^{c}\right)}{v_{dc,i}} \tag{3.81}$$

For households without the solar panel, $P_{pv,i}$ is equal to zero in (3.81). Based on (3.81),

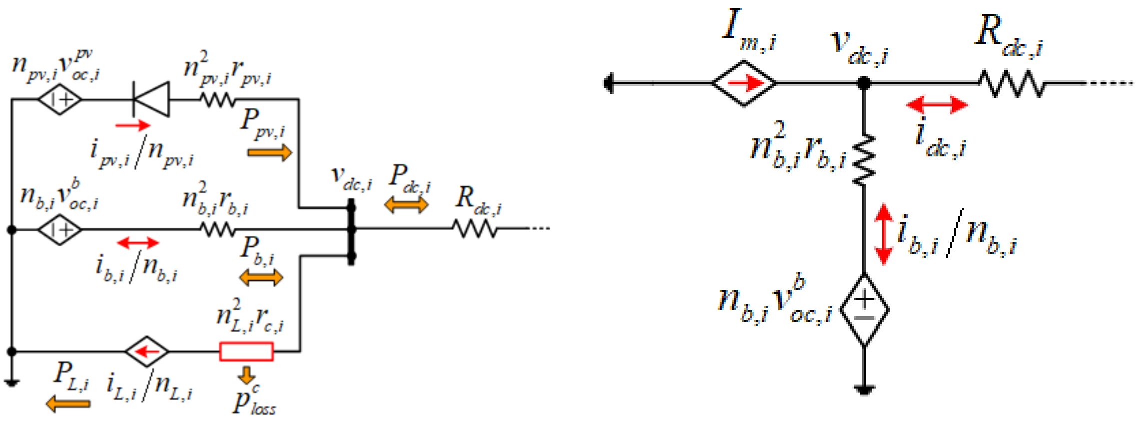

(a) (b)

Figure 3.35: Simplified equivalent circuit models of a household, Hi with (a) solar panel equivalent circuit and (b) without solar panel equivalent circuit.

Figure 3.35a was further simplified to that shown in Figure 3.35b, which represents the simplified equivalent circuit model of either a household or hub in the solar nano-grid.

3.7.2 Equivalent Circuit Model of a Solar Nano-Grid

Finally, by combining n number of simplified equivalent circuit models of households shown in Figure 3.35b together, the overall equivalent circuit model of the solar nano-grid was obtained as shown in Figure 3.36, where the resistance, $R_{dc,0}$ of the cable connecting the FPC at the hub to the DC bus was considered to be small but non-negligible, i.e. $R_{dc,0} << R_{dc,1}, \ldots, R_{dc,n}$.

Applying KCL to Figure 3.36, the distribution line current expression at Hi was obtained as follows

$$i_{dc,i} = -I_{m,i} - I_{b,i} \tag{3.82}$$

where $I_{b,i}$ is defined as

$$I_{b,i} = \frac{i_{b,i}}{n_{b,i}} \tag{3.83}$$

According to the law of conservation of current, the algebraic sum of currents, I_{sum} in the solar nano-grid must be equal to zero as follows

$$I_{sum} = \sum_{i=0}^{n} i_{dc,i} = -\sum_{i=0}^{n} \left(I_{m,i} + I_{b,i}\right) = 0 \tag{3.84}$$

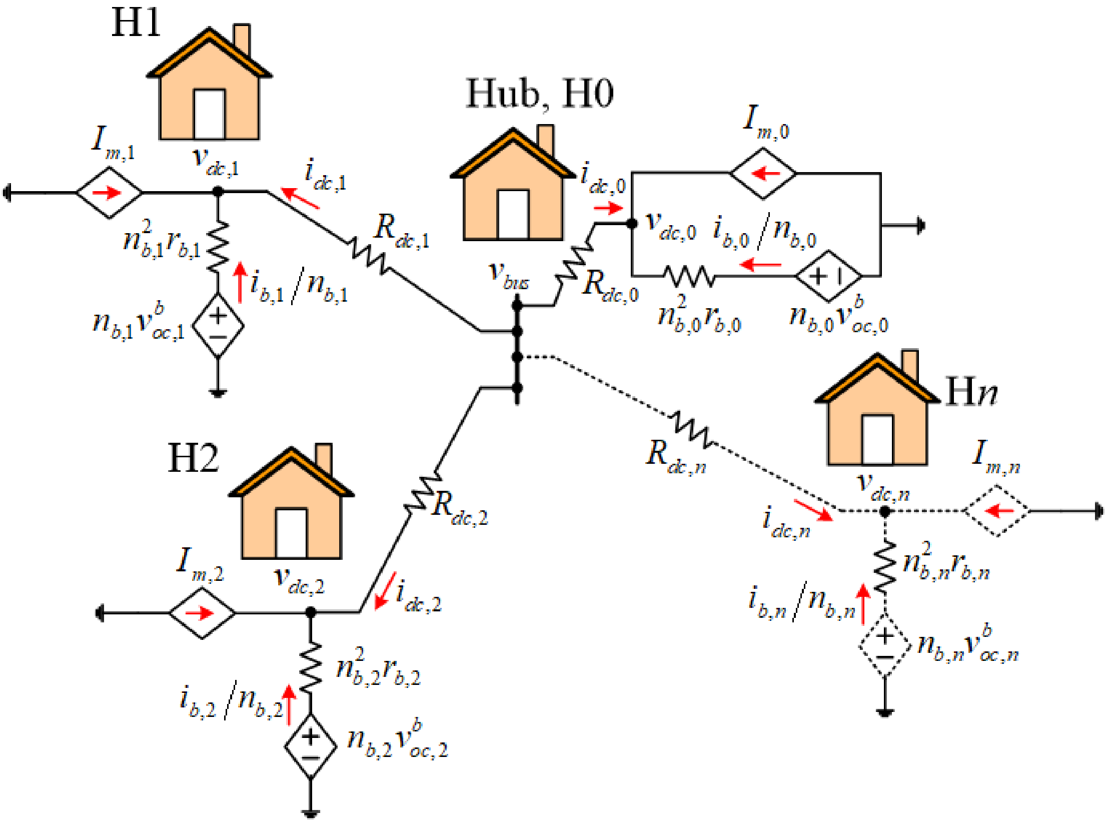

Figure 3.36: Equivalent circuit model of a solar nano-grid.

Equations (3.80) to (3.84) in addition to the mathematical expressions of the individual component models presented in Section 3.1 to Section 3.6 represent the model of the solar nano-grid.

3.8 Power Loss Optimisation Problem Formulation of the Solar Nano-Grid

This section presents the power loss optimisation problem of the solar nano-grid. The main objective of the optimisation problem is to minimise the total of battery charge and discharge losses, distribution line losses and FPC losses in the solar nano-grid while satisfying operational constraints of the solar nano-grid such as the KCLs.

In the solar nano-grid, batteries are the only dispatchable energy resources as they charge energy from the solar panels and discharge energy to the DC loads whenever there is need. Thus, to minimise the total power loss in the solar nano-grid, optimal dispatch of the batteries is required. However, the output parameters (i.e. voltage, power, current) of the batteries in the solar nano-grid are not directly regulated; these therefore cannot be used to control the current flow in the distribution lines. Thus, determination of optimal distribution voltages corresponding to the results of the optimal dispatch of the batteries are also required to completely solve the power loss problem.

The need to both dispatch the batteries and determine the distribution voltages therefore suggested that the power loss problem of the solar nano-grid consisted of two sub-problems. The sub-problems include the Optimal Battery Dispatch Problem (OBDP) for optimally charging and discharging the batteries in order to minimise the total power loss, and the Optimal Current Flow Problem (OCFP) for determining the optimal distribution voltages which correspond to the optimal battery charge and discharge currents from the OBDP. The determination of the distribution line voltages was framed as an OCFP to avoid linearising power flow equations given by (3.79), which are generally non-linear and non-convex [64] - a brief introduction to convex optimisation is presented in Appendix A.

To jointly address the two interdependent power loss sub-problems, the overall power loss optimisation problem of the solar nano-grid was formulated as a bi-level optimisation problem as illustrated in Figure 3.37. The overall power loss optimisation problem was viewed as a closed loop control system where the OCFP is the plant and OBDP is the controller. The inputs were the battery SoCs, the power generation from the solar panels and the load demands in the households. The ultimate outputs were the optimal distribution voltages which were used to regulate the current flow in the distribution network and as reference signals to the FPCs. The feedback loop was used to keep the errors resulting from separately solving each sub-problem to a minimum. The OBDP and the OCFP are discussed in more depth in the next subsections.

3.8.1 Optimal Battery Dispatch Problem

The main objective of the OBDP was to optimally dispatch the charge and discharge operation of the batteries in order to minimise the total power losses in the solar nano-grid while satisfying the operational constraints. The outputs from the OBDP were used as inputs to

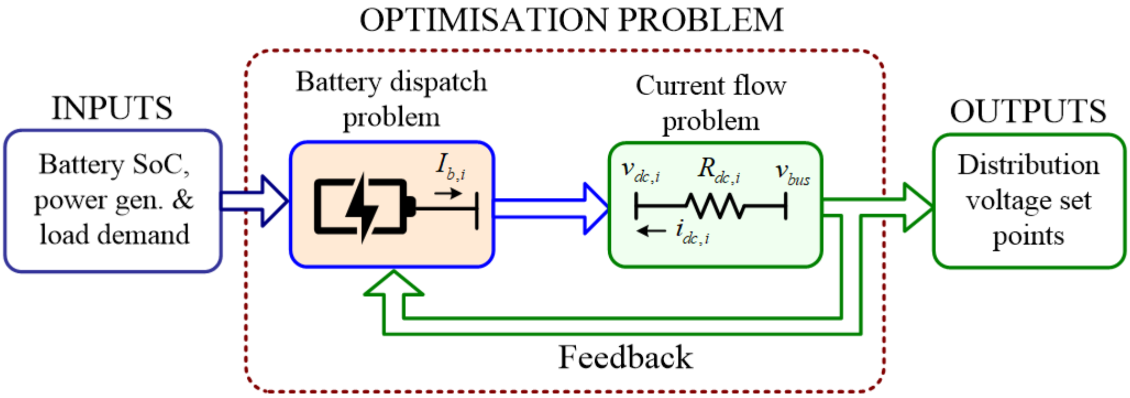

Figure 3.37: Logic diagram of the formulated power loss optimisation problem.

the OCFP. The decision variables, objective function and the constraints of the OBDP are presented in the next subsections while utilising the brief on convex optimisation in Appendix A.

Decision Variables and the Objective Function

The battery, the distribution line and the FPC were modelled as resistors as shown in Figure 3.36. According to James Joule [179], the power loss by each of these components (i.e. the battery, the distribution line and the FPC) is equal to their resistance multiplied by the square of the current flowing through them. Since only batteries were dispatchable, it was logical to choose the battery charge and discharge currents $I_{b,i}\ \ i = 0, 1, \ldots, n$ as decision variables. These were organised in an n dimensional vector as follows

$$\mathbf{I_b} = \left[I_{b,0}, I_{b,1}, \ldots, I_{b,n}\right]^T \tag{3.85}$$

Denoting the battery charge and discharge power loss as $p^b_{loss,i}$ and the distribution line power loss as $p^d_{loss,i}$, the objective function was formulated as follows

$$P^{total}_{loss} = \sum_{i=0}^{n} \left(p^b_{loss,i} + p^d_{loss,i} + p^c_{loss,i}\right) \tag{3.86a}$$

where

$$p_{loss,i}^{b} = I_{b,i}^{2} n_{b,i}^{2} r_{b,i} \tag{3.86b}$$

$$p_{loss,i}^{d} = \left(-I_{b,i} - I_{m,i}\right)^{2} R_{dc,i} \tag{3.86c}$$

Substituting (3.80) and (3.81) in (3.86), the objective function was rewritten as a function of the decision variables $\mathbf{I_b}$ as follows

$$P_{loss}^{total} = \sum_{i=0}^{n} F_i\left(I_{b,i}\right) = \sum_{i=0}^{n} \left(\alpha_i I_{b,i}^{2} + \beta_i I_{b,i} + \gamma_i\right) \tag{3.87a}$$

where

$$\alpha_i = \left(\frac{v_{dc,i}}{v_{b,i}}\right)^{2} r_{b,i} + R_{dc,i} \tag{3.87b}$$

$$\beta_i = \frac{2R_{dc,i}}{v_{dc,i}} \left(P_{pv,i} - P_{L,i} - p_{loss,i}^{c}\right) \tag{3.87c}$$

$$\gamma_i = \frac{R_{dc,i}}{v_{dc,i}^{2}} \left(P_{pv,i} - P_{L,i} - p_{loss,i}^{c}\right)^{2} + p_{loss,i}^{c} \tag{3.87d}$$

Constraints

Constraints are mathematical equality and inequality expressions that a solution to an optimisation problem must satisfy. In the present research, the constraints were characterised by the expressions of current balance, limits on the battery SoC, limits on the battery charge and discharge power and limits on the distribution voltage as follows.

- **Current balance equation:** According to the law of conservation of current, the algebraic sum of currents in the solar nano-grid must equal to zero at every time instant. Substituting (3.80) and (3.81) in (3.84), the following expression was obtained

$$\sum_{i=0}^{n} I_{b,i} = \sum_{i=0}^{n} I_{D,i} \tag{3.88a}$$

where

$$I_{D,i} = -I_{m,i} = \left(\frac{P_{L,i} + p^{c}_{loss,i} - P_{pv,i}}{v_{dc,i}} \right) \tag{3.88b}$$

- **Limits on the battery state of charge:** Just like the fuel gauge in a car, the SoC which is expressed by (3.73) indicates the amount of energy available in the battery before the battery can be recharged. The SoC is 0% if the battery is empty (over-discharged); it is 100% when it is full (over-charged). However, operating the battery at these extreme points can lead to heat generation in the battery as explained in Subsection 3.5.2 which shortens the lifetime of the battery [180–182]. To avoid either overcharging or over discharging the batteries, limits on the SoC of every battery in the solar nano-grid were placed as follows

  $$SoC_{min,i} \leq SoC,i \leq SoC_{max,i} \tag{3.89}$$

  where SoC,i is given by the expression in (3.73), $SoC_{min,i}$ which is greater than 0% is the minimum SoC threshold of the battery and $SoC_{max,i}$ which is less than 100% is the maximum SoC threshold of the battery. In this research, the SoC thresholds according to Figure 3.31 were chosen as $SoC_{min,i} = 20\%$ and $SoC_{max,i} = 80\%$.

- **Limits on the battery charge and discharge power:** There is a limit to the amount of power that a physical battery can either charge or discharge at a given time. This is so in order to limit heat generation in the battery and to obey the current ratings of the FPC [182]. The lower power limit, $P^{b}_{min,i}$ and the upper power limit, $P^{b}_{max,i}$ of every battery in the solar nano-grid was expressed as follows

  $$P^{b}_{min,i} \leq P_{b,i} \leq P^{b}_{max,i} \tag{3.90}$$

  where $P_{b,i}$ is the battery power which was re-calculated according to Figure 3.36 and (3.83) as follows

  $$P_{b,i} = I_{b,i} v_{dc,i} \tag{3.91}$$

- **Limits on the distribution voltage:** Limits on the distribution voltage were imposed in order to keep the distribution voltages from varying too far from their nominal values, which otherwise would violate the voltage ratings of the FPC. The limits were expressed as

  $$v^{dc}_{min,i} \leq v_{dc,i} \leq v^{dc}_{max,i} \tag{3.92}$$

  where $v^{dc}_{min,i}$ is the lower limit and $v^{dc}_{min,i}$ is the upper limit.

3.8.2 Summary of the Optimal Battery Dispatch Problem

With the decision variables given by (3.85), the objective function expressed in (3.87) and the constraints given by (3.88b), (3.89), (3.90) and (3.92), the OBDP was summarised as follows

$$\underset{I_b}{\text{minimise}} \quad P^{total}_{loss} = \sum_{i=0}^{n} F_i\left(I_{b,i}\right) = \sum_{i=0}^{n} \left(\alpha_i I^2_{b,i} + \beta_i I_{b,i} + \gamma_i\right) \tag{3.93a}$$

$$\text{subject to:} \quad (1)\ \sum_{i=0}^{n} I_{b,i} = \sum_{i=0}^{n} I_{D,i} \tag{3.93b}$$

$$(2)\ SoC_{min,i} \leq SoC,i \leq SoC_{max,i} \tag{3.93c}$$

$$(3)\ P^b_{min,i} \leq P_{b,i} \leq P^b_{max,i} \tag{3.93d}$$

$$(4)\ v^{dc}_{min,i} \leq v_{dc,i} \leq v^{dc}_{max,i} \tag{3.93e}$$

The function $F_i\left(I_{b,i}\right) = \alpha_i I^2_{b,i} + \beta_i I_{b,i} + \gamma_i$ was viewed as the total power loss incurred for using the i-th battery to meet the current balance given by (3.93b). The α_i, β_i and γ_i were viewed as power loss coefficients of the i-th battery. The optimal solution to the problem in (3.93) was given by

$$\mathbf{I_b} = \left[I^*_{b,0}, I^*_{b,1}, \ldots, I^*_{b,n}\right]^T \tag{3.94}$$

However, the power loss coefficients; α_i, β_i, γ_i and $I_{D,i}$ in (3.93) are not constants but a function of $v_{b,i}$ and $v_{dc,i}$ (which are unknown at every time interval) as given in (3.87) and (3.88). According to the theory of convex optimisation in Appendix A, the inclusion of α_i, β_i, γ_i, and $I_{D,i}$ in (3.93) therefore causes the OBDP (3.93) to be a non-convex optimisation problem. Optimality of solutions obtained from a non-convex optimisation problem are not guaranteed [183]. To convert the OBDP (3.93) to a convex optimisation problem, the parameters; $v_{b,i}$ and $v_{dc,i}$ were treated as constants at every time interval prior to solving the OBDP and these were updated after solving it. As a result, α_i, β_i, γ_i and $I_{D,i}$ in (3.93) were viewed as constants at every time interval, thus converting the OBDP (3.93) to a convex optimisation problem with a guaranteed global optimal solution. Due to the feedback loop in Figure 3.37, the errors caused by keeping $v_{b,i}$ and $v_{dc,i}$ constant at each time interval were kept to a minimum.

3.8.3 Optimal Current Flow Problem

The main objective of the OCFP was to determine suitable distribution voltage set points that correspond to the optimal battery current, $\mathbf{I_b}$ from the OBDP. Therefore, this problem was viewed as the plant to be controlled using $\mathbf{I_b}$ from the OBDP as shown in Figure 3.37.

The distribution current associated with each $I^*_{b,i}$ (3.94) from the OBDP was obtained by substituting $I^*_{b,i}$ and (3.88b) in (3.82) to obtain the following expression

$$i_{dc,i} = I_{D,i} - I^*_{b,i} \quad i = 0, 1, \ldots, n \tag{3.95}$$

Then with reference to Figure 3.36, the aim of the OCFP was to determine the $v_{dc,i}$ for all $i = 0, 1, \ldots, n$ which corresponds to the (known) $i_{dc,i}$ given in (3.95). This was achieved by solving the following system of linear equations

$$i_{dc,i} = I_{D,i} - I^*_{b,i} = \frac{1}{R_{dc,i}} \left(-v_{dc,i} + \frac{\sum\limits_{i=0}^{n} \frac{v_{dc,i}}{R_{dc,i}}}{\sum\limits_{i=0}^{n} \frac{1}{R_{dc,i}}} \right) \tag{3.96}$$

The solution to the OCFP in (3.96) at every time interval was an n-dimensional vector given by

$$\mathbf{V_{dc}} = \left[v_{dc,0}, v_{dc,1}, \ldots, v_{dc,n} \right]^T \tag{3.97}$$

The $\mathbf{V_{dc}}$ in (3.97) was then used as feedback to the OBDP for use to update the $v_{b,i}$ and

$v_{dc,i}$ for all $i = 0, 1, \ldots, n$ which were previously treated as constants. The $v_{b,i}$ at every time interval was updated by substituting the $I^*_{b,i}$ from the OBDP (3.93) and the $v_{dc,i}$ from the OCFP (3.96) in (3.75) as follows

$$v_{b,i} = \frac{v^b_{oc,i} + \sqrt{(v^b_{oc,i})^2 - 4r_{b,i}\left(I^*_{b,i}v_{dc,i}\right)}}{2} \tag{3.98}$$

The obtained $v_{b,i}$ from (3.98) was further used to update the battery charge and discharge efficiency as given in (3.74).

3.9 Summary

This chapter answers the following research question:

How can the solar nano-grid e.g. with a star configuration as shown in Figure 1.4 be modelled at steady-state and have a convex power loss optimisation problem formulated?

A high fidelity steady-state model of the star solar nano-grid configuration was developed and is presented in Section 3.7. The solar nano-grid model was developed by combining detailed circuit based models of the solar nano-grid components including the FPC. Since the FPC considered in this research was new and not reported anywhere in literature, the development of the solar nano-grid model contributed to knowledge through the: (1) detailed FPC power loss model developed which can be used for theoretical understanding and further optimisation of the FPC design and (2) simplified FPC power loss model developed which can be used for real-time estimation of FPC system loss and power loss optimisation problem formulation of the solar nano-grid.

A contribution to knowledge was also made in this chapter through the formulation of a novel convex power loss optimisation problem of the solar nano-grid based on the solar nano-grid model developed as presented in Section 3.8. The formulated power loss optimisation problem consisted of two stages. The first stage was an OBDP for determining optimal battery charge and discharge currents. The second stage was an OCFP for determining optimal distribution voltages which corresponds to the optimal battery currents. The proposed formulation allowed the power loss problem to be solved without linearising any power flow equations. Thus, it was scalable and computationally efficient compared to existing approaches [46, 118]. In addition, the solar panel MPPT developed and the non-linear variations of the battery charge and discharge efficiency were also included in the formulation.

In Chapters, 4 and 5, control algorithms are presented that aim to solve the convex power loss optimisation problem which was formulated in this chapter.

Chapter 4

Centralised Control Algorithm for Minimising Power losses of a Solar Nano-Grid

In Chapter 3, the steady state modelling and power loss optimisation problem formulation of the solar nano-grid was presented. In this chapter, a centralised control algorithm which solves the formulated power loss optimisation problem at every time instant is presented. A centralised control based algorithm was chosen to solve the power loss problem because it is accurate and has a broad observability due to the centrally managed control actions [184].

The algorithm proposed eliminates the challenge that comes with traditional approaches [46] such as low accuracy and high computational time due to linearisation of power flow equations (3.79). This makes the traditional approaches difficult to scale-up in the context of the considered solar nano-grids. For this reason, performance of the algorithm proposed in this chapter is verified by comparing its results to those obtained through the traditional approach for a star solar nano-grid configuration (shown in Figure 1.4) with two households and hub.

To understand the implementation of the algorithm proposed, Section 4.1 describes the considered control architecture. The centralised control algorithm proposed is presented in Section 4.2. Section 4.3 presents simulation results which verify the performance and suitability of the algorithm proposed for minimising the power loss of the solar nano-grid.

4.1 System Description

Figure 4.1 shows the considered control architecture for the star solar nano-grid configuration that can be used to implement the algorithm proposed. Central to the control architecture is the central agent (or controller) which consists of an intelligent computing device that has internet access and which communicates with every Four-Port DC-DC Converter (FPC) in the solar nano-grid. The main functions of the agent are to:

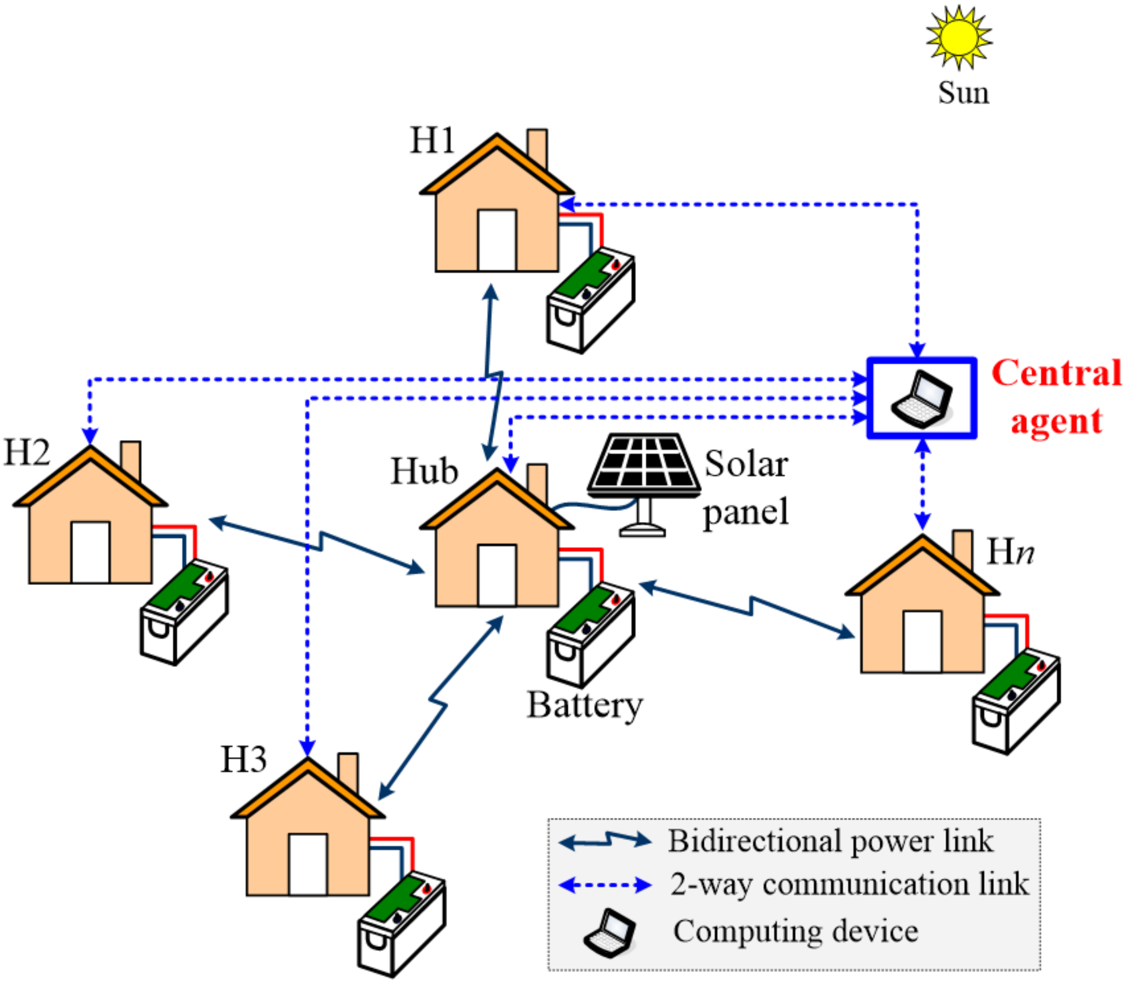

Figure 4.1: The considered centralised control architecture of the solar nano-grid.

- Collect relevant information (e.g. information about load demand and power generation) from every FPC in the solar nano-grid through communication links to a single place.

- Perform computations by running the centralised control algorithm presented in this chapter with the collected information as inputs in order to generate optimal distribution voltages which minimise the power loss.
- Send the optimal distribution voltages back to the FPC via the communication links for control implementation.

The communication network can be either wired/wireless based on cost and other physical constraints such as distance and compatibility issues [185]. Given the star solar nano-grid configuration, the agent can be stationed at the hub (or even in one of the households depending on the locality of that household in the solar nano-grid). By having access to all the relevant sensor information in the solar nano-grid, it means that the agent generates best control decisions and has a broad observability of the solar nano-grid.

4.2 The Centralised Control Algorithm Proposed

The algorithm proposed was designed to solve the power loss optimisation problem presented in Chapter 3, in particular, the Optimal Battery Dispatch Problem (OBDP) and the Optimal Current Flow Problem (OCFP) given by (3.93) and (3.96) respectively.

Figure 4.2 shows the schematic diagram of the centralised-control algorithm proposed. It consists of two iterative algorithms developed, namely, the Fast Lambda Iteration Algorithm

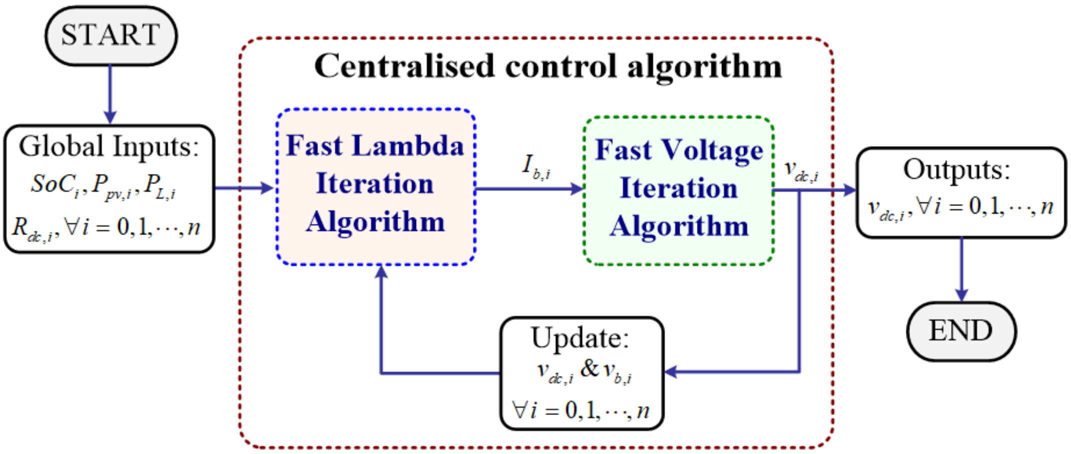

Figure 4.2: Schematic diagram of the centralised control algorithm proposed.

(FLIA) and the Fast Voltage Iteration Algorithm (FVIA). The algorithm was designed based on the solution framework shown in Figure 3.37. The FLIA was designed to solve the OBDP. The FVIA was designed to solve the OCFP. The inputs to the control algorithm proposed were the battery State of Charge (SoC), SoC_i, power generation, $P_{pv,i}$, load demand, $P_{L,i}$ and the resistance of the distribution lines, $R_{dc,i}$ for $i = 0, 1, \ldots, n$. The feedback loop was designed to update the battery voltage, $v_{b,i}$, and distribution voltage $v_{dc,i}$, which are treated as constants in the FLIA when solving the OBDP. Together, the FLIA and the FVIA uniquely solve the power loss optimisation problem of the solar nano-grid by generating optimal distribution voltage values, $v_{dc,i}, \quad \forall i = 0, 1, \ldots, n$. In the next subsections, the FLIA and the FVIA are described in more depth.

4.2.1 The Fast Lambda Iteration Algorithm

The main objective of the FLIA was to solve the OBDP given by (3.93). Since the formulated OBDP is convex, Karush-Kuhn-Tucker (KKT) optimality conditions were necessary and sufficient conditions for optimality [183].

Given that the OBDP in (3.93) is quadratic and convex, it would have been easily solved using well known solvers for convex optimisation such as CVXOPT [186]. However, the use of solvers usually abstracts (useful) details which are required for deeper understanding of the solution. These details were required in this research to develop the control algorithm which is presented in Chapter 5. Thus, the method of Lagrange multipliers [187] was used as follows.

Equal Incremental Loss Principle

There are many lambda iteration algorithms in literature which use a similar approach like the equal incremental loss principle proposed in this section [188–192]. However, the existing approaches focus on solving the economic dispatch problems of conventional AC power systems. The FLIA and equal incremental loss principle proposed in this chapter are different from the existing AC power system-based approaches because they focus on solar nano-grids and have the objective of minimising the solar nano-grid power losses. It is to the best knowledge of the author that this is the first time the equal incremental loss principle is developed to coordinate the battery operation in order to minimise the solar nano-grid power losses.

To start of with, the battery inequality constraints given by (3.93c) and (3.93d) were not considered for simplicity. Also since $v_{dc,i}$ was treated as a constant, the inequality constraint given by (3.93d) only ensured that the initialisation of $v_{dc,i}$ in the OBDP was within the required range and was ignored. Then, considering the equality constraint given by (3.93b) and using the Lagrangian operator L, the OBDP in (3.93) was converted to an unconstrained optimisation problem as follows

$$L\left(I_{b,i},\lambda\right)=\sum_{i=0}^{n}F_i\left(I_{b,i}\right)+\lambda\left(\sum_{i=0}^{n}I_{D,i}-\sum_{i=0}^{n}I_{b,i}\right) \tag{4.1}$$

where λ is a Lagrange multiplier associated with the equality constraint (3.93b).

According to the KKT optimality conditions, the operator L was minimised when its partial derivative with respect to each variable, $I_{b,i}$ $,i=0,1,\ldots,n$ was zero as follows

$$\frac{\partial L\left(I_{b,i},\lambda\right)}{\partial I_{b,i}}=0 \tag{4.2a}$$

$$\frac{\partial L\left(I_{b,i},\lambda\right)}{\partial \lambda}=0 \tag{4.2b}$$

or, equivalently

$$\frac{\sum\limits_{i=0}^{n}F_i\left(I_{b,i}\right)}{\partial I_{b,i}}=\lambda \quad i=0,1,\ldots,n \tag{4.3a}$$

$$\sum_{i=0}^{n}I_{D,i}-\sum_{i=0}^{n}I_{b,i}=0 \tag{4.3b}$$

Equation (4.3a) states that, in order to minimise the total power losses in the solar nano-grid, the necessary condition is to have the incremental loss rate, $\frac{\partial\sum\limits_{i=0}^{n}F_i\left(I_{b,i}\right)}{\partial I_{b,i}}$ of all the batteries in the solar nano-grid the same and equal to λ. For this reason, λ was referred to as the global incremental loss. The λ_i which is the partial derivative of $F_i\left(I_{b,i}\right)$ with respect to each variable $I_{b,i}$ was referred to as the local incremental loss of the i-th battery. Then, the condition for minimum power losses, i.e. $\lambda = \lambda_i \ , \forall i = 0, 1, \ldots, n$ was referred to as the equal incremental loss principle.

From (4.3a), the λ_i for the i-th battery was obtained as follows

$$\lambda_i = 2\alpha_i I_{b,i} + \beta_i \tag{4.4}$$

Then by substituting (4.4) in (4.3b), the following expression for λ was obtained

$$\lambda = \left(\sum_{i=0}^{n} \frac{\beta_i}{2\alpha_i} + \sum_{i=0}^{n} I_{D,i} \right) \Big/ \sum_{i=0}^{n} \left(\frac{1}{2\alpha_i} \right) \tag{4.5}$$

Using the equal incremental loss principle, the corresponding expression for the optimal charge and discharge current, $I^*_{b,i}$ for the i-th battery was obtained by replacing λ_i with λ in (4.4) and thereafter solving for $I_{b,i}$ as follows

$$I^*_{b,i} = \frac{\lambda - \beta_i}{2\alpha_i} \tag{4.6}$$

Consequently, according to (3.91), the optimal battery charge and discharge power was expressed as

$$P^*_{b,i} = \frac{v_{dc,i} \left(\lambda - \beta_i \right)}{2\alpha_i} \tag{4.7}$$

Lastly, taking the battery inequality constraints given by (3.93c) and (3.93d) into consideration, (4.7) was modified as follows

$$P^*_{b,i} = \begin{cases} \frac{v_{dc,i}(\lambda - \beta_i)}{2\alpha_i}, & \text{if } P^b_{min,i} \leq \frac{v_{dc,i}(\lambda - \beta_i)}{2\alpha_i} \leq P^b_{max,i} \ \& \ SoC_{min,i} \leq SoC_i \leq SoC_{max,i} \\ P^b_{max,i}, & \text{if } \frac{v_{dc,i}(\lambda - \beta_i)}{2\alpha_i} > P^b_{max,i} \ \& \ SoC_{min,i} \leq SoC_i \leq SoC_{max,i} \\ P^b_{min,i}, & \text{if } \frac{v_{dc,i}(\lambda - \beta_i)}{2\alpha_i} < P^b_{min,i} \ \& \ SoC_{min,i} \leq SoC_i \leq SoC_{max,i} \\ 0, & \text{otherwise.} \end{cases} \tag{4.8}$$

Then the $I^*_{b,i}$ which satisfied (3.93c) and (3.93d) was modified according to (4.8) as follows

$$I^*_{b,i} = \frac{P^*_{b,i}}{v_{dc,i}} \tag{4.9}$$

However by including the battery inequality constraints as given in (4.8), the equal incremental loss principle, $\lambda = \lambda_i$ required to minimise the total power losses may not work when one battery hits either the power limits; $P^b_{min,i}$, $P^b_{max,i}$ or the SoC limits; $SoC_{min,i}$, $SoC_{max,i}$. The current balance constraint (3.93b) may also not get satisfied when one battery hits its operation limits. Therefore modification of λ was required in order to always guarantee the optimality of the solution and the satisfaction of the equality constraint (3.93b) provided that the batteries did not hit their limits at the same time, otherwise minimising the power losses would be unnecessary.

The λ was modified using the following FLIA developed

$$\lambda^{(k+1)} = \lambda^{(k)} + e_\lambda \Delta I^{(k)} \tag{4.10}$$

where k is the iteration number, $\lambda^{(k+1)}$ is the approximated value of λ at iteration $k+1$ using the previous value of λ, i.e. $\lambda^{(k)}$ obtained at k-th iteration, e_λ is a small positive number that defines the convergence speed of the algorithm (4.10) and $\Delta I^{(k)}$ was defined from (4.3b) as a supply-demand current mismatch at k-th iteration as follows

$$\Delta I^{(k)} = \sum_{i=0}^{n} I_{D,i} - \sum_{i=0}^{n} I^{(k)}_{b,i} \tag{4.11}$$

According to (4.11), if $\Delta I^{(k)} = 0$, it means that current is being dispatched optimally from the batteries using the equal incremental loss principle without any battery hitting its limits. However, if $\Delta I^{(k)} \neq 0$, it means that certain batteries have hit their limits with their output currents either equal to zero or saturated at their absolute maximum values - such batteries are herein referred to as ‘in-active’ batteries. To achieve $\Delta I^{(k)} = 0$ in this case, the batteries which have not hit their operating limits (which are herein referred to as ‘active’ batteries) should supply and absorb more current than the ‘in-active’ ones while obeying the optimality rule given by the equal incremental loss principle.

With reference to (3.88b) and (4.3b), $\Delta I^{(k)} < 0$ means that the total load demand in the solar nano-grid exceeds the power generation from the solar panel and batteries must discharge power to meet the load demand. On the other hand, $\Delta I^{(k)} > 0$ means that the power generated from the solar panel exceeds the total load demand in the solar nano-grid and the batteries must charge the surplus power. Then according to (4.10), $\lambda^{(k+1)}$ was iteratively increased when $\Delta I^{(k)}$ was greater than zero, thereby making the 'active' batteries to increase their discharging rates more than the 'in-active' ones. Conversely, $\lambda^{(k+1)}$ was iteratively decreased when $\Delta I^{(k)}$ was less than zero causing the 'active' batteries to increase their charging rates more than the 'in-active' ones.

Implementation of the Fast Lambda Iteration Algorithm

Figure 4.3 shows a flowchart for implementing the FLIA proposed. The inputs to the algorithm are SoC_i, $P_{pv,i}$ and $P_{L,i}$ from all the households in the solar nano-grid. Starting with an initial $\Delta I^{(0)} = 0$ (i.e. assuming that all batteries are 'active'), the optimal λ was initially determined from (4.5) and thereafter either increased or decreased based on whether ΔI (4.11) was positive or negative respectively at each iteration.

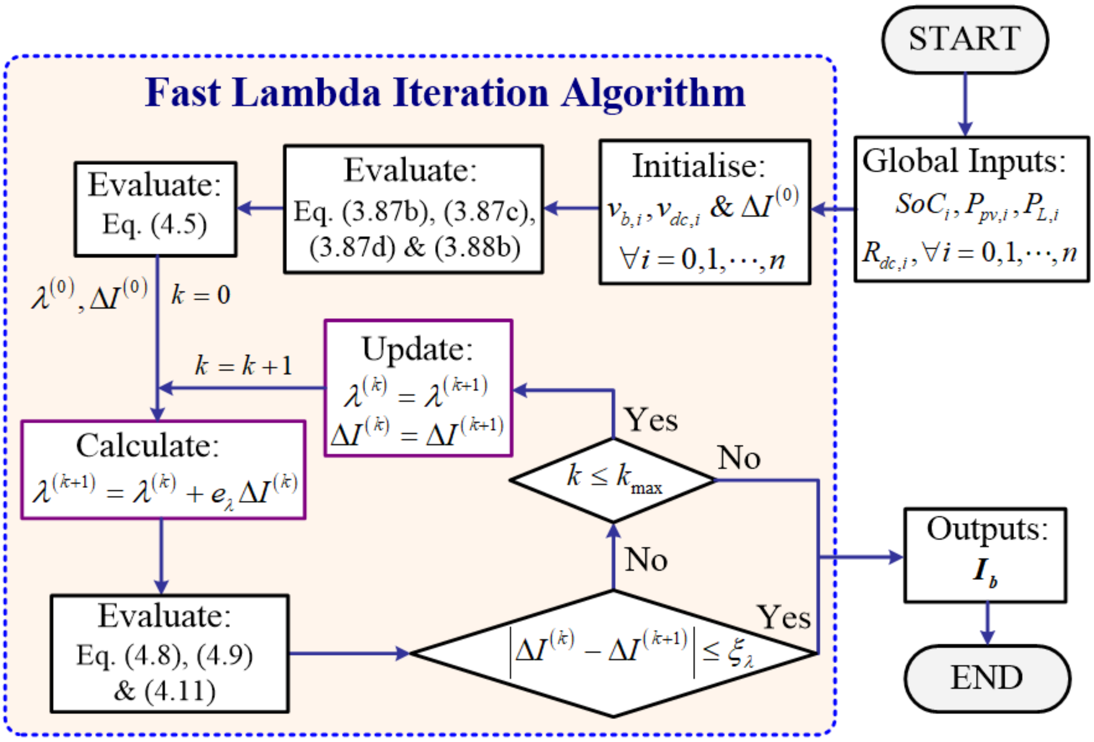

Figure 4.3: Flowchart for implementing the FLIA proposed.

Convergence Analysis of the Fast Lambda Iteration Algorithm

The iteration process for the algorithm (4.10) in Figure 4.3 was stopped when either the maximum number of iterations, k_{max} were exceeded or when the difference between $\Delta I^{(k+1)}$ and $\Delta I^{(k)}$ was less than or equal to the desired accuracy, ξ_λ, i.e. $\left|\Delta I^{(k+1)} - \Delta I^{(k)}\right| \leq \xi_\lambda$. When all the batteries were 'active' (i.e. $\Delta I^{(k)} = 0$), only one iteration was required for convergence where λ was directly determined from (4.5). For other battery operating conditions, convergence rate was determined by the value of e_λ, this is shown later in Section 4.3. The $\Delta I^{(k)} = 0$ condition could not be used to check the convergence of the algorithm because when all batteries were 'in-active', $\Delta I^{(k)} \neq 0$ was always obtained, making the iteration process to unnecessarily continue running until k_{max} was exceeded.

4.2.2 The Fast Voltage Iteration Algorithm

The main objective of the FVIA is to solve the OCFP given in (3.96). Given the optimal battery currents, $\mathbf{I_b} = \left[I^*_{b,0}, \ldots, I^*_{b,n}\right]^T$ from the FLIA, the corresponding optimal distribution currents, $i_{dc,i},\ \ i = 0, 1, \ldots, n$ were obtained by substituting $\mathbf{I_b}$ in (3.95). Thereafter, the distribution voltages were obtained by solving (3.96).

In a compact form, the system of linear equations given by (3.96) were re-written as follows

$$v_{dc,i} - \sum_{j=0}^{n} \left(w_{ij} v_{dc,j}\right) = -R_{dc,i} i_{dc,i} \tag{4.12a}$$

where

$$w_{ij} = \frac{1}{R_{dc,j} \sum\limits_{j=0}^{n} \frac{1}{R_{dc,j}}} \tag{4.12b}$$

That is, the difference between the DC bus voltage ($\sum\limits_{j=0}^{n} \left(w_{ij} v_{dc,j}\right)$) and household's distribution voltage ($v_{dc,i}$) must be equal to the voltage drop ($R_{dc,i} i_{dc,i}$). In matrix form, (4.12) was written as follows

$$\mathbf{Ax} = \mathbf{b} \tag{4.13}$$

where $\mathbf{x} = \left[v_{dc,0}, \dots, v_{dc,n}\right]^T$, $\mathbf{b} = \left[-R_{dc,0}i_{dc,0}, \dots, -R_{dc,n}i_{dc,n}\right]^T$, $\mathbf{A} = (a_{ij})_{n\times n}$ is a coefficient matrix with a_{ij} defined as follows

$$a_{ij} = \begin{cases} 1 - w_{ij}\,, & \text{if } i = j \\ -w_{ij}\,, & \text{otherwise.} \end{cases} \tag{4.14}$$

It was verified from (4.13) that each row of $\mathbf{A}$ summed to zero, i.e. $\sum_j a_{ij} = 0$. Thus, $\mathbf{A}$ was singular and solving (4.13) directly as $\mathbf{x} = \mathbf{A}^{-1}\mathbf{b}$ would yield infinite number of solutions. To circumvent this problem, (4.12) was iteratively solved using the following FVIA developed

$$v_{dc,i}^{(q+1)} = \sum_{j=0}^{n} \left(w_{ij} v_{dc,j}^{(q)}\right) - R_{dc,i} i_{dc,i} \tag{4.15}$$

where q is the iteration number and $v_{dc,i}^{(q+1)}$ is the updated approximation of the distribution voltage of i-th household with respect to the previous approximations of the distribution voltages, $v_{dc,j}^{(q)}$, $j = 0, 1, \dots, n$ of other j-th households.

The solution to (4.15) is achieved when the term, $\sum_{j=0}^{n} \left(w_{ij} v_{dc,j}^{(q)}\right)$ tends to a constant value as k tends to infinity. In fact, $\sum_{j=0}^{n} \left(w_{ij} v_{dc,j}^{(q)}\right)$ is the expression of the DC bus voltage as given in (3.78). Thus, the main aim of solving the OCFP using (4.15) was to find the DC bus voltage which was common to every household.

Considering the voltage limits (3.93e), the FVIA expressed by (4.15) was modified as follows

$$v_{dc,i}^{(q+1)} = \begin{cases} \sum_{j=0}^{n} \left(w_{ij} v_{dc,j}^{(q)}\right) - R_{dc,i} i_{dc,i}, \text{ if } v_{min,i}^{dc} \leq \sum_{j=0}^{n} \left(w_{ij} v_{dc,j}^{(q)}\right) - R_{dc,i} i_{dc,i} \leq v_{max,i}^{dc} \\ v_{max,i}^{dc}\,, \text{ if } \sum_{j=0}^{n} \left(w_{ij} v_{dc,j}^{(q)}\right) - R_{dc,i} i_{dc,i} > v_{max,i}^{dc} \\ v_{min,i}^{dc} \quad \text{otherwise.} \end{cases} \tag{4.16}$$

The solution to the FVIA (4.16) was given by an n-dimensional vector, $\mathbf{V_{dc}}$ as follows

$$\mathbf{V_{dc}} = \left[v_{dc,0}, \dots, v_{dc,n}\right]^T \tag{4.17}$$

Implementation of the Fast Voltage Iteration Algorithm

Figure 4.4 shows the implementation of the FVIA. The inputs to the algorithm are $I_{D,i}$, $I^*_{b,i}$ and $R_{dc,i}$ for all $i = 0, 1, \ldots, n$. Starting with an initial $\mathbf{V_{dc}}^{(0)}$, (4.16) was iteratively solved until it converged.

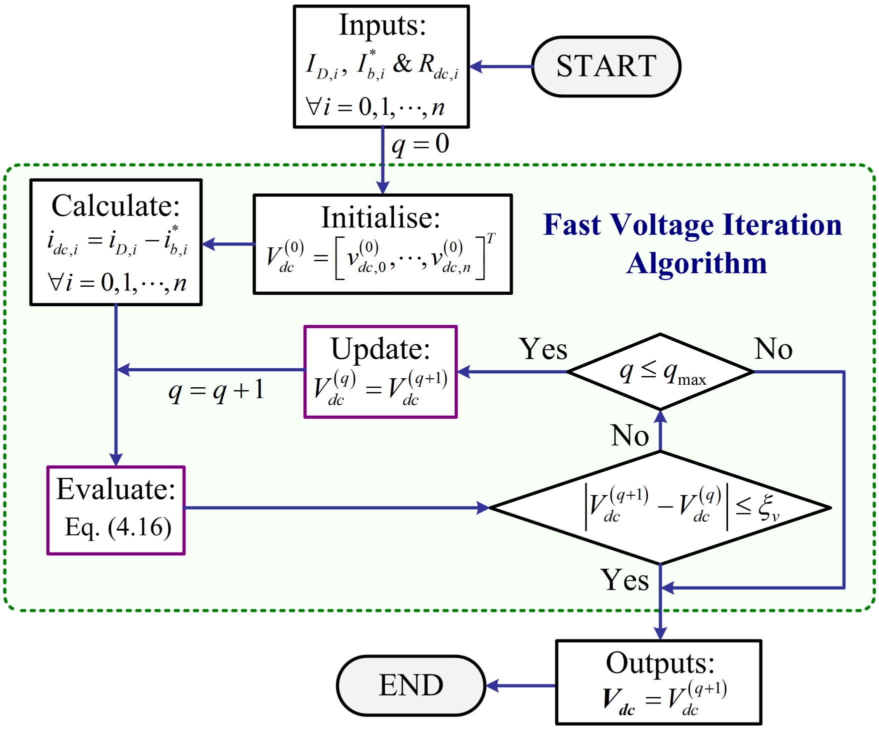

Figure 4.4: Flowchart for implementing the FVIA proposed.

Convergence Analysis of Fast Voltage Iteration Algorithm

The convergence analysis and the initialisation of the FVIA was analysed by rewriting (4.15) in a matrix form for any q as follows

$$\mathbf{V_{dc}}^{(q+1)} = \mathbf{W}\mathbf{V_{dc}}^{(q)} + \mathbf{c} \tag{4.18}$$

where $\mathbf{V_{dc}}^{(q)} = \left[v^{(q)}_{dc,0}, \ldots, v^{(q)}_{dc,n}\right]^T$ are approximated voltage values at q-th iteration, $\mathbf{W} = (w_{ij})_{n \times n}$, is a non-negative iterative matrix and $\mathbf{c} = \left[-R_{dc,0}i_{dc,0}, \ldots, -R_{dc,n}i_{dc,n}\right]^T$ is an $n \times 1$ column vector of voltage drops.

The matrix $\mathbf{W}$ had the following characteristics:

- all the entries were greater than zero, i.e. $w_{ij} > 0$, $\forall i, j = 0, 1, \ldots, n$,

- the sum of each row was equal to one, i.e $\sum_{j=0}^{n} w_{ij} = 1, \forall i = 0, 1, \ldots, n$,
- all the rows were identical, thus $\mathbf{W}$ was singular, i.e. $\det(\mathbf{W}) = 0$,
- $\mu_0 = 1$ was a simple eigenvalue of $\mathbf{W}$ and all other eigenvalues; $\mu_1, \ldots, \mu_n$ were zero,
- an n dimensional vector given by $\mathbf{1} = [1, \ldots, 1]^T$ was a right eigenvector of $\mathbf{W}$ associated with $\mu_0 = 1$, i.e. $\mathbf{W1} = \mathbf{1}$,
- an n dimensional row vector given by $\pi_{\mathbf{w}} = [w_{i0}, w_{i1}, \ldots, w_{in}]$, $i = 0, 1, \ldots, n$ was a left eigenvector of $\mathbf{W}$ associated with $\mu_0 = 1$, i.e. $\pi_{\mathbf{w}}\mathbf{W} = \pi_{\mathbf{w}}$.

The above characteristics verified that $\mathbf{W}$ was a row stochastic matrix and according to Perron-Frobenius theorem [193, 194], the convergence of $\mathbf{W}$ and the convergence of the algorithm thereof existed.

Pre-multiplying (4.18) by $\pi_{\mathbf{w}}$, the following expression was obtained

$$\pi_{\mathbf{w}}\mathbf{V_{dc}}^{(q+1)} = \pi_{\mathbf{w}}\mathbf{W}\mathbf{V_{dc}}^{(q)} + \pi_{\mathbf{w}}\mathbf{c} \tag{4.19}$$

Noticing that $\pi_{\mathbf{w}}\mathbf{W} = \pi_{\mathbf{w}}$ and that $\pi_{\mathbf{w}}\mathbf{c} = -\left(\sum_{i=0}^{n} i_{dc,i}\right) / \sum_{i=0}^{n} \frac{1}{R_{dc,i}}$, the expression in (4.19) was further simplified as follows

$$\pi_{\mathbf{w}}\left[\mathbf{V_{dc}}^{(q+1)} - \mathbf{V_{dc}}^{(q)}\right] = -\frac{\sum_{i=0}^{n} i_{dc,i}}{\sum_{i=0}^{n} \frac{1}{R_{dc,i}}} \tag{4.20}$$

or, equivalently

$$\sum_{i=0}^{n} v_{dc,i}^{(q+1)} - \sum_{i=0}^{n} v_{dc,i}^{(q)} = -R_{dc,i}\sum_{i=0}^{n} i_{dc,i} \tag{4.21}$$

Since $\sum_{i=0}^{n} i_{dc,i}$ in (4.21) is generally zero from the law of conservation of current, taking limits at both sides of (4.21) as q tends to infinity (i.e. $q \rightarrow \infty$) yielded the following expression

$$\lim_{q\to\infty}\sum_{i=0}^{n} v_{dc,i}^{(q+1)} = \lim_{q\to\infty}\sum_{i=0}^{n} v_{dc,i}^{(q)} \tag{4.22}$$

That is, as $q \to \infty$, the difference between $v_{dc,i}^{(q+1)}$ and $v_{dc,i}^{(q)}$ is approximately equal to zero and the voltage iteration algorithm (4.15) convergences for any choice of initial values, $\mathbf{V_{dc}}^{(0)} = \left[v_{dc,0}^{(0)}, \ldots, v_{dc,n}^{(0)}\right]^T$.

Specifying the desired accuracy of the approximated voltage solution by a small constant ξ_v, the algorithm (4.15) was terminated when the absolute difference between $v_{dc,i}^{(q+1)}$ and $v_{dc,i}^{(q)}$ for all $i = 0, 1, \ldots, n$ was less than or equal to ξ_v, i.e. $\left|v_{dc,i}^{(q+1)} - v_{dc,i}^{(q)}\right| \leq \xi_v \;\; \forall i = 0, 1, \ldots, n$. To prevent the iterations from going on forever under unexpected circumstances, the algorithm was stopped when the maximum number of predetermined iterations, q_{max} was exceeded. The q_{max} was calculated as follows [116]

$$q_{max} = \frac{-1}{\log_{\xi_v}(1/|\mu_1|)} \tag{4.23}$$

where μ_1 is the second largest eigenvalue of $\mathbf{W}$. However, $\mathbf{W}$ had $\mu_1 = 0$. Then, evaluating (4.23) for $\mu_1 = 0$ and taking $\xi_v = 0.01$, q_{max} was found to be approximately equal to 1. This means that only one iteration ($q_{max} = 1$) was expected for the algorithm (4.18) to converge, provided that the voltage limits were not exceeded.

4.2.3 Solar Power Curtailment and Load Shedding

The distribution currents, $i_{dc,i}$ obtained by evaluating (3.95) denotes the desired amount of current that a household must receive from the distribution network while obeying the equality constraint given by (3.93b) and the inequality constraints given by (3.93c) and (3.93d). Because current flow in the distribution network is intuitively by voltage difference, introducing the voltage limits in the FVIA (4.16) effectively limits the amount of current that gets received by a household from the distribution network.

Using $\mathbf{V_{dc}}$ from Figure 4.4, the proportion of $i_{dc,i}$ that gets received by a household from the distribution network due to voltage limits was calculated as follows

$$i_{r,i} = \frac{1}{R_{dc,i}} \left(-v_{dc,i} + \sum_{j=0}^{n} w_{ij} v_{dc,j} \right) \tag{4.24}$$

That is, $i_{r,i}$ given by (4.24) is equal to $i_{dc,i}$ given by (3.95) if and only if $v_{dc,i}$ in (4.24) is within the voltage limits as $v^{dc}_{min,i} \leq v_{dc,i} \leq v^{dc}_{max,i}, \forall i = 0, 1, \ldots, n$. Otherwise $i_{r,i}$ is less than $i_{dc,i}$. By the law of conservation of current, the sum of $i_{r,i}$ in the distribution network must also equal to zero as follows

$$\sum_{i=0}^{n} i_{r,i} = 0, \quad \forall i = 0, 1, \cdots, n \tag{4.25}$$

The proportion of $i_{dc,i}$ that is not received by a household due to the voltage limits was given by the following expression

$$i_{nr,i} = i_{dc,i} - i_{r,i} \tag{4.26}$$

That is, if $i_{r,i} = i_{dc,i}$, then $i_{nr,i} = 0$ and the desired current, $i_{dc,i}$ is what gets received by the households. To maintain the current balance given by (4.25), $i_{nr,i}$ was viewed as an excess current that must be either discharged (if $i_{dc,i} > 0$) or charged (if $i_{dc,i} < 0$) by the i-th battery. However, where the battery limits given by (3.93c) or (3.93d) are reached, $i_{nr,i}$ was viewed as the proportion of $I_{D,i}$ that should be reduced through either solar power curtailment or load shedding as follows.

Solar Power Curtailment

The power generation from the solar panel was curtailed (reduced) if all of the following conditions were satisfied, that:

- $I_{D,i} < 0$, i.e. when the power ($P_{pv,i}$) generated from the solar panel was more than the total local load demand ($P_{L,i} + p^{c}_{loss,i}$) as expressed by (3.88b),
- $i_{dc,i} < 0$, i.e. when a household was supplying current to the distribution network,
- either $SoC_i > SoC_{max,i}$ or $P^{*}_{b,i} > P^{b}_{min,i}$ from (3.93c) and (3.93d) respectively,
- $i_{nr,i} \neq 0$, i.e. proportion of $I_{D,i}$ that should be reduced through solar power curtailment due to battery charge and discharge limits is not equal to zero.

Making use of Figure 3.34 and the voltage ratios given in (3.80a), the proportion of $I_{D,i}$ that was curtailed from the solar panel was calculated as follows

$$i^{c}_{pv,i} = \left(\frac{v_{dc,i}}{v_{mp,i}}\right) i_{nr,i} \tag{4.27}$$

where $i^{c}_{pv,i}$ is the actual amount of current curtailed from the solar panel.

To implement the curtailment, the MPPT algorithm shown in Figure 3.29 was modified by including a new solar panel manager between the MPPT algorithm and the outputs as shown in Figure 4.5.

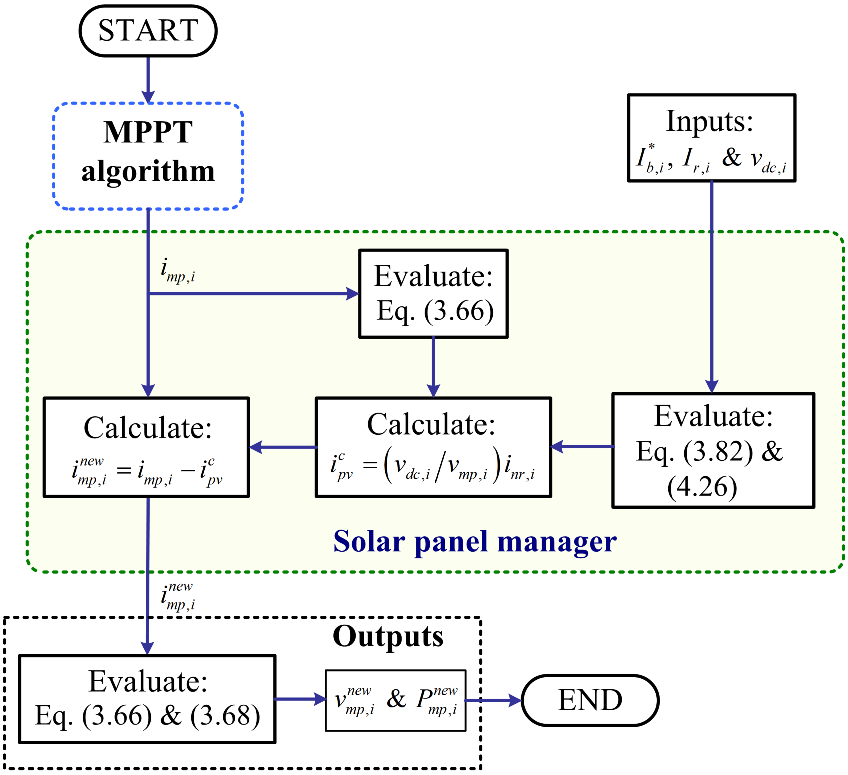

Figure 4.5: Power generation curtailment using the solar panel manager.

The new current at MPP, $i^{new}_{mp,i}$ was obtained by subtracting $i^{c}_{pv,i}$ from $i_{mp,i}$. Thereafter, the new reference voltage $v^{new}_{mp,i}$ and the new power output $P^{new}_{mp,i}$ were obtained by substituting $i^{new}_{mp,i}$ in (3.66) and (3.68) respectively.

The solar power curtailment procedure developed required only local information i.e. the $v_{dc,i}$ and $i_{nr,i}$ which were specific to a single household. Therefore, the solar panel management shown in Figure 4.5 was implemented in a decentralised manner.

Load Shedding

The load demand was load shed (reduced) if the following conditions were satisfied, that:

- $I_{D,i} > 0$, i.e. according to (3.88b), when the total load demand ($P_{L,i} + p^c_{loss,i}$) was more than the power ($P_{pv,i}$) generated from the solar panel,
- $i_{dc,i} \geq 0$, i.e. when a household was receiving current from the distribution network,
- either $SoC_i < SoC_{min,i}$ or $P^*_{b,i} > P^b_{max,i}$ from (3.93c) and (3.93d) respectively,
- $i_{nr,i} \neq 0$, i.e. proportion of $I_{D,i}$ that should be reduced through load shedding due to battery charge and discharge limits is not equal to zero.

The proportion of $I_{D,i}$ that was reduced by reducing the local load demand, $P_{L,i}$ based on $i_{nr,i}$ was calculated as follows

$$P^{shed}_{L,i} = P_{L,i} - v_{dc,i} i_{nr,i} \tag{4.28}$$

The selection of the physical DC loads to be switched off based on $P^{shed}_{L,i}$ was however beyond the current scope. Advanced methods such as the Knapsack problem in [195, 196] could be used in this case.

Similar to the solar power curtailment procedure, the load shedding process developed uses local information only i.e. the $v_{dc,i}$ and $i_{nr,i}$ to reduce the load demand. Therefore, it was also implemented in a decentralised manner.

4.2.4 Implementation of the Centralised Control Algorithm

Figure 4.6 shows the implementation of the centralised control algorithm proposed at every optimisation time step. The FLIA is shown in Figure 4.3 while the FVIA is shown in Figure 4.4. The solar panel and load manager developed are presented in Subsection 4.2.3.

The inputs to the algorithm were SoC_i, $P_{pv,i}$ and $P_{L,i}$ from all the households in the solar nano-grid. At every m-th iteration, the output $\mathbf{V_{dc}}^{(m+1)}$ from the FVIA was used to update the $\mathbf{V_{dc}}^{(m)}$ which were constants in the FLIA. It was found that updating the $v_{b,i}$ and $v_{dc,i}$ at the same time as shown in Figure 4.2 delayed the execution of the algorithm. To circumvent

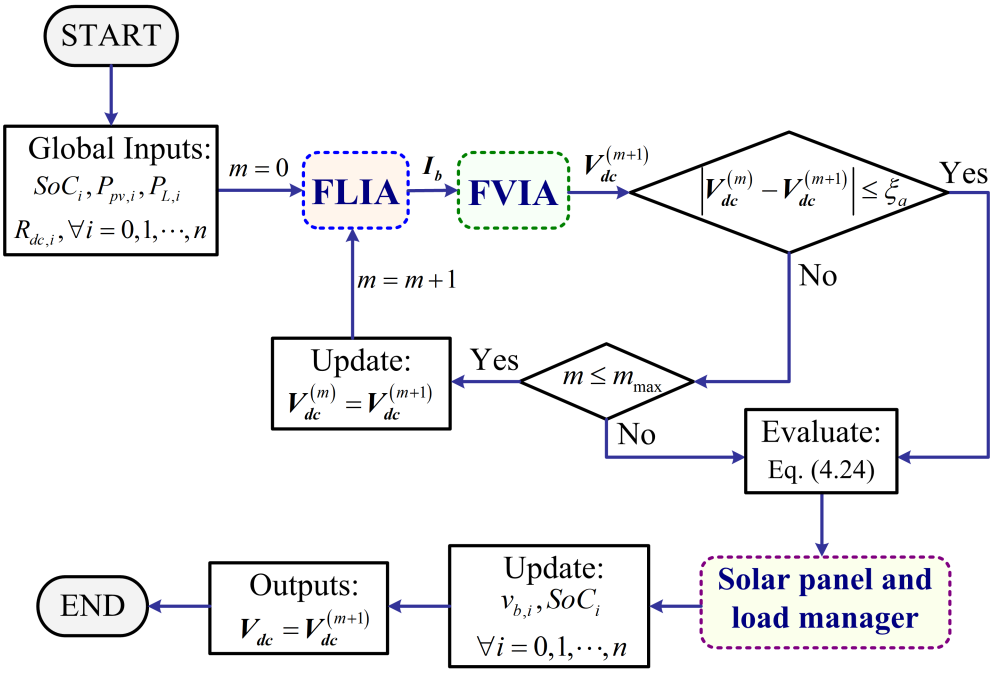

Figure 4.6: Implementation of the centralised control algorithm proposed.

this problem, the update of the $v_{b,i}$ was carried out after the m iterations and the updates was to be used in the next optimisation time step.

The iteration process was stopped when the difference between the approximation of $\mathbf{V_{dc}}^{(m+1)}$ at $(m+1)$-th iteration and the previous approximation of $\mathbf{V_{dc}}^{(m)}$ at m-th iteration was less or equal to the desired solution accuracy, ξ_a i.e. $\left|\mathbf{V_{dc}}^{(m+1)} - \mathbf{V_{dc}}^{(m)}\right| \leq \xi_a$. When the desired solution accuracy was achieved, the obtained $\mathbf{V_{dc}}^{(m+1)}$ were regarded as the optimal distribution voltages that minimised the power losses in the solar nano-grid while satisfying the operational constraints. The iterations were also forced to stop when the maximum number of iterations, m_{max} was reached.

The output $\mathbf{V_{dc}}^{(m+1)}$ from the FVIA was thereafter used in the solar panel and load manager in order to reduce the power generation and load demand if necessary respectively. After that, the $v_{b,i}$ and SoC_i for the next optimisation time step were updated. The $v_{b,i}$ was updated by using the expression given by (3.98). The SoC_i was updated by using (3.73), (3.74), (3.80b), (3.83) and (3.98).

Finally, the output voltages $\mathbf{V_{dc}} = \mathbf{V_{dc}}^{(m+1)}$ from the centralised algorithm were treated as the optimal distribution voltage references that minimise the power losses in the solar nano-grid. With reference to Figures 1.7 and 4.1, $\mathbf{V_{dc}}$ were the optimal reference control

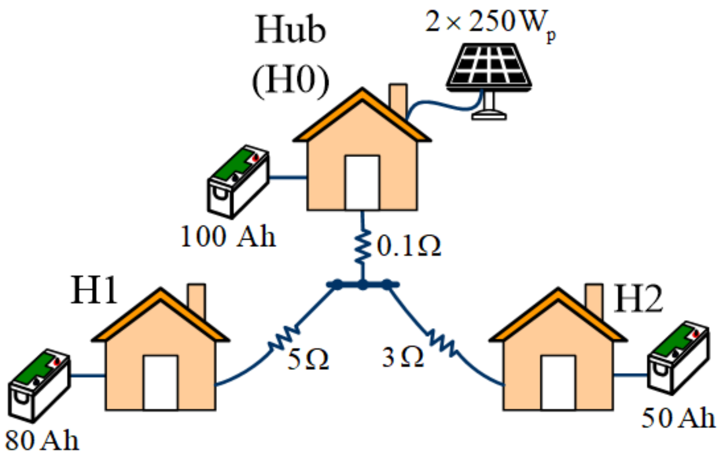

Figure 4.7: A test solar nano-grid for simulation purposes.

signals that were sent to the low level control of the FPCs for control implementation via the communication links. Low level control of the FPCs was however, beyond the scope of the present research.

4.3 Simulation Results and Discussion

In this section, the performance of the centralised control algorithm proposed is presented. Figure 4.7 shows a test solar nano-grid that consists of a hub (H0) and two households H1 and H2. Typical distribution line lengths of 372 m (equivalent to 5Ω loop resistance) and 223 m (equivalent to 3Ω loop resistance) of 2.5 mm^2 copper wires were considered (other distribution line lengths can be considered also) to connect H1 and H2 to the DC bus bar in the hub respectively. The loop resistance, 0.1Ω represents the lumped resistance of the DC bus bar, the protection equipment and the connection cables in the hub. A 2×250 W, 24 V Suntech monocrystalline solar panel with specifications given in Table 3.6 was used for the simulations. The solar irradiance profile shown in Figure 4.12a was considered to be the same every day and was used to generate the solar power output at the temperature of 25°C and at every time instant. The solar panel and the batteries were sized to support the load demand profiles shown in Figure 4.13a for a day. The solar nano-grid was simulated using a Python programming language.

To verify the performance of the algorithm proposed, two case studies were considered for simulation. In the first case study, constant values of the solar power and the household load demand were used. The objective of the first case study was to investigate the convergence and execution time of the algorithm proposed. In the second case study, time varying values of the solar power and household load demand were used. The objective of the second case study was to verify the effectiveness of the algorithm proposed for: 1) facilitating power exchange between the households while strictly satisfying the operational constraints and 2) minimising the total energy losses of the solar nano-grid. For each case study, the results were compared to those obtained by an existing approach given in [46] (hereafter referred to as traditional approach). The traditional approach involves formulating the power loss problem of the solar nano-grid through linearisation of power flow equations (around operating points) and then solving the power loss optimisation problem using a CVXOPT solver.

4.3.1 CASE STUDY 1: with constant load demand and power generation

In this case study, power generation from the solar panels and the load demand in each household were taken to be constants, thus representing a specific operating point of the solar nano-grid. Table 4.1 shows a summary of the considered simulation parameters of the solar nano-grid shown in Figure 4.7.

Table 4.1: Solar nano-grid parameters.

	H0	H1	H2
Solar panel rating (Wp)	2×250	0	0
Battery capacity (Ah)	100	80	50
Battery power limits (W)	[-120, 120]	[-120, 120]	[-120, 120]
Battery SoC range (%)	[20, 80]	[20, 80]	[20, 80]
Initial battery SoC (%)	60	50	30
Nominal battery voltage (V)	12	12	12
Line resistance (Ω)	0.1	5	3
Distribution voltage range (V)	[100, 120]	[100, 120]	[100, 120]
Nominal distribution voltage (V)	110	110	110

In addition to Table 4.1, Table 4.2 provides the summary of the power values and other derived simulation parameters, e.g. α, β, γ for each household in Figure 4.7. The derived parameters were calculated using their respective mathematical equations which have been presented in Chapter 3.

Table 4.2: Additional simulation parameters for case study 1.

	H0	H1	H2
Solar panel power output, P_{pv} (W)	500	0	0
Total demand, $P_L + p^c_{loss}$ (W)	100	50	80
Distribution voltage, v_{dc} (V)	110	110	110
Battery output voltage, v_b (V)	12	12	12
demand current, I_D (A)	-3.64	0.45	0.73
Power loss coefficient, α	0.51	5.52	3.85
Power loss coefficient, β	0.73	-4.55	-4.36
Power loss coefficient, γ	1.32	1.03	1.59
Battery's internal resistance, r_b (mΩ)	4.91	6.20	10.12

Since the control algorithm proposed which is shown in Figure 4.6 consists of the FLIA and the FVIA, these were first investigated individually for their convergence speeds and then jointly investigated for the performance of the overall centralised control algorithm.

Convergence Speed of the Fast Lambda Iteration Algorithm

Convergence of the FLIA is mainly affected by the choice of the convergence factor, e_λ and whether batteries are 'active' or not as explained in Subsection 4.2.1.

If all the batteries in the solar nano-grid are 'active' (that is, if they operate without hitting their power and SoC limits), only one iteration is required to run the FLIA, where the incremental power loss λ is directly computed using (4.5) and then the battery charge and discharge currents are calculated using (4.6). However, in the event that certain batteries in the solar nano-grid operate at either their power or SoC limits, convergence of the FLIA is purely decided by adjusting e_λ.

Figure 4.8 shows the convergence rate of the FLIA for different values of e_λ.

As shown in Figure 4.8, increasing the value of e_λ from $e_\lambda = 0.5$ W/A^2 to $e_\lambda = 8.8$ W/A^2 increases the rate of convergence of the FLIA algorithm. The incremental loss corresponding to the various values of e_λ all approached -10.59 W/A within 40 iterations. The supply-demand current mismatch, ΔI also approached zero for all the choices of e_λ considered. This shows that the FLIA proposed converges and achieves the current balance in the solar nano-grid. It was noted however that for higher values of e_λ (e.g. $e_\lambda = 8.8$ W/A^2), the FLIA became unstable (with the results oscillating about their final values). This suggests that

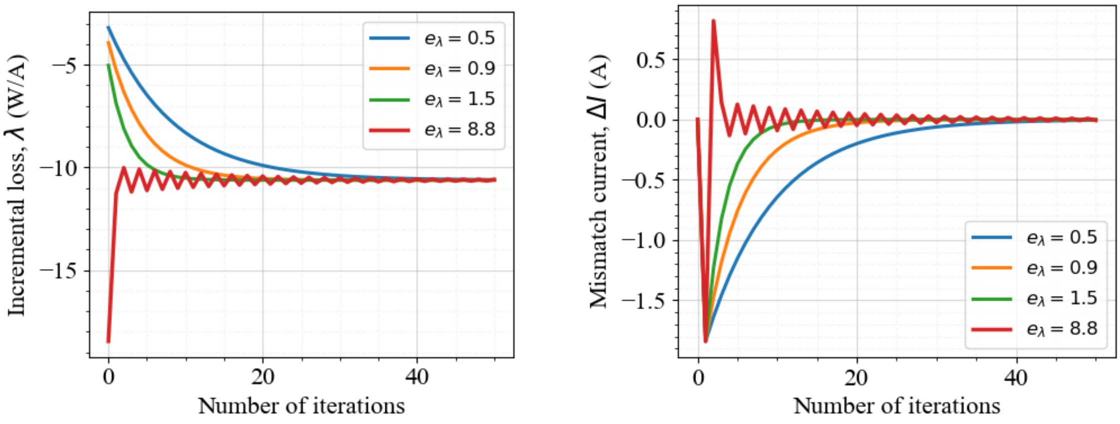

(a) (b)

Figure 4.8: Convergence speed of the FLIA: (a) global incremental loss and (b) mismatch current ΔI for different values of e_λ.

convergence of the algorithm is guaranteed with small values (which are less than one) of e_λ. For the rest of this chapter, $e_\lambda = 0.5$ W/A^2 was used.

Substituting the obtained $\lambda = -10.59$ W/A in (4.8) and (4.9) yielded battery charge powers as follows; $P_{b,0} = -120$ W, $P_{b,1} = -60.89$ W and $P_{b,2} = -89.90$ W and battery charge currents as follows; $i_{b,0} = -1.091$ A, $i_{b,1} = -0.55$ A and $i_{b,2} = -0.82$ A. The battery powers and currents were negative showing that the batteries were charging due to the solar power (500 W) which is more than the total load demand (230 W) as shown in Table 4.2. In addition, the results show that the battery in H0 had reached its power limit while the batteries in H1 and H2 did not. This explains why the algorithm had more than one iteration as shown in Figure 4.8. It also suggests that the algorithm prioritises charging and discharging batteries in households that have low resistive distribution lines in its quest to minimise the power losses since the charging power of the battery in H2 (-89.90 W), where the distribution line resistance is 3Ω, was greater than that of the battery in H1 (-60.89 W), where the distribution line resistance is 5Ω.

Convergence Speed of the Fast Voltage Iteration Algorithm

The distribution line currents for H0, H1 and H2 corresponding to the battery charge currents obtained from the FLIA in the previous subsection were obtained from (3.95) as -2.545 A, 1.0 A and 1.544 A respectively. Using these distribution current values, the convergence speed of the FVIA was investigated as shown in Figure 4.9a.

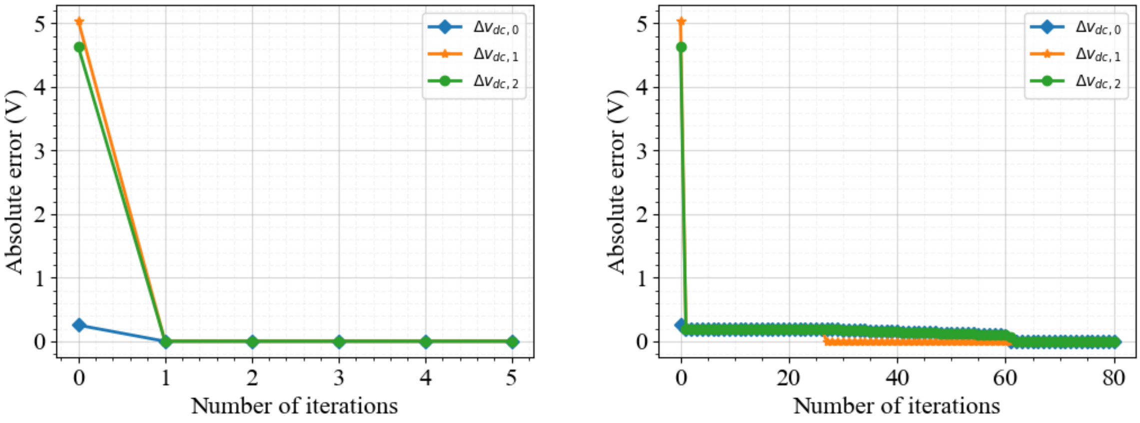

(a) (b)

Figure 4.9: Convergence speed of the FVIA for (a) balanced and (b) unbalanced distribution line currents.

As shown in Figure 4.9a, the FVIA converged in one iteration as claimed in Subsection 4.2.2. This was always the case provided that the distribution line currents were balanced, i.e. $\sum_{i=0}^{n} i_{dc,i} = 0$. Figure 4.9b shows that convergence of the FVIA was also ensured for unbalanced distribution line currents; -2.545 A, -1.0 A and 1.544 A for H0, H1 and H2 respectively (which can happen when all the batteries in the solar nano-grid are overcharged or over discharged) mainly due to voltage limits. Convergence speed however, was delayed compared to the case in Figure 4.9a where the currents were balanced. This suggested that convergence of the FVIA was guaranteed regardless of whether the battery currents from the FVIA resulted in balanced or unbalanced distribution line currents.

Convergence Speed of the Centralised Control Algorithm

In the previous subsections, convergence speed was investigated for separate FLIA and FVIA. In this subsection, convergence speed was investigated when both the FLIA and FVIA were operated together forming the centralised control algorithm proposed. This was done by analysing the total number of iterations taken by the centralised control algorithm to generate the final battery power outputs and distribution line voltages.

Generally, the convergence speed of the algorithm proposed is affected by the number of households in the solar nano-grid. Considering this fact, the convergence speed of the algorithm proposed was analysed for a solar nano-grid having 5 to 100 number of households with a constant power generation of 500 W at the hub. For brevity, the simulation parameters of H2 were duplicated in the extra (homogeneous) households, Hi, $i = 3, 4, \ldots, 100$ that were added to the solar nano-grid in Figure 4.7. The extra households were labelled as H2+ for ease of reference as shown in Figure 4.10b.

Figure 4.10a shows the variation of the total number of iterations required for the algorithm proposed to converge for different number of households in the solar nano-grid. As shown in Figure 4.10a, increasing the number of households from 5 to 100, the total number of iterations decreased to 3 iterations where they remained constant after 16 households. This phenomenon was best explained by plotting the battery output powers in the households as shown in Figure 4.10b.

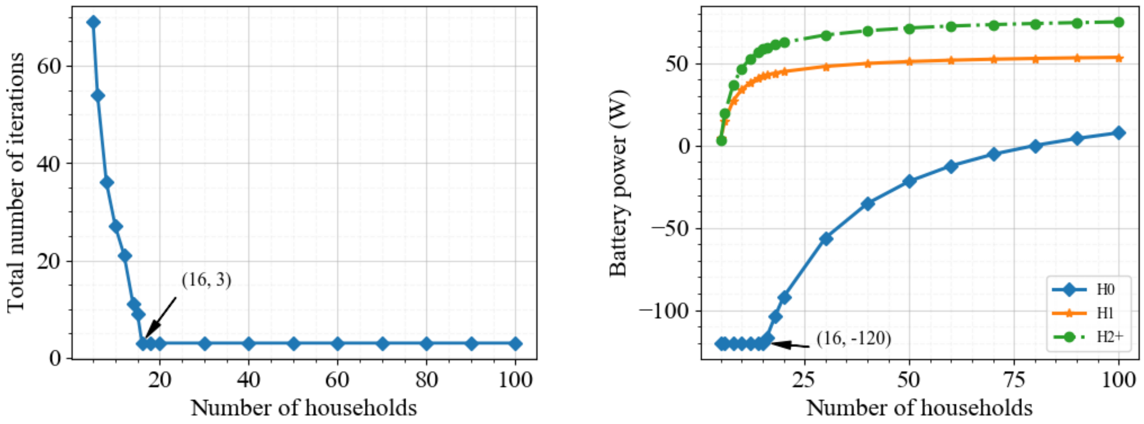

(a)

(b)

Figure 4.10: Showing in (a) the total number of iterations required for the centralised control algorithm proposed to converge and (b) the battery power outputs for the different number of households, where the battery capacities in H1 and H2+ are 80 Ah and 50 Ah respectively, and the distribution line resistances of H1 and H2+ are 5 Ω and 3 Ω respectively.

Between 5 and 16 households, the number of iterations were high due to the battery in H0 which hit its charge power limit (i.e. -120 W) as shown in Figure 4.10b, causing the ΔI which is given by (4.11) to be large and non-zero. The larger the value of ΔI, the higher the number of iterations required to drive the value of ΔI to zero as explained in Subsection 4.2.1.

Increasing the number of households from 16 to 100 households (which significantly increases the load demand in the solar nano-grid), decreased the amount of power required to charge the battery in H0 as more power was used to supply the increased load demand in H2+. Thus, between 16 and 100 households, the batteries in H0, H1 and H2+ neither charged nor discharged with maximum power as shown in Figure 4.10b. As a consequence, the ΔI given by (4.11) was equal to zero as explained in Subsection 4.2.1 and the incremental loss, λ was directly computed from (4.5). That resulted to 3 iterations between 16 and 100 households, mainly due to voltage updates in the feedback back loop of Figure 4.6.

To observe what happens if some of the batteries reach their discharge power limits, the previous simulation was repeated by changing; the battery capacities in H1 and H2+ from 80 Ah and 50 Ah to 56 Ah and 13 Ah respectively, and the distribution line resistances of H1 and H2+ from 5 Ω and 3 Ω to 5 Ω and 10 Ω respectively. The results of the simulation are shown in Figure 4.11.

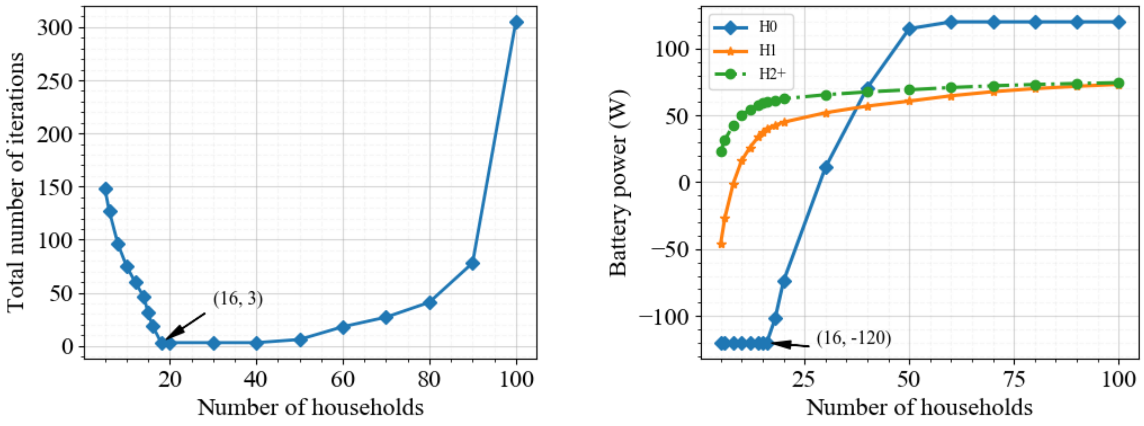

(a)

(b)

Figure 4.11: Showing in (a) the total number of iterations required for the centralised control algorithm proposed to converge and (b) the battery power outputs for the different number of households, where the battery capacities in H1 and H2+ are 56 Ah and 13 Ah respectively, and the distribution line resistances of H1 and H2+ are 5 Ω and 10 Ω respectively.

Figure 4.11 shows that the number of iterations increased exponentially with the number of households as the batteries approach their discharge power limits.

From the simulation results, it was noted that:

- The algorithm proposed was scalable, able to minimise the power losses in a solar nano-grid with many households.
- The algorithm proposed converged within three iterations regardless of the number

of households in the solar nano-grid, provided that the batteries neither charged nor discharged with maximum power, which in practice is the most operating state of the batteries.

- The number of iterations grew exponentially with the number of households when any of the batteries approached their charge and discharge power limit.

Comparison Between the Algorithm Proposed and the Traditional Approach

This subsection presents a comparison of power loss and execution time results between the algorithm proposed and the traditional approach. The test solar nano-grid shown in Figure 4.7 having simulation parameters in Table 4.1 and Table 4.2 was considered. Table 4.3 shows this comparison.

As shown in Table 4.3, the algorithm proposed gave a total power loss of 23.290 W while the traditional approach gave a total power loss of 24.072 W (3.25% higher), suggesting that the algorithm proposed was more accurate than the traditional approach. The execution time for the algorithm proposed was 0.1655 s compared to 0.1770 s for the traditional approach, demonstrating the suitability of the algorithm proposed for a real-time implementation.

Table 4.3: Comparison of total power loss and execution time results between the algorithm proposed and traditional approach.

	Traditional	**Proposed**
Total power loss (W)	24.072	**23.29**
Execution time (s)	0.1770	**0.1655**

4.3.2 CASE STUDY 2: with time varying load demand and solar panel output power

In this case study, the performance of the algorithm proposed using time varying load demand and solar panel output power is presented. Unlike case study 1 in Subsection 4.3.1, the parameters shown in Table 4.2 were updated during each optimisation time step. Figure

4.12a shows the 24 hour solar irradiance (one minute resolution) used in this research, which was obtained from Kenya on a cloud day of 14/07/2014. The irradiance was considered to be constant for two days. The corresponding power output from the 2× 250 W solar panels (obtained for 48 hours) is shown in Figure 4.12b.

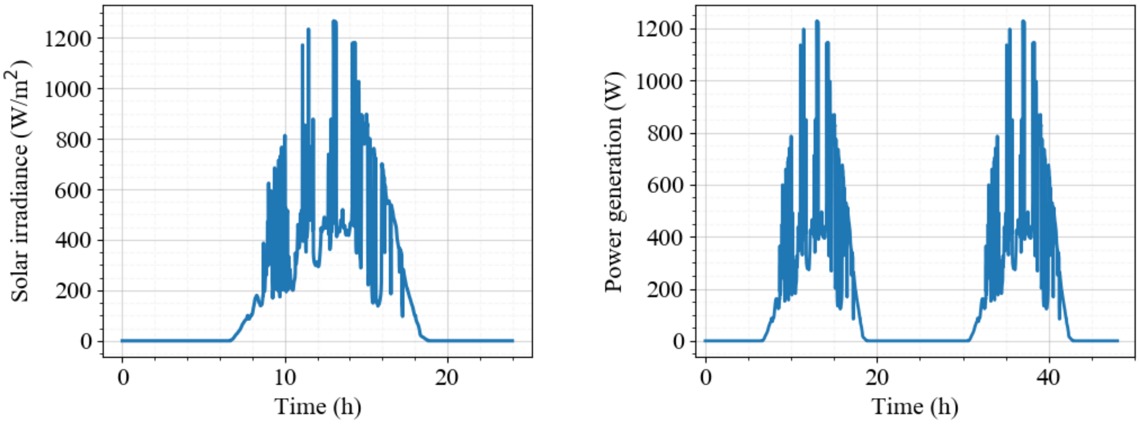

(a) (b)

Figure 4.12: Showing in (a) 24 hour solar irradiance on a cloudy day and (b) 48 hour power generation profile from the solar panels.

Figure 4.13a shows 48 hour load demand profiles (one minute resolution) [197] for the considered households and hub. The total power generation from the solar panels and the total load demand in the solar nano-grid for two days were calculated from Figure 4.12b and Figure 4.13a and are as shown in Figure 4.13b.

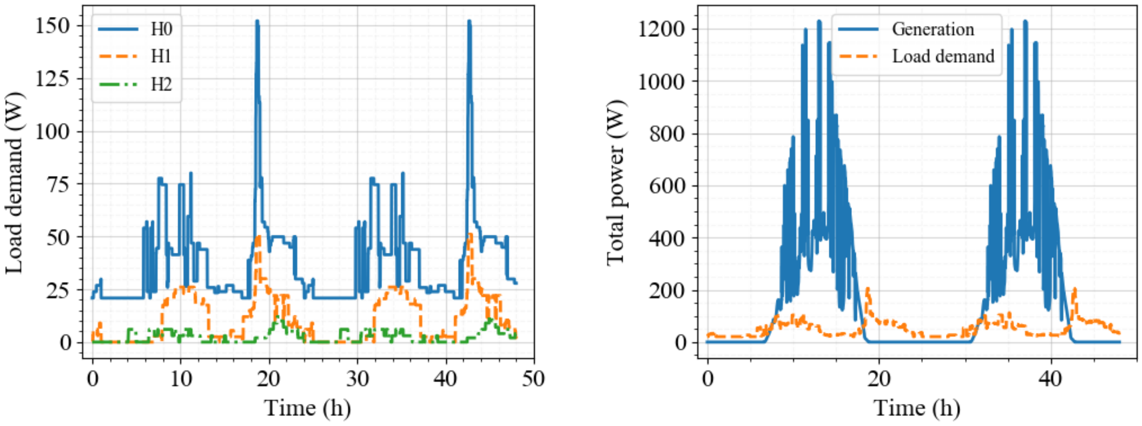

(a) (b)

Figure 4.13: Profiles of (a) load demand in the households and hub, and (b) total power generation and load demand in the solar nano-grid.

As shown in Figure 4.13b, the total power generation is greater than the total load demand between 8 h and 18 h and between 32 h and 42 h. Therefore, through power exchange between the households, the batteries were expected to charge power during these periods and to supply (discharge) power otherwise in order to satisfy the total load demand.

The performance and suitability of the algorithm proposed for: (i) managing the power exchange between the households while satisfying the operational constraints, and (ii) minimising the time varying power losses of the solar nano-grid is presented in the next subsections.

Power Management Performance of the Centralised Algorithm Proposed

Figure 4.14 shows the power management performance of the algorithm proposed. The battery SoC response is shown in Figure 4.14b and the battery output power (positive for discharging and negative for charging) is shown in Figure 4.14b. The distribution voltage and the power exchange (positive when power is received from nearby households and negative otherwise) between the households are shown in Figure 4.14d and Figure 4.14c respectively.

With reference to Figure 4.13b, Figure 4.14a shows that the batteries were able to charge and discharge the surplus and deficit power generation respectively. The charge and discharge operation of the batteries is reflected by the increase and decrease in the SoC respectively as shown in Figure 4.14b. The battery powers were observed to be within ±120 W and the battery SoCs were observed to vary between 20% and 80%. This verified the effectiveness of the algorithm proposed for coordinating the operation of the batteries while satisfying the battery operational constraints, i.e. maintaining the battery charge and discharge power within ±120 W and SoC between 20% and 80%.

Figure 4.14c shows the power exchange between the households. As shown in Figure 4.14c, deficit power was received by H2 from H0 between 3 h and 9 h when the battery SoC in H2 was equal to 20%. Surplus power generation in H0 was shared with H1 and H2 in other operating periods when the battery SoC in H0 was approaching 80%. This verified that the algorithm proposed allows power exchange between the households in the solar nano-grid while meeting the supply-demand balance. The results also confirmed the advantages

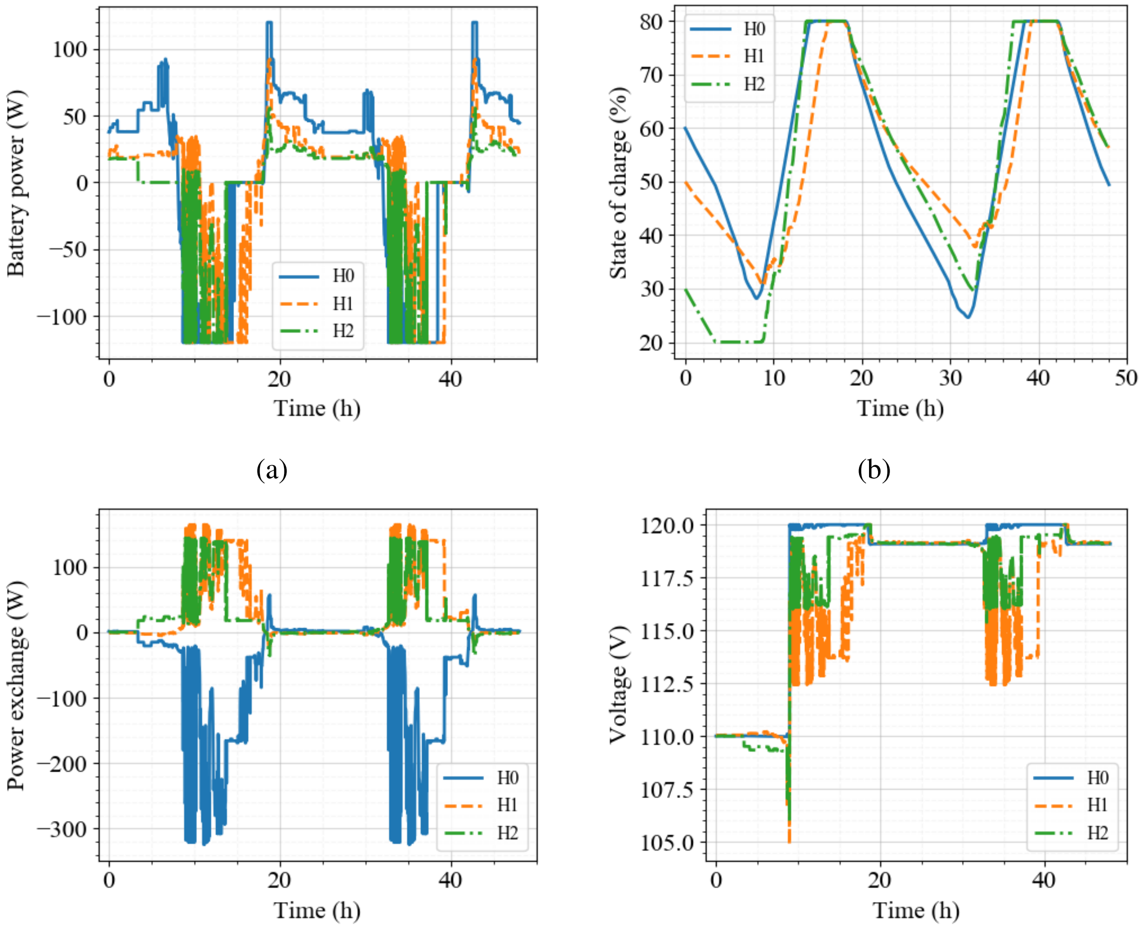

(a) (b)

(c) (d)

Figure 4.14: Power management performance of the algorithm proposed (a) battery charge and discharge power, (b) battery SoC, (c) power exchange between households and (d) distribution line voltage.

of interconnecting households in the solar nano-grid that households tend to share the energy resources with each other thereby increasing the availability of power supply for productive use.

Figure 4.14d shows the distribution voltage profile of the households during power exchange. As shown in Figure 4.14d, the voltages were within the desired range of between 100 V and 120 V. This shows that the algorithm proposed also satisfies the voltage constraint of the solar nano-grid.

Comparison between the Algorithm Proposed and the Traditional Approach

The simulation in the previous subsection was repeated by using the traditional approach in order to verify the effectiveness of the algorithm proposed for minimising the power loss. Table 4.4 compares the total energy loss results from the two methods.

Table 4.4: Comparison of energy loss results between the centralised control algorithm and traditional approach.

	Traditional	**Proposed**
Battery loss (Wh)	18.98	**18.44**
Distribution line loss (Wh)	98.01	**97.45**
FPC loss (Wh)	2644.31	**2644.31**
Total energy loss (Wh)	**2761.3**	**2760.2**

As shown in Table 4.4, the battery and distribution line losses for the algorithm proposed were lower than those for the traditional approach, verifying the effectiveness of the algorithm proposed for minimising the power losses. The algorithm proposed and the traditional approach had the same FPC loss (3.57) due to the use of the same load demand profiles for both algorithms during simulation. FPC losses accounted for the majority of the energy losses in the solar nano-grid, followed by distribution line losses and then the battery losses. This shows that neglecting the FPC loss can significantly affect the operation of the solar nano-grid. The results in Table 4.4 also suggests that the real power loss problem of solar nano-grids lies with the design of power electronics converters, in this case the FPCs. Much research is therefore required to improve the efficiency of FPCs (which are relative new in literature) while at the same time making them affordable if reasonable FPC losses are to be obtained in solar nano-grids. A Python program has been developed in this research as shown in Figure 3.18 which can be used for this purpose.

On average, both control methods had the same utilisation of the energy generated from the solar panels as reflected in the SoC obtained at the end of the 48 h simulation as shown in Figure 4.15. This further verified the consistency in the results of the algorithm proposed when compared to the traditional method.

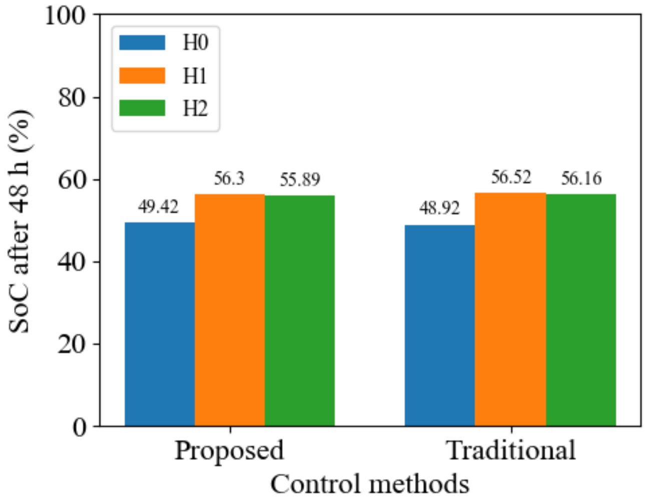

Figure 4.15: Battery state of charge after 48 h when the initial battery SoCs for H0, H1 and H2 were respectively (a) 60%, 50% and 30%, and (b) when the initial SoCs were all the same at 50%.

4.4 Summary

This chapter considered the following research question:

How can the power losses of the star solar nano-grid configuration be quantified and minimised?

Quantification of the power losses of the solar nano-grid with a star configuration was carried out in this chapter and a novel centralised control algorithm was developed to minimise the solar nano-grid power losses. The key contribution to knowledge made in this chapter was through the development of the centralised control algorithm which consisted of two new algorithms, the FLIA and FVIA, which solved the two sub-problems of the formulated power loss optimisation problem (in Chapter 3), i.e. the OBDP and OCFP respectively. The FLIA solved the OBDP by finding battery charge or discharge currents which satisfied the equal incremental power loss principle as described in Subsection 4.2.1. The FVIA solved the OCFP by solving a system of linear distribution current equations for distribution voltages corresponding to the output battery currents from the FLIA as described in Subsection 4.2.2. The output distribution voltages from the FVIA were the solutions to the power loss optimisation problem of the solar nano-grid.

A contribution to knowledge was also made in this chapter through the development of decentralised solar power curtailment and load shedding procedures which required local information to be implemented as described in Subsection 4.2.3.

The performance of the centralised control algorithm proposed was verified through various simulation case studies while comparing the results to the existing traditional control approach [46]. The following were noted from the simulation results:

- The algorithm proposed converged within three iterations regardless of the number of households in the solar nano-grid, provided that the batteries neither charged nor discharged at maximum power. This suggested that the algorithm proposed was computationally efficient.
- The number of iterations grew exponentially with the increase in the number of households when any one of the batteries in the solar nano-grid either charged or discharged with maximum power.
- The algorithm proposed was scalable with verified capability to minimise power losses of a solar nano-grid with 100 households.
- The FPC losses in the solar nano-grid were more than 20 times higher than the distribution line losses and more than 100 times higher than the battery losses.

The main advantage of the algorithm proposed over the existing traditional approach [46] is that the former is accurate, computationally efficient and easily scalable to minimise power losses of solar nano-grids with finite number of households.

The main drawback of the algorithm proposed is that it requires a single agent to implement it, making the algorithm susceptible to single points of failure. In addition, the application of the algorithm proposed is limited to a solar nano-grid with a few number of households in order to reduce the cost, storage and computational requirements of the single agent.

In the next chapter, a distributed control algorithm will be presented, which addresses the limitations of the centralised algorithm presented in this chapter.

Chapter 5

A Quasi-Consensus Based Distributed Control Algorithm for Power Loss Minimisation in Solar Nano-Grids

In Chapter 4, the power loss problem was solved using the equal incremental loss principle given by the Fast Lambda Iteration Algorithm (FLIA) in (4.5) and (4.10), and the Fast Voltage Iteration Algorithm (FVIA) given by (4.16). The solution of both the FLIA and the FVIA was obtained in a centralised manner using a single central agent and two-way communication link between every household and the agent. Information such as power generation, load demand, battery State of Charge (SoC) from every household in the solar nano-grid were first collected by the agent via communication links. Then the agent computed the FLIA and the FVIA in order to generate the reference distribution voltages which were dispatched to the Four Port DC-DC Converters (FPCs) at once via the communication links. Despite accuracy in the global optimal decision, the central agent itself is a source of a single point of failure, thus imposes a reliability risk. For a large scale and dynamic solar nano-grid which is often characterised by frequent (dis)connections of households, heavy computation burden and disruptions in operation is another issue. The centralised control algorithm needs to be updated each time a household is connected or disconnected.

In this chapter, a Quasi-Consensus based Distributed Control Algorithm (QCDCA) is presented. The QCDCA is designed to asymptomatically approximate the solution of the centralised control algorithm in a distributed manner. Thus, the QCDCA may not be optimal as the centralised control algorithm but will help to address the drawbacks of the centralised control algorithm.

5.1 System Description

In this section, the considered distributed control architecture of the solar nano-grid is described. The control architecture is shown in Figure 5.1. It is a multi-agent system which consists of n number of agents, where the number of agents is equal to the number of households. The agents are allowed to communicate with a few of their neighbours, exchanging relevant information via communication links while individually and asymptotically estimating the optimal solution of the centralised algorithm presented in Chapter 4.

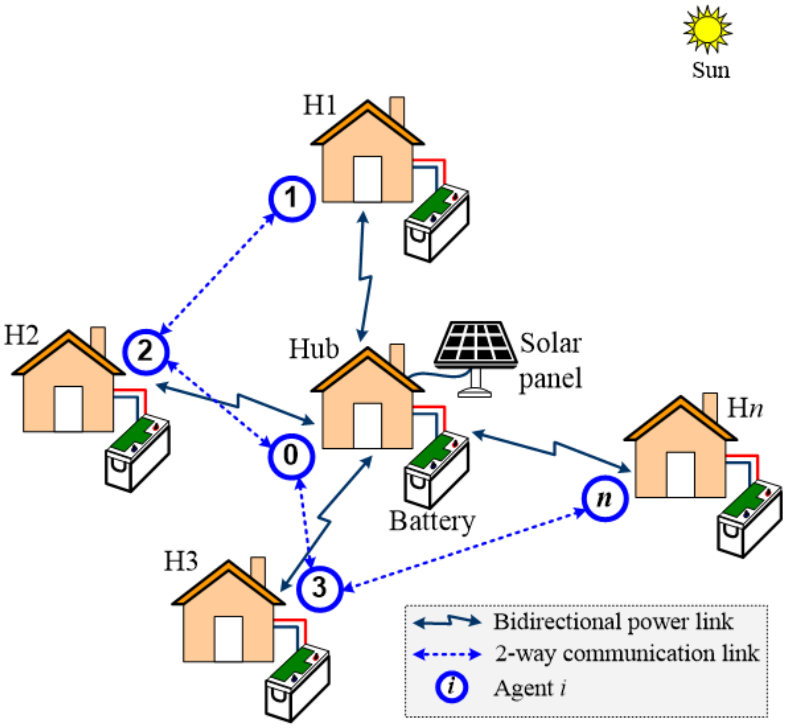

Figure 5.1: The considered distributed control architecture.

In this chapter and the present research, only the design of the updating rule which allows the agents to asymptomatically solve the power loss problem through information exchange with their neighbours is presented. The information exchange between the agents is considered to be perfect with no cyber security issues and loss of information. The communication between the agents is also considered to be synchronised [198]: at every time, each agent triggers information exchange with all of its neighbouring agents simultaneously to update its local scalar state, implying that fastest communication links are considered.

5.2 The Proposed Quasi-Consensus Based Distributed Control Algorithm

This section outlines in more depth the designed QCDCA for addressing the power loss problem formulated in Chapter 3, in particular the Optimal Battery Dispatch Problem (OBDP) and Optimal Current Flow Problem (OCFP).

In Chapter 4, the OBDP and the OCFP were solved in a centralised manner using the FLIA and the FVIA respectively. The FLIA was used to achieve the minimum power loss condition given by the equal incremental loss principle which states that $\lambda = \lambda_i$ for all $i = 0, 1, \ldots, n$. The FVIA was used to solve the current flow problem given in (3.96). In essence, the FVIA was used to achieve the law of conservation of current. According to Figure 3.36, the law can be stated as follows: the distribution currents $i_{dc,i}$ are balanced as given in (3.84) if the DC bus voltages $v_{bus,i}$ estimated from each i-th household are the same, i.e. $v_{bus} = v_{bus,i}$ for all $i = 0, 1, \ldots, n$. Thus, by satisfying these two conditions, $\lambda = \lambda_i$ and $v_{bus} = v_{bus,i}$ for all $i = 0, 1, \ldots, n$, power losses of the solar nano-grid were minimised.

In this chapter, the $\lambda = \lambda_i$ and $v_{bus} = v_{bus,i}$ for all $i = 0, 1, \ldots, n$ conditions were achieved in a distributed manner by allowing the agents to exchange the incremental loss and voltage information with their neighbours. Figure 5.2 shows the schematic diagram of the QCDCA proposed, which is based on the solution framework in Figure 3.37. Unlike the centralised control algorithm in Figure 4.2, the inputs to the QCDCA are the battery SoC SoC_i, power generation $P_{pv,i}$, load demand $P_{L,i}$, and distribution line resistance $R_{dc,i}$, which are all local to a particular household. Where a household does not have solar panels, the power generation input is zero.

The algorithm proposed consists of two algorithms, Incremental Loss Consensus Al-

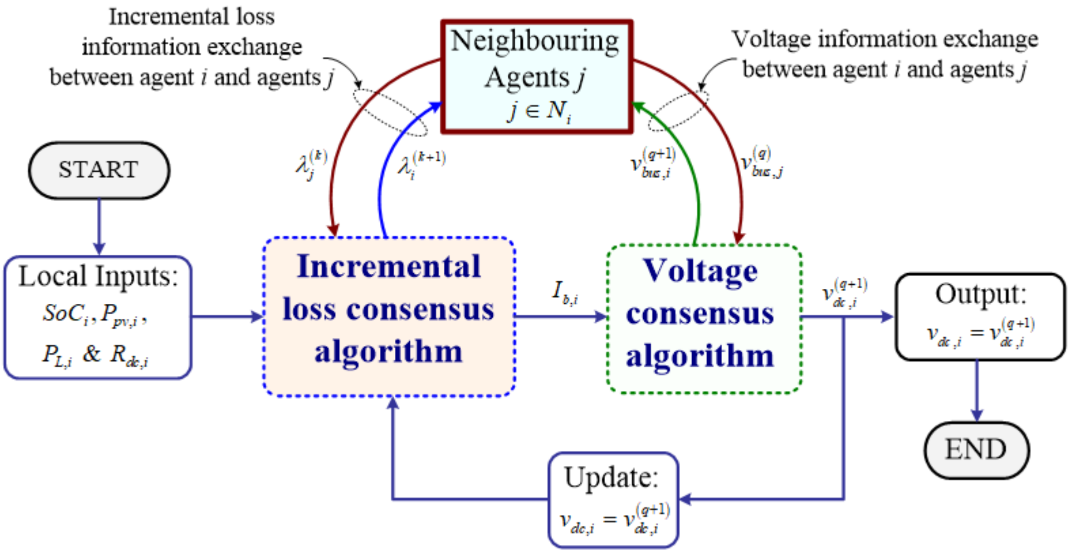

Figure 5.2: Schematic diagram of the quasi-consensus based distributed control algorithm proposed.

gorithm (ILCA) and Voltage Consensus Algorithm (VCA) running sequentially. The ILCA allows the agents to reach consensus on the common λ, thus solving the OBDP. The VCA allows the agents to reach consensus on the common v_{bus}, thus solving the OCFP to provide the optimal distribution voltage outputs. The challenge, however, was on how to make the agents discover the supply-demand mismatch current, ΔI given by (4.11) and the current balance, $I_{sum} = 0$ given by (3.84), which are a pre-requisite for successful achievement of the $\lambda = \lambda_i$ and $v_{bus} = v_{bus,i}$ conditions in a distributed manner. To obtain the $\Delta I = 0$ and $I_{sum} = 0$ using the QCDCA, one agent which is hereafter referred to as a leader agent (for easy reference) was chosen to have access to ΔI_i and $i_{dc,i}$ information from all the households in the solar nano-grid. The other n-1 agents, hereafter referred to as follower agents did not have to compute for ΔI and I_{sum}. Thus, on one hand the leader agent behaved like a centralised controller when accessing the ΔI_i and $i_{dc,i}$ information from all the households in the solar nano-grid and on the other hand, it behaved like a distributed controller when handling the $\lambda = \lambda_i$ and the $v_{bus} = v_{bus,i}$ conditions. For this reason, the algorithm proposed was referred to as quasi and offers advantages of both the centralised and distributed control approaches in terms of accuracy and low computation burden for large scale solar nano-grids. The next subsections present in more depth the implementation of the ILCA and VCA.

5.2.1 The Incremental Loss Consensus Algorithm

The main objective of the ILCA proposed was to allow an i-th agent to reach consensus on the common λ by using its local λ_i information and the λ_j information from its neighbouring agents j, $j \in N_i$. To achieve consensus on the common λ, each i-th agent updated its λ_i by running the following ILCA proposed

$$\lambda_i^{(k+1)} = \sum_{j=1}^{n} d_{ij}\lambda_j^{(k)} + \varepsilon \Delta I^{(k)}, \quad \varepsilon \in [0, e_\lambda] \tag{5.1}$$

where k is the iteration number, $\lambda_i^{(k)}$ is the incremental loss of agent i at k-th iteration, $\lambda_i^{(k+1)}$ is the update of $\lambda_i^{(k)}$ with respect to $\lambda_j^{(k)}$ from neighbouring agents j, d_{ij} is defined in (B.1), ΔI is defined in (4.11) and e_λ is the convergence factor which is defined in (4.10).

Since the follower agents did not have to compute for ΔI, substituting $\varepsilon = 0$ in (5.1) therefore represented the ILCA for the follower agents and for the leader agent otherwise. Each agent i updated its optimal battery charge and discharge power at every k-th iteration by substituting the $\lambda_i^{(k+1)}$ obtained from (5.1) in (4.8). The local battery charge and discharge current was updated using (4.9) after updating the battery charge and discharge power. Based on (4.8), (4.9) and (5.1), the optimal charge and discharge powers and currents of the batteries which minimises the power losses in the solar nano-grid were therefore obtained in a distributed manner. Convergence and optimality of the algorithm proposed was proved as presented in the next subsections.

Convergence of the Incremental Loss Consensus Algorithm

Denoting the leader agent by index 0, convergence of the ILCA (5.1) was analysed by first rewriting it in matrix form as follows

$$\lambda^{(k+1)} = \mathbf{D}\lambda^{(k)} + \mathbf{E}^{(k)} \tag{5.2}$$

where $\lambda^{(k)} = \left[\lambda_0^{(k)}, \lambda_1^{(k)}, \ldots, \lambda_n^{(k)}\right]^T$, $\mathbf{E}^{(k)} = [\varepsilon \Delta I^{(k)}, 0, \ldots, 0]^T$ and $\mathbf{D} = (d_{ij})n \times n$ is a doubly stochastic matrix which describes the information exchange on a communication graph as explained in Appendix B.

Then, pre-multiplying (5.2) by $\mathbf{1}^T$ and taking limits as $k \to \infty$ on both sides of (5.2), the following expression was obtained as follows

$$\lim_{k\to\infty} \mathbf{1}^T \lambda^{(k+1)} = \lim_{k\to\infty} \mathbf{1}^T \mathbf{D}\lambda^{(k)} + \lim_{k\to\infty} \mathbf{1}^T \mathbf{E}^{(k)} \tag{5.3}$$

Noting that $\mathbf{1}^T\mathbf{D} = 1$ because $\mathbf{D}$ is doubly stochastic and that at equilibrium, $\Delta I = 0$ making $\mathbf{E}^{(k)} = 0$, (5.3) simplified to the following expression

$$\lim_{k\to\infty} \mathbf{1}^T \lambda^{(k+1)} = \lim_{k\to\infty} \mathbf{1}^T \lambda^{(k)} \tag{5.4}$$

That is, as $k \to \infty$, the equal incremental loss principle, $\lambda_i(\infty) = \lambda_j(\infty) = \lambda$ was always achieved and that the ILCA converges. The ILCA can be initialised using (4.4) and (4.11) as follows

$$\begin{cases} \Delta I^{(0)} = 0 \\ I_{b,i}^{(0)} = I_{D,oi} \\ \lambda_i^{(0)} = 2\alpha_{oi} I_{b,i}^{(0)} + \beta_{oi} \end{cases} \tag{5.5}$$

Implementation of the Incremental Loss Consensus Algorithm

Figure 5.3 shows the flowchart for implementing the ILCA proposed for each agent i. The algorithm uses local information and the information about the incremental loss from the neighbouring agents j to generate the optimal battery currents. At every k-th iteration, only the leader agent is allowed to compute and update the current mismatch $\Delta I^{(k)}$ as shown in Figure 5.3. The algorithm proposed is somewhat similar to the algorithm reported in [199] for economic dispatch problems. However, they are different because the ILCA proposed aims to minimise the power losses of the solar nano-grid by coordinating the operation of the batteries whereas [199] aims to minimise the cost of operating parallel generators in a conventional AC power system.

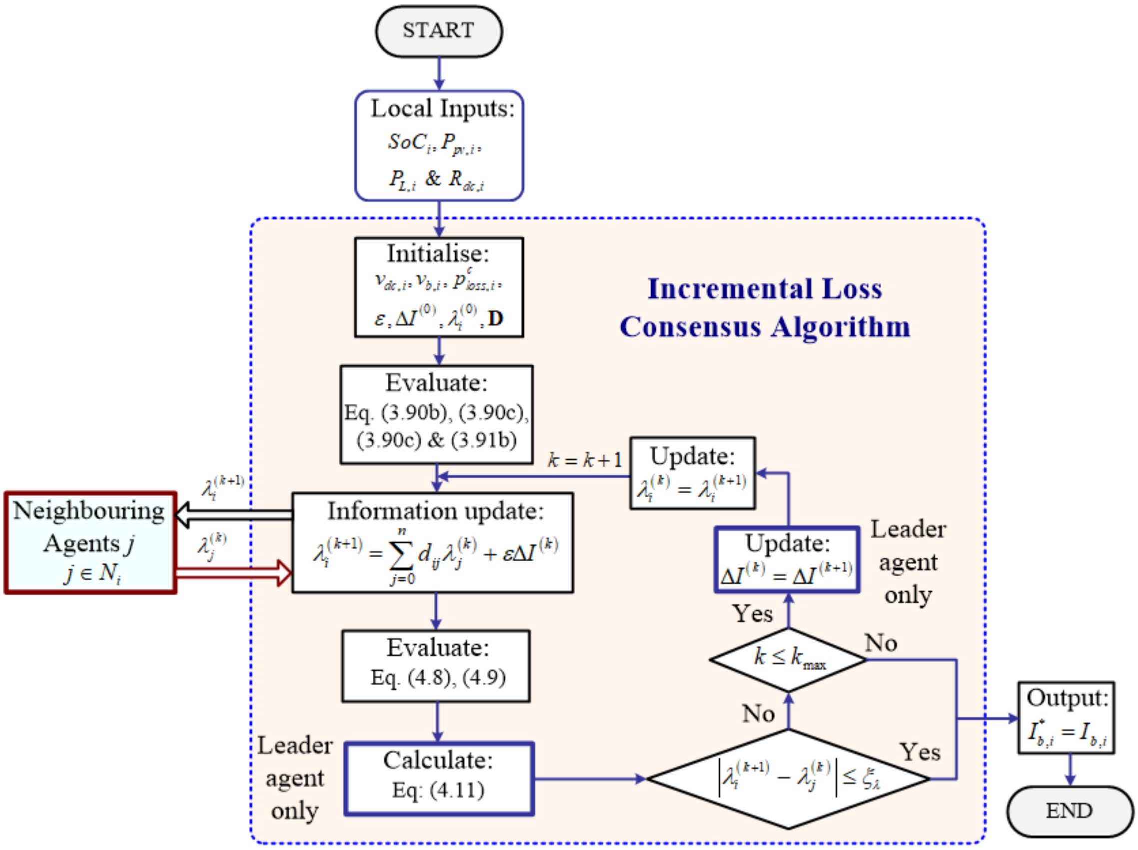

Figure 5.3: Implementation of the ILCA proposed for every agent i in the solar nano-grid.

5.2.2 The Voltage Consensus Algorithm

The main objective of the VCA proposed was to allow each agent in the solar nano-grid to reach consensus on the common v_{bus}. Each agent updated its local $v_{bus,i}$ by running the following VCA proposed

$$v_{bus,i}^{(q+1)} = \sum_{j=0}^{n} \left(d_{ij} v_{bus,j}^{(q)} \right) - \varepsilon I_{sum}^{(q)}, \quad \varepsilon \in [0, e_v] \tag{5.6}$$

where q is the iteration number, $v_{bus,i}^{(q)}$ is the bus voltage estimated by i-th agent at q, $v_{bus,i}^{(q+1)}$ is the update of $v_{bus,i}^{(q)}$ with respect to $v_{bus,j}^{(q)}$ from neighbouring agents j, d_{ij} is given by (B.1), I_{sum} is given by (3.84) and e_v is a small positive convergence factor which determines the convergence of the VCA.

Similar to the ILCA, substituting $\varepsilon = 0$ in (5.6) represented the VCA for the follower agents and substituting $\varepsilon = e_V$ represented the VCA for the leader agent. Taking the voltage limits (3.93e) into account, every agent updated its distribution voltage after every iteration as follows

$$v_{dc,i}^{(q+1)} = \begin{cases} v_{bus,i}^{(q+1)} - R_{dc,i}i_{dc,i}, \text{ if } v_{min,i}^{dc} \leq v_{bus,i}^{(q+1)} - R_{dc,i}i_{dc,i} \leq v_{max,i}^{dc} \\ v_{max,i}^{dc}, \text{ if } v_{bus,i}^{(q+1)} - R_{dc,i}i_{dc,i} > v_{max,i}^{dc} \\ v_{min,i}^{dc} \text{ otherwise.} \end{cases} \tag{5.7}$$

Due to the voltage limits in (5.7), each agent computed a new distribution line current as follows

$$i_{dc,i}^{(q+1)} = \frac{v_{bus,i}^{(q+1)} - v_{dc,i}^{(q+1)}}{R_{dc,i}} \tag{5.8}$$

Thereafter the leader agent collected all the $i_{dc,i}^{(q+1)}$ from the agents to calculate I_{sum} (3.84). Convergence of the VCA was achieved when I_{sum} was equal to zero.

Convergence of Voltage Consensus Algorithm

Similar to the ILCA, denoting the leader agent by index 0, convergence of the VCA was analysed by rewriting (5.6) in matrix form as follows

$$\mathbf{V_{bus}}^{(q+1)} = \mathbf{D}\mathbf{V_{bus}}^{(q)} - \mathbf{H}^{(q)} \tag{5.9}$$

where $\mathbf{V_{bus}}^{(q+1)} = \left[v_{bus,0}^{(q+1)}, \ldots, v_{bus,n}^{(q+1)}\right]^T$, $\mathbf{D} = (d_{ij})n \times n$ is the doubly stochastic matrix and $\mathbf{H}^{(q)} = [-\varepsilon I_{sum}^{(q)}, 0, \ldots, 0]^T$.

Then, pre-multiplying (5.9) by $\mathbf{1}^T$ and taking limits as $q \to \infty$ on both sides of (5.9), the following expression was obtained

$$\lim_{q\to\infty} \mathbf{1}^T\mathbf{V_{bus}}^{(q+1)} = \lim_{q\to\infty} \mathbf{1}^T\mathbf{D}\mathbf{V_{bus}}^{(q)} + \lim_{q\to\infty} \mathbf{1}^T\mathbf{H}^{(q)} \tag{5.10}$$

Since $\mathbf{1}^T\mathbf{D} = 1$ and that at equilibrium, $I_{sum} = 0$ making $\mathbf{H}^{(q)} = 0$, (5.10) simplified to the following expression

$$\lim_{q\to\infty} \mathbf{1}^T\mathbf{V_{bus}}^{(q+1)} = \lim_{q\to\infty} \mathbf{1}^T\mathbf{V_{bus}}^{(q)} \tag{5.11}$$

That is, as $q \to \infty$, all the bus voltages converges as, $v_{bus,i}^{(\infty)} = v_{bus,j}^{(\infty)} = v_{bus}$ for any initial values of the DC bus voltage. Thus, VCA can be initialised as follows

$$\begin{cases} I_{sum}^{(0)} = 0 \\ v_{bus,i}^{(0)} = v_{nom} \end{cases} \tag{5.12}$$

where v_{nom} is the nominal distribution voltage.

Implementation of the Voltage Consensus Algorithm

Figure 5.4 shows the flowchart for implementing the VCA for each agent i. The inputs to the algorithm are the local parameters; $I_{D,i}$, $I_{b,i}^{*}$ and $R_{dc,i}$. The output from the algorithm is the local distribution voltage, $v_{dc,i}$, which is obtained using the local inputs and the exchange of DC bus voltage information with neighbouring agents j.

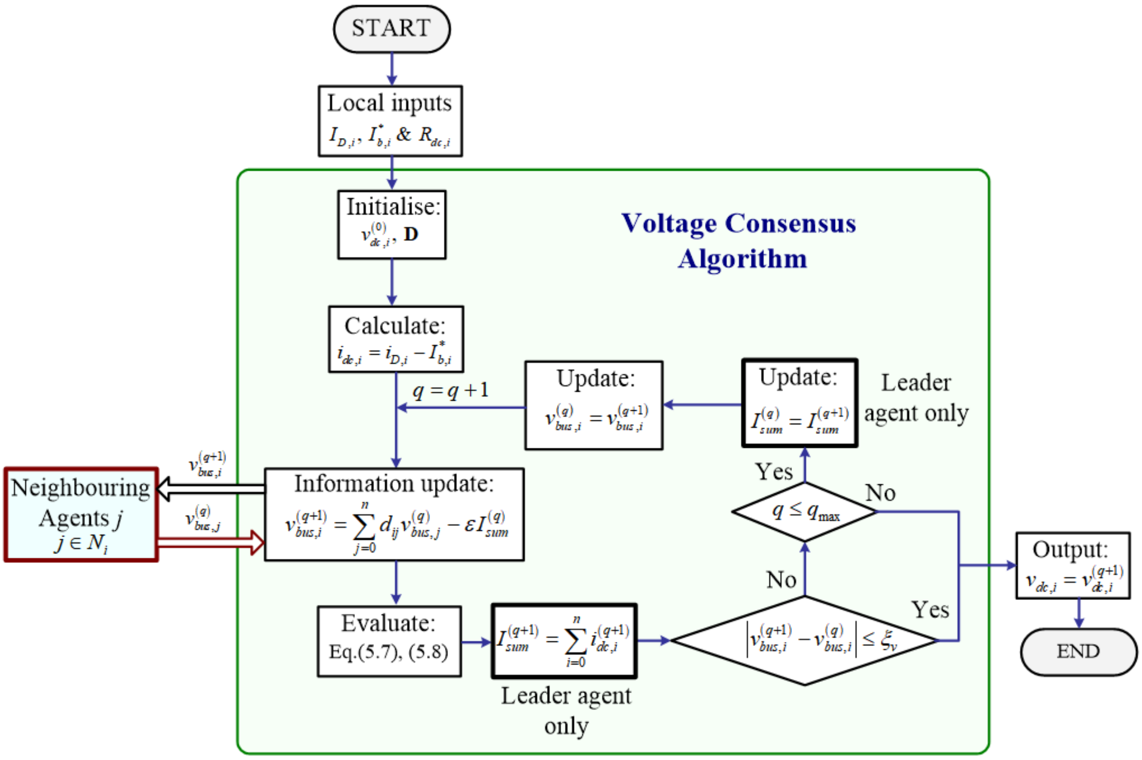

Figure 5.4: Implementation of the VCA proposed for every agent i in the solar nano-grid.

5.2.3 Implementation of the Quasi-Consensus Based Distributed Control Algorithm Proposed

Figure 5.5 shows the flowchart for implementing the QCDCA proposed. The inputs to the algorithm are battery SoC, power generation, load demand and distribution line resistance, which are local to every agent *i*. The ILCA and VCA are implemented in a quasi-distributed manner as shown in Figure 5.3 and Figure 5.4 respectively. The implementation of the solar panel and load manager, and the updates of the battery voltage and SoC are handled in a decentralised manner like the centralised algorithm in Subsection 4.2.4. The final output from the QCDCA is the local distribution line voltage, $v_{dc,i}$, which can be sent to the low level control to change the operating state of the solar nano-grid.

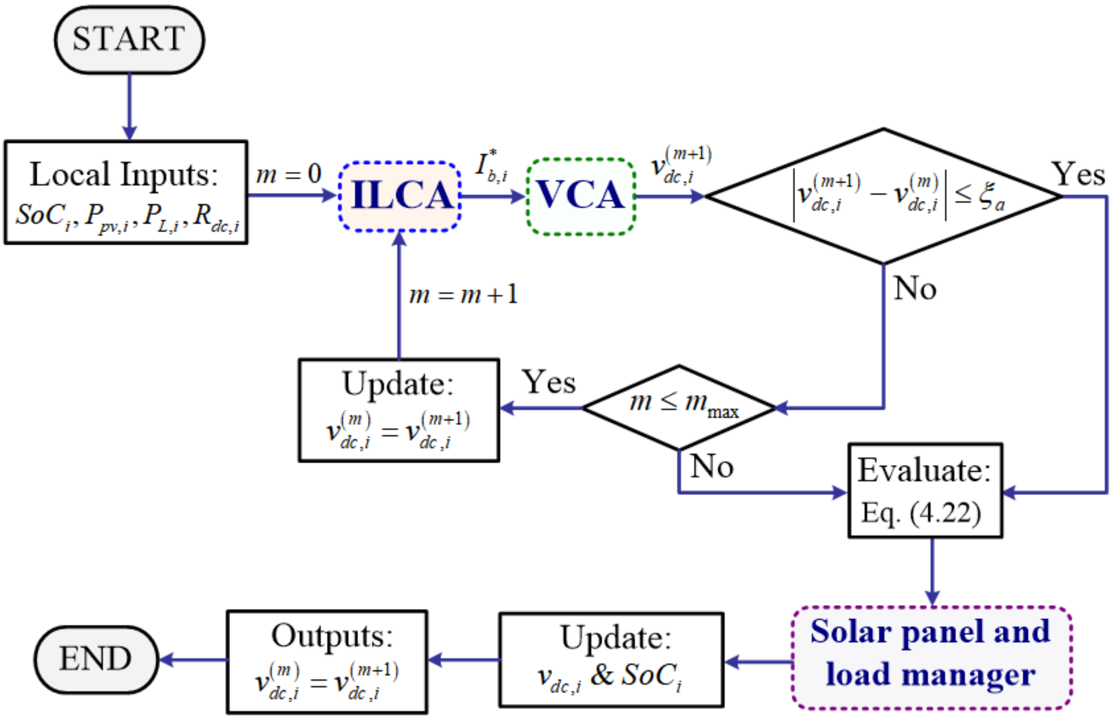

Figure 5.5: Flowchart for implementing the QCDCA proposed for each agent *i*.

5.3 Simulation Results and Discussion

In this section, the effectiveness of the QCDCA proposed for asymptotically approximating the solution of the centralised algorithm is presented. The same test solar nano-grid considered for the centralised algorithm, which is shown in Figure 4.7 is also used in this section. This is re-shown in Figure 5.6 in order to highlight the position and labels of the agents. The considered communication topologies for the connection of the agents are shown in Figure 5.7. Agent 0 is the leader agent for topology *a* while agent 2 is the leader agent for topology *b*. The simulation parameters and initial conditions of the solar nano-grid are the same ones given in Table 4.1.

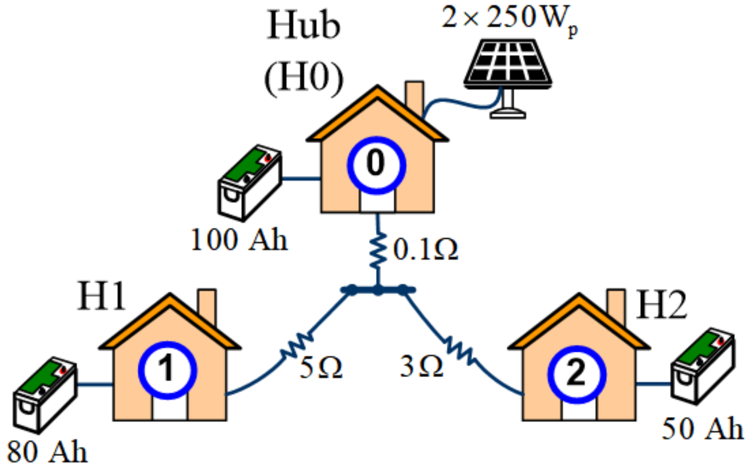

Figure 5.6: A test solar nano-grid for simulation purposes.

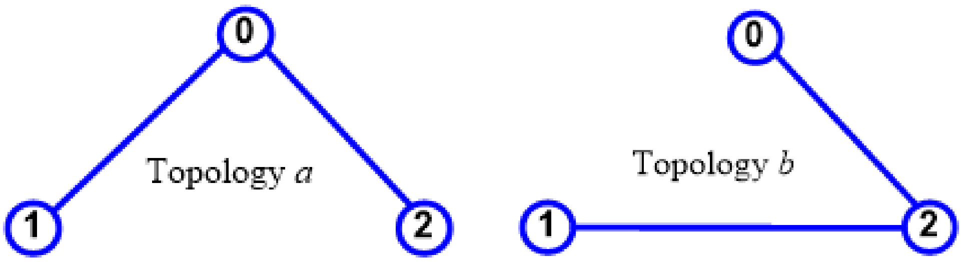

(a)

(b)

Figure 5.7: Connection of the agents in Figure 5.6 using communication (a) topology *a* where agent 0 is the leader agent, agents 1 and 2 are follower agents and (b) topology *b* where agent 2 is the leader agent, agents 0 and 1 are follower agents .

5.3.1 Convergence Analysis of Incremental Loss Consensus Algorithm

To verify whether the ILCA converges or not, two case studies were considered. The first case study considered the communication topology *a* while the second cased study considered the communication topology *b*. In both case studies the impact of convergence factor,

e_λ on the convergence of the ILCA was investigated. The power values and other derived simulation parameters for each household in Figure 5.6 are given in Table 4.2.

Case Study 1: with communication topology *a*

Figure 5.8 shows the convergence of the ILCA for $e_\lambda = 0.8$ W/A^2 and $e_\lambda = 10$ W/A^2 with topology a. As shown in the figure, the larger the value of e_λ, the faster the ILCA converges.

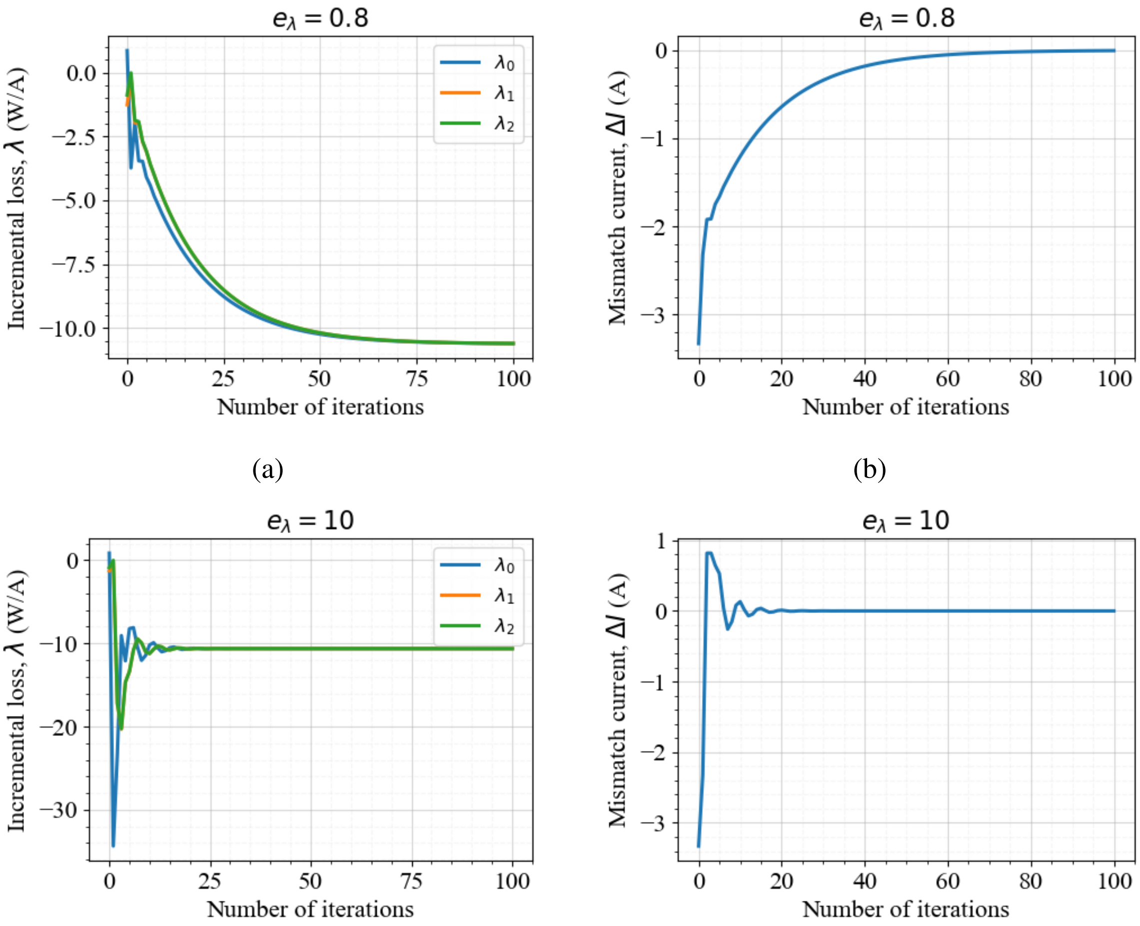

(a) (b)

(c) (d)

Figure 5.8: Convergence speed of the ILCA for $e_\lambda = 0.8$ W/A^2 and $e_\lambda = 10$ W/A^2 with the communication topology a.

It was noted from Figure 5.8 that convergence was achieved with the ILCA proposed and that all the agents were able to reach consensus on the common λ. The common λ was found to be $\lambda = \lambda_0 = \lambda_1 = \lambda_2 = -10.59$ W/A as shown in Figure 5.8c. It was verified that the obtained $\lambda = -10.59$ W/A was equal to the λ value, which was obtained using the centralised based FLIA in Chapter 4. That suggested that the ILCA proposed effectively estimated the solution of the centralised algorithm. Further, it was noted that larger values of e_λ caused the ILCA to be unstable (i.e. to oscillate about the final value) as shown in Figures 5.8c and 5.8d. To always ensure stability, small values of e_λ less than 1 were found to be appropriate, though the convergence speed was delayed as shown in Figures 5.8a and 5.8b.

Case Study 2: with communication topology *b*

The impact of using communication topology b on the convergence of the ILCA proposed was investigated in this case study. Repeating case study 1 with communication topology b, the results shown in Figure 5.9 were obtained. Comparing Figure 5.8 to Figure 5.9, it was observed that in both figures, the algorithm converged to the same equilibrium values at almost the same number of iterations. This showed that convergence of the ILCA proposed is achieved even with a different communication topology.

5.3.2 Convergence Analysis of the Voltage Consensus Algorithm

In this subsection, the convergence of the VCA proposed was investigated for different values of e_v and communication topologies. Distribution line currents corresponding to $\lambda = -10.59$ W/A were obtained in Chapter 4 as -2.545 A, 1.0 A and 1.544 A for H0, H1 and H2 respectively. These were used in this subsection to analyse the convergence of the VCA proposed.

Case Study 1: with communication topology *a*

The impact of different values of e_v, e.g. $e_v = 0.5$ V/A and $e_v = 5$ V/A on the convergence of the VCA using communication topology a was investigated in this case study. Figure 5.10 shows that convergence of the VCA was ensured for both values of e_v.

It was noted, however, that the final value of the DC bus voltage was somewhat dependent on the choice of e_v, with $e_v = 0.5$ V/A providing a DC bus voltage of 107.5 V and $e_v = 5$ V/A a voltage of 108.5 V. Nevertheless, small values of e_v less than 1 were observed to maintain stability of the algorithm most of the time for different distribution line currents.

Overall, Figure 5.10 demonstrates how the VCA proposed can allow the agents to reach

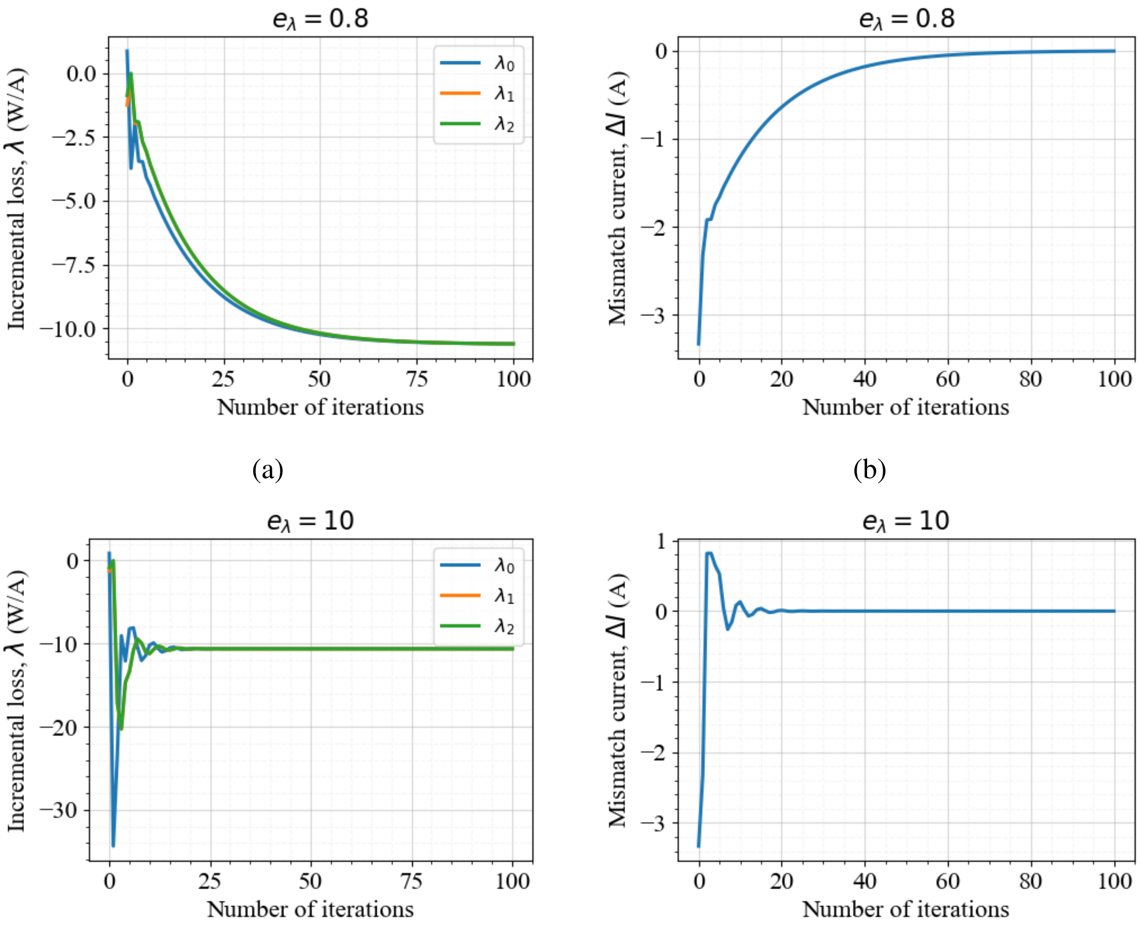

(a) (b)

(c) (d)

Figure 5.9: Convergence speed of the ILCA for $e_\lambda = 0.8$ W/A^2 and $e_\lambda = 10$ W/A^2 with the communication topology *b*.

consensus on the common DC bus voltage while satisfying the law of conservation of current, i.e. $I_{sum} = 0$ (3.84) in a distributed manner.

Case Study 2: with communication topology *b*

In this case study, the communication topology *b* was considered and the simulation of the previous case study was repeated.

Figure 5.11 demonstrates that the VCA proposed converges even with a different communication topology. The final values of the DC bus voltage and mismatch current are equal to those obtained in the previous case study.

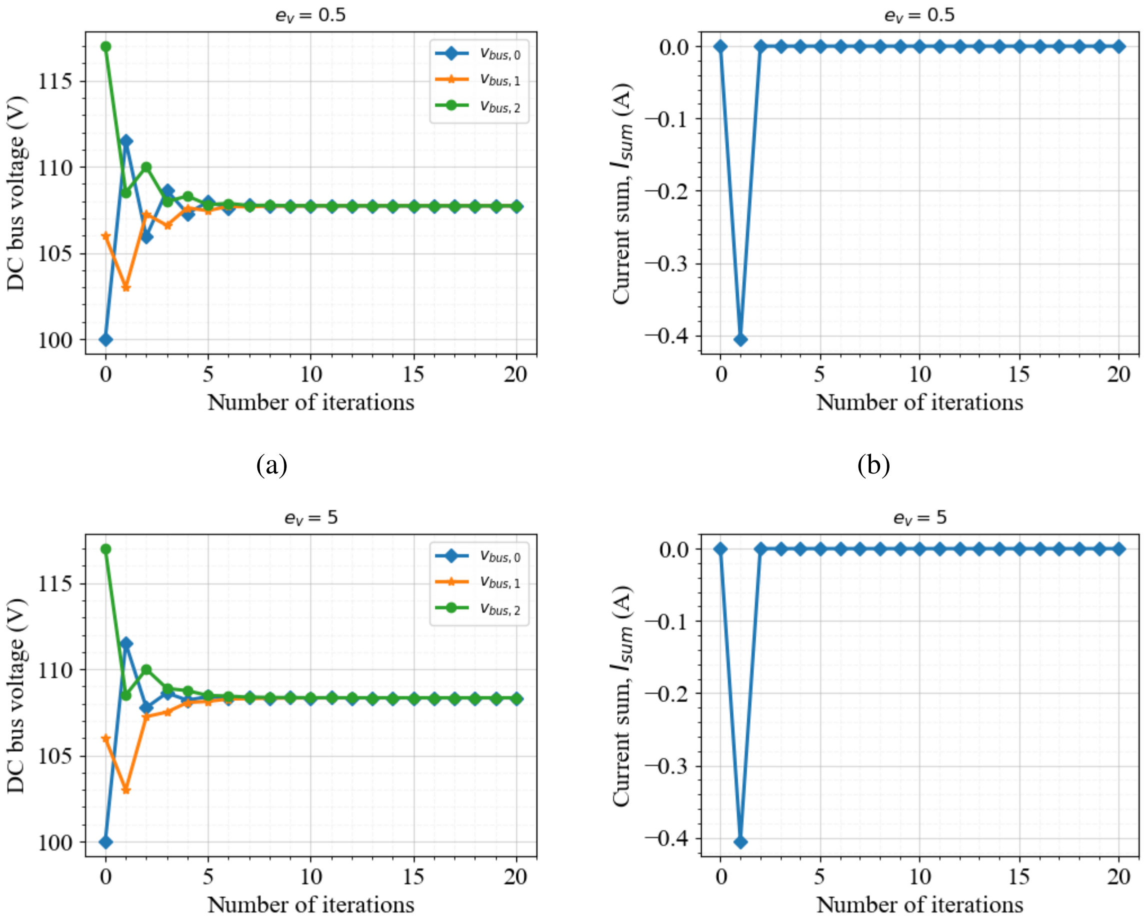

(a) (b)

(c) (d)

Figure 5.10: Convergence speed of the VCA for $e_v = 0.5$ V/A and $e_v = 5$ V/A with the communication topology a.

Convergence Speed of the Quasi-Consensus Based Distributed Control Algorithm

In this subsection, convergence speed of the QCDCA proposed, which consists of the ILCA and VCA is presented. Convergence of the algorithm proposed was investigated by analysing the total number of iterations taken by both the ILCA and VCA to generate the final battery power outputs for different number of households. This analysis is similar in methodology and objective to the one carried out in Subsection 4.3.1 for the centralised control algorithm. Thus, a comparative study where the results of the QCDCA are compared to those of the centralised algorithm is presented. In the first instance, the battery and distribution line parameters used to obtain the results shown in Figure 4.10 were used. In the second instance, the battery and distribution line parameters used to obtain the results shown in Figure 4.11 were

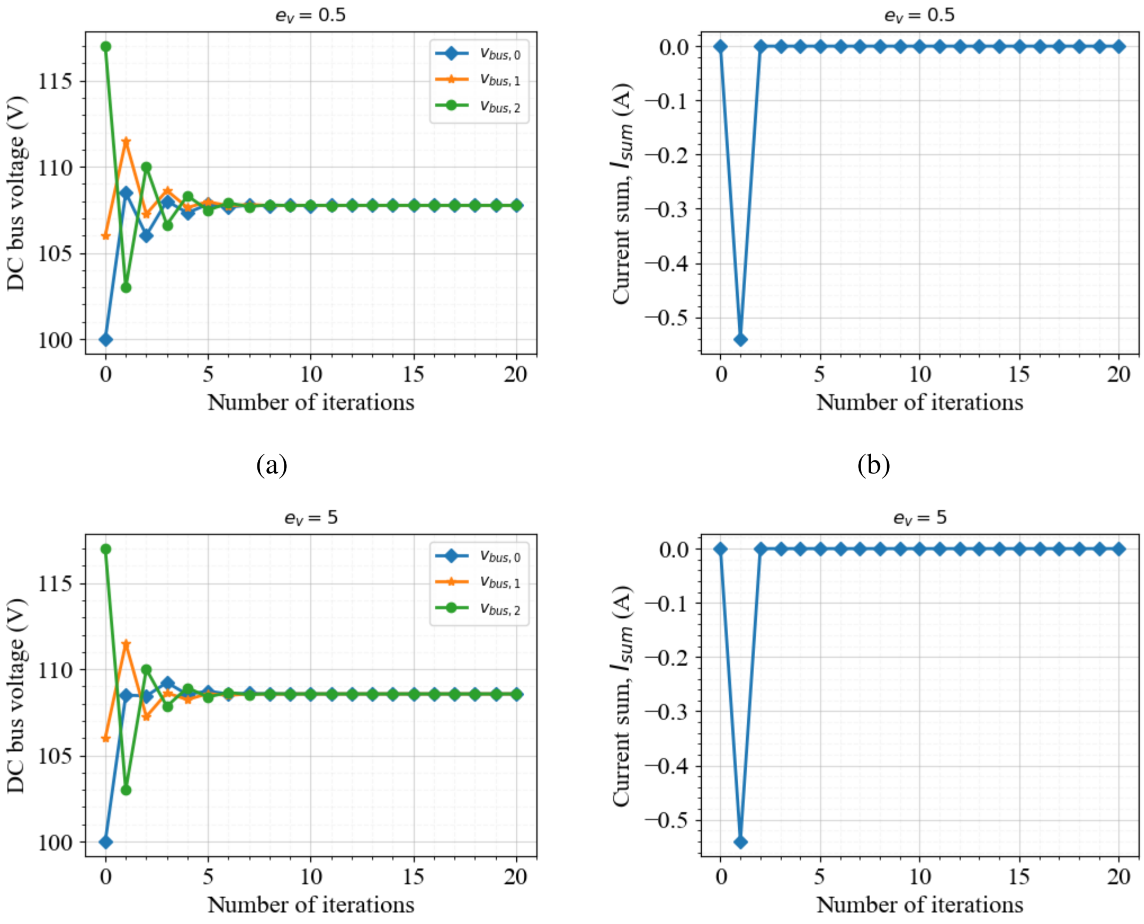

(a) (b)

(c) (d)

Figure 5.11: Convergence speed of the VCA for $e_v = 0.5$ V/A and $e_v = 5$ V/A with the communication topology *b*.

considered. In both instances, communication topology *a* was considered and the values of e_λ and e_v considered were 0.021 W/A^2 and 0.001 V/A respectively.

Figures 5.12 and 5.13 shows the results for the first and second instance respectively. Comparing Figures 5.12 and 5.13 to Figures 4.10 and 4.11 respectively, the following points were noted, that:

- Convergence speeds of both algorithms depended on the operating status of the battery; the number of iterations were low when the batteries charged and discharged with power less than the maximum battery power limit.

- The QCDCA asymptotically approximated the solution of the centralised control algorithm as observed by comparing the battery powers in Figure 4.10b to those in Figure 5.13b. The discrepancy in the result was due to the fact that QCDCA asymptotic-

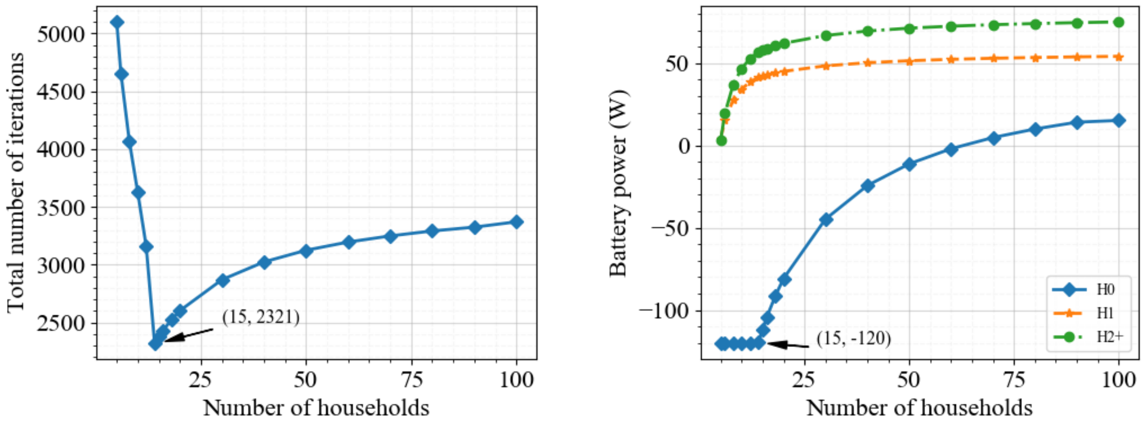

(a)

(b)

Figure 5.12: Showing in (a) the total number of iterations required for the QCDCA to converge and (b) the battery power outputs for 5 to 100 households, where the battery capacities in H1 and H2+ are 80 Ah and 50 Ah respectively, and the distribution line resistances of H1 and H2+ are 5 Ω and 3 Ω respectively.

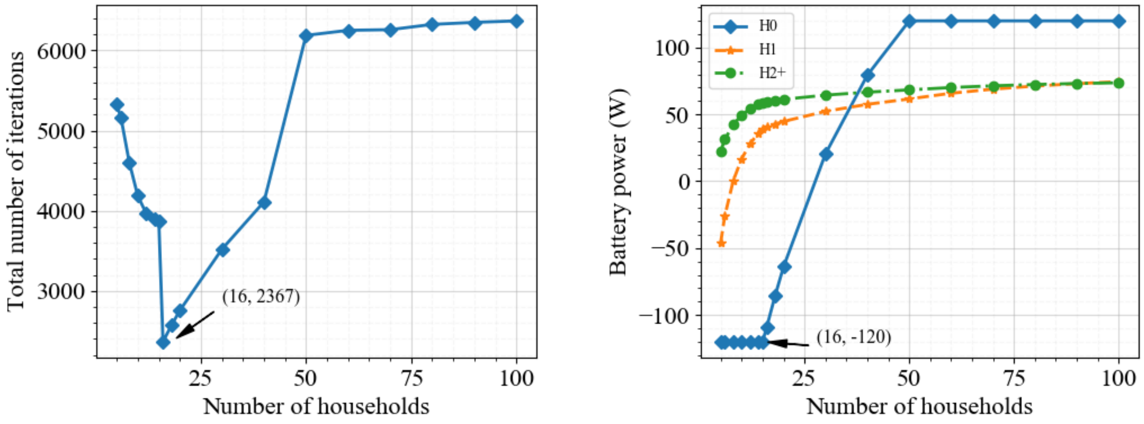

(a)

(b)

Figure 5.13: Showing in (a) the total number of iterations required for the QCDCA to converge and (b) the battery power outputs for 5 to 100 households, where the battery capacities in H1 and H2+ are 56 Ah and 13 Ah respectively, and the distribution line resistances of H1 and H2+ are 5 Ω and 10 Ω respectively.

ally approximated the solution of the centralised algorithm and thus an exact solution was not expected.

- The number of iterations required by the QCDCA were large compared to those of a centralised control algorithm. This was mainly due to the small values of the convergence factor used i.e. $e_\lambda = 0.021$ W/A^2 and $e_v = 0.001$ V/A, which were maintained when obtaining the iterations across the 100 households. It was however noted that, in order to obtain faster iterations, the e_λ and e_v were required to be specifically adjusted for each particular number of households. For example, choosing $e_\lambda = 0.81$ W/A^2 and $e_v = 0.001$ V/A with the simulation parameters of the first instance for up-to 11 households gave the results shown in Figure 5.14, where the total number of iterations were observed to be as low as 48. Overall, the number of iterations for the QCDCA were larger than those for the centralised control algorithm, implying that the centralised control algorithm was faster than the QCDCA.

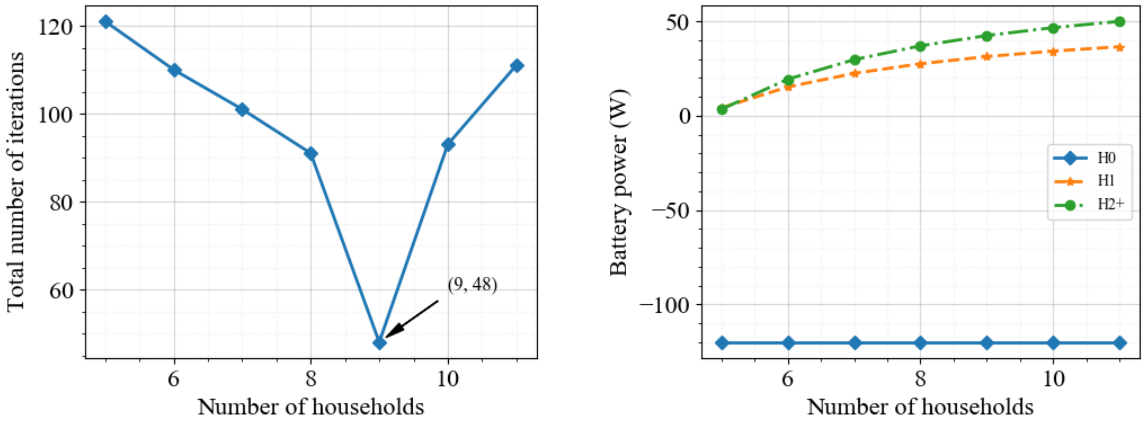

(a)

(b)

Figure 5.14: Showing in (a) the total number of iterations required for the QCDCA to converge and (b) the battery power outputs for 11 households with $e_\lambda = 0.81$ W/A^2 and $e_v = 0.001$ V/A.

5.4 Summary

This chapter considered the following research question:

How to minimise the power losses of a solar nano-grid that has a star configuration and many households?

A novel QCDCA which addresses the research question in a distributed manner was developed and is presented in this chapter. Due to the distributed nature of the QCDCA, limitations of the centralised control algorithm such as heavy computation burden and high storage and processor requirement for a solar nano-grid with many households were reduced.

The key contribution to knowledge in this chapter is through the novel development of the ILCA and VCA which together form the QCDCA developed as described in Section 5.2. Through simulation results, the effectiveness of the QCDCA to minimise power losses in a solar nano-grid with up-to 100 households was verified.

From the results, it was noted that:

- The QCDCA effectively approximated the solution of the centralised control algorithm which was presented in Chapter 4. This suggests that the QCDCA is accurate and is suitable for minimising power losses in a solar nano-grid with multiple households.
- Similar to the centralised control algorithm, the convergence speed of the QCDCA was found to strongly depend on the operating state of the batteries. The speed was fast when all the batteries in the solar nano-grid were neither charged nor discharged with maximum power. In addition, the choice of the convergence factors e_λ and e_v was found to be specific for each number of households. They were to be adjusted for each particular number of households if fast convergence speeds of the QCDCA were to be achieved.

Chapter 6

Distributed State of Charge-based Droop Control Algorithm for Reducing Power Losses in Solar Nano-Grids

In Chapters 3, 4 and 5, the star solar nano-grid configuration where all households in a village are connected to a central hub as shown in Figure 1.4 was considered. The solar nano-grid power loss problem was addressed through optimisation by first formulating it as a mathematical optimisation problem as described in Chapter 3 and then, solving the formulated mathematical optimisation problem using either the centralised or distributed control algorithms, which are presented in Chapter 4 and Chapter 5 respectively.

In this chapter, the hybrid solar nano-grid configuration where some households are connected to their neighbours as shown in Figure 1.8 is considered. The hybrid configuration represents a general configuration which a solar nano-grid can take as it grows in size as indicated in Chapter 1, Section 1.3. Since the hybrid configuration is technically different from the star configuration in terms of their electric circuits, the power loss optimisation problem and control algorithms developed in Chapters 3, 4 and 5 for a star configuration cannot be used to minimise the power losses of the hybrid configuration. Doing so would all together require a new formulation of the power loss optimisation problem and a new design of control algorithms each time the solar nano-grid changes configuration. This is time consuming and impractical given that a solar nano-grid can take on any configuration at any time depending on how frequent new households get connected to the solar nano-grid or old households get disconnected from the solar nano-grid. A general control approach which is independent of a solar nano-grid configuration is required to reduce the power losses.

This chapter presents a novel distributed State-of-Charge (SoC) based droop control algorithm that aims to address the power loss problem of solar nano-grids with arbitrary configurations. The algorithm proposed addresses the power loss problem by reducing the magnitude of current flow in the solar nano-grid through balancing the battery SoCs in a distributed manner. Due to the distributed nature of the algorithm proposed, the algorithm is scalable and resilient to single points of failure. Furthermore, balancing the battery SoCs also avoids overuse of one battery, accelerated battery degradation, reduction of battery capacity and uneven over-charge and over-discharge [105–111]. To implement the algorithm proposed, only local distribution voltage measurements and estimations of the battery SoC are required. Thus, the algorithm proposed is suitable for any kind of a solar nano-grid configuration. Unlike the existing SoC balancing methods which aim to prolong the battery life-time [105–111], the algorithm proposed is unique in the following ways: (1) does not have an off-set voltage in the equation, (2) uses average distribution voltage and battery SoC at every time instant to update the SoC coefficient in a distributed manner and (3) has the control objective of reducing the power losses of the solar nano-grid.

6.1 System Description

Figure 6.1 shows the considered control architecture of the hybrid solar nano-grid configuration.

Similar to the control architecture of the Quasi-Consensus based Distributed Control Algorithm (QCDCA) in Chapter 5, a sparse communication network is employed between (few) neighbouring households in order to allow the agents in every household to exchange the relevant information required to balance the SoC of the batteries in a distributed manner.

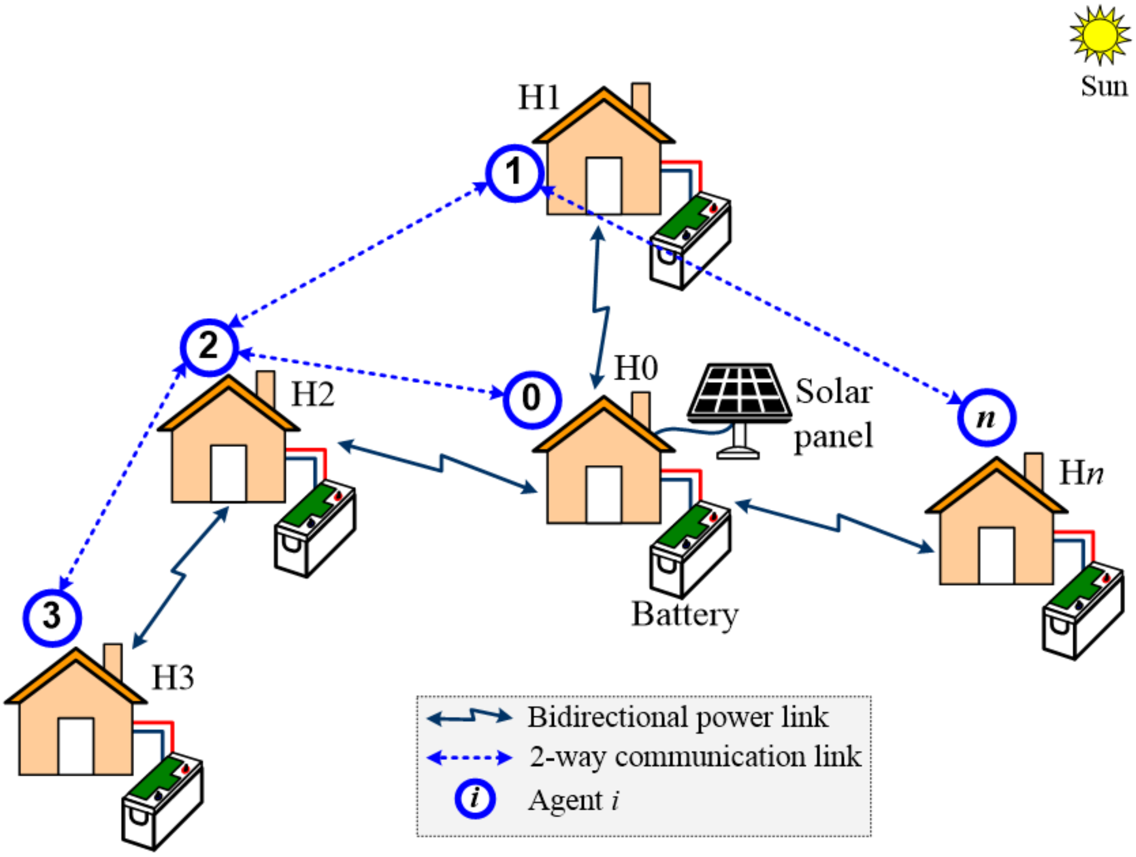

Figure 6.1: Distributed control architecture of the hybrid solar nano-grid configuration.

6.2 The Proposed Distributed State of Charge Based Droop Control Algorithm

This section presents the distributed SoC based droop control algorithm proposed. The idea of the droop algorithm proposed is to adjust the distribution voltage, $v_{dc,i}(t)$ of every household in direct proportion to the SoC of the local battery as follows

$$v_{dc,i}(t) = \alpha_{SoC} SoC_i(t) \tag{6.1}$$

where $SoC_i(t)$ is the SoC of the local battery at time instant t and α_{SoC} is the SoC coefficient.

According to (6.1), any slight change in the battery SoC creates a voltage difference which triggers an automatic current flow between the households. Thus, with the algorithm proposed, each household is automatically placed in either a surplus mode with power drawn from it when the SoC is high or in a deficit mode with power supplied to it by other households when the SoC is low. Power exchange stops when the battery SoCs are balanced, i.e. when they reach a common SoC value where the distribution voltages are equal.

How balancing the battery SoCs using the algorithm proposed keeps currents and power losses low in the solar nano-grid is detailed in the next subsections.

6.2.1 Equivalent Circuit Model of a Solar Nano-Grid

In this subsection, the behaviour of the solar nano-grid when controlled according to (6.1) is presented. The expression of the SoC in (3.73) was rewritten in a continuous time domain as follows

$$SoC_i(t) = SoC_i(0) - \frac{\eta_{b,i}}{C_{b,i}} \int_0^t I_{b,i}(t)dt \tag{6.2}$$

where $I_{b,i}(t)$ is given by (3.83).

Substituting (6.2) in (6.1), the algorithm (6.1) was rewritten as follows

$$v_{dc,i}(t) = v_{dc,i}(0) + \frac{q_i(t)}{C_i} \tag{6.3}$$

where $v_{dc,i}(0)$ is initial voltage of capacitor, C_i is equivalent capacitance, $q_i(t)$ is charge flowing into the capacitor, which are all expressed as follows

$$v_{dc,i}(0) = \alpha_{SoC} SoC_i(0) \tag{6.4a}$$

$$C_i = \frac{C_{b,i}}{\alpha_{SoC}\eta_{b,i}}, \quad \eta_{b,i} > 0 \tag{6.4b}$$

$$q_i(t) = -\int_0^t I_{b,i}(t)dt \tag{6.4c}$$

According to (6.3), every droop controlled-household in the solar nano-grid behaves like a capacitive node due to the time domain based operation of the batteries as expressed by the SoC in (6.2). The capacitance (6.4b) is directly proportional to the battery capacity and varies inversely with the SoC coefficient and battery efficiency. Effectively, batteries in every household can be replaced by their equivalent capacitances without loss of generalisation. Consequently, considering Figure 3.36, the solar nano-grid which is shown in Figure 6.1 was modelled as a Resistor-Capacitor (RC) circuit as shown in Figure 6.2.

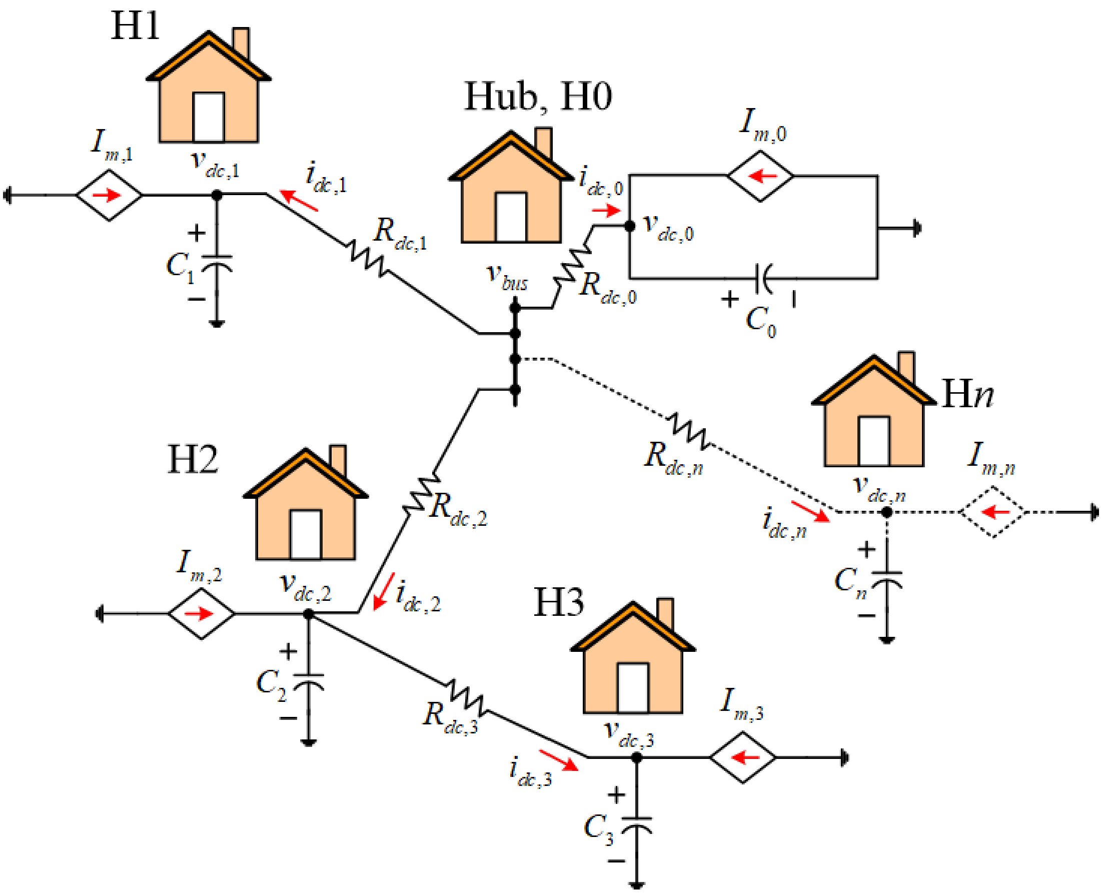

Figure 6.2: Equivalent circuit model of a solar nano-grid in Figure 6.1 when controlled using the algorithm proposed.

It can be seen from Figure 6.2 that all the input energy sources are current sources. This suggests that energy dissipation in the distribution lines during the process of charging and discharging the capacitors is lowest [200]. For the sake of this analysis, the values of the current sources and capacitors were considered to be constant so that only the dynamics caused by the charge and discharge processes of the capacitors were analysed.

6.2.2 Energy Loss Analysis

Figure 6.3 shows the equivalent circuit model for two interconnected households. The aim of this subsection is to analyse the energy loss in the resistor when charging and discharging the capacitors. There are three main operating conditions of the circuit in Figure 6.3 which are based on the charge statuses of the capacitors (a) both capacitors are fully charged, (b) capacitor C_j is fully charged and C_k is not fully charged and (c) both capacitors are not fully

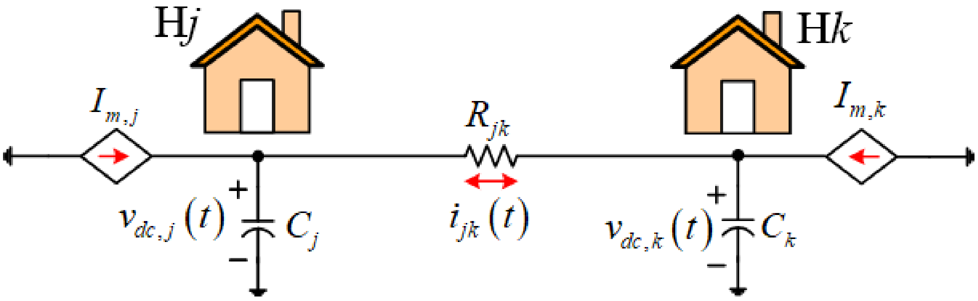

Figure 6.3: Equivalent circuit model of two interconnected households.

charged. These three operating conditions are illustrated in Figure 6.4. Other operating conditions can be obtained by reversing the current direction for the presented operating conditions without affecting the analysis carried out in this section. The impact of each operational condition on energy loss was analysed as presented in the following subsections.

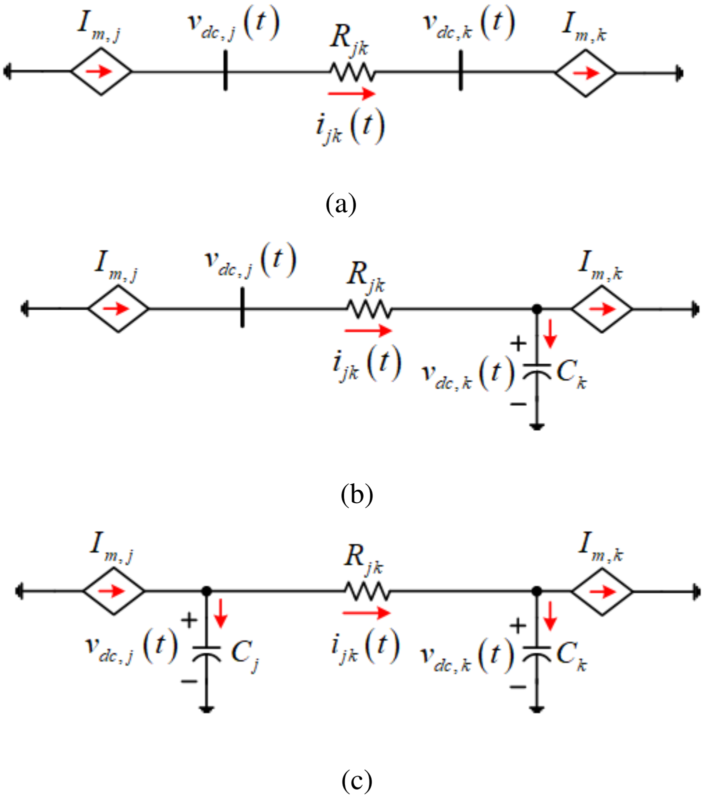

Figure 6.4: Operating condition when (a) both capacitors are fully charged, (b) capacitor C_j is fully charged and C_k is not fully charged and (c) both capacitors are not fully charged.

Energy Loss when both Capacitors are Fully Charged

Figure 6.4a shows the operating condition when both capacitors are fully charged. In practice, this can happen when the following expression is satisfied

$$I_{m,j} = i_{jk}(t) = \frac{v_{dc,j}(t) - v_{dc,k}(t)}{R_{jk}} = I_{m,k} \tag{6.5}$$

The energy loss in the resistor is externally determined from either $I_{m,j}$ or $I_{m,k}$ as follows

$$E_{loss}(t) = R_{jk} \int_0^t i_{jk}^2(t)dt = I_{m,j}^2 R_{jk} t = I_{m,k}^2 R_{jk} t \tag{6.6}$$

That is, the energy loss increases proportionally with time and magnitude of the current source. The longer the time that the circuit stays on, the higher the energy loss.

Energy Loss when C_j is Fully Charged and C_k is not

Figure 6.4b shows the operating condition where C_j is fully charged while C_k is not. For a time, t greater than zero, the dynamics of the circuit were described by the following expression

$$I_{m,j}(t) - I_{m,k}(t) = C_k \frac{dv_{dc,k}(t)}{dt} \tag{6.7}$$

Solving (6.7) for $v_{dc,k}(t)$, the following voltage expression was obtained

$$v_{dc,k}(t) = v_{dc,k}(0) + \frac{I_{m,j} - I_{m,k}}{C_k} t \tag{6.8}$$

The energy loss in the resistor was obtained as follows

$$E_{loss}(t) = R_{jk} \int_0^t i_{jk}^2(t)dt = I_{m,j}^2 R_{jk} t \tag{6.9}$$

The obtained energy loss is equal to the energy loss in (6.6) if $I_{m,j}$ in both cases is the same.

Energy Loss when both C_j and C_k are not Fully Charged

Figure 6.4b shows the operating condition where both capacitors are neither fully charged nor empty. For $t > 0$, the dynamics of the circuit were described as follows

$$I_{m,j} - \left(\frac{v_{dc,j}(t) - v_{dc,k}(t)}{R_{jk}}\right) = C_j \frac{dv_{dc,j}(t)}{dt} \tag{6.10a}$$

$$-I_{m,k} + \left(\frac{v_{dc,j}(t) - v_{dc,k}(t)}{R_{jk}}\right) = C_k \frac{dv_{dc,k}(t)}{dt} \tag{6.10b}$$

For simplicity, letting C_j to be equal to C_k in magnitude, i.e. $C_j = C_k = C_{eq}$, (6.10) was solved for $v_{dc,j}(t)$ and $v_{dc,k}(t)$ as follows

$$\begin{cases} v_{dc,j}(t) = X - Z\exp\left(\frac{-2t}{\tau}\right) + \frac{\left(I_{m,j}-I_{m,k}\right)}{2C_{eq}}t \\ v_{dc,k}(t) = Y + Z\exp\left(\frac{-2t}{\tau}\right) + \frac{\left(I_{m,j}-I_{m,k}\right)}{2C_{eq}}t \end{cases} \tag{6.11}$$

where $\tau = R_{jk}C_{eq}$ and

$$X = \frac{2\alpha_{SoC}\left[SoC_j(0) + SoC_k(0)\right]}{4} + \frac{\left(I_{m,j} + I_{m,k}\right)R_{jk}}{4} \tag{6.12a}$$

$$Y = \frac{2\alpha_{SoC}\left[SoC_j(0) + SoC_k(0)\right]}{4} - \frac{\left(I_{m,j} + I_{m,k}\right)R_{jk}}{4} \tag{6.12b}$$

$$Z = \frac{2\alpha_{SoC}\left[SoC_k(0) - SoC_j(0)\right]}{4} + \frac{\left(I_{m,j} + I_{m,k}\right)R_{jk}}{4} \tag{6.12c}$$

The voltage expressions in (6.11) consist of three terms. The first term (that is X or Y) is a constant that is independent of time. The second term is an exponential function that decays with time. The third term is a proportional term that increases with time. Figure 6.5 shows the voltage response for $\alpha_{SoC} = 220$ V, $R_{jk} = 1.5\Omega$, $C_{eq} = 1669.76$ F (which corresponds to battery capacity of 100 Ah and battery efficiency of 98%), $I_{m,j} = 5$ A, $I_{m,k} = 3$ A, $SoC_j = 60\%$ and $SoC_k = 20\%$. According to (6.11), the voltage response in Figure 6.5 can be described in two stages. Firstly, the voltage increases or decreases exponentially to equalise the stored charge in the capacitors and then the voltage increases proportionally with time since $I_{m,j} > I_{m,k}$, otherwise it will decrease proportionally with time. The equalisation of charge among the capacitors when the voltage increases or decreases exponentially is analogous to equalisation of the SoC among the batteries when using the algorithm proposed.

Using (6.11), the magnitude of current flow in the resistor was expressed as

$$i_{jk}(t) = \frac{\alpha_{SoC}\left[SoC_j(0) - SoC_k(0)\right]}{R_{jk}} \exp\left(\frac{-2t}{\tau}\right) + \left(\frac{I_{m,j}+I_{m,k}}{2}\right)\left[1-\exp\left(\frac{-2t}{\tau}\right)\right] \quad (6.13)$$

Figure 6.6 shows that the magnitude of current flow strongly depends on the difference between the initial SoCs, i.e. $\Delta SoC = SoC_j(0) - SoC_k(0)$. The lower the ΔSoC, the lower the initial magnitude of current flow. The energy loss was expressed from (6.13) as follows

$$\begin{aligned} E_{loss}(t) = {} & C_{eq}Z^2\left[1-\exp\left(\frac{-4t}{\tau}\right)\right] - Z\tau\left(I_{m,j}+I_{m,k}\right)\left[1-\exp\left(\frac{-2t}{\tau}\right)\right] \\ & + \frac{\left(I_{m,j}+I_{m,k}\right)^2 R_{jk}}{4} t \end{aligned} \quad (6.14)$$

Similar to current flow in (6.13), the energy loss is a function of Z, which is a function of the initial SoCs. Figure 6.7 shows the variation of the energy loss with respect to the initial SoCs. As shown in Figure 6.7, the energy loss is lowest when the initial SoCs are close to each other. Thus, by keeping the battery SoCs close to each other at every time interval, the magnitude of the distribution current and the distribution energy loss is reduced. Effectively, the total losses of the solar nano-grid reduce by balancing the SoCs.

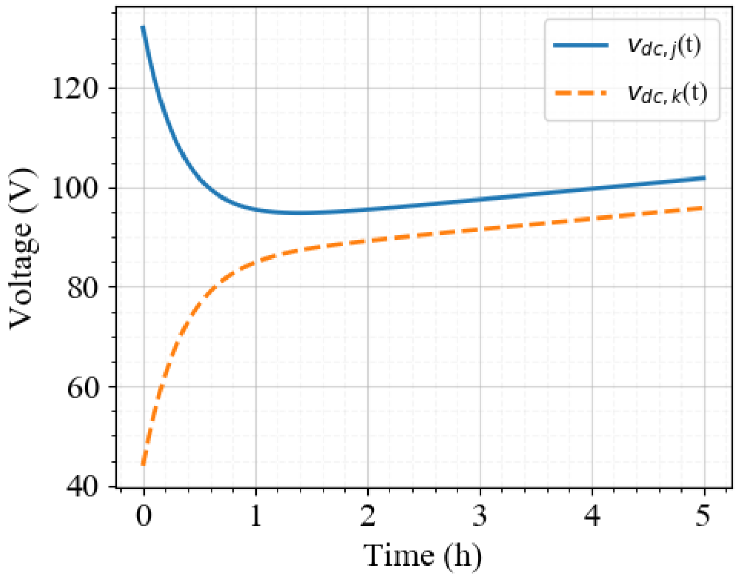

Figure 6.5: Variation of distribution voltage with time.

6.3 Determination of the State of Charge Coefficient

In this section, the determination of the SoC coefficient, α_{SoC} of the algorithm in (6.1) is presented. The α_{SoC} was expressed from (6.1) as follows

$$\alpha_{SoC} = \frac{v_{dc,i}(t)}{SoC_i(t)} \tag{6.15}$$

Since both $v_{dc,i}(t)$ and $SoC_i(t)$ are different in every household due to different power generation and load demand patterns, consensus on the common α_{SoC} at every time interval was required. The α_{SoC} should be the same in every household if the battery SoCs are to track each other.

Consensus on the common α_{SoC} was achieved in a distributed manner by allowing agents in the solar nano-grid to exchange information with their neighbours. Two consensus based algorithms, namely average voltage consensus algorithm and average SoC consensus algorithm running in parallel were proposed in this work to achieve consensus on the common α_{SoC} as presented in the next subsections. A brief on graph theory and the concept of consensus algorithms is described in Appendix B.

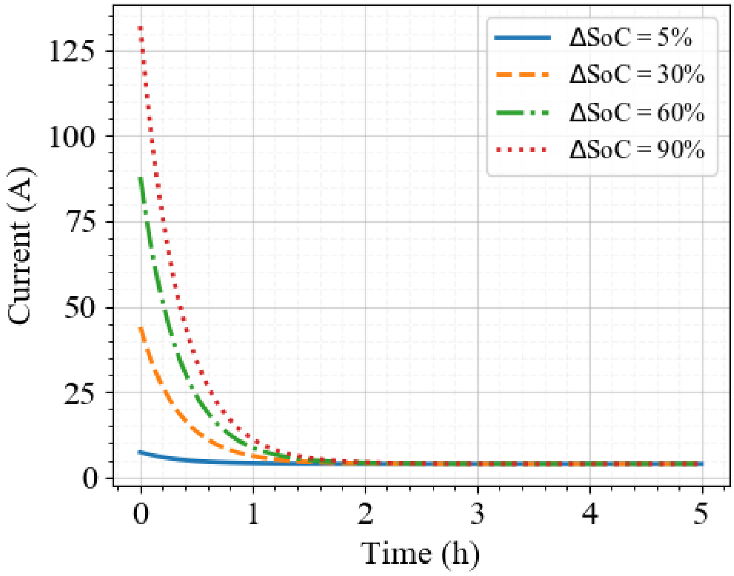

Figure 6.6: Variation of distribution current with time.

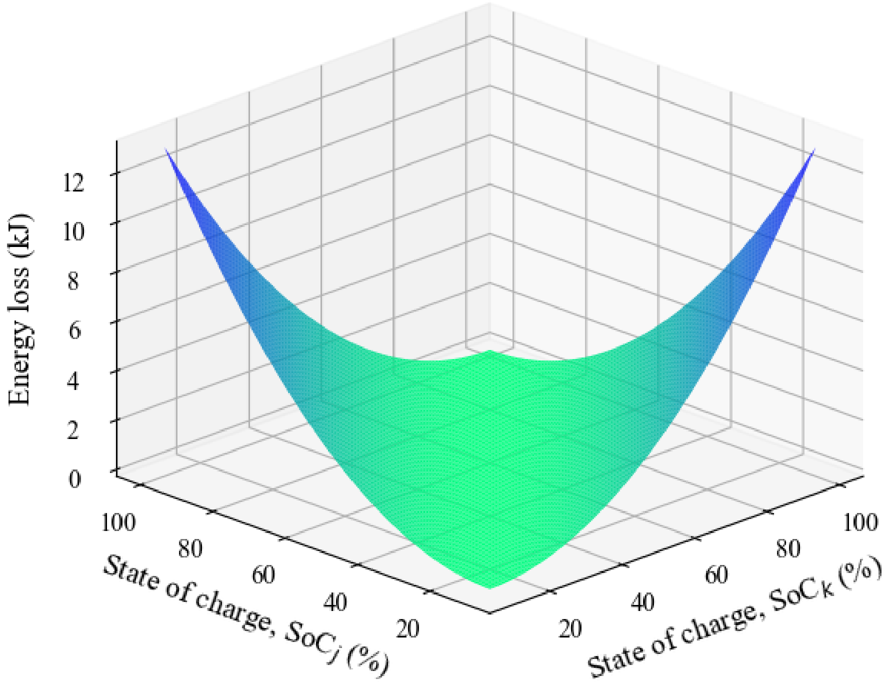

Figure 6.7: Variation of energy loss with battery state of charge.

6.3.1 Average Voltage Consensus Algorithm

The main objective of the average voltage consensus algorithm was to allow the agents in the solar nano-grid to reach consensus on the average distribution voltage by the rule

$$\vartheta_i^{(k+1)} = \sum_{j=0}^{n} d_{ij}\vartheta_j^{(k)} \tag{6.16}$$

where k is the iteration number, ϑ_i^{k+1} is the updated approximation of the average distribution voltage by agent i at $k+1$ using the information of the average distribution voltage, ϑ_j^k approximated by neighbouring agents j at k, and d_{ij} is given in Appendix B.

Convergence Analysis of the Average Voltage Consensus Algorithm

The convergence of the average voltage consensus algorithm in (6.16) was analysed by first rewriting it in a matrix form as follows

$$\vartheta^{(k+1)} = \mathbf{D}\vartheta^{(k)} \tag{6.17}$$

where $\vartheta^{(k)} = \left[\vartheta_0^{(k)}, \vartheta_1^{(k)}, \ldots, \vartheta_n^{(k)}\right]^T$ is an n dimensional column vector of average distribution voltages of all agents at k and $\mathbf{D} = (d_{ij})n \times n$ is the symmetric adjacency matrix which describes the information exchange between the neighbouring agents.

Pre-multiplying (6.16) by $\mathbf{1}^T$ and thereafter taking limits as $k \to \infty$ on both sides, the following expression was obtained

$$\lim_{k\to\infty} \mathbf{1}^T \vartheta^{(k+1)} = \lim_{k\to\infty} \mathbf{1}^T \mathbf{D} \vartheta^{(k)} \tag{6.18}$$

Since $\mathbf{D}$ is a doubly stochastic matrix, (6.18) was simplified as follows

$$\lim_{k\to\infty} \mathbf{1}^T \vartheta^{(k+1)} = \lim_{k\to\infty} \mathbf{1}^T \vartheta^{(k)} \tag{6.19}$$

This means that as $k \to \infty$, consensus on the average voltage is achieved, i.e. $\vartheta_i(\infty) = \vartheta_j(\infty)$ and the algorithm is guaranteed to converge for any initial values of ϑ_j, $j = 0, 1, \ldots, n$.

6.3.2 Implementation of the Average Voltage Consensus Algorithm

Figure 6.8 shows the flowchart for implementing the average voltage consensus algorithm proposed for agent i at every time interval. The $\vartheta_i^{(0)}$ was initialised to take on the nominal

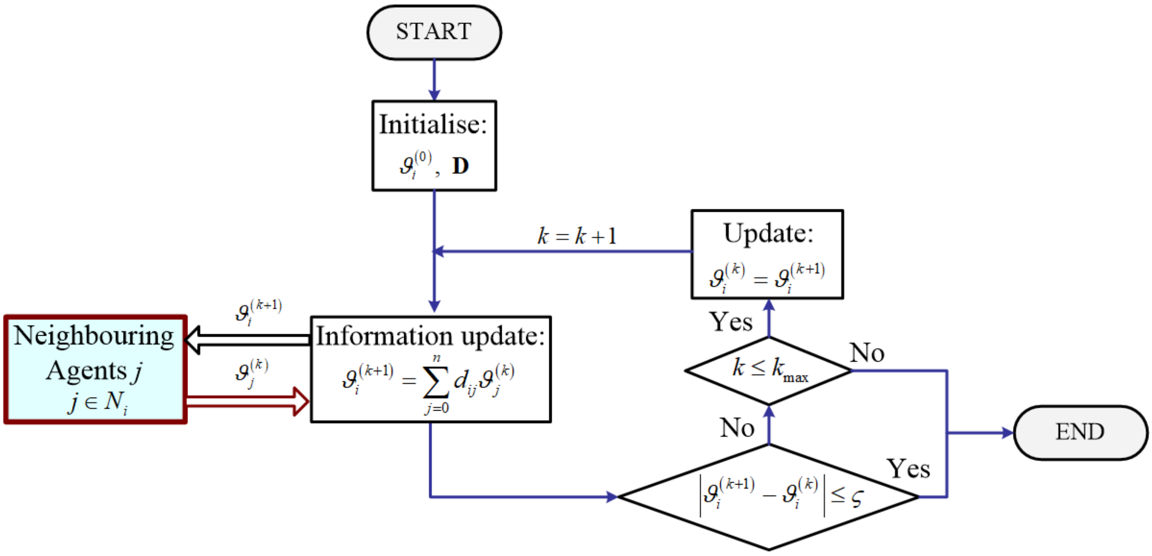

Figure 6.8: Flowchart for implementing the average voltage consensus algorithm for agent i.

distribution voltage value. The **D** was initialised by having a prior knowledge of the communication topology. Thereafter, local communications between agent i and the neighbouring agents $j,\ j \in N_i$ where N_i is the total number of neighbours to agent i were initiated while updating the local average voltage estimate, $\vartheta_i^{(k+1)}$ at each iteration. The iterations of the algorithm were stopped when either the maximum number of iterations, k_{max} was exceeded or when the desired solution accuracy given by $\varsigma = 0.0001$ was achieved, i.e. if the condition $\left|\vartheta_i^{(k+1)} - \vartheta_i^{(k)}\right| \leq \varsigma$ was satisfied.

6.3.3 Average State of Charge Consensus Algorithm

The average SoC consensus algorithm was designed to allow the agents in the solar nano-grid to reach consensus on the average SoC by the rule

$$\chi_i^{(k+1)} = \sum_{j=0}^{n} d_{ij}\chi_j^{(k)} \tag{6.20}$$

where χ_i^{k+1} is the updated approximation of the average SoC by agent i at $k+1$ using the information of the average SoC, χ_j^k from the neighbouring agents j at k.

Convergence Analysis of the Average State of Charge Consensus Algorithm

The convergence analysis of the average SoC consensus algorithm is similar to that of the average voltage consensus algorithm since both algorithms share the same adjacency matrix, $\mathbf{D} = (d_{ij})n \times n$. Thus, as $k \to \infty$, the average SoC estimated by the individual agents tends to the same value, i.e. $\chi_i(\infty) = \chi_j(\infty)$ regardless of the initial values taken by χ_i, $i = 0, 1, \ldots, n$.

Implementation of the Average State of Charge Consensus Algorithm

The average SoC consensus algorithm was run in parallel with the average voltage consensus algorithm and was implemented in a similar manner like the average voltage consensus algorithm as shown in Figure 6.9. The χ_i at start of the algorithm was initialised to be equal to

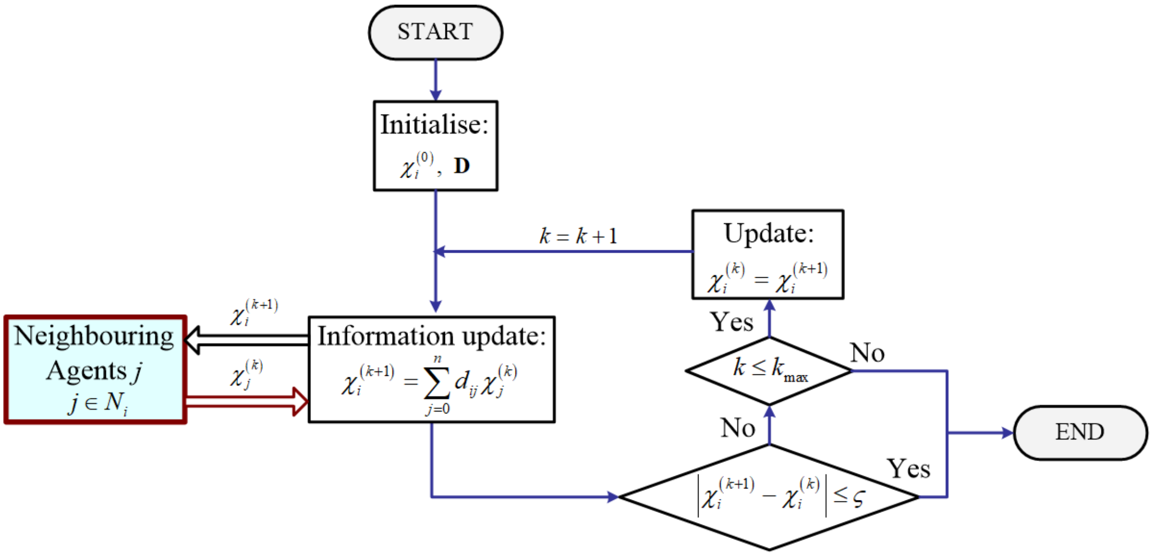

Figure 6.9: Flowchart for implementing the average SoC consensus algorithm.

50%; any other value within the SoC limits (3.89) could also be used. The χ_i for agent i at every iteration was then estimated through information exchange with neighbouring agents j. Convergence was achieved and the iterations stopped when the desired solution accuracy ς was achieved, i.e. when the condition, $\left|\chi_i^{(k+1)} - \chi_i^{(k)}\right| \le \varsigma$ was satisfied.

6.3.4 Determination of the State of Charge Coefficient

After convergence of the average voltage and SoC consensus algorithms as $k \to \infty$ was achieved, each agent was allowed to locally determine the common α_{SoC} as follows

$$\alpha_{SoC} = \frac{\vartheta_i^{(\infty)}}{\chi_i^{(\infty)}} \tag{6.21}$$

6.4 Implementation of the Distributed State of Charge based Droop Control Algorithm Proposed

Figure 6.10 shows the flowchart for implementing the distributed SoC based droop control algorithm proposed for agent i. The implementation follows four steps.

1. **Estimation of the battery SoC:** the first step involves the estimation of the local battery SoC using (3.73), which is an input to the algorithm.

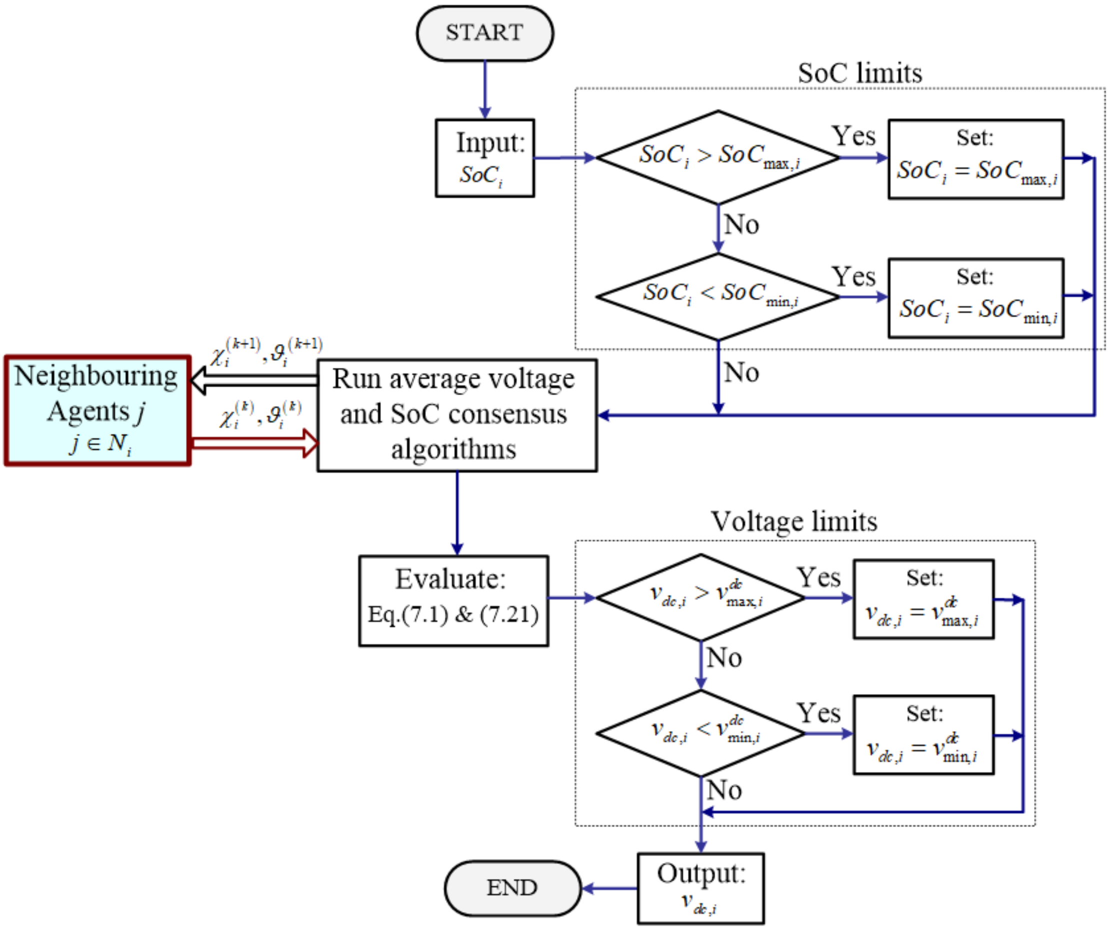

Figure 6.10: Implementation of the average voltage consensus algorithm.

2. **Satisfaction of SoC limits:** the second step involves checking whether the estimated SoC is within the allowed limits (3.89) or not. The battery output power limit (3.90) violations can be avoided by having battery current limiters in the low level control, which were however, beyond the scope of this chapter.

3. **Implementation of the average voltage and SoC algorithms:** the third step is the implementation of the average voltage and SoC consensus algorithms through information exchange with neighbouring agents j. The results from the third step are the average distribution voltage and battery SoC in the solar nano-grid, which are used to determine the SoC coefficient in (6.15) and the distribution voltage in (6.1).

4. **Satisfaction of voltage limits:** the last step involves ensuring that the determined distribution voltage in Step 3 is within the allowed range as given in (3.92). The outcome from the voltage limit check is the final reference distribution voltage signal.

6.5 Simulation Results and Discussion

In this section, the performance of the distributed SoC based droop control algorithm proposed is presented. The algorithm proposed was evaluated for a solar nano-grid with star and hybrid configurations.

6.5.1 Power Management Performance of the Algorithm Proposed for a Solar Nano-grid with a Star Configuration

In this subsection, the star solar nano-grid configuration was considered in order to compare the performance of the distributed SoC-based droop control algorithm with the centralised control algorithm presented in Chapter 4. For this reason, the test solar nano-grid network shown in Figure 5.6 with simulation parameters given in Table 4.1 and Figure 4.13b were used.

Since the distributed SoC-based droop control algorithm consists of the average voltage and SoC algorithms running in parallel, these were first investigated for their convergence speeds as presented in the next four subsections. Thereafter, power management performance of the SoC-based droop control algorithm proposed was investigated.

Convergence Speed of the Average State of Charge Algorithm with Different Communication Topologies

To verify the convergence speed of the average SoC algorithm for the topologies shown in Figure 5.7, the agents were assigned initial SoC values as follows: 30%, 50% and 70% for agent 0, agent 1 and agent 2 respectively. This means that after a finite number of iterations, each agent was expected to estimate the average SoC given by

$$SoC_{avg} = \left(\frac{30+50+70}{3}\right)\% = 50\% \tag{6.22}$$

Figure 6.11 shows the average SoC estimated by each agent for 30 iterations. The agents reached consensus on the average SoC of 50% within 6 iterations for both topologies, sug-

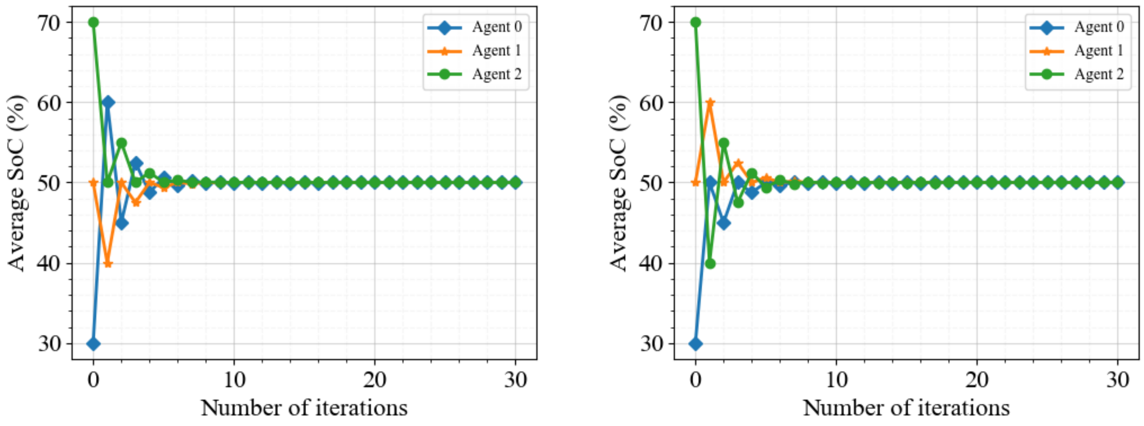

(a) (b)

Figure 6.11: Convergence speed of the average SoC algorithm for a solar nano-grid with communication (a) topology *a* and (b) topology *b*.

gesting that convergence of the algorithm was guaranteed for any initial SoC values and communication topology.

Convergence Speed of the Average State of Charge Algorithm with Different Number of Households

In this subsection, it was investigated how the convergence speed of the average SoC algorithm was influenced by the number of households in the nano-grid. Communication topology *a* in Figure 5.7a was considered where agents in the households were connected to agent 0 at the hub. In the first instance, 20 households were considered and in the second instance, 50 households were considered. The agents were initialised to have random SoC values. Figure 6.12 shows that convergence of the algorithm was guaranteed regardless of the number of households, thus it is scalable.

However, the convergence speed for 20 households was observed to be two times faster than that of 50 households, suggesting that the higher the number of households, the slower the convergence rate of the algorithm.

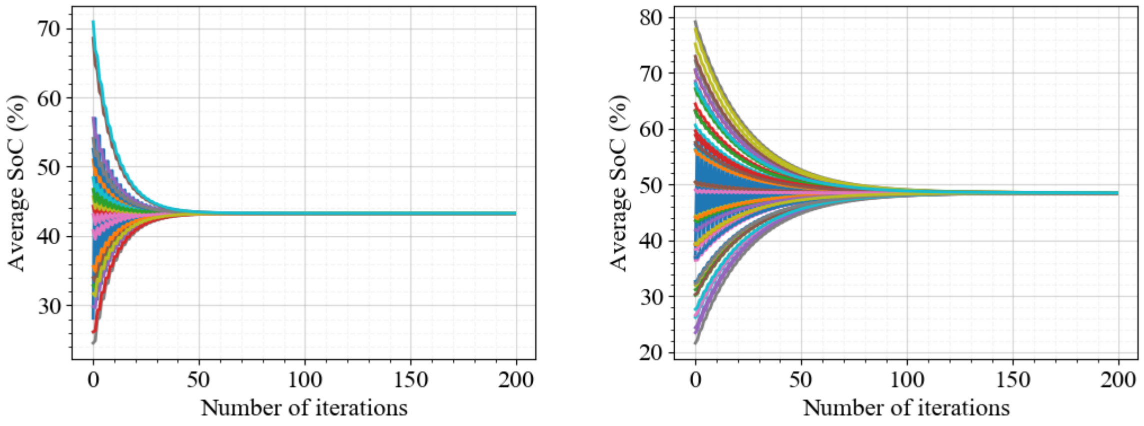

(a) (b)

Figure 6.12: Convergence speed of the average SoC algorithm for a solar nano-grid with (a) 20 households and (b) 50 households.

Convergence Speed of the Average Voltage Algorithm with Different Communication Topologies

The convergence speed of the average voltage algorithm for different communication topologies as shown in Figure 5.7 was verified by assigning initial voltage values; 100 V, 110 V and 120 V to agent 0, agent 1 and agent 2 respectively. This means that after a finite number of iterations, each agent was expected to estimate, in a distributed manner, the following average voltage

$$V_{avg} = \frac{100+110+120}{3} = 110\text{V} \tag{6.23}$$

Figure 6.11 shows that the agents reached consensus on the average 110 V after 6 iterations for both communication topologies. That suggested that convergence of the algorithm was guaranteed for any initial voltage values of the agents and communication topology.

Convergence Speed of the Average Voltage Algorithm with Different Number of Households

Figure 6.12 shows the convergence speed of the average voltage algorithm with different number of households while considering the communication topology *a* in Figure 5.7a. The agents were initialised to have random voltage values. As shown in the figure, the algorithm

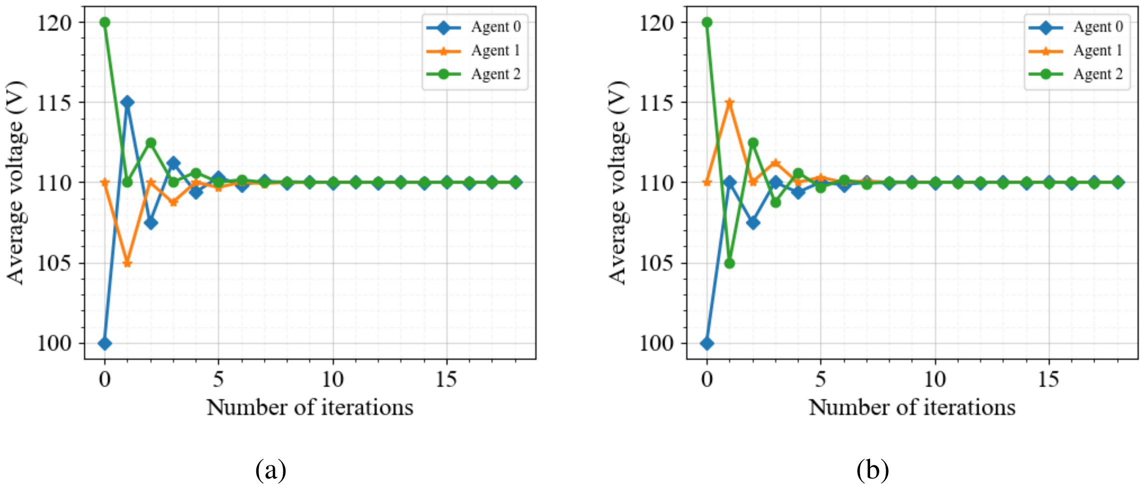

Figure 6.13: Convergence speed of the average voltage algorithm for a solar nano-grid with communication (a) topology *a* and (b) topology *b*.

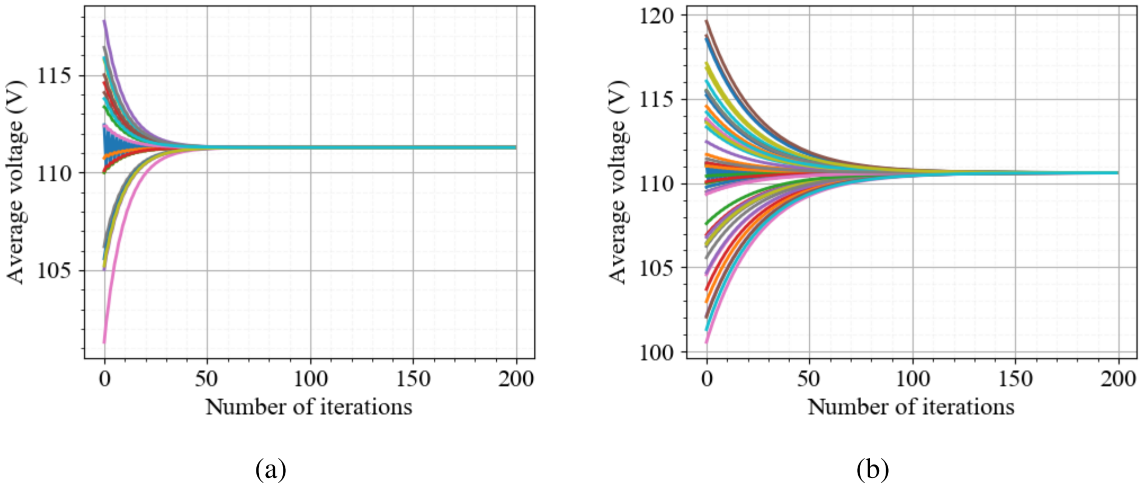

Figure 6.14: Convergence speed of the average voltage algorithm for a solar nano-grid with (a) 20 households and (b) 50 households.

converged for all the number of households considered. This also suggested that the algorithm is scalable.

From the above results, it was noted that both the average SoC and voltage algorithms had the same number of iterations for the case studies considered. This was due to the same adjacency matrix **D** used in both algorithms. Since the algorithms were run in parallel, the total number of iterations required to determine the SoC coefficient in (6.21) was equal to the number of iterations required by each algorithm to converge. For example, the number of iterations required by the average SoC algorithm in Figure 6.11 was 6. This means that it took 6 iterations also to determine the SoC coefficient.

Power Management Performance of the Droop Algorithm with different Initial Battery State of Charge Proposed

In this subsection, the effectiveness of the distributed SoC-based droop algorithm proposed for managing power in the solar nano-grid is presented. For comparison with the centralised control algorithm presented in Chapter 4, the simulation parameters considered for obtaining the results which are shown in Figure 4.14 were used in this subsection. The communication topology *a* which is shown in Figure 5.7a was used to connect the agents. The results of the simulation are as shown in Figure 6.15.

As shown in Figure 6.15, the droop algorithm proposed achieved balanced battery SoC

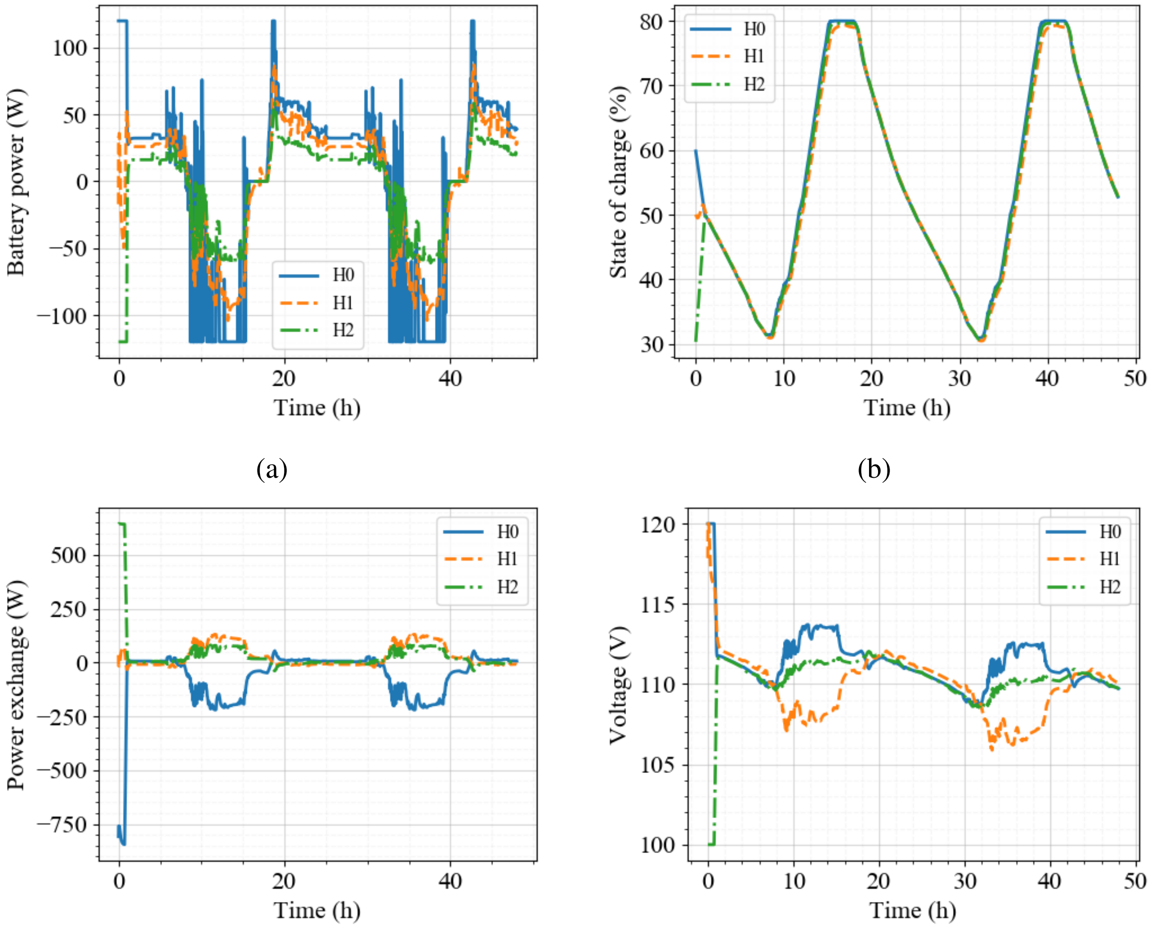

(a) (b)

(c) (d)

Figure 6.15: Power management performance of the distributed SoC based droop control algorithm proposed for the solar nano-grid with a star configuration and different initial battery SoCs of 60%, 50% and 30% for H0, H1 and H2 respectively: (a) battery charge and discharge power, (b) battery SoC, (c) power exchange between households and (d) distribution line voltage.

regardless of the changes in power generation and load demand. The battery SoC and voltage constraints were also satisfied through the droop algorithm proposed. The energy loss results of the droop algorithm proposed are as shown in Table 6.1 where they are compared with those obtained through the centralised control algorithm.

Table 6.1: Comparison of energy loss results between the algorithm proposed and the centralised control algorithm for different initial battery SoCs.

	Centralised Algorithm	**Proposed Droop**
Battery loss (Wh)	18.44	**14.87**
Distribution line loss (Wh)	97.45	**197.07**
FPC loss (Wh)	2644.31	**2644.31**
Total energy loss (Wh)	**2760.2**	**2856.28**

Table 6.1 showed that the energy losses of the droop algorithm proposed were 3.5% higher than those of the centralised algorithm. This was mainly due to high distribution line losses, which were caused by high initial powers in the solar nano-grid as shown in Figure 6.15. The high initial powers were caused by the capacitive behaviour of the solar nano-grid (as explained in Subsection 6.2.2) which tends to have different capacitor charge levels when the battery SoCs are different, resulting in high initial power flows during the equalisation of charge levels.

In practice, the high initial powers can happen if a new battery with a different initial SoC is connected to the solar nano-grid. To avoid this from happening, the new battery needs to be charged or discharged separately before connecting it to the solar nano-grid in order to bring its SoC close to the SoCs of the existing (old) batteries. The other way of avoiding the high initial powers is through the use of current limiters in the low level control of the solar nano-grid to saturate the initial distribution line and battery currents to pre-defined levels.

Despite the high initial powers, the droop algorithm proposed yielded low peak power exchange after 5h (after the initial transients had decayed) compared to the centralised control algorithm in Figure 4.14. It was noted that the peak power exchange with the droop algorithm proposed was 31.25% lower than the peak power exchange of the centralised control algorithm after 5h. This suggested that the high energy losses recorded by the droop algorithm proposed as shown in Table 6.1 were due to the high initial powers. Thus, lowering the initial powers of the solar nano-grid, significant improvement in the energy losses can be achieved for the droop algorithm proposed as presented in the following subsection.

Power Management Performance of the Droop Algorithm with Equal Initial Battery State of Charge Proposed

To observe the performance of the droop algorithm proposed when the battery SoCs are equal, the previous simulation was repeated with equal battery SoCs of 50%. The results of the simulation are shown in Figure 6.16. Figure 6.16 shows that with equal initial battery SoCs, the high initial powers and voltages which occur when the initial battery SoCs are different were eliminated.

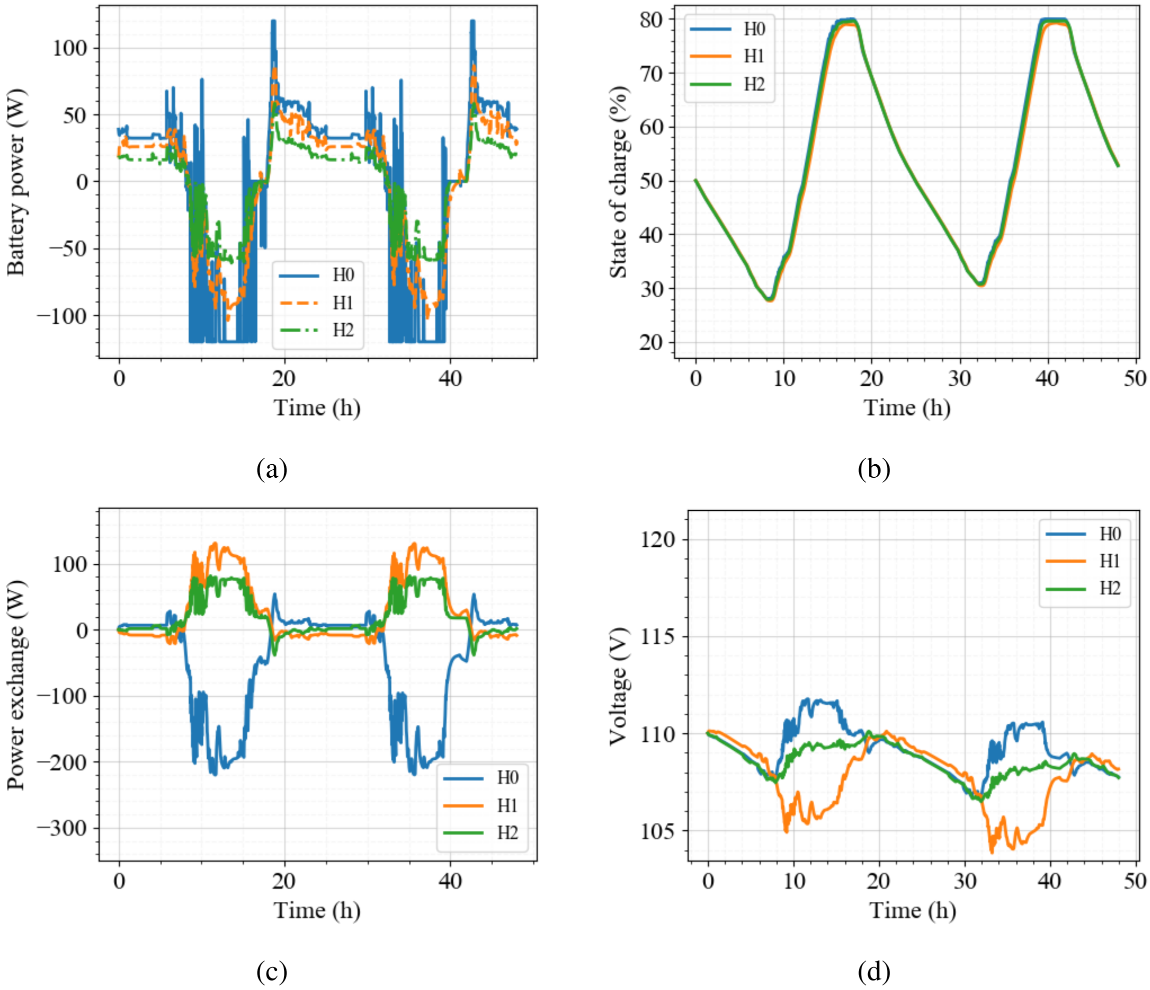

Figure 6.16: Power management performance of the distributed SoC based droop control algorithm proposed for the solar nano-grid with a star configuration and equal initial battery SoCs of 50% for H0, H1 and H2: (a) battery charge and discharge power, (b) battery SoC, (c) power exchange between households and (d) distribution line voltage.

To compare the energy losses between the droop algorithm proposed and centralised control algorithm when the initial battery SoCs are equal, a repeat of the simulation that was used to obtain Figure 4.14 was carried out while keeping the initial battery SoCs the same at 50%. Table 6.2 shows the effectiveness of the algorithm proposed for reducing the power losses of the solar nano-grid compared to the centralised control algorithm.

Table 6.2: Comparison of energy loss results between the algorithm proposed and the centralised control algorithm for same initial battery SoCs.

	Centralised Algorithm	**Proposed Droop**
Battery loss (Wh)	18.23	**13.82**
Distribution line loss (Wh)	95.67	**93.10**
FPC loss (Wh)	2644.31	**2644.31**
Total energy loss (Wh)	**2758.21**	**2751.23**

From Table 6.2, the droop algorithm proposed was observed to have low battery and distribution line losses compared to the centralised algorithm. This was always the case even for different initial battery SoCs, provided that the difference between the initial battery SoCs was less 4%. As shown in Table 6.2, the battery and distribution losses for the droop algorithm proposed were 24.2% and 2.7% lower than those for the centralised control algorithm respectively. Since the FPC loss is the function of the load demand (3.57), and because same load demand profiles were used for both algorithms, the FPC loss result was the same for both algorithms as shown in Table 6.2.

The results in Table 6.2 were not expected especially that the centralised control algorithm sought to minimise the power losses of the solar nano-grid through optimisation by explicitly finding the operating state of the solar nano-grid where the losses are a minimum. One would have therefore expected the energy losses obtained through the centralised control algorithm to be lower than those obtained through the algorithm proposed which does not minimise any mathematical objective function.

The higher power loss by the centralised control algorithm was attributed to the fact that the centralised control algorithm developed in this research optimised the power losses of the solar nano-grid at every time instant. This caused the power exchange to be high each time there was a surplus or deficit generation in any one of the households and hub and the power exchange to be near zero when the households and hub were self-sufficient (i.e. batteries were neither fully charged nor discharged) as shown in Figure 4.14c.

On the other hand, the droop algorithm proposed allowed automatic power exchange between the households even when the households and hub were self sufficient as shown in Figure 6.16c between 20 h and 30 h in its quest to balance the battery SoCs. As a result, the magnitude of current and power flow in the solar nano-grid was always maintained low, thereby reducing the power losses. In the future, it will be interesting to compare the results of the droop algorithm proposed with those obtained from a method that can solve the power loss optimisation problem of the solar nano-grid over a time interval. However, the author still holds the view that any method that will not perform like the centralised control algorithm proposed in this research will be bound to perform like the droop algorithm proposed by allowing automatic power exchange even when households and hub are self sufficient. In that case, the energy losses of that particular method are expected to be higher or equal to those of the droop algorithm proposed.

6.5.2 Power Management Performance of the Droop Algorithm Proposed for the Solar Nano-grid with a Hybrid Configuration

In the previous subsection, it was verified for a star solar nano-grid configuration that solar nano-grid power losses were reduced when the battery SoCs were balanced during operation. In this subsection, it was necessary and sufficient to only show that the droop algorithm proposed can achieve a battery SoC balance for a hybrid solar nano-grid configuration, a different number of households and a different communication topology as shown in Figure 6.17. The considered power generation profile was the same as that shown in Figure 4.12b. The considered load demand profiles [197, 201] are as shown in Figure 6.18a. All the considered batteries had the same initial SoC of 50%.

It was verified as shown in Figure 6.18b that the droop algorithm proposed was capable of balancing the battery SoCs in the solar nano-grid regardless of the number of households, battery size, solar nano-grid configuration, communication topology, changes in power generation and consumption patterns.

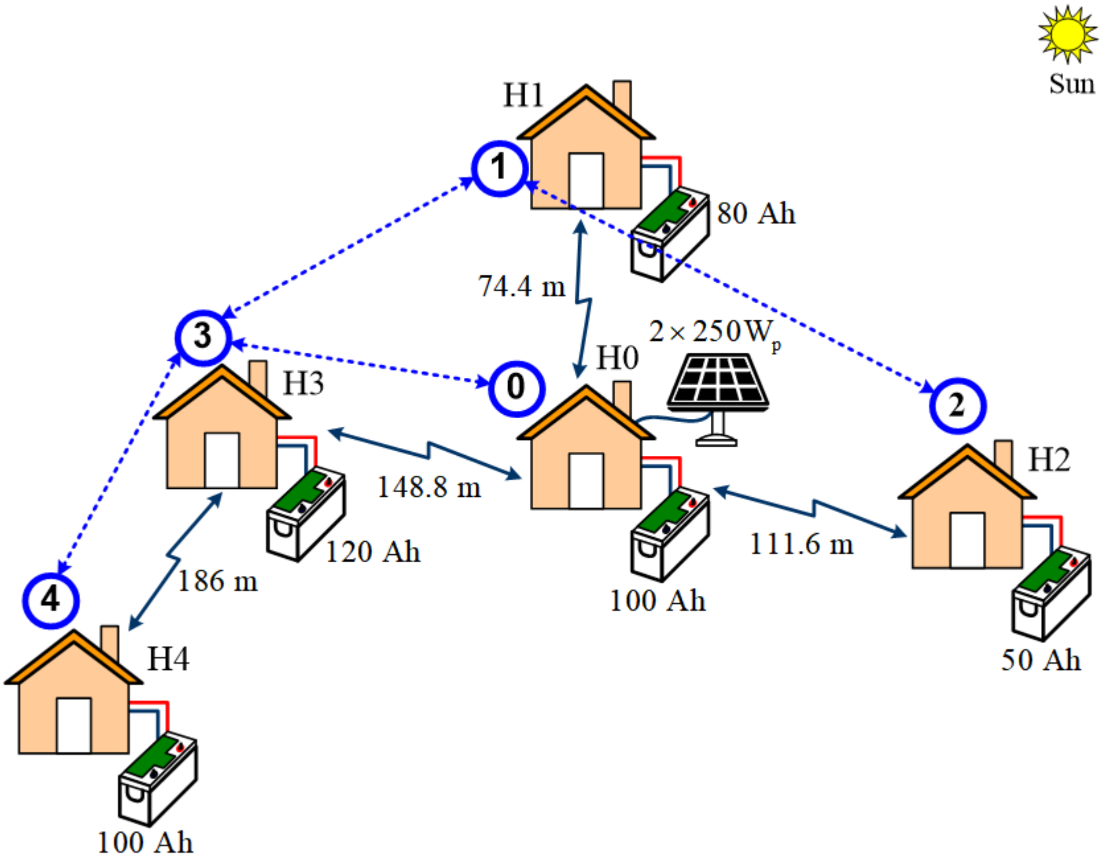

Figure 6.17: A hybrid solar nano-grid configuration for simulation purposes.

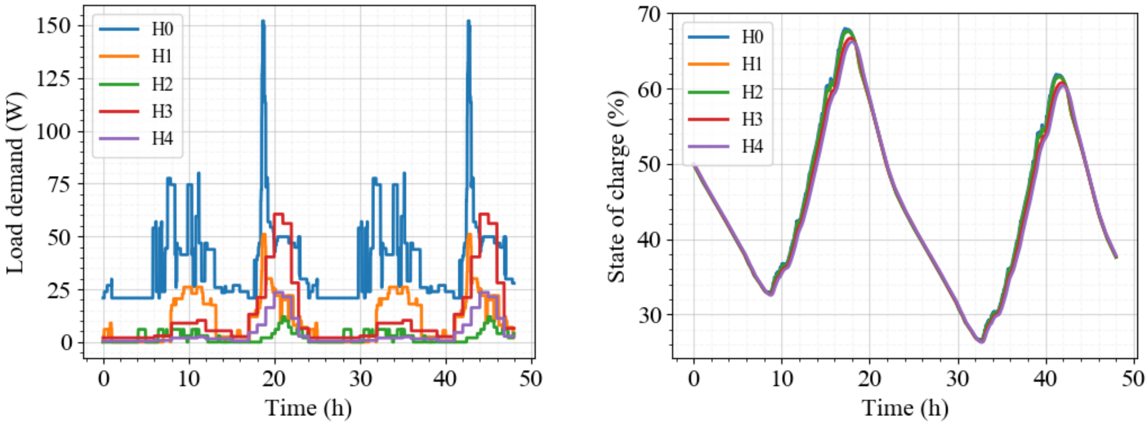

(a) (b)

Figure 6.18: Showing in (a) 48 hour load demand profiles and (b) the battery SoC response for the hybrid solar nano-grid configuration.

6.6 Summary

This chapter considered the following research questions:

- *How can the power losses of a solar nano-grid that has a hybrid configuration as* *shown in Figure 1.8 be minimised?*

- *Is there an all-in-one control algorithm that can reduce power losses of a solar nano-grid that has an arbitrary configuration and number of households?*

In trying to answer the first question, it was found that the centralised control algorithm and QCDCA which are presented in Chapters 4 and 5 respectively could not be directly applied to minimise the power loss of the solar nano-grid with a hybrid configuration since these were developed for a star solar nano-grid configuration. To address this drawback, a novel fully distributed SoC based droop control algorithm was developed and is presented in this chapter. The algorithm proposed enabled the batteries in the solar nano-grid to balance their SoCs at every time instant during operation. Numerical results presented in this chapter showed how balancing the battery SoCs reduced the magnitude of current flow and the power losses thereof in the solar nano-grid.

Simulation results presented for a solar nano-grid with star and hybrid configurations showed an effective power management performance of the algorithm proposed and its capability to balance the battery SoCs regardless of the solar nano-grid configuration, number of households, power generation and load demand patterns. Comparative results between the algorithm proposed and centralised control algorithm for the star solar nano-grid configuration showed that the algorithm proposed reduced the peak power flows in the solar nano-grid by 31.25% compared to the centralised control algorithm. This resulted in low power losses for the algorithm proposed compared to the centralised control algorithm. The battery and distribution losses for the algorithm proposed were found to be 24.2% and 2.7% lower than those for the centralised control algorithm respectively.

To answer the second research question, the distributed SoC-based droop control algorithm was found to be an all-in-one control algorithm that can reduce the power losses of a solar nano-grid with arbitrary configuration and number of households. This is because, the algorithm proposed did not require any prior knowledge of the solar nano-grid configuration and that it was a fully distributed control algorithm that only required a sparse communication network for implementation. Thus, the algorithm proposed was robust, reliable, scalable and straightforward to implement.

Chapter 7

Conclusion and Future Work

The overarching research question considered in this research was as follows:
What control algorithms can be developed to address the problem of maximising energy efficiency of Four-Port DC-DC Converter (FPC)-enabled solar nano-grids that are designed for energy access?

To address the research question, two solar nano-grid configurations were considered, namely, star and hybrid configurations as shown in Figure 1.4 and Figure 1.8 respectively. The energy efficiency in both configurations was maximised by minimising the solar nano-grid power losses, which include battery charge and discharge losses, distribution line losses and FPC losses. To minimise the solar nano-grid power losses, the following five secondary research questions were considered:

1. *How can the solar nano-grid e.g. with a star configuration as shown in Figure 1.4 be modelled at steady-state and have a convex power loss optimisation problem formulated?*

   In Chapter 3, a steady state model of solar nano-grid with a star configuration was developed and a convex power loss optimisation problem of the solar nano-grid was formulated. The solar nano-grid model was developed by combining detailed circuit based models of the key solar nano-grid components, i.e. batteries, solar panels, DC loads and FPCs. Known steady-state models from literature of the batteries, solar panels and DC loads were used. Since the FPC considered in this research was new and not reported anywhere in literature, two power loss models of the FPC were developed from (1) its switching circuit and (2) experimental results. The FPC power loss model which was obtained from the switching circuit was used to understand the FPC operation and constituent power losses of the FPC. The FPC power loss model which was obtained from the experimental results is what was used in the solar nano-grid model due to its simplicity. Kirchhoff's voltage and current laws were then used to complete the model of the solar nano-grid by obtaining the relevant mathematical relationships. Due to the use of detailed models of the solar nano-grid components which were experimentally verified, the modelled solar nano-grid was accurate and a true representation of the physical behaviour of the solar nano-grid. The modelled solar nano-grid can be used for power flow studies such as optimisation of the power losses (which was considered in this research) and operational costs. The key contributions to knowledge made through modelling of the solar nano-grid were development of:

- an accurate steady state model of the solar nano-grid from experimentally verified solar nano-grid component models;
- a detailed FPC loss model from a switching circuit, which can be used to optimise the FPC design by having efficiency as a design parameter;
- a simplified FPC loss model from FPC experimental results, which can be used for real time estimation of the FPC power loss.

After the solar nano-grid was modelled, a novel contribution to knowledge was also made through the formulation of a convex power loss optimisation problem. To avoid the linearisation of power flow equations which are inherently non-linear and non-convex, the power loss problem was formulated as a two-stage optimisation problem. The first stage was formulated as an Optimal Battery Dispatch Problem (OBDP) where the battery charge and discharge operation was scheduled to minimise the power loss of the solar nano-grid while keeping the distribution voltages constant. The output from the first stage were the optimal battery charge and discharge currents. The second stage of the optimisation problem was formulated as an Optimal Current Flow Problem (OCFP) where optimal distribution voltages corresponding to the optimal battery charge and discharge currents from the first stage were determined. The output from the second stage were distribution voltages which were considered as final solutions to the power loss optimisation problem. To eliminate errors emanating from keeping the distribution voltages constant in the first stage of the optimisation problem, the whole optimisation problem was cast as a closed loop control system with the feedback loop containing updates of the distribution voltages.

The main advantage of the formulation proposed over existing approaches [46] was that it did not require any linearisation or convex relaxation of power flow equations. Thus, the formulation proposed was more accurate and computationally efficient, suitable for a real-time implementation. In addition, the formulation proposed had $2(n+1)$ number of decision variables compared to $3(n+1)$ for the existing approaches for a solar nano-grid with n households and hub. Thus, the formulation proposed was easily scalable.

2. *How can the power losses of the star solar nano-grid configuration be quantified and minimised?*

   In Chapter 4, quantification of the power losses of the solar nano-grid with a star configuration were carried out and a novel centralised control algorithm was developed to minimise the power losses. The power losses were quantified during simulation by recording the total power loss of the batteries, distribution lines and FPCs in the solar nano-grid. FPC losses in the solar nano-grid were found to be more than 20 times higher than the distribution line losses and more than 100 times higher than the battery losses.

   The power losses of the solar nano-grid were minimised through optimisation by solving the convex power loss optimisation problem which was formulated in Chapter 3 in a centralised manner. The star configuration of the solar nano-grid motivated the use of a centralised control approach. A centralised control algorithm which consisted of two iterative algorithms, the Fast Lambda Iteration Algorithm (FLIA) and Fast Voltage

Iteration Algorithm (FVIA) was developed to solve the power loss optimisation problem while meeting the operational constraints of the solar nano-grid such as power supply-demand balance. The FLIA solved the OBDP to obtain the optimal battery charge and discharge currents while the FVIA solved the OCFP to obtain the optimal distribution voltages. Inputs to the centralised control algorithm were power generation, load demand and battery state of charge (SoC) from every household in the solar nano-grid. The outputs were the optimal distribution voltages from the FVIA. Firstly, the inputs were collected from all the households in the solar nano-grid via communication links to a central agent. Then, the agent computed the FLIA and FVIA to generate the optimal distribution voltages.

A key contribution to knowledge made was through the development of both the FLIA and FVIA, which use iterations to solve the power loss optimisation problem. For this reason, the centralised control algorithm proposed can be easily scaled and modified, e.g. to solve the power loss problem in a distributed manner compared to existing methods e.g. in [46] which use software packages. Another contribution to knowledge made was through the development of decentralised solar power curtailment and load shedding procedures which only require local information to be implemented as described in Subsection 4.2.3.

3. *How can the power losses of the star solar nano-grid configuration having many households be minimised?*

   In Chapter 5, a novel Quasi-Consensus based Distributed Control Algorithm (QCDCA) was proposed to minimise the power losses of a solar nano-grid that has a star configuration and many households while meeting the operational constraints of the solar nano-grid like supply-demand balance. A multi-agent based system where multiple agents solved the power loss optimisation problem individually and then communicated the results to their neighbours was used to implement the algorithm proposed. This approach eliminated the drawbacks of the centralised control algorithm (which was developed in Chapter 4) such as heavy computation burden, high storage and processor requirements which come when a solar nano-grid has many households due to the centrally managed control decisions.

The algorithm proposed consists of two novel quasi-distributed control algorithms, Incremental Loss Consensus Algorithm (ILCA) and Voltage Consensus Algorithm (VCA) running sequentially. The ILCA was a modification of the FLIA and solved the OBDP in a quasi distributed manner by allowing the agents to reach consensus on the common incremental power loss through the exchange of (individually computed incremental power loss) information with their neighbours. Similarly, the VCA was a modification of the FVIA and solved the OCFP in a quasi-distributed manner by allowing the agents to reach consensus on the common DC bus voltage through the exchange of (individually computed DC bus voltage) information with their neighbours. To always ensure supply-demand balance in the solar nano-grid, one agent in the solar nano-grid was made to be a leader agent and the others as follower agents. The leader agent computed the amount of supply-demand mismatch current in the solar nano-grid and set a bar for which consensus on the common incremental power loss and DC bus voltage was to be achieved by all the agents. The follower agents on the other hand did not have to compute the supply-demand mismatch current but to just reach consensus on the common incremental power loss and DC bus voltage. The algorithm proposed had advantages of both accuracy and low computation burden for a solar nano-grid with many households because on one hand, the algorithm behaved like a centralised algorithm due to the leader agent which had access to information from other agents and on the other hand, like a distributed algorithm due to the decentralised computation of the power loss optimisation problem.

4. *How can the power losses of a solar nano-grid that has a hybrid configuration as shown in Figure 1.8 be minimised?*

   In Chapter 6, a novel fully distributed SoC-based droop control algorithm was developed to reduce the power losses of a solar nano-grid that had a hybrid configuration while meeting the operational constraints of the solar nano-grid like power supply-demand balance. Unlike the algorithms which were developed in Chapters 4 and 5 to minimise the power losses of the star solar nano-grid configuration through optimisation, the algorithm proposed reduced the power losses of the hybrid solar nano-grid configuration by reducing the magnitude of current flow in the solar nano-grid through balancing the battery SoCs. This eliminated the need of re-designing the centralised control algorithm and QCDCA developed in Chapters 4 and 5 respectively each time the solar nano-grid configuration changed, e.g. from star to hybrid configuration. The algorithm proposed adjusted the household distribution voltages proportional to their local battery SoCs. Thus, it placed each household in either a surplus mode with power drawn from it when the SoC was high or in a deficit mode with power supplied to it by other households when the SoC was low. Power exchange between the households stopped when the battery SoCs were balanced. Due to the automatic power exchange, the magnitude of current flow at every time instant in the solar nano-grid was low, thus, keeping the power losses to a minimum. The algorithm proposed achieved the SoC balance in a distributed manner regardless of the power generation and load demand patterns in the households. Thus, it was scalable and resilient to single points of failure. The inputs to the algorithm proposed were local distribution voltages and battery SoCs, making the algorithm proposed suitable for any kind of a solar nano-grid configuration.

5. *Is there an all-in-one control algorithm that can reduce the power losses of a solar nano-grid that has an arbitrary configuration and number of households?*

   Yes!, the distributed SoC-based droop control algorithm was found to be an all-in-one control algorithm that was capable of reducing the power losses of a solar nano-grid with an arbitrary configuration and number of households. This was due to the following reasons, that the distributed SoC-based droop control algorithm:

   - Did not require formulation of a convex power loss optimisation problem to reduce the solar nano-grid power losses. Thus, the algorithm proposed was straightforward to implement.
   - Was a fully distributed control algorithm that only required a sparse communication network for implementation. Thus, the algorithm proposed was robust,

reliable and scalable.

- Did not require any prior knowledge of the solar nano-grid configuration. Thus, the algorithm proposed was capable of reducing the power losses of any solar nano-grid configuration.
- Achieved a near perfect balancing of the battery SoC regardless of the power generation and load demand patterns, battery capacities, solar nano-grid configuration and number of households. Apart from reducing the power losses, balancing the battery SoCs is also crucial for avoiding overuse of one battery, accelerated battery degradation, reduction of battery capacity and uneven over-charge and over-discharge [105–111].
- Required only the distribution voltages and battery SoCs as inputs, thus privacy of household power generation and consumption was preserved.
- Can be implemented in the low control level as well so that if there is a breakdown in communication, the solar nano-grid can continue with the operations.

In conclusion, three control algorithms, namely centralised control algorithm, QCDCA and distributed SoC based droop control algorithm were developed in this research to address the problem of maximising energy efficiency of FPC-enabled solar nano-grids that are designed for energy access. The algorithms proposed maximised the solar nano-grid efficiency by reducing the solar nano-grid power losses as presented in Chapters 4, 5 and 6.

The work carried out in this research has contributed towards the universal energy access agenda by focussing specifically on the third target of the United Nation's Sustainable Development Goal 7 - doubling the global rate of improvement in energy efficiency by 2030. There is a lot of work that still needs to be done to achieve this goal. Nonetheless, the present research has made a significant step towards improving energy efficiency by developing control algorithms that minimise power losses, which currently are viewed as one of the technical barriers hindering the practical deployment and operation of FPC-enabled solar nano-grids in rural areas.

7.1 Recommendations and Future Work

This research mainly focussed on developing high level control algorithms that can minimise power losses in solar nano-grids, specifically the FPC-enabled solar nano-grids. The research can be advanced through the following five recommendations.

7.1.1 Implementation of the Control Algorithms Developed on a Physical Solar Nano-grid System

The control algorithms developed in this research have not been implemented on a physical and real solar nano-grid network. Future work is therefore required to implement them and take measurements.

7.1.2 Information Sharing Process and Design of Communication Protocols

This research has neither covered the information sharing process between the agents nor has it designed the communication protocols required for information exchange between the agents via the communication network. Future work is therefore required to achieve this for successful implementation of the control algorithms developed. Proper communication techniques are required to ensure an efficient and economic dissemination of the relevant information.

7.1.3 Low Level Control Design and Stability Analysis of Solar Nano-Grids

This research mainly focussed on the steady state operation of the solar nano-grid where control algorithms, which can provide reference control signals to the low control level, were designed. To implement the algorithms developed in practice, design of the low control level is still required. Moreover, most of the appliances in rural areas are constant power loads. Therefore, stability analysis of the solar nano-grid is also required in order to ensure a stable operation of the solar nano-grid during load changes and electrical faults. Insights on how to carry out the stability analysis can be found in [202].

7.1.4 Uncertainty of Solar Power Generation and Load Demand

This research considered the solar irradiance (and the power generation) and the load demand to be known in advance and the same each day. In practice however this is not always the case. Uncertainties in power generation and load demand are inevitable due to numerous factors such as shade, cloud cover, number of appliances in use and whether its a weekend or weekday. In future work, it will be interesting to include the uncertainties of power generation and load consumption in the control algorithms developed.

7.1.5 Algorithms for Peer-to-Peer Energy Trading

Research is required to explore the peer-to-peer energy trading option in rural areas in order to monetise the power exchange in solar nano-grids. The revenue can be used to maintain the solar nano-grid or to motivate individual households to expand their installed generation capacity.

References

[1] World Bank, “World bank open data,” 2019. [Online]. Available: https://data.worldbank.org/indicator

[2] United Nations Development Programme, “Human development data report 2019,” 2019. [Online]. Available: http://hdr.undp.org/en/data

[3] World Bank, “State of electricity access report 2017,” World Bank, Tech. Rep., 2017.

[4] C. Zhao, S. D. Round, and J. W. Kolar, “An isolated three-port bidirectional DC-DC converter with decoupled power flow management,” *IEEE transactions on power electronics*, vol. 23, no. 5, pp. 2443–2453, 2008.

[5] B. Mikul and A. Nicolina, “Beyond connections: Energy access redefined,” World Bank, Tech. Rep., 2015. [Online]. Available: https://www.worldbank.org/content/dam/Worldbank/Topics/Energy%20and%20Extract/Beyond_Connections_Energy_Access_Redefined_Exec_ESMAP_2015.pdf

[6] Ferroxcube, “Design of planar power transformer: Application note,” 1997.

[7] Suntech, “250 W monocrystalline solar module,” 2012. [Online]. Available: https://www.evoenergy.co.uk/wp-content/uploads/2012/05/Suntech-250-Datasheet.pdf

[8] T. Kim and W. Qiao, “A hybrid battery model capable of capturing dynamic circuit characteristics and nonlinear capacity effects,” *IEEE Transactions on Energy Conversion*, vol. 26, no. 4, pp. 1172–1180, 2011.

[9] International Energy Agency, “World energy outlook 2019, IEA, paris,” World Bank, Tech. Rep., 2019. [Online]. Available: https://www.iea.org/reports/world-energy-outlook-2019

[10] Energy Sector Management Assistance Program, “Mini grids for half a billion people : Market outlook and handbook for decision makers. ESMAP technical report;014/19. world bank, washington, DC.” World Bank, Tech. Rep., 2019. [Online]. Available: http://hdl.handle.net/10986/31926

[11] Solar Aid and SunnyMoney. (2015) Impact report: autumn 2015. [Online]. Available: https://www.solar-aid.org/assets/Uploads/Impact-week-2015/SolarAid-IMPACT-REPORT-2015.pdf

[12] P. Alstone, C. Niethammer, B. Mendonça, and A. Eftimie, "Expanding women's role in africa's modern off-grid lighting market," World bank, Tech. Rep., 2011.

[13] K. Harrison, A. Scott, and R. Hogarth, "Accelerating access to electricity in africa with off-grid solar: The impact of solar household solutions," *Overseas Development Institute ODI Report*, p. 9, 2016.

[14] E.-j. Quak, "Lighting and electricity services for off-grid populations in sub-sahara africa," K4D Helpdesk Report no. 317. Brighton, UK: Institute of Development Studies, Tech. Rep., 2018.

[15] E. Adkins, K. Oppelstrup, and V. Modi, "Rural household energy consumption in the millennium villages in sub-saharan africa," *Energy for Sustainable Development*, vol. 16, no. 3, pp. 249–259, 2012.

[16] S. Collings, "Phone charging micro-businesses in tanzania and uganda," *Global Village Energy Partnership International*, 2011.

[17] Global Off-Grid Lighting Association and others, "Global off-grid solar market report - semi-annual sales and impact data," Technical Report, Tech. Rep., 2019. [Online]. Available: https://www.gogla.org/

[18] E. Tedsen, "Black carbon emissions from kerosene lamps," *Potential for a new CCAC Initiative*, 2013.

[19] Panel Africa Progress, "Power people planet: seizing africa's energy and climate opportunities," p. 182, 2015. [Online]. Available: https://reliefweb.int/report/world/africa-progress-report-2015-power-people-planet-seizing-africas-energy-and-climate

[20] E. Rehfuess, W. H. Organization *et al.*, "Fuel for life: household energy and health," World Health Organization, Tech. Rep., 2006.

[21] World Health Organisation. (2018) Household air pollution and health. [Online]. Available: https://www.who.int/en/news-room/fact-sheets/detail/household-air-pollution-and-health

[22] A. Castellano, A. Kendall, M. Nikomarov, and T. Swemmer, "Brighter africa: The growth potential of the sub-saharan electricity sector," McKinsey & Company, Tech. Rep., 2015. [Online]. Available: https://www.mckinsey.com/~/media/McKinsey/dotcom/client_service/EPNG/PDFs/Brighter_Africa-The_growth_potential_of_the_sub-Saharan_electricity_sector.ashx

[23] World Bank, "Access to energy is at the heart of development," 2020. [Online]. Available: https://www.worldbank.org/en/news/feature/2018/04/18/access-energy-sustainable-development-goal-7

[24] IEA, IRENA, UNSD, WB, WHO *et al.*, "Tracking SDG 7: The energy progress report 2020," 2020. [Online]. Available: https://trackingsdg7.esmap.org/downloads

[25] International Energy Agency, "Energy access outlook 2017: From poverty to prosperity," International Energy Agency, Tech. Rep., 2017.

[26] M. Nasir, Z. Jin, H. A. Khan, N. A. Zaffar, J. C. Vasquez, and J. M. Guerrero, "A decentralized control architecture applied to dc nanogrid clusters for rural electrification in developing regions," *IEEE Transactions on Power Electronics*, vol. 34, no. 2, pp. 1773–1785, 2018.

[27] A. Clements, "Data-driven approaches enabling the design of community energy systems in the global south," Ph.D. dissertation, University of Oxford, 2018.

[28] H. Kirchhoff, "Identifying hidden resources in solar home systems as the basis for bottom-up grids," in *Decentralized Solutions for Developing Economies*. Springer, 2015, pp. 23–32.

[29] A. G. Dagnachew, P. L. Lucas, A. F. Hof, D. E. Gernaat, H.-S. de Boer, and D. P. van Vuuren, "The role of decentralized systems in providing universal electricity access in sub-saharan africa–a model-based approach," *Energy*, vol. 139, pp. 184–195, 2017.

[30] F. F. Nerini, O. Broad, D. Mentis, M. Welsch, M. Bazilian, and M. Howells, "A cost comparison of technology approaches for improving access to electricity services," *Energy*, vol. 95, pp. 255–265, 2016.

[31] T. Levin and V. M. Thomas, "Can developing countries leapfrog the centralized electrification paradigm?" *Energy for Sustainable Development*, vol. 31, pp. 97–107, 2016.

[32] N. Narayan, A. Chamseddine, V. Vega-Garita, Z. Qin, J. Popovic-Gerber, P. Bauer, and M. Zeman, "Exploring the boundaries of Solar Home Systems (SHS) for off-grid electrification: Optimal SHS sizing for the multi-tier framework for household electricity access," *Applied energy*, vol. 240, pp. 907–917, 2019.

[33] H. Kirchhoff and K. Strunz, "Key drivers for successful development of peer-to-peer microgrids for swarm electrification," *Applied Energy*, vol. 244, pp. 46–62, 2019.

[34] N. Narayan, A. Chamseddine, V. Vega-Garita, Z. Qin, J. Popovic-Gerber, P. Bauer, and M. Zeman, "Quantifying the benefits of a Solar Home System-Based DC microgrid for rural electrification," *Energies*, vol. 12, no. 5, p. 938, 2019.

[35] Univeristy of Oxford, “Robust extra low cost nano grid - enabling access for every person to affordable, smart, productive power.” 2020. [Online]. Available: https://epg.eng.ox.ac.uk/our-research/relcon/

[36] S. Vazquez, S. M. Lukic, E. Galvan, L. G. Franquelo, and J. M. Carrasco, “Energy storage systems for transport and grid applications,” *IEEE Transactions on Industrial Electronics*, vol. 57, no. 12, pp. 3881–3895, 2010.

[37] M. Nasir, H. A. Khan, A. Hussain, L. Mateen, and N. A. Zaffar, “Solar pv-based scalable DC microgrid for rural electrification in developing regions,” *IEEE Transactions on sustainable energy*, vol. 9, no. 1, pp. 390–399, 2017.

[38] H. Akagi, S.-i. Kinouchi, and Y. Miyazaki, “Bidirectional isolated dual-active-bridge (DAB) DC-DC converters using 1.2-kV 400-A SiC-MOSFET dual modules,” *CPSS Transactions on Power Electronics and Applications*, vol. 1, no. 1, pp. 33–40, 2016.

[39] T. Dragičević, X. Lu, J. C. Vasquez, and J. M. Guerrero, “DC microgridspart ii: A review of power architectures, applications, and standardization issues,” *IEEE transactions on power electronics*, vol. 31, no. 5, pp. 3528–3549, 2015.

[40] J. Kumar, A. Agarwal, and V. Agarwal, “A review on overall control of DC microgrids,” *Journal of energy storage*, vol. 21, pp. 113–138, 2019.

[41] J. M. Guerrero, J. C. Vasquez, J. Matas, L. G. De Vicuña, and M. Castilla, “Hierarchical control of droop-controlled AC and DC microgridsa general approach toward standardization,” *IEEE Transactions on industrial electronics*, vol. 58, no. 1, pp. 158–172, 2010.

[42] M. Amin, Y. Arafat, S. Lundberg, and S. Mangold, “Low voltage DC distribution system compared with 230 V AC,” in *2011 IEEE Electrical Power and Energy Conference*. IEEE, 2011, pp. 340–345.

[43] S. Moussa, M. J.-B. Ghorbal, and I. Slama-Belkhodja, “Bus voltage level choice for standalone residential DC nanogrid,” *Sustainable Cities and Society*, vol. 46, p. 101431, 2019.

[44] J. W. Stevens and G. P. Corey, “A study of lead-acid battery efficiency near top-of-charge and the impact on PV system design,” in *Conference Record of the Twenty Fifth IEEE Photovoltaic Specialists Conference-1996*. IEEE, 1996, pp. 1485–1488.

[45] F. A. Amoroso and G. Cappuccino, “Impact of charging efficiency variations on the effectiveness of variable-rate-based charging strategies for electric vehicles,” *Journal of Power Sources*, vol. 196, no. 22, pp. 9574–9578, 2011.

[46] T. Morstyn, B. Hredzak, R. P. Aguilera, and V. G. Agelidis, “Model predictive control for distributed microgrid battery energy storage systems,” *IEEE Transactions on Control Systems Technology*, vol. 26, no. 3, pp. 1107–1114, 2017.

[47] M. Jafari, Z. Malekjamshidi, G. Platt, J. G. Zhu, and D. G. Dorrell, “A multi-port converter based renewable energy system for residential consumers of smart grid,” in *IECON 2015 - 41st Annual Conference of the IEEE Industrial Electronics Society*, 2015, pp. 005 168–005 173.

[48] L. Piris-Botalla, G. G. Oggier, A. M. Airabella, and G. O. García, “Power losses evaluation of a bidirectional three-port DC–DC converter for hybrid electric system,” *International Journal of Electrical Power & Energy Systems*, vol. 58, pp. 1–8, 2014.

[49] C. Fischer, S. Mariéthoz, and M. Morari, “An optimal modulation strategy for minimising the losses of isolated multisource DC-DC converters,” in *IECON 2012-38th Annual Conference on IEEE Industrial Electronics Society*. IEEE, 2012, pp. 2174–2179.

[50] S. Mishra and O. Ray, “Advances in nanogrid technology and its integration into rural electrification in india,” in *2014 International Power Electronics Conference (IPEC-Hiroshima 2014 - ECCE ASIA)*, 2014, pp. 2707–2713.

[51] M. Ahmed, U. Amin, S. A. Qureshi, and Z. Ahmed, “Implementation of nanogrids for future power system.” *Science International*, vol. 27, no. 1, 2015.

[52] A. Werth, N. Kitamura, and K. Tanaka, “Conceptual study for open energy systems: Distributed energy network using interconnected DC nanogrids,” *IEEE Transactions on Smart Grid*, vol. 6, no. 4, pp. 1621–1630, 2015.

[53] E. R. Daz, X. Su, M. Savaghebi, J. C. Vasquez, M. Han, and J. M. Guerrero, “Intelligent DC microgrid living laboratories - a chinese-danish cooperation project,” in *2015 IEEE First International Conference on DC Microgrids (ICDCM)*, 2015, pp. 365–370.

[54] M. Noritake, K. Yuasa, T. Takeda, K. Shimomachi, R. Hara, H. Kita, and T. Matsumura, “Experimental study of a 400 V class DC microgrid for commercial buildings,” in *2015 9th International Conference on Power Electronics and ECCE Asia (ICPE-ECCE Asia)*, 2015, pp. 1730–1735.

[55] H. Kim, Y. Cho, J. Kim, J. Cho, and J. Kim, “Demonstration of the LVDC distribution system in an island,” *CIRED-Open Access Proceedings Journal*, vol. 2017, no. 1, pp. 2215–2218, 2017.

[56] S. Anand and B. G. Fernandes, “Optimal voltage level for DC microgrids,” in *IECON 2010 - 36th Annual Conference on IEEE Industrial Electronics Society*, 2010, pp. 3034–3039.

[57] P. Hollberg, “Swarm grids-innovation in rural electrification,” Master’s thesis, 2015.

[58] B. Soltowski, J. Bowes, S. Strachan, and O. limpo Anaya-Lara, “A simulation-based evaluation of the benefits and barriers to interconnected solar home systems in east africa,” in *2018 IEEE PES/IAS PowerAfrica*. IEEE, 2018, pp. 491–496.

[59] B. Soltowski, D. Campos-Gaona, S. Strachan, and O. Anaya-Lara, “Bottom-up electrification introducing new smart grids architectureconcept based on feasibility studies conducted in rwanda,” *Energies*, vol. 12, no. 12, p. 2439, 2019.

[60] P. A. Madduri, J. Rosa, S. R. Sanders, E. A. Brewer, and M. Podolsky, “Design and verification of smart and scalable DC microgrids for emerging regions,” in *2013 IEEE Energy Conversion Congress and Exposition*, 2013, pp. 73–79.

[61] International Energy Agency, “Energy efficiency 2019, IEA, paris,” 2019. [Online]. Available: https://www.iea.org/reports/energy-efficiency-2019

[62] . Luca, I. Cvetkovic, H. Sarnago, D. Boroyevich, P. Mattavelli, and F. C. Lee, “Design of home appliances for a DC-based nanogrid system: An induction range study case,” *IEEE Journal of Emerging and Selected Topics in Power Electronics*, vol. 1, no. 4, pp. 315–326, 2013.

[63] R. V. Buskirk, “Doubling the global pace of progress for energy efficiency (EE): Applying a” moore’s law” of EE to technology innovation for off-grid applications,” Lawrence Berkeley National Laboratory, Tech. Rep., 2015. [Online]. Available: https://escholarship.org/uc/item/2zn1x958

[64] S. H. Low, “Convex relaxation of optimal power flowpart ii: Exactness,” *IEEE Transactions on Control of Network Systems*, vol. 1, no. 2, pp. 177–189, 2014.

[65] J. Li, F. Liu, Z. Wang, S. H. Low, and S. Mei, “Optimal power flow in stand-alone DC microgrids,” *IEEE Transactions on Power Systems*, vol. 33, no. 5, pp. 5496–5506, 2018.

[66] V. Krishnamurthy and A. Kwasinski, “Effects of power electronics, energy storage, power distribution architecture, and lifeline dependencies on microgrid resiliency during extreme events,” *IEEE Journal of Emerging and Selected Topics in Power Electronics*, vol. 4, no. 4, pp. 1310–1323, 2016.

[67] G. Manavalan, H. M. Tania, J. K. Patra, M. G. Poongothai, and S. Prema, “A closed loop system to stabilize a 24 V solar DC nano grid,” in *2017 International Conference on Smart grids, Power and Advanced Control Engineering (ICSPACE)*, 2017, pp. 177–182.

[68] T. L. Nguyen, J. M. Guerrero, and G. Griepentrog, “A self-sustained and flexible control strategy for islanded DC nanogrids without communication links,” *IEEE Journal of Emerging and Selected Topics in Power Electronics*, vol. 8, no. 1, pp. 877–892, 2020.

[69] M. R. Khan and E. D. Brown, “DC nanogrids: A low cost PV based solution for livelihood enhancement for rural bangladesh,” in *2014 3rd International Conference on the Developments in Renewable Energy Technology (ICDRET)*, 2014, pp. 1–5.

[70] R. M. Pindoriya, N. M. Pindoriya, and S. Rajendran, “Simulation of DC/DC converter for DC nano-grid integrated with solar PV generation,” in *2015 IEEE Innovative Smart Grid Technologies - Asia (ISGT ASIA)*, 2015, pp. 1–6.

[71] Y. Kado, D. Shichijo, K. Wada, and K. Iwatsuki, “Multiport power router and its impact on future smart grids,” *Radio Science*, vol. 51, no. 7, pp. 1234–1246, 2016.

[72] L. H. P. N. Gunawardena and D. R. Nayanasiri, “Networked DC nano-grid based on multi-port power converters,” in *TENCON 2017 - 2017 IEEE Region 10 Conference*, 2017, pp. 2727–2732.

[73] ME SOLshare Ltd., “From energy access in bangladesh to the future of energy utilities globally,” 2020. [Online]. Available: https://www.me-solshare.com/

[74] M. M. H. Sajeeb, A. Rahman, and S. Arif, “Feasibility analysis of solar DC nano grid for off grid rural bangladesh,” in *2015 3rd International Conference on Green Energy and Technology (ICGET)*, 2015, pp. 1–5.

[75] N. Narayan, “Solar home systems for improving electricity access: An off-grid solar perspective towards achieving universal electrification,” Ph.D. dissertation, 2019.

[76] M. Nasir, N. A. Zaffar, and H. A. Khan, “Analysis on central and distributed architectures of solar powered DC microgrids,” in *2016 Clemson University Power Systems Conference (PSC)*, 2016, pp. 1–6.

[77] L. Wu, W. Kihinet, E. Robelo, E. Bezabih, K. Longwood, T. Tshimanga, M. Saeedifard, F. Lambert, and R. Harley, “Development of a solar-power-based nanogrid system for village huts in haiti mountain area,” in *2016 North American Power Symposium (NAPS)*, 2016, pp. 1–5.

[78] P. Loomba, S. Asgotraa, and R. Podmore, "DC solar microgrids a successful technology for rural sustainable development," in *2016 IEEE PES PowerAfrica*, 2016, pp. 204–208.

[79] S. A. Chowdhury, "Solar DC grids for rural electrification," in *Micro Perspectives for Decentralized Energy Supply: Proceedings of the International Conference (2015, Bangalore): Universitätsverlag der TU Berlin*, 2015, p. 71.

[80] S. Mishra and O. Ray, "Advances in nanogrid technology and its integration into rural electrification in india," in *2014 International Power Electronics Conference (IPEC-Hiroshima 2014-ECCE ASIA)*. IEEE, 2014, pp. 2707–2713.

[81] A. Werth, N. Kitamura, and K. Tanaka, "Conceptual study for open energy systems: distributed energy network using interconnected DC nanogrids," *IEEE Transactions on Smart Grid*, vol. 6, no. 4, pp. 1621–1630, 2015.

[82] J. J. Justo, F. Mwasilu, J. Lee, and J.-W. Jung, "AC-microgrids versus DC-microgrids with distributed energy resources: A review," *Renewable and sustainable energy reviews*, vol. 24, pp. 387–405, 2013.

[83] Schneider Electric, "2 kW to 24 kW AC Micro Grid solution for electrification of off-grid," 2020. [Online]. Available: https://www.se.com/ph/en/product-range/62209-ac-micro-grid/?parent-subcategory-id=8610&filter=business-12-access-to-energy&subNodeId=12145062293en_PH

[84] K. Garbesi, V. Vossos, and H. Shen, "Catalog of DC appliances and power systems," Lawrence Berkeley National Lab.(LBNL), Berkeley, CA (United States), Tech. Rep., 2010.

[85] EMerge Alliance, "Alliance FAQs," 2020. [Online]. Available: https://www.emergealliance.org/about/alliance-faqs/

[86] K. I. Hwu and T. J. Peng, "A novel buckboost converter combining KY and buck converters," *IEEE Transactions on Power Electronics*, vol. 27, no. 5, pp. 2236–2241, 2012.

[87] B. M. Kumar, A. Kumar, A. H. Bhat, and P. Agarwal, "Comparative study of dual active bridge isolated DC to DC converter with single phase shift and dual phase shift control techniques," in *2017 Recent Developments in Control, Automation Power Engineering (RDCAPE)*, 2017, pp. 453–458.

[88] R. Gopinath, Sangsun Kim, Jae-Hong Hahn, P. N. Enjeti, M. B. Yeary, and J. W. Howze, "Development of a low cost fuel cell inverter system with DSP control," *IEEE Transactions on Power Electronics*, vol. 19, no. 5, pp. 1256–1262, 2004.

[89] J. Zeng, W. Qiao, L. Qu, and Y. Jiao, “An isolated multiport DCDC converter for simultaneous power management of multiple different renewable energy sources,” *IEEE Journal of Emerging and Selected Topics in Power Electronics*, vol. 2, no. 1, pp. 70–78, 2014.

[90] H. Tao, A. Kotsopoulos, J. L. Duarte, and M. A. M. Hendrix, “Family of multiport bidirectional DC-DC converters,” *IEE Proceedings - Electric Power Applications*, vol. 153, no. 3, pp. 451–458, 2006.

[91] H. Behjati and A. Davoudi, “Single-stage multi-port DC-DC converter topology,” *IET Power Electronics*, vol. 6, no. 2, pp. 392–403, 2013.

[92] F. Gonzalez-Longatt, B. S. Rajpurohit, and S. N. Singh, “Optimal structure of a smart dc micro-grid for a cluster of zero net energy buildings,” in *2016 IEEE International Energy Conference (ENERGYCON)*, 2016, pp. 1–7.

[93] D. Palit and G. K. Sarangi, “Renewable energy based mini-grids for enhancing electricity access: Experiences and lessons from india,” in *2014 International Conference and Utility Exhibition on Green Energy for Sustainable Development (ICUE)*, 2014, pp. 1–8.

[94] Shneider Electric, “0.5 kW to 10 kW prepaid DC Micro Grid solution with centralized generation and distributed storage,” 2020. [Online]. Available: https://www.se.com/ph/en/product-range-presentation/62210-dc-micro-grid/

[95] A. G. Tsikalakis and N. D. Hatziargyriou, “Centralized control for optimizing microgrids operation,” in *2011 IEEE power and energy society general meeting*. IEEE, 2011, pp. 1–8.

[96] L. Meng, Q. Shafiee, G. F. Trecate, H. Karimi, D. Fulwani, X. Lu, and J. M. Guerrero, “Review on control of DC microgrids and multiple microgrid clusters,” *IEEE Journal of Emerging and Selected Topics in Power Electronics*, vol. 5, no. 3, pp. 928–948, 2017.

[97] T. Morstyn, B. Hredzak, and V. G. Agelidis, “Control strategies for microgrids with distributed energy storage systems: An overview,” *IEEE Transactions on Smart Grid*, vol. 9, no. 4, pp. 3652–3666, 2018.

[98] B. Soltowski, S. Strachan, O. Anaya-Lara, D. Frame, and M. Dolan, “Using smart power management control to maximize energy utilization and reliability within a microgrid of interconnected solar home systems,” in *2017 IEEE Global Humanitarian Technology Conference (GHTC)*. IEEE, 2017, pp. 1–5.

[99] W. Fan, N. Liu, and J. Zhang, “An online lyapunov-based algorithm of resource sharing for interconnected DC nanogrids,” in *2016 IEEE 11th Conference on Industrial Electronics and Applications (ICIEA)*, 2016, pp. 2299–2304.

[100] S. Xu, H. Pourbabak, and W. Su, “Distributed cooperative control for economic operation of multiple plug-in electric vehicle parking decks,” *International Transactions on Electrical Energy Systems*, vol. 27, no. 9, p. e2348, 2017.

[101] U. B. Tayab, M. A. B. Roslan, L. J. Hwai, and M. Kashif, “A review of droop control techniques for microgrid,” *Renewable and Sustainable Energy Reviews*, vol. 76, pp. 717–727, 2017.

[102] J. Bryan, R. Duke, and S. Round, “Decentralized generator scheduling in a nanogrid using DC bus signaling,” in *IEEE Power Engineering Society General Meeting, 2004.*, 2004, pp. 977–982 Vol.1.

[103] L. Zhang, T. Wu, Y. Xing, K. Sun, and J. M. Gurrero, “Power control of DC microgrid using DC bus signaling,” in *2011 Twenty-Sixth Annual IEEE Applied Power Electronics Conference and Exposition (APEC)*, 2011, pp. 1926–1932.

[104] H. Kirchhoff, M. Schmid, P. Adelmann, and K. Strunz, “Passive droop control in a decentralized 12v DC energy access microgrid with lead acid batteries,” in *Micro Perspectives for Decentralized Energy Supply: Proceedings of the International Conference (2015, Bangalore): Universitätsverlag der TU Berlin*, 2015, p. 61.

[105] X. Lu, K. Sun, J. M. Guerrero, J. C. Vasquez, and L. Huang, “State-of-charge balance using adaptive droop control for distributed energy storage systems in DC microgrid applications,” *IEEE Transactions on Industrial Electronics*, vol. 61, no. 6, pp. 2804–2815, 2014.

[106] W. Han, C. Zou, C. Zhou, and L. Zhang, “Estimation of cell SOC evolution and system performance in module-based battery charge equalization systems,” *IEEE Transactions on Smart Grid*, vol. 10, no. 5, pp. 4717–4728, 2019.

[107] X. Lu, K. Sun, J. M. Guerrero, J. C. Vasquez, and L. Huang, “Double-quadrant state-of-charge-based droop control method for distributed energy storage systems in autonomous DC microgrids,” *IEEE Transactions on Smart Grid*, vol. 6, no. 1, pp. 147–157, 2015.

[108] Chendan Li, T. Dragicevic, N. L. Diaz, J. C. Vasquez, and J. M. Guerrero, “Voltage scheduling droop control for state-of-charge balance of distributed energy storage in DC microgrids,” in *2014 IEEE International Energy Conference (ENERGYCON)*, 2014, pp. 1310–1314.

[109] R. K. Chauhan, K. Chauhan, A. Mehrotra, A. K. Agarwal, B. R. Subrahmanyam, A. G. Singh, and D. Singh, "Droop control based battery management system for automated DC microgrid," in *2020 International Conference on Contemporary Computing and Applications (IC3A)*, 2020, pp. 81–86.

[110] R. Zhao, Y. Yang, C. Zhang, Z. Wei, and M. Deng, "Multi-energy storage control based on SOC for dc-microgrid," in *2019 IEEE 4th Advanced Information Technology, Electronic and Automation Control Conference (IAEAC)*, vol. 1, 2019, pp. 222–226.

[111] Rui Hu and W. W. Weaver, "Dc microgrid droop control based on battery state of charge balancing," in *2016 IEEE Power and Energy Conference at Illinois (PECI)*, 2016, pp. 1–8.

[112] M. Shahbazi, B. Kazemtabrizi, and C. Dent, "Coordinated control of DC voltage magnitudes and state of charges in a cluster of DC microgrids," in *2016 IEEE PES Innovative Smart Grid Technologies Conference Europe (ISGT-Europe)*, 2016, pp. 1–5.

[113] V. Nasirian, Q. Shafiee, J. M. Guerrero, F. L. Lewis, and A. Davoudi, "Droop-free distributed control for AC microgrids," *IEEE Transactions on Power Electronics*, vol. 31, no. 2, pp. 1600–1617, 2016.

[114] S. Moayedi and A. Davoudi, "Distributed tertiary control of DC microgrid clusters," *IEEE Transactions on Power Electronics*, vol. 31, no. 2, pp. 1717–1733, 2015.

[115] R. Olfati-Saber, J. A. Fax, and R. M. Murray, "Consensus and cooperation in networked multi-agent systems," *Proceedings of the IEEE*, vol. 95, no. 1, pp. 215–233, 2007.

[116] L. Xiao and S. Boyd, "Fast linear iterations for distributed averaging," *Systems & Control Letters*, vol. 53, no. 1, pp. 65–78, 2004.

[117] S. Boyd, A. Ghosh, B. Prabhakar, and D. Shah, "Randomized gossip algorithms," *IEEE transactions on information theory*, vol. 52, no. 6, pp. 2508–2530, 2006.

[118] N. Liu and J. Wang, "Energy sharing for interconnected microgrids with a battery storage system and renewable energy sources based on the alternating direction method of multipliers," *Applied Sciences*, vol. 8, no. 4, p. 590, 2018.

[119] S. Sahoo, S. Mishra, S. Jha, and B. Singh, "A cooperative adaptive droop based energy management and optimal voltage regulation scheme for dc microgrids," *IEEE Transactions on Industrial Electronics*, vol. 67, no. 4, pp. 2894–2904, 2019.

[120] Q. Shafiee, T. Dragičević, J. C. Vasquez, and J. M. Guerrero, "Hierarchical control for multiple DC-microgrids clusters," *IEEE Transactions on Energy Conversion*, vol. 29, no. 4, pp. 922–933, 2014.

[121] V. Nasirian, S. Moayedi, A. Davoudi, and F. L. Lewis, “Distributed cooperative control of DC microgrids,” *IEEE Transactions on Power Electronics*, vol. 30, no. 4, pp. 2288–2303, 2014.

[122] L. Meng, T. Dragicevic, J. C. Vasquez, and J. M. Guerrero, “Tertiary and secondary control levels for efficiency optimization and system damping in droop controlled DC–DC converters,” *IEEE Transactions on Smart Grid*, vol. 6, no. 6, pp. 2615–2626, 2015.

[123] Z. Zhao, J. Hu, H. Xue, R. Huang, X. Li, and X. Zhang, “Large signal stability analysis of DC microgrid under droop control with constant power load,” in *2017 Chinese Automation Congress (CAC)*, 2017, pp. 1046–1051.

[124] N. Ghanbari and S. Bhattacharya, “Constant power load challenges in droop controlled DC microgrids,” in *IECON 2019 - 45th Annual Conference of the IEEE Industrial Electronics Society*, vol. 1, 2019, pp. 3871–3876.

[125] K. Unger, “Organically grown microgrids: The development and simulation of a solar home system-based microgrid,” Master’s thesis, University of Waterloo, 2012.

[126] L. Strenge, “Modeling and simulation of a droop controlled swarm type low voltage DC microgrid in a DAE framework,” Master’s thesis, 2015.

[127] M. R. Khan and E. D. Brown, “A concept of DC nano-grid for low cost energy access in rural bangladesh,” in *Decentralized Solutions for Developing Economies*. Springer, 2015, pp. 33–42.

[128] S. Groh, D. Philipp, B. E. Lasch, and H. Kirchhoff, “Swarm electrification: Investigating a paradigm shift through the building of microgrids bottom-up,” in *Decentralized Solutions for Developing Economies*. Springer, 2015, pp. 3–22.

[129] M. M. Hoffmann and D. Ansari, “Simulating the potential of swarm grids for pre-electrified communities–a case study from yemen,” *Renewable and Sustainable Energy Reviews*, vol. 108, pp. 289–302, 2019.

[130] A. Magnasco, H. Kirchhoff, S. Chowdhury, and S. Groh, “Data services for real time optimization of DC nanogrids with organic growth,” *Energy Procedia*, vol. 103, pp. 369–374, 2016.

[131] M. Nasir, S. Iqbal, and H. A. Khan, “Optimal planning and design of low-voltage low-power solar DC microgrids,” *IEEE Transactions on Power Systems*, vol. 33, no. 3, pp. 2919–2928, 2017.

[132] M. Hamza, M. Shehroz, S. Fazal, M. Nasir, and H. A. Khan, “Design and analysis of solar PV based low-power low-voltage DC microgrid architectures for rural electrification,” in *2017 IEEE Power & Energy Society General Meeting*. IEEE, 2017, pp. 1–5.

[133] R. Khan, N. N. Schulz, and M. Nasir, “Distribution loss analysis of DC microgrids for rural electrification,” in *2019 IEEE Global Humanitarian Technology Conference (GHTC)*. IEEE, 2019, pp. 1–8.

[134] N. Lidula and A. Rajapakse, “Microgrids research: A review of experimental microgrids and test systems,” *Renewable and Sustainable Energy Reviews*, vol. 15, no. 1, pp. 186–202, 2011.

[135] M. Aragüés-Peñalba, A. Egea-Àlvarez, O. Gomis-Bellmunt, and A. Sumper, “Optimum voltage control for loss minimization in HVDC multi-terminal transmission systems for large offshore wind farms,” *Electric power systems research*, vol. 89, pp. 54–63, 2012.

[136] C. Ahn and H. Peng, “Decentralized voltage control to minimize distribution power loss of microgrids,” *IEEE Transactions on Smart Grid*, vol. 4, no. 3, pp. 1297–1304, 2013.

[137] J. Ma, L. Yuan, Z. Zhao, and F. He, “Transmission loss optimization-based optimal power flow strategy by hierarchical control for DC microgrids,” *IEEE Transactions on Power Electronics*, vol. 32, no. 3, pp. 1952–1963, 2016.

[138] F. Mangiatordi, E. Pallotti, D. Panzieri, and L. Capodiferro, “Multi agent system for cooperative energy management in microgrids,” in *2016 IEEE 16th International Conference on Environment and Electrical Engineering (EEEIC)*. IEEE, 2016, pp. 1–5.

[139] C. Wei, Z. M. Fadlullah, N. Kato, and I. Stojmenovic, “On optimally reducing power loss in micro-grids with power storage devices,” *IEEE Journal on Selected Areas in Communications*, vol. 32, no. 7, pp. 1361–1370, 2014.

[140] T. Zhu, Z. Huang, A. Sharma, J. Su, D. Irwin, A. Mishra, D. Menasche, and P. Shenoy, “Sharing renewable energy in smart microgrids,” in *2013 ACM/IEEE International Conference on Cyber-Physical Systems (ICCPS)*. IEEE, 2013, pp. 219–228.

[141] W. Saad, Z. Han, and H. V. Poor, “Coalitional game theory for cooperative micro-grid distribution networks,” in *2011 IEEE international conference on communications workshops (ICC)*. IEEE, 2011, pp. 1–5.

[142] Y. Xu, W. Zhang, G. Hug, S. Kar, and Z. Li, “Cooperative control of distributed energy storage systems in a microgrid,” *IEEE Transactions on smart grid*, vol. 6, no. 1, pp. 238–248, 2014.

[143] Z. Wang, F. Liu, Y. Chen, S. H. Low, and S. Mei, “Unified distributed control of stand-alone DC microgrids,” *IEEE Transactions on Smart Grid*, vol. 10, no. 1, pp. 1013–1024, 2017.

[144] C. Zhao, J. He, P. Cheng, and J. Chen, “Consensus-based energy management in smart grid with transmission losses and directed communication,” *IEEE Transactions on smart grid*, vol. 8, no. 5, pp. 2049–2061, 2016.

[145] G. Binetti, A. Davoudi, F. L. Lewis, D. Naso, and B. Turchiano, “Distributed consensus-based economic dispatch with transmission losses,” *IEEE Transactions on Power Systems*, vol. 29, no. 4, pp. 1711–1720, 2014.

[146] J.-H. Teng, S.-W. Luan, D.-J. Lee, and Y.-Q. Huang, “Optimal charging/discharging scheduling of battery storage systems for distribution systems interconnected with sizeable pv generation systems,” *IEEE Transactions on Power Systems*, vol. 28, no. 2, pp. 1425–1433, 2012.

[147] M. Farasat and A. Arabali, “Voltage and power control for minimising converter and distribution losses in autonomous microgrids,” *IET Generation, Transmission & Distribution*, vol. 9, no. 13, pp. 1614–1620, 2015.

[148] S. Boyd, S. P. Boyd, and L. Vandenberghe, *Convex optimization*. Cambridge university press, 2004.

[149] S. Falcones, R. Ayyanar, and X. Mao, “A DC–DC multiport-converter-based solid-state transformer integrating distributed generation and storage,” *IEEE Transactions on Power Electronics*, vol. 28, no. 5, pp. 2192–2203, 2012.

[150] M. Kheraluwala, R. W. Gascoigne, D. M. Divan, and E. D. Baumann, “Performance characterization of a high-power dual active bridge DC-to-DC converter,” *IEEE Transactions on industry applications*, vol. 28, no. 6, pp. 1294–1301, 1992.

[151] R. W. Erickson and D. Maksimovic, *Fundamentals of power electronics*. Springer Science & Business Media, 2007.

[152] L. Balogh, “Design and application guide for high speed MOSFET gate drive circuits,” in *Power Supply Design Seminar SEM-1400, Topic*, vol. 2, 2001.

[153] C. W. T. McLyman, *Transformer and inductor design handbook*. CRC press, 2017.

[154] J. Reinert, A. Brockmeyer, and R. W. De Doncker, “Calculation of losses in ferro-and ferrimagnetic materials based on the modified steinmetz equation,” *IEEE Transactions on Industry applications*, vol. 37, no. 4, pp. 1055–1061, 2001.

[155] A. Van den Bossche, V. C. Valchev, and G. B. Georgiev, “Measurement and loss model of ferrites with non-sinusoidal waveforms,” in *2004 IEEE 35th Annual Power Electronics Specialists Conference (IEEE Cat. No. 04CH37551)*, vol. 6. IEEE, 2004, pp. 4814–4818.

[156] R. Zhong and K. Wille, “Equal arc segment method for averaging data plots exemplified for averaging stress versus strain curves of pervious concrete,” *Journal of Materials in Civil Engineering*, vol. 28, no. 1, p. 04015071, 2016.

[157] A. Arif, Z. Wang, J. Wang, B. Mather, H. Bashualdo, and D. Zhao, “Load modelinga review,” *IEEE Transactions on Smart Grid*, vol. 9, no. 6, pp. 5986–5999, 2017.

[158] K. Lindén and I. Segerqvist, “Modelling of load devices and studying load/system characteristics,” pp. 1–10, 1992.

[159] H. L. Willis, *Power distribution planning reference book.* CRC press, 2004.

[160] C. Cresswell, “Steady state load models for power system analysis,” Ph.D. dissertation, University of Edinburgh, 2009.

[161] L. Cristaldi, M. Faifer, M. Rossi, and S. Toscani, “An improved model-based maximum power point tracker for photovoltaic panels,” *IEEE transactions on instrumentation and measurement*, vol. 63, no. 1, pp. 63–71, 2013.

[162] G. Walker *et al.*, “Evaluating mppt converter topologies using a MATLAB PV model,” *Journal of Electrical & Electronics Engineering*, vol. 21, no. 1, pp. 49–56, 2001.

[163] M. G. Villalva, J. R. Gazoli, and E. Ruppert Filho, “Comprehensive approach to modeling and simulation of photovoltaic arrays,” *IEEE Transactions on power electronics*, vol. 24, no. 5, pp. 1198–1208, 2009.

[164] Y. Riffonneau, S. Bacha, F. Barruel, and S. Ploix, “Optimal power flow management for grid connected PV systems with batteries,” *IEEE Transactions on sustainable energy*, vol. 2, no. 3, pp. 309–320, 2011.

[165] L. Cristaldi, M. Faifer, M. Rossi, and F. Ponci, “A simple photovoltaic panel model: Characterization procedure and evaluation of the role of environmental measurements,” *IEEE Transactions on Instrumentation and Measurement*, vol. 61, no. 10, pp. 2632–2641, 2012.

[166] M. G. Wanzeller, R. N. C. Alves, J. V. da Fonseca Neto, and W. A. S. Fonseca, “Current control loop for tracking of maximum power point supplied for photovoltaic array,” *IEEE Transactions on Instrumentation and Measurement*, vol. 53, no. 4, pp. 1304–1310, 2004.

[167] C. Carrero, J. Amador, and S. Arnaltes, “A single procedure for helping PV designers to select silicon PV modules and evaluate the loss resistances,” *Renewable Energy*, vol. 32, no. 15, pp. 2579–2589, 2007. [Online]. Available: https://ideas.repec.org/a/eee/renene/v32y2007i15p2579-2589.html

[168] H.-L. Tsai, T. Ci-Siang, and S. Yi-Jie, “Development of generalized photovoltaic model using matlab/simulink,” *Lecture Notes in Engineering and Computer Science*, vol. 2173, 10 2008.

[169] A. M. Bizeray, S. Zhao, S. R. Duncan, and D. A. Howey, “Lithium-ion battery thermal-electrochemical model-based state estimation using orthogonal collocation and a modified extended kalman filter,” *Journal of Power Sources*, vol. 296, pp. 400–412, 2015.

[170] K. A. Smith, C. D. Rahn, and C.-Y. Wang, “Model-based electrochemical estimation of lithium-ion batteries,” in *2008 IEEE International Conference on Control Applications*. IEEE, 2008, pp. 714–719.

[171] C. Birkl and D. Howey, “Model identification and parameter estimation for LiFePO4 batteries,” in *IET Hybrid and Electric Vehicles Conference 2013 (HEVC 2013)*, 2013, pp. 1–6.

[172] S. Zhao and D. A. Howey, “Global sensitivity analysis of battery equivalent circuit model parameters,” in *2016 IEEE Vehicle Power and Propulsion Conference (VPPC)*. IEEE, 2016, pp. 1–4.

[173] M. Ansarey, M. S. Panahi, H. Ziarati, and M. Mahjoob, “Optimal energy management in a dual-storage fuel-cell hybrid vehicle using multi-dimensional dynamic programming,” *Journal of Power Sources*, vol. 250, pp. 359–371, 2014.

[174] T. Morstyn, B. Hredzak, and V. G. Agelidis, “Dynamic optimal power flow for DC microgrids with distributed battery energy storage systems,” in *2016 IEEE Energy Conversion Congress and Exposition (ECCE)*. IEEE, 2016, pp. 1–6.

[175] B. Liu, Z. Lu, K. Yao, and F. Gao, “A MPC operation method for a photovoltaic system with batteries,” *IFAC-PapersOnLine*, vol. 48, no. 8, pp. 807–812, 2015.

[176] F. R. Islam, K. Al Mamun, and M. T. O. Amanullah, *Smart Energy Grid Design for Island Countries: Challenges and Opportunities*. Springer, 2017.

[177] T. L. Vandoorn, J. D. De Kooning, B. Meersman, J. M. Guerrero, and L. Vandevelde, "Automatic power-sharing modification of *p*/*v* droop controllers in low-voltage resistive microgrids," *IEEE Transactions on Power Delivery*, vol. 27, no. 4, pp. 2318–2325, 2012.

[178] Climate-data.org, "Africa climate," 2020. [Online]. Available: https://en.climate-data.org/north-america/panama/bocas-del-toro/africa-874631/

[179] J. P. Joule, "XXXVIII. on the heat evolved by metallic conductors of electricity, and in the cells of a battery during electrolysis," *The London, Edinburgh, and Dublin Philosophical Magazine and Journal of Science*, vol. 19, no. 124, pp. 260–277, 1841.

[180] S. Erol, M. E. Orazem, and R. P. Muller, "Influence of overcharge and over-discharge on the impedance response of LiCoO2—C batteries," *Journal of power sources*, vol. 270, pp. 92–100, 2014.

[181] D. Ouyang, M. Chen, J. Liu, R. Wei, J. Weng, and J. Wang, "Investigation of a commercial lithium-ion battery under overcharge/over-discharge failure conditions," *RSC advances*, vol. 8, no. 58, pp. 33 414–33 424, 2018.

[182] Y. Saito, M. Shikano, and H. Kobayashi, "Heat generation behavior during charging and discharging of lithium-ion batteries after long-time storage," *Journal of Power Sources*, vol. 244, pp. 294–299, 2013.

[183] S. Boyd, S. P. Boyd, and L. Vandenberghe, *Convex optimization*. Cambridge university press, 2004.

[184] D. E. Olivares, C. A. Cañizares, and M. Kazerani, "A centralized energy management system for isolated microgrids," *IEEE Transactions on smart grid*, vol. 5, no. 4, pp. 1864–1875, 2014.

[185] Z. M. Fadlullah and N. Kato, *Considered Smart Grid Model: Evolution of Smart Grids*. Springer, 2015.

[186] S. Leyffer and A. Mahajan, "Nonlinear constrained optimization: methods and software," *Argonee National Laboratory, Argonne, Illinois*, vol. 60439, 2010.

[187] R. T. Rockafellar, "Lagrange multipliers and optimality," *SIAM review*, vol. 35, no. 2, pp. 183–238, 1993.

[188] J. Zhan, Q. Wu, C. Guo, and X. Zhou, "Fast lambda iteration method for economic dispatch with prohibited operating zones," *IEEE Transactions on power systems*, vol. 29, no. 2, pp. 990–991, 2013.

[189] G. Chauhan, A. Jain, and N. Verma, “Solving economic dispatch problem using mipower by lambda iteration method,” in *2017 1st International Conference on Intelligent Systems and Information Management (ICISIM)*, 2017, pp. 95–99.

[190] P. K. Singhal, R. Naresh, V. Sharma, and Goutham Kumar N, “Enhanced lambda iteration algorithm for the solution of large scale economic dispatch problem,” in *International Conference on Recent Advances and Innovations in Engineering (ICRAIE-2014)*, 2014, pp. 1–6.

[191] D. Dike Obioma and A. M. Izuchukwu, “Comparative analysis of techniques for economic dispatch of generated power with modified lambda-iteration method,” in *2013 IEEE International Conference on Emerging Sustainable Technologies for Power ICT in a Developing Society (NIGERCON)*, 2013, pp. 231–237.

[192] A. J. Wood, B. F. Wollenberg, and G. B. Sheblé, *Power generation, operation, and control*. John Wiley & Sons, 2013.

[193] H. Perfect and L. Mirsky, “Spectral properties of doubly-stochastic matrices,” *Monatshefte für Mathematik*, vol. 69, no. 1, pp. 35–57, 1965.

[194] G. M. Engel, H. Schneider, and S. Sergeev, “On sets of eigenvalues of matrices with prescribed row sums and prescribed graph.”

[195] K. Das, A. Nitsas, M. Altin, A. D. Hansen, and P. E. Sørensen, “Improved load-shedding scheme considering distributed generation,” *IEEE Transactions on Power Delivery*, vol. 32, no. 1, pp. 515–524, 2016.

[196] R. Lamedica, E. Santini, S. Teodori, and D. Z. Romito, “Electrical loads management in energy emergency conditions,” *International Journal of Electrical Power & Energy Systems*, vol. 66, pp. 86–96, 2015.

[197] N. Nishant, “Electrical power consumption load profiles for households with DC appliances related to multi-tier framework for household electricity access,” 2018. [Online]. Available: https://data.4tu.nl/repository/uuid:c8efa325-87fe-4125-961e-9f2684cd2086

[198] R. Olfati-Saber and R. M. Murray, “Consensus problems in networks of agents with switching topology and time-delays,” *IEEE Transactions on automatic control*, vol. 49, no. 9, pp. 1520–1533, 2004.

[199] Z. Zhang and M.-Y. Chow, “Convergence analysis of the incremental cost consensus algorithm under different communication network topologies in a smart grid,” *IEEE Transactions on Power Systems*, vol. 27, no. 4, pp. 1761–1768, 2012.

[200] R. Smunyahirun and E. L. Tan, “Derivation of the most energy-efficient source functions by using calculus of variations,” *IEEE Transactions on Circuits and Systems I: Regular Papers*, vol. 63, no. 4, pp. 494–502, 2016.

[201] X. Li, S. James, and R. Tim, “Microgrid load and LCOE modelling results,” 2018. [Online]. Available: https://data.nrel.gov/submissions/79

[202] T. L. Nguyen and G. Griepentrog, “Modeling, control and stability analysis for a DC nanogrid system,” in *2018 IEEE 19th Workshop on Control and Modeling for Power Electronics (COMPEL)*, 2018, pp. 1–8.

[203] D. B. West *et al.*, *Introduction to graph theory*. Prentice hall Upper Saddle River, 2001, vol. 2.

[204] Y. Xu and W. Liu, “Novel multiagent based load restoration algorithm for microgrids,” *IEEE Transactions on Smart Grid*, vol. 2, no. 1, pp. 152–161, 2011.

[205] A. W. Marshall, I. Olkin, and B. C. Arnold, *Inequalities: theory of majorization and its applications*. Springer, 1979, vol. 143.

[206] S.-i. Baik and K. Bang, “Limit theorem of the doubly stochastic matrices,” *Kangweon-Kyungki Math. Jour*, vol. 11, no. 2, pp. 155–160, 2003.

[207] K. Cai and H. Ishii, “Average consensus on general strongly connected digraphs,” *Automatica*, vol. 48, no. 11, pp. 2750–2761, 2012.

Appendix A

Theory of Convex Optimisation

In this appendix, the theory of convex optimisation which was necessary for gauging whether the formulated optimisation problem in Chapter 3 was either convex or non-convex is presented. Unlike non-convex optimisation problems, convex optimisation problems have guaranteed optimal solutions. Therefore, it was necessary to first understand the concept of convex optimisation before formulating the optimisation problem of the solar nano-grid. The next subsections therefore introduces the concepts of convex optimisation which are based on the material presented in [148].

A.1 Definition of an Optimisation Problem

A standard optimisation problem is stated as follows [148]:

$$\begin{aligned} \underset{x}{\text{minimise}} \;\; & f(x) && \text{(A.1a)} \\ \text{subject to} \;\; & h_i(x) = 0 \;\; i = 1, \dots, p && \text{(A.1b)} \\ & g_i(x) \leq 0 \;\; i = 1, \dots, m && \text{(A.1c)} \end{aligned}$$

where $x = [x_1, x_2 \cdots, x_n] \in \mathbf{R}^n$ is a vector of decision variables, $f : \mathbf{R}^n \rightarrow \mathbf{R}$ is an objective function which quantifies the decision of choosing x, (A.1b) and (A.1c) are a set of equality constraints and a set of inequality constraints respectively that should be satisfied by $x \in \mathbf{R}^n$, p and m are the total number of equality and inequality constraints respectively.

Based on the nature of (A.1a), (A.1b) and (A.1c), the optimisation problem in (A.1) can be classified as either a convex optimisation problem or a non-convex optimisation problem. Convex sets and convex functions are important for classifying the optimisation problem, these are presented in the next subsections.

A.2 Convex Sets

When the constraints; (A.1b) and (A.1c) in (A.1) are intersected, the points that are common to each one of them form a feasible set, $\mathbf{S}$. If $\mathbf{S}$ is empty while $p \geq 1$ and $m \geq 1$, it means

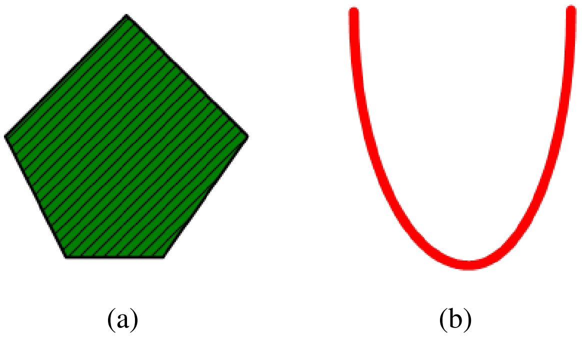

Figure A.1: Basic example of (a) a convex set and (b) a non-convex set.

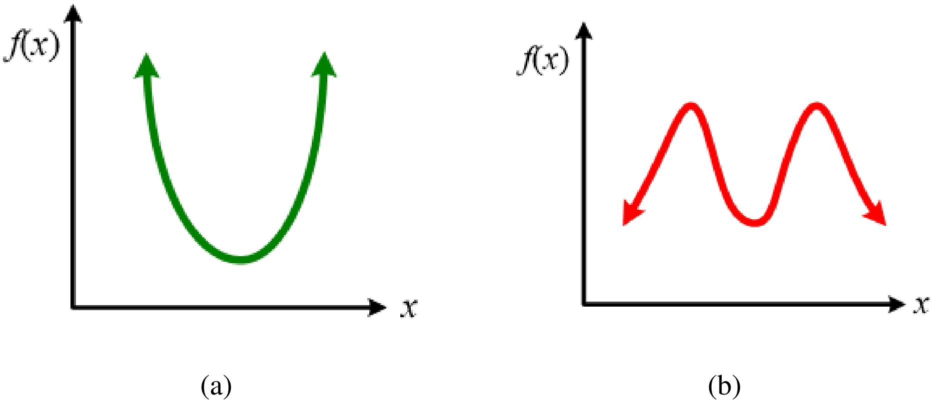

Figure A.2: Basic example of (a) a convex function and (b) a non-convex function.

that the problem (A.1) at hand cannot be optimised. In other words, **S** is a short list of all potential $x \in \mathbf{R}^n$ that can solve the optimisation problem (A.1) while satisfying (A.1b) and (A.1c). The **S** is a convex set if a line segment connecting two arbitrary points; θ_1 and θ_2 in **S** entirely lies in **S**, i.e.

$$\varsigma\theta_1 + (1-\varsigma)\theta_2 \in \mathbf{S}, \quad \forall\theta_1, \theta_2 \in \mathbf{S}, \quad \forall\varsigma \in [0,1]. \tag{A.2}$$

The **S** is non-convex if it does not satisfy the definition given in (A.2). Figure A.1 shows a basic example of a convex set and a non-convex set. As shown in Figure A.1, a set **S** formed by linear constraints is convex and a set **S** formed by quadratic constraint(s) is non-convex.

A.3 Convex Functions

An objective function, $f(x)$ given by (A.1a) is a convex function if a line segment connecting two arbitrary points; $(x_1, f(x_1))$ and $(x_2, f(x_2))$ on the curve of $f(x)$ lies on or above the curve of $f(x)$, i.e.

$$f(\varsigma x_1 + (1-\varsigma)x_2) \leq \varsigma f(x_1) + (1-\varsigma)f(x_2), \quad \forall x_1, x_2 \in \text{domain}(f), \quad \forall\varsigma \in [0,1]. \tag{A.3}$$

The $f(x)$ is a non-convex function if it does not satisfy the definition given in (A.3). Figure A.2 shows an example of a convex function and a non-convex function. As shown in Figure A.2, a quadratic function is convex while a polynomial is non-convex.

A.4 Convex Versus Non-Convex Optimisation Problem

An optimisation problem is convex if $f(x)$ is a convex function and **S** is a convex set (i.e. if all constraints are convex functions). Otherwise it is a non-convex optimisation problem. This kind of classification was used in this research to classify the optimisation problem that was formulated to minimise the power losses in the solar nano-grid.

Appendix B

Graph Theory and Consensus Algorithm

In this appendix, concepts of graph theory and average consensus algorithms are introduced, which were used to design the control algorithms in Chapter 5 and Chapter 6.

B.1 Graph Theory

The topology of the agents and the communication links between them in the cyber layer can be defined by a graph, G. Mathematically, G is defined as $G = (V, E)$, where V is a set of n agents labelled by an index $i = 0, \ldots, n$ and $E \subseteq V \times V$ is a set of unordered pairs (i, j) of agents called edges (i.e. communication links) [203]. An edge $(i, j) \in E$ shows that agent i and agent j are neighbours and can exchange information with each other. The set of neighbours of agent i is denoted by N_i, and the number of neighbours of agent i is denoted by d_i. Then, G is undirected if the edges are bidirectional i.e. $(i, j) \in E \Leftrightarrow (j, i) \in E$. The G is connected if there is a path from any agent i to any other agent j. The agents can exchange information on G with different communication gains, d_{ij}. For example, if agent j sends information x_j to agent i through the edge (i, j) with a gain of d_{ij}, then the information received by agent i is $d_{ij}x_j$. Thus, $d_{ij} > 0$ indicates that agent i can exchange information with agent j and $d_{ij} = 0$ indicates otherwise. The G can be represented by a symmetric adjacency matrix $\mathbf{D} = (d_{ij})_{n\times n}$ where d_{ij} can be computed as [204]

$$d_{ij} = \begin{cases} \frac{2}{d_i+d_j+1} & \text{if } i \neq j \\ 1 - \sum_{j\in N_i} \left(\frac{2}{d_i+d_j+1}\right) & \text{if } i = j \\ 0 & \text{otherwise} \end{cases} \tag{B.1}$$

where d_i and d_j are the number of agents which are neighbours to agent i and agent j respectively.

B.2 Average Consensus Algorithm

Each agent in the cyber layer only has direct access to its local information. One of the challenges of having multiple agents in the cyber layer is how to coordinate the agents so that they can accomplish a common difficult task or decision while satisfying their individual objectives. This challenge involves solving a distributed control problem, e.g. a consensus problem. Here, the agents are supposed to reach a consensus (i.e. agreement) on the best common decision that satisfies the requirements of all the agents in the network.

Consensus problems are easily solved by average consensus algorithms (hereafter referred to as consensus algorithms) which are computer-based rules that are given to each agent to ensure that all agents in the cyber layer reach consensus on a common decision through the exchange of information with their neighbours [204]. For example, suppose that agent i has a local scalar state, $x_i(k)$ in discrete time domain, k, $k \geq 0$ which it can exchange with agent j having a scalar state, $x_j(k)$. A consensus problem involves designing of an updating rule (i.e. consensus algorithm) that allows both agents to reach consensus on a common scalar state, x_a by (iteratively) updating their scalar states through information exchange with each other. The general updating rule of each agent in a network of n agents is proposed in literature as follows [116]

$$x_i^{(k+1)} = \sum_{j=0}^{n} d_{ij} x_j^{(k)} \tag{B.2}$$

where k is the iteration number and $x_i^{(k+1)}$ is the updated scalar state of agent i at $k+1$ as a weighted combination of its own $x_i^{(k)}$ and $x_j^{(k)}$, $j = 0, \dots, n$ received from other agents. The rule in (B.2) can be also written in matrix form as

$$\mathbf{X}^{(k+1)} = \mathbf{D}\mathbf{X}^{(k)} \tag{B.3}$$

where $\mathbf{X}^{(k)} = [x_0^{(k)}, x_1^{(k)}, \dots, x_n^{(k)}]^T$ is a n-dimensional vector of local scalar states of all the agents at discrete time k, $\mathbf{D} = (d_{ij}) n \times n$ is the symmetric adjacency matrix which describes the information exchange on G and $X(k+1) = [x_0^{(k+1)}, x_1^{(k+1)}, \dots, x_n^{(k+1)}]^T$ is the n-dimensional vector of updated local scalar states of all agents after information exchange at $k+1$.

If the row and column sum of $\mathbf{D}$ is 1, i.e. $\sum_j d_{ij} = 1$, $j = 0, 1, \dots, n$ and $\sum_i d_{ij} = 1$, $i = 0, 1, \dots, n$ respectively, then $\mathbf{D}$ is a doubly stochastic matrix [205]. According to Perron-Frobenius theorem [193], if $\mathbf{D}$ is a doubly stochastic matrix, then $\mu_0 = 1$ is a simple eigenvalue of $\mathbf{D}$ with all other eigenvalues, $\mu_1, \dots, \mu_n$ located within a unit circle. Consequently, $\mathbf{1} = [1, \dots, 1]^T$ and $\mathbf{1}^T$ are the n-dimensional right and left eigenvectors associated with $\mu_0 = 1$, i.e. $\mathbf{1}^T\mathbf{D} = 1$ and $\mathbf{D}\mathbf{1} = 1$. According to the limit theorem of doubly stochastic matrices [206] and if G is strongly connected [207], then the algorithm (B.3) is guaranteed to converge to the suitable x_a with time, i.e. $x_i^{(k)} = x_a$ as $k \to \infty$ for all $i = 0, 1, \dots, n$. If $x_i(\infty) = x_a = \mathbf{1}^T x_i^{(0)}/n$ where $x_i(0)$ is the initial value of x_i, the algorithm (B.3) is called an average consensus algorithm [116].

At convergence, the difference between the present and previous scalar states of each agent should be less than some predefined tolerance, $\left|x_i^{(k+1)} - x_i^{(k)}\right| \leq \xi_a$. The number of iterations, k_{max} needed to reach convergence is given in [116] as follows

$$k_{max} = \frac{-1}{\log_{\xi_a}(1/|\mu_1|)} \tag{B.4}$$

where μ_1 is the second largest eigenvalue of $\mathbf{D}$.

The theory of graphs and the basics of average consensus algorithms which are described above were used in this research to design distributed control algorithms to solve the power loss problem of the solar nano-grid.